STRUCTURAL AND SPECTROSCOPIC INVESTIGATIONS OF ORGANIC-INORGANIC HYBRID LEAD HALIDE PEROVSKITES

By

PRONOY NANDI

(PHYS07201304007)

INSTITUTE OF PHYSICS, BHUBANESWAR

A thesis submitted to the

Board of studies in Physical Sciences

In partial fulfillment of the requirements

For the Degree of

DOCTOR OF PHILOSOPHY
of
HOMI BHABHA NATIONAL INSTITUTE

October, 2019

Homi Bhabha National Institute

Recommendations of the Viva Voce Committee

As members of the Viva Voce Committee, we certify that we have read the dissertation prepared by Mr. Pronoy Nandi (HBNI Enrolment No. PHYS07201304007) entitled "**Structural and Spectroscopic Investigations of Organic-Inorganic Hybrid Lead Halide Perovskites"** and recommend that it may be accepted as fulfilling the thesis requirement for the award of Degree of Doctor of Philosophy.

Chairman - Prof. Arun M Jayannavar **Date:** 18/10/2019

Guide / Convener – Dr. Dinesh Topwal **Date:** 18/10/2019

—

Co-guide - <Name> (if any) **Date:** —

Examiner – Prof. Sameer Sapra **Date:** 18/10/2019

Member 1- Prof. Biju Raja Sekhar **Date:** 18/10/2019

Member 2- Dr. Goutam Tripathy **Date:** 18/10/19

Final approval and acceptance of this dissertation is contingent upon the candidate's submission of the final copies of the dissertation to HBNI.

I hereby certify that I have read this dissertation prepared under my direction and recommend that it may be accepted as fulfilling the dissertation requirement.

Date: 18/10/19

Place: Institute of Physics
Bhubaneswar

—

Co-guide (if applicable)

Guide
(DINESH TOPWAL)

Statement by author

This dissertation has been submitted in partial fulfillment of requirements for an advanced degree at Homi Bhabha National Institute (HBNI) and is deposited in the Library to be made available to borrowers under rules of the HBNI.

Brief quotations from this dissertation are allowable without special permission, provided that accurate acknowledgement of source is made. Requests for permission for extended quotation from or reproduction of this manuscript in whole or in part may be granted by the Competent Authority of HBNI when in his or her judgment the proposed use of the material is in the interests of scholarship. In all other instances, however, permission must be obtained from the author.

Pronoy Nandi

(Pronoy Nandi)

Declaration

I, Pronoy Nandi, hereby declare that the investigation presented in the thesis has been carried out by me. The work is original and has not been submitted earlier as a whole or in part for a degree / diploma at this or any other University / Institution.

Pronoy Nandi.

(Pronoy Nandi)

List of Publications:

1. * "$CH_3NH_3PbI_3$, A Potential Solar Cell Candidate: Structural and Spectroscopic Investigations", **Pronoy Nandi**, C. Giri, B. Joseph, S. Rath, U. Manju and D. Topwal, *J. Phys. Chem. A*, **2016**, *120*, 9732-9739.
2. * "Temperature Dependent Photo-induced Reversible Phase Separation in Mixed Halide Perovskite", **Pronoy Nandi**, C. Giri, D. Swain, U. Manju, S. D. Mahanti and D. Topwal, *ACS appl. Energy Mater.*, **2018**, *1*, 3807-3814.
3. "Role of Local Structural Distortion in Driving Ferroelectricity in $GdCrO_3$", S. Mahana, U. Manju, **Pronoy Nandi**, E. Welter, K. R. Priolkar and D. Topwal, *Phys. Rev. B*, **2018**, *97*, 224107.
4. "Self-Immobilized Pd Nanowires as an Excellent Platform for a Continuous Flow Reactor: Efficiency, Stability and Regeneration", L. Sahoo, M. Rana, S. Mandal, M. Mittal, **Pronoy Nandi**, A. Gloskovskii, U. Manju, D. Topwal, and U. K. Goutam, *Nanoscale,* **2018**, *10*, 21396-21405.
5. * "Room Temperature Growth of $CH_3NH_3PbCl_3$ Single Crystals by Solvent Evaporation Method", **Pronoy Nandi**, C. Giri, D. Swain, U. Manju, and D. Topwal, *CrystEngComm.*, **2019**, *21*, 656-661.
6. "Influence of grain size on local work function and optoelectronic properties of n-ZTO / p-Si heterostructures", R. Singh, A. Datta, **Pronoy Nandi**, S. K. Srivastava, and T. Som, *Appl. Sur. Sci.*, **2019**,

Conference Proceedings:

1. * "$CH_3NH_3PbI_3$ Based Solar Cell: Modified by Antisolvent Treatment", **Pronoy Nandi**, C. Giri, U. Bansode and D. Topwal; *AIP Conf. procc.*, **2017**, *1832*, 080065.

Communicated manuscripts:

1. * "Electronic structure of Hybrid Perovskites in Cubic phase", **Pronoy Nandi**, S. K. Pandey, C. Giri, V. Singh, L. Petaccia, U. Manju, Subhendra D. Mahanti and D. Topwal.
2. * "Role of Organic Cation in Dual Emission of Hybrid Perovskite $CH_3NH_3PbBr_3$", **Pronoy Nandi**, C. Giri, S. Sarkar, P. Mahadevan, U. Manju, and D. Topwal.
3. * "Defects and its engineering in Methyl ammonium Lead Bromide Perovskite Single Crystals", **Pronoy Nandi**, C. Giri, and D. Topwal.

4. * “Understanding the Behavior of PbX_6 Octahedra with Phase Transition in $CH_3NH_3PbX_3$ (X= I, Br)”, **Pronoy Nandi**, S. Mahana, K. R. Priolkar, and D. Topwal.
5. * “Antisolvent Vapor Sensitive Methylammonium Lead Iodide Film Formation for Efficient Solar Cells under Ambient Conditions”, **Pronoy Nandi**, C. Giri, and D. Topwal.
6. * “Crystal Face Dependent Photoluminescence in $CH_3NH_3PbBr_3$”, **Pronoy Nandi**, and D. Topwal.
7. “Site-substitution in $GdMnO_3$: Effects on Structural, Electronic and Magnetic Properties”, S. Mahana, B. Rakshit, **Pronoy Nandi**, R. Basu, S. Dhara, U. Manju, S. D. Mahanti, and D. Topwal.

Conference Presentations:

1. * National conference on “Frontiers in Advanced Materials (FAM-2015)” during 15th - 18th June, 2015 at IISC, Bangalore (Poster presentation: Structural and spectroscopic investigations of $CH_3NH_3PbI_3$).
2. * National conference on “Emerging Trends in Advanced Functional Materials” (ETAFM) during 18th-21st January, 2016 at IOP, Bhubaneswar, India (Poster presentation: Structural and spectroscopic investigations of $MAPbX_3$ (X=I, Br, Cl)
3. * “National conference on solar energy and photovoltaic” (NCSEP-2016) at KIIT University, Bhubaneswar (Poster Presentation: Morphology engineering for highly efficient organic-inorganic hybrid perovskite solar cells).
4. * “61st DAE Solid State Physics Symposium” (DAE SSPS-2016) during 26th - 30th December 2016 at KIIT University, Bhubaneswar, India (Poster presentation: $CH_3NH_3PbI_3$ based solar cell: Modified by antisolvent treatment) **(Best Poster Award).**
5. * “28th AGM of Materials Research Society of India” (MRSI-AGM-2017) at IIT Bombay (Poster presentation: Engineering the defect states of hybrid perovskite single crystals).
6. * “9th International Conference on Materials for Advanced Technologies” (ICMAT-2017) during 18th - 23rd June 2017 at Suntec, Singapore (Oral presentation: Novel approach to synthesize defect free lead halide perovskite crystals, and Poster presentation: Reduced defect states and structural evolution indicate efficiency enhancement of hybrid perovskite solar cell).
7. * “A meeting on Hybrid Perovskites” (HyPe-2017) at S. N. Bose National Centre for Basic Sciences, Kolkata (Poster presentation: Role of ‘A’-site cation in dual emission of hybrid perovskites).

8. * “HBNI’s Research Scholar Meet” (RSM-2018) at IGCAR, Kalpakkam (Oral Presentation: Temperature dependent photo-induced reversible phase separation in mixed halide perovskite).

9. * “IOP-NISER-IIT Bhubaneswar meet” during 26th – 27th February, 2018 at NISER, Bhubaneswar (Poster Presentation: Understanding the valence band dispersion of hybrid perovskite in cubic phase using photo-emission spectroscopy).

10. * “International conference on microscope & XXXIX meeting of electron microscope society of India” (EMSI-2018) during 18th – 20th July, 2018 at Mayfair Convention Center, Bhubaneswar (Poster Presentation: Structural evolution of $CH_3NH_3PbI_3$ indicate efficiency enhancement).

* Indicates the papers on which this thesis is based.

Pronoy Nandi

(Pronoy Nandi)

DEDICATED TO MY FAMILY

(Grandparents, Parents, Uncle-Aunt, Brothers, Sister-in-law
& beloved “Abhra”)

Acknowledgments

The printed pages of this dissertation is not just a mere culmination of the research work carried out by me, rather a sum of experiences and interactions with many generous and inspiring people who have influenced me both in the professional and personal levels, and led to the fruition of this thesis. Now, I would like to express my sincere gratitude towards them who have helped me finishing this thesis work in different regards.

First and foremost, I would like to show my heartfelt gratitude to my thesis supervisor Dr. Dinesh Topwal for his guidance, advice, support, patience, monitoring and constant encouragement throughout my Ph.D. research period. Working with him gave me immense freedom in development of my research motivations and ideas, which I have enjoyed a lot. I must extend my great depth of gratitude and indebtedness to him for giving this full freedom to carry out research works. I must thank him for providing a well-equipped laboratory and also for arranging several necessary experiments for this thesis work through his contacts and collaborations. I truly consider myself fortunate being a Ph.D. scholar under his guidance. I do hope more supports in the future. Apart from these, affection, hospitality and different non-academic discussions dealing with different aspects of life will always remain memorable for me forever.

Next, I would like to acknowledge all my collaborators. I am honestly obliged to Prof. Subhendra D. Mahanti (Michigan State University, USA) for his useful suggestions, discussions and concealed help during the course of theoretical calculations. I am also thankful to Prof. P. Mahadevan (SNBNCBS, Kolkata) and her students Dr. S. Sarkar and Dr. S. K. Pandey for doing all the theoretical calculations present in this thesis. I thank Dr. V. Singh (CEA-LITEN, France) for his suggestions during theoretical calculations. I am gratified to Dr. Manju Unnikrishnan (IMMT, Bhubaneswar) for X-ray photoemission spectroscopy (XPS) results as well as for her kind cooperation in my research work. I would like to acknowledge Prof. T. N. Guru Row (IISc, Bangalore) and his student Dr. D. Swain for carrying out several single-crystal and powder X-ray diffraction measurements for me. It is my great pleasure to thank Prof. S. C. Ogale (NCL and IISER, Pune) for allowing me to make solar cell devices and measure their power conversion efficiency (PCE) in his lab. I must thank his group members, especially Dr. U. Bansode for his help and labor in doing PCE measurements. I thank Dr. S. Rath (IIT, Bhubaneswar) and S. Dhara (IGCAR, Kalpakkam) for their help in carrying out Raman experiments. I thank Prof. K. Priolkar (Goa University, Goa) for helping me to learn

EXAFS data analysis. I am also thankful to Dr. P. Mal, Dr. S. Barman and Dr. C. S. Purohit (NISER, Bhubaneswar) for their help in sample preparation at the initial stage of my research career. I would like to acknowledge Prof. T. Som (IOP, Bhubaneswar) and his group members (especially Dr. Ranveer Singh) for allowing and helping in performing UV-Visible absorption measurements. I thank Prof. P. V. Satyam (IOP, Bhubaneswar) and his group members (Dr. Puspendu Guha and Ms. Paramita Maity) for their support in carrying out scanning electron microscope (SEM) and vapor deposition experiments.

I got the opportunity to perform experiments at XRD1, XPRESS, Badelph and circular polarization (CIPO) beamline at ELLETRA synchrotron centre, Italy, and P02 and P65 beam line at Petra III, DESY, Germany. I gratefully acknowledge the people of these beamlines for their support during the beam times. Special thank should go to Dr. B. Joseph, Dr. L. Petaccia, Dr. E. Welter and Dr. K. Glazyrin for their help and support during various strenuous beam times. I thank Department of Science and Technology, Govt. of India for the financial support provided for participating in beam times. I also thank the administrative staff of ELLETRA and DESY synchrotron centre for their excellent support.

I am grateful to all the instructors of the pre-doctoral course work, especially, Prof. A. Srivastava, Prof. S. Mukherji, Dr. A. Virmani, Prof. K. Kundu and Prof. P. Agrawal for their excellent classes which not only imparted knowledge on physics, but also enormously enriched my thinking ability. I would also extend my sincere gratitude to all my Ph.D. review committee members; Prof. A. M Jayannavar, Prof. B. R. Sekhar and Dr. G. Tripathy for their attention, critical evaluation and encouraging words. Along the same line, I pay regards to HBNI dean Prof. P. Agrawal, for his considerate help at various occasions, mainly at the time of Singapore visit and thesis submission.

My earnest appreciation to all the Directors and Registers of IOP for their support and kindness over these years. I thank the administrative and support staff of IOP for their direct or indirect help in many cases. I would to like to acknowledge the excellent library and computer facilities provided by the IOP and all the members of IOP. I am thankful to Dr. K. C. Patra for his help at various occasions. My sincere regards to Mr. A. K. Das for his timely help. I am also thankful to all the Ion Beam Laboratory (IBL) staff for their technical help at various times. The support provided by the workshop staff Mr. R. N. Naik and Mr. S. Tripathy, especially during the modification of sample holder of PL cryostat was really thankworthy. I express my gratitude to them who have offered pieces of advice, support and companionship, directly or indirectly, even if they remain unnamed. I also like to remember that it is essentially the efforts and teaching of my teachers from primary standard to master's level which lead me to the current academic position. I will remain indebted to all of them forever. I also express my gratitude towards all my critic for their criticism, which boosted my self-confidence and provided me strength to complete this thesis.

I convey my gratefulness to all my labmates; Dr. Sudipta Mahana (Asst. Prof., Rajdhani Degree College, Bhubaneswar), Dr. R. Bommali (Asst. Prof., St. Xavier's College, Ranchi), Dr. Chandan Giri (PDF, Universidad Autonoma de Madrid), Dr. A. Ghosh, Dr. R. Das and Mr. S. Majumdar for their immense help and support at various occasions. They have provided a friendly, concerted and an excellent research environment in the lab. It is my innermost urge to thank *Chandan da* for his help in preparing single crystals of hybrid perovskites via different innovative ways. I can't thank enough *Sudipta* for her constant support, guidance, and cooperation in various aspects of research work. It gave me immense pleasure working and discussing with her both in academic and social aspects. Her enthusiastic approach towards research and hard labor was a constant source of motivation for me. Her companion and caring attitude during the beam times and other visits are unforgettable. Thanks for being an awesome friend and it is this friendship which I shall treasure forever. I wish best of luck for her future endeavors.

I am fortunate enough to have batch mates like Arpan, Ashis, Bharat, Chandan, Debashis, Mahesh, Ranveer and Paramita. I am also very much thankful to all my senior scholars, especially Tanmoy da, Himanshu da, Soumya da, Sabya da, Amina di, Puspendu da, Shreyansh da, Priyo da and junior scholars, especially Partha, Ganesh, Biswajit, Vikas, Sujay, Atanu, Amir, Dibyendu, Sayan, Subhadip, Sudarshan, Rupam, Gupteswar, Pritam and Aisha for making enjoyable and memorable experience during my whole stay here. I thank all of them from bottom of my heart. I would also like to thank all near and dears who come close to me in this time period. I am happy to mention my thanks to social media, especially YouTube, Facebook, WhatsApp, and Instagram for providing refreshment during this tough journey.

I would be amiss if I did not mention *Thakuma*, *Kaku*, *Kakima*, *Dada*, *Boudi*, *Soumya* and Little "*Abhra*" whose support, motivation, love and affection was a driving force in the journey and help to wrap-up the thesis in time. Last but not the least, word fall short to thank my *Maa* and *Baba*, who have always been there for me, to share my joy on sunny days and to encourage me on rainy days. This thesis would have been incomplete without the constant support from my family members. This thesis is dedicated to them.

Thank you very much, everyone !!!

Contents

Statement by author i

Declaration iii

List of Publications v

Dedications ix

Acknowledgments xi

Synopsis xix

List of Figures xxix

List of Tables xxxvii

Chapter 1: Introduction 1

- 1.1 Preamble 2
  - 1.1.1 Basic Physics of Solar Cells 2
  - 1.1.2 Solar Cell Characteristics 3
  - 1.1.3 Solar Cell Generations 5
- 1.2 Objective and Scope of the thesis 7
- 1.3 Overview of organic-Inorganic Hybrid Perovskites 8
  - 1.3.1 Crystal Structure 10
  - 1.3.2 Electronic Structure 13
  - 1.3.3 Optical Properties 15
  - 1.3.4 Electrical Properties 19
- 1.4 Device Configuration 20
- 1.5 Challenges concerning Hybrid Perovskites 21
- 1.6 Organization of Thesis 22

Chapter 2: Experimental and Theoretical Methodologies 27

- 2.1 Introduction 28
- 2.2 Sample Synthesis 28
  - 2.2.1 Single Crystal Growth 28
  - 2.2.2 Thin Film Growth 33
- 2.3 X-ray diffraction and Rietveld refinement 34
- 2.4 Physical property measurement system – PPMS Evercool – II 38
  - 2.4.1 Heat capacity 39
  - 2.4.2 Dc magnetic measurement system – SQUID VSM 40
- 2.5 Scanning Electron Microscopy- SEM 41
- 2.6 Optical Spectroscopy 42
  - 2.6.1 Ultraviolet-visible-near infrared (UV-Vis-NIR) Spectroscopy 43
  - 2.6.2 Photoluminescence (PL) Spectroscopy 43
  - 2.6.3 Raman Spectroscopy 47

2.7 Electrical measurements 49

2.8 Photoemission Spectroscopy 49

2.8.1 X-ray Photoemission Spectroscopy 52

2.8.2 Ultraviolet Photoemission Spectroscopy 53

2.9 Extended X-ray Absorption Fine Structure (EXAFS) 54

2.10 Theoretical methodology 57

2.11 Summary 60

Chapter 3: Optimization of Single Crystal Growth 61

3.1 Defects and its Engineering in Methylammonium Lead Bromide 62

3.1.1 Introduction 62

3.1.2 Experimental details 64

3.1.2.1 Sample Preparation methods 64

3.1.2.2 Experimental techniques 65

3.1.3 Results and discussion 66

3.1.3.1 Structural studies 66

3.1.3.2 Optical studies 67

3.1.3.3 Magnetic studies 75

3.1.4 Conclusion 76

3.2 Growth of $CH_3NH_3PbCl_3$ Single Crystals by Solvent Evaporation 77

3.2.1 Introduction 77

3.2.2 Experimental Details 78

3.2.2.1 Growth of $CH_3NH_3PbCl_3$ Single Crystals 79

3.2.2.2 Characterizations and Measurements 79

3.2.3 Results and Discussion 80

3.2.3.1 Structural Studies 80

3.2.3.2 Optical Studies 81

3.2.3.3 Transport Measurement 85

3.2.4 Conclusion 87

Chapter 4: Structural Investigations of Hybrid Perovskites 89

4.1 Introduction 90

4.2 Experimental Details 92

4.2.1 Sample synthesis 92

4.2.2 Experimental techniques 92

4.3 Results and Discussions 93

4.3.1 Structural studies: Global 93

4.3.2 Structural Studies: Local 100

4.4 Conclusion 109

Chapter 5: Spectroscopic Investigations of Hybrid Perovskites 111
5.1 Band Gap Engineering and Dual Emission of Hybrid Perovskites 112
  5.1.1 Introduction 112
  5.1.2 Experimental details 114
    5.1.2.1 Sample synthesis 114
    5.1.2.2 Experimental techniques 115
    5.1.2.3 Computational details 115
  5.1.3 Results and Discussion 116
    5.1.3.1 UV-Visible Absorption Studies of $CH_3NH_3PbBr_3$ 116
    5.1.3.2 Temperature-dependent Photoluminescence (PL) Studies 117
    5.1.3.3 Origin of Dual Emission of $CH_3NH_3PbBr_3$ 119
    5.1.3.4 Theoretical Understanding 122
    5.1.3.5 Optical properties of $CH_3NH_3PbI_3$ and $CH_3NH_3PbCl_3$ 124
    5.1.3.6 Raman Spectroscopy 128
    5.1.3.7 Crystal Face Dependent PL of $CH_3NH_3PbBr_3$ 130
  5.1.4 Conclusion 134
5.2 Electronic Structure of Hybrid Perovskites in Cubic Phase 135
  5.2.1 Introduction 135
  5.2.2 Experimental and Computational Details 138
  5.2.3 Resulta and Discussions 139
    5.2.3.1 X-ray Photoemission Spectroscopy (XPS) Studies 139
    5.2.3.2 Ultra-Violet Photoemission Spectroscopy (UPS) Studies 143
  5.2.4 Conclusion 156

Chapter 6: Temperature Dependent Photo-induced Phase Separation in Mixed Halide Perovskite 159
6.1 Introduction 160
6.2 Experimental details 161
  6.2.1 Materials 161
  6.2.2 Synthesis of $CH_3NH_3Pb(I_{1-x}Br_x)_3$ Crystals/Thin films 162
  6.2.3 Single Crystal/ Powder XRD and SEM 162
  6.2.4 Temperature Dependent Photoluminescence 163
6.3 Results and discussion 163
  6.3.1 Structural Studies 163
  6.3.2 Optical Studies 166
  6.3.3 Carrier Lifetime Measurement 174
6.4 Conclusion 176

Chapter 7: Solar Cell Device 179
7.1 Introduction 180
7.2 Experimental Details 183
  7.2.1 CH_3NH_3I Preparation 183

7.2.2 Perovskite Film Preparation 183
7.2.3 Solar Cell Device Fabrication 183
7.2.4 Characterization Techniques 184
7.3 Results and discussion 185
7.3.1 Structural Studies 185
7.3.2 Optical Studies 188
7.3.3 Power Conversion Efficiency (PCE) Measurement 189
7.4 Conclusion 191

Chapter 8: Summary and Future plans **193**
8.1 Summary 194
8.1.1 Structural Investigations 194
8.1.2 Spectroscopic Investigations 195
8.1.3 Photo-induced Phase Separation of Mixed Halide Perovskites 197
8.1.4 Solar Cell Device 197
8.2 Future Plans 198
8.2.1 Tandem Solar Cell 199
8.2.2 Field Effect Transistor 199
8.2.3 Photodetector 199
8.2.4 Solar Heat Harvesting 199

References **201**

Synopsis

This thesis deals with structural and spectroscopic investigations of organic-inorganic hybrid perovskites, a light absorbing material, which has shown considerable potential to be used as a solar cell material. World relies on fossil fuel for most of its energy requirements, which unfortunately are fast depleting. Due to ever-increasing demand of energy for growth, development and sustainability, we are heading towards a global energy crisis. Search for alternative and renewable energy sources like wind, rain, tides, waves, geothermal heat, converting biomass to energy, solar energy etc. has hence gained momentum [1,2]. A total of 174 PW solar energy approaches earth, but only 89 PW is absorbed by the land and oceans, and the rest is reflected out in space by the atmosphere [2]. The solar energy sector of India has a very good opportunity to harness solar energy for plenty of applications, as India receives sufficient and continuous supply of solar radiation throughout the calendar. Till date, various types of solar cells have been developed and they can be categorized as: First generation: single crystalline Si (present efficiency ~27.6%), GaAs (efficiency ~28.8%) and their multi-junctions (efficiency ~46%); Second generation: amorphous silicon (a-Si) (efficiency ~13%), cadmium telluride (CdTe) (efficiency ~22.1%), copper indium gallium diselenide (CIGS) (efficiency ~22.6%) etc.; Third generation: thin-film solar cells i.e., polymer cells (efficiency ~10%), dye-sensitized cells (efficiency ~11.9%) etc. and Fourth generation: Organic-inorganic hybrid solar cells (efficiency ~22.1%) [3]. Among them organic-inorganic hybrid perovskite solar cell is of current interest to the solar cell community because of their low processing cost, ease of fabrication process and high power conversion efficiency [4]. These perovskites are exotic class of hybrid materials which combines the potentials of organic and inorganic semiconductors: high absorption coefficient [5], long charge carrier diffusion length [6], large mobilities [7], and tunable band gap [8] with the possibility of easy device fabrication [9]. Due to superior properties like flexibility [10], semitransparency [11], and vivid colors [12]; hybrid perovskites became attractive for niche applications such as built-in photovoltaics [4, 13], portable lightweight chargers [13], Light emitting diodes [14], Lasers [15], x-ray and photo detector etc. [16].

Perovskite usually has a stoichiometry of ABX_3 three-dimensional structure; where "A" is the larger cation, "B" is the smaller cation and "X" is the anion. In our studies the 'A' moiety in hybrid perovskites is a monovalent organic ($CH_3NH_3^+$ or $CH(NH_2)_2^+$) or inorganic (Cs^+) cation, 'B' is group IV divalent cation (Pb^{2+} or Sn^{2+}), and 'X' is a halide anion (I^-, Br^-, Cl^- or mixtures of them) [17]. This class of perovskite experience crystallographic phase transition (Orthorhombic → Tetragonal → Cubic) with the increase of temperature [18]. High absorption coefficient in the visible region and tunable optical bandgap from blue to red regions of wavelength (3.06eV to 1.58 eV) just by changing the halide ion [8] makes the family of organic-inorganic hybrid perovskite potential candidates for application in multijunction/tandem solar cells [19], and tunable LEDs [14]. Band structure calculations show that modification in metal-cation (M-X bond) has a profound effect on the conduction band minima (CBM) and valence band maxima (VBM). In $CH_3NH_3PbX_3$, it is estimated that CBM is composed of antibonding states of Pb-p and X-s orbitals, whereas VBM is composed of mainly antibonding of Pb-s and X-p orbitals [20].

In this thesis work, synthesis of organic-inorganic and all inorganic hybrid perovskite single crystals via four different wet chemical methods (Inverse Temperature Crystallization method (ITC), Solution Temperature Lowering method (STL), Anti-solvent Vapor Assisted Crystallization method (AVC) and Solvent Evaporation at room temperature method (SERT)) are explored. Further, growth of hybrid perovskite thin films and solar cell module on Fluorine doped Titanium oxide (FTO) substrate using spin-coating technique is also presented. These single crystals and thin film are characterized via powder and single crystal x-ray diffraction (XRD), Physical property measurement system (PPMS), scanning electron microscopy (SEM), extended x-ray absorption fine structure (EXAFS) study, UV-Visible absorption spectroscopy, photoluminescence (PL), photoelectron spectroscopy (XPS and UPS), Raman spectroscopy etc. to understand their structure and photophysics. In addition, first-principles density functional theory (DFT) based calculations are also performed to correlate the experimentally observed structural and electronic properties of hybrid perovskites. Following these, power conversion efficiency (PCE) of solar cell devices made by us are also studied by I-V measurements using Newport solar simulator.

The thesis is organized in eight chapters. **Chapter 1** provides a brief introduction and motivation on the topic and **chapter 2** describe the experimental and theoretical techniques used in the present study.

In **chapter 3** we discuss an effective approach to synthesize high-quality defect free single crystals of organic-inorganic hybrid perovskites ($CH_3NH_3PbX_3$; X=Br, Cl) to achieve better device performance. For this purpose, we have synthesized single crystals of $CH_3NH_3PbBr_3$ via STL, ITC and AVC method and $CH_3NH_3PbCl_3$ via ITC and SERT methods. Identical XRD patterns and heat capacity confirm the phase purity and the presence of three crystallographic phase transitions in all four samples synthesized by different techniques. However, an inter-band broad emission peak (between 600 nm and 700 nm) was observed for crystals grown at high temperatures (in ITC and STL) and low boiling point antisolvent (dichloromethane) vapor assisted crystallization (AVC) method, whereas it was absent in high boiling point antisolvent (Ethyl acetate) assisted AVC and SERT method in optical studies. Herein, using UV-Visible absorption, temperature dependent photoluminescence, time-resolved spectroscopy and dc magnetization studies we observe that defect-assisted extrinsic self-trapping is dominant over the intrinsic self-trapping process in the case of sample synthesized by ITC, STL and DCM diffused AVC method and are responsible for inter-band broad emission. Furthermore, a comparison of formation energy calculations with the experimentally obtained energy level confirms that excess Pb in interstitial positions are predominantly responsible for the extrinsic self-trapping process for the samples whose growth rate is high. Further, optimizing the synthesis condition to obtain low defect concentration (as seen from optical and charge transport points of view) and longer diffusion length of $CH_3NH_3PbCl_3$ synthesized by SERT method than that of ITC method indicate that these hybrid perovskite crystals are promising candidates to work as an active component in visible-blind UV detectors. We have used crystals grown by AVC and SERT methods for detailed structural and spectroscopic characterization in the following chapters.

In **Chapter 4** we discuss the crystal structures and structural phase transitions of hybrid perovskites using XRD and EXAFS measurements. As the temperature is lowered, at 330.8 K (236.1 K), the high-temperature cubic phase transformed to body-centered tetragonal phase for $CH_3NH_3PbI_3$ ($CH_3NH_3PbBr_3$). Variation of lattice and order parameters, tetragonal distortion and linear expansion coefficients clearly indicate that it is a first order phase transition and rule out the possibility of phase coexistence. Upon cooling further, the tetragonal phases transformed into a low-temperature orthorhombic phase around 161.8 K (149.8 K), again via a first-order phase transition. Nonpolar or centrosymmetric space group in all three phases rules out the possibility of ferroelectricity or second harmonic generation in this system. Further, variation of bond-length and bond-angle of $CH_3NH_3PbX_3$ (X= I, Br) clearly demonstrates octahedral distortion near the phase transition temperatures, which is absent in $CsPbBr_3$. Based upon these results, we discuss the impact of the structural phase transitions on photovoltaic performance of organic-inorganic hybrid perovskite-based solar cells.

Chapter 5 is divided into two parts. In the first part, optical properties of solid solutions of $APbX_3$ (A=CH_3NH_3, $CH(NH_2)_2$, Cs and X=I, Br, Cl) is discussed which include variation of optical bandgap; excitonic binding energy, exciton-phonon interaction etc. Further, emission spectra from a single crystal/polycrystalline $CH_3NH_3PbBr_3$ system is found to exhibit two peaks. The high energy peak (535 nm), is attributed to the band to band direct transition, consistent with UV-Visible absorption and thin film PL studies and is blue shifted with increasing temperature; whereas the low energy peak (545 nm) is red shifted. To understand the origin of two peaks in the emission and absorption spectrum, two more lead bromide samples $CH(NH_2)_2PbBr_3$ and $CsPbBr_3$ were synthesized by changing the 'A' site cation. It was observed that dual nature of emission peaks remain unaffected by changing the ammonium group from methyl to formamidine. However, the replacement of organic cation with inorganic cesium (Cs) cation led to the disappearance of the second emission peak, which suggests that the origin of the dual emission is associated with the nature of the organic cation. Using first-principle DFT calculations and MD simulations, by considering different orientations of the organic molecule we obtain a complex potential energy landscape with two closely spaced minima at the gamma point with a separation of 13.7 meV which somewhat matches the experimentally observed energy difference between the two PL peaks (40 meV) in orthorhombic phase. It is believed that molecular rotation/orientation of $CH_3NH_3^+$ results into octahedral distortions. Detailed nature of this octahedral distortion due to methylammonium orientation in orthorhombic phase is further manifested in face dependent PL studies on single crystal samples. In the second part of this chapter, photoemission studies (XPS and UPS) of hybrid perovskites are discussed. Narrow scan XPS spectra of different constituent core level elements of hybrid perovskites were performed to identify spin-orbit splitting and oxidation states of these elements. Further, angle-integrated, angle-resolved photoemission spectroscopy and density functional theory were used to investigate the electronic structure and valence band dispersion of hybrid perovskites. The experimental band structure shows a good agreement with the *ab-initio* calculations. These results demonstrate that the top of the valence band arise due to formation of bonding-antibonding levels because of the Pb-Cl/Br interaction. Further, highly reproducible dispersive feature of the valence band and constant energy cuts reveals binding energies of Brillouin zone boundaries ($\overline{M}$,$\overline{X}$) are higher than that of zone center ($\overline{\Gamma}$). Hole effective mass and carrier mobility were also determined along $\overline{\Gamma}$-$\overline{X}$ and $\overline{\Gamma}$-$\overline{M}$ direction which shows good consistency with other measurements.

One way to utilize the entire visible and near-infrared part of solar spectrum and to increase the efficiency of solar cell is by coupling the perovskite material with commercially available Si, Germanium and Copper indium gallium selenide (CIGS) cells compared to the respective single junction cells. [19] However, when mixed-halides perovskites was employed as solar cell absorber layers by replacing some I with Br, the increase in bandgap (of the perovskite material) does not yield a corresponding increase in open circuit voltage. It was observed that, mixed halide perovskite undergoes a reversible complex dynamic phenomenon namely ‘photoinduced phase separation’ into low bandgap I-rich and high bandgap Br-rich domains under illumination. Through our careful experiments in **chapter 6** we show that photoinduced phase separation occurs only in a narrow temperature range (190 K to 275 K) and above a particular bromine (x>0.2) concentration for $CH_3NH_3Pb(I_{1-x}Br_x)_3$. It is also observed that continuous illumination creates polaronic strain at the grain boundary and stimulates the formation of iodide rich domain and bromine-rich clusters. Longer carrier lifetime of photo-induced state confirms the presence of strong electron-phonon interaction (polaronic effect). Further, longer saturation time of cluster formation confirms that grain boundary plays a crucial role in phase separation. Detailed temperature PL studies on this mixed halide perovskite system reveal phase separation can be avoided by working at an elevated temperature and using large grained films which in turn increase the possibility of their use in tandem solar cell. These photo-induced reversible transitions with temperature may also enable applications of mixed halide perovskites in optical memory, sensing and switching. We have extended the photo-induced phase separation picture of mixed halide hybrid perovskite to a broader temperature region.

Fabrication of mesoporous ‘methylammonium lead iodide’ solar cells and the effect of antisolvent in morphology and power conversion efficiency (PCEs) are discussed in **chapter 7**. In this chapter, we discuss antisolvent vapor assisted crystallization technique that helps in controlled nucleation and crystallization of $CH_3NH_3PbI_3$ films for fabricating mesoporous perovskite solar cells. Solar cells based on hybrid perovskite $CH_3NH_3PbI_3$ as an absorber in FTO/ compact TiO_2/ Mesoporous TiO_2/ $CH_3NH_3PbI_3$/ Spiro-OMeTAD/Au geometry were deposited using spin-coating technique. Thereafter, high (DCM) and low (EA) boiling point antisolvents were diffused to the $CH_3NH_3PbI_3$ films and a new morphology (microrods) was evolved for the case of EA treated films. Further, we also observed that due to better morphology for the mesoporous films, EA diffused film exhibits better fill factor and as a result, there is a 32% power conversion efficiency enhancement than the DCM diffused (5.8%) and as-deposited films (5.6%). Thus, we believe that high boiling point antisolvent vapor diffusion technique is a potential method to achieve better device performance.

Summary and future plans are discussed in **Chapter 8**.

References:

[1] T. B. Johansson, H. Kelly, A. K. N. Reddy, R. Williams, T. E. Drennen, Renewable energy: sources for fuels and electricity, Washington, DC, Island Press, (1993).

[2] T. Jackson, Renewable energy sources, Centre for Environmental Strategy, University of Surrey, (1998).

[3] https://www.nrel.gov/pv/ Photovoltaic Research, Accessed: 4 May 2017, (2017).

[4] W. S. Yang, B.-W. Park, E. H. Jung *et al.* Iodide management in formamidinium-lead-halide-based perovskite layers for efficient solar cells, Science, 356, 1376-1379, (2017).

[5] S. D. Wolf, J. Holovsky, S.-J. Moon *et al.* Organometallic halide perovskites: sharp optical absorption edge and its relation to photovoltaic performance, J. Phys. Chem. Lett., 5, 1035–1039, (2014).

[6] S. D. Stranks, G. E. Eperon, G. Grancini *et al.* Electron-hole diffusion lengths exceeding 1 micrometer in an organometal trihalide perovskite absorber, Science, 342, 341-344, (2013).

[7] Y. Wang, Y. Zhang, P. Zhang *et al.* High intrinsic carrier mobility and photon absorption in the perovskite $CH_3NH_3PbI_3$, Phys. Chem. Chem. Phys., 17, 11516-11520, (2015).

[8] C. M. Sutter-Fella, Y. Li, M. Amani, J. W. AgerIII *et al.* High photoluminescence quantum yield in band gap tunable bromide containing mixed halide perovskites, Nano Lett., 16, 800–806, (2016).

[9] P. Nandi, C. Giri, U. Bansode *et al.* $CH_3NH_3PbI_3$ based solar cell: Modified by antisolvent treatment. AIP Conference Proceedings, 1832, 080065, (2017).

[10] D. Gui, L. Ji, A. Muhammad *et al.* Jahn-Teller effect on framework flexibility of hybrid organic-inorganic perovskites. J. Phys. Chem. Lett., 9, 751-755, (2018).

[11] G. E. Eperon, V. M. Burlakov, A. Goriely *et al.* Neutral color semitransparent microstructured perovskite solar cells. ACS Nano, 8, 591-598, (2014).

[12] Y. Deng, Q. Wang, Y. Yuana *et al.* Vividly colorful hybrid perovskite solar cells by doctor-blade coating with perovskite photonic nanostructures. Mater. Horiz., 2, 578-583, (2015).

[13] Z. Xiao, Y. Yuan, Y. Shao et al. Giant switchable photovoltaic effect in organometal trihalide perovskite devices. Nat. Mater., 14, 193-198, (2015).

[14] R. Babu, L. Giribabu, S. P. Singh, Recent advances in halide-based perovskite crystals and their optoelectronic applications. Cryst. Growth Des., 18, 2645−2664 (2018).

[15] Q. Zhang, R. Su, W. Du *et al.* Advances in small perovskite-based lasers. Small Methods, 1, 1700163, (2017).

[16] H. Wei, Y. Fang *et al.* Sensitive X-ray detectors made of methylammonium lead tribromide perovskite single crystals, Nat. Photon., 10, 333-339, (2016).

[17] D. Weber, Z. Naturforsch, $CH_3NH_3PbX_3$, a Pb(II)-system with cubic perovskite structure, *B: J. Chem. Sci.*, *33*, 1443-1445, (1978).

[18] P. Nandi, C. Giri, B. Joseph *et al.* $CH_3NH_3PbI_3$, A potential solar cell candidate: structural and spectroscopic investigations. J. Phys. Chem. A., 120, 9732-9739, (2016).

[19] M. T. Hörantner, T. Leijtens, M. E. Ziffer *et al.* The potential of multijunction perovskite solar cells. ACS Energy Lett., 2, 2506-2513, (2017).

[20] R. Lindblad, N. R. Jena, B. Philippe *et al.* Electronic structure of $CH_3NH_3PbX_3$ perovskites: Dependence on the halide moiety. J. Phys. Chem. C, 119, 1818-1825, (2015).

List of Figures

1.1 (a) Solar spectrum and spectral flux density as a function of incident photon wavelength, (b) Schematic depiction of p-n junction solar cell. (Data from ASTM) 3

1.2 (a) Current density-Applied bias (J-V) characteristics of the solar cell under dark and 1 Sun illumination, (b) Universal way of representing the J-V data, obtained by changing the sign of photocurrent. This usually done as power generated by the device is positive. 4

1.3 Timeline of the highest efficiencies in various solar cell technologies. Black dotted curve in the figure shows the rapid development in efficiency of hybrid perovskite solar cell. 6

1.4 Overview of organic-inorganic hybrid perovskite and their applications. Highlighted topics are focused in this thesis. 7

1.5 Crystal structure of $CH_3NH_3PbI_3$ in (a) Orthorhombic phase, (b) Tetragonal phase and (c) Cubic phase; (d) Cubic $CsPbI_3$. 9

1.6 Calculated transition energy levels of donor-like and acceptor-like point defects in (a) $CH_3NH_3PbI_3$ and (b) $CH_3NH_3PbBr_3$. 13

1.7 Schematic representation of Wannier, Frenkel and Charge transfer excitons. 17

1.8 Schematic representation of Polaron. 18

1.9 Evolution of Organic-inorganic hybrid perovskite solar cell technology starting from the electrolyte-based mesoscopic Dye-sensitized solar cells (DSSC) and solid state(ss) DSSC 20

2.1 Temperature-dependent solubility of (A) $CH_3NH_3PbI_3$ in GBL and (B) $CH(NH_2)_2PbI_3$ in GBL, (C) $CH_3NH_3PbBr_3$ in DMF, and (D) $CH(NH_2)_2PbBr_3$ in DMF : GBL (1 : 1 v/v). 30

2.2 Schematic representation of single crystal growth of organic-inorganic hybrid perovskite via different techniques. 32

2.3 Thin Film growth systems used for the work in this thesis: (a) High vacuum coating unit (Thermal evaporator), (b) Spin-coating unit. 34

2.4 (a) Schematic representation of X-ray diffraction from the parallel planes of the periodic crystal lattice. (b) X-ray diffraction pattern of corundum (standard sample) collected in our lab; peak indices are also marked. (c) X-ray diffraction set-up at Institute of Physics, Bhubaneswar. 35

2.5 (a) PPMS Evercool-II set up at Institute of Physics, Bhubaneswar, (b) The sample holder used for heat capacity measurements in PPMS, (c) Vibrating-sample magnetometer (VSM) pick-up coil, (d) sample holder, (e) VSM head/motor used for DC magnetization measurements in PPMS. 39

2.6 FIB-SEM crossbeam system at Institute of Physics, Bhubaneswar. 41

2.7 Schematic representation of UV-Vis-NIR spectrophotometer. 43

2.8 (a) Jablonski diagram shows the possible relaxation processes in a molecule after the molecule has absorbed a photon; (b) Schematic representation of cryostat for performing temperature-dependent photoluminescence (PL) measurement; (c) PL spectrometer at Institute of Physics, Bhubaneswar. 45

2.9 Schematic representation of Time-Correlated Single Photon Counting (TCSPC) Technique. 46

2.10 (a) Mechanism of Raman Scattering effect when molecule exposed to LASER light; (b) Raman spectrometer at Institute of Physics, Bhubaneswar. 48

2.11 Newport solar simulator for device characterization. 49

2.12 (a) A schematic representation of photoemission experiment where the characteristics of photoelectrons are defined by its kinetic energy (E_{kin}) and momentum (p).The value of momentum is determined from the polar angles (θ and Φ) of emission; (b) An intuitive representation to describe the energy level profile inside the solid and resulting photoemission spectra. 50

2.13 Schematic representation of X-ray photoelectron spectrometer. 53

2.14 (a) Schematic representation of EXAFS process; (b) XAFS spectrum of $CH_3NH_3PbI_3$ showing the pre-edge, XANES and EXAFS regions. 55

3.1 (a) Room temperature powder X-ray diffraction patterns and (b) heat capacity of $CH_3NH_3PbBr_3$ grown by ITC, STC, DCM and EA diffused AVC method. 67

3.2 Room temperature UV-VIS absorbance spectra of four $CH_3NH_3PbBr_3$ samples grown by ITC, STC and AVC (DCM and EA diffused) method. 68

3.3 Temperature dependent photoluminescence spectra of $CH_3NH_3PbBr_3$ grown by (a) ITC, (b) STC, (c) DCM diffused and (d) EA diffused AVC method. Inset shows the variation of first two peaks with temperature. 70

3.4 Time correlated single photon counting (TCSPC) data corresponding to 650 nm and 531 nm (Inset) emission peaks at 77 K of $CH_3NH_3PbBr_3$ grown by ITC method. Hollow dots represents the experimental data and solid lines denote the biexponential fitting of the data. 72

3.5 Calculated transition energy levels of intrinsic point defects in $CH_3NH_3PbBr_3$. 73

3.6 (a) Photoluminescence spectra of $CH_3NH_3PbCl_3$ grown by ITC and EA diffused AVC method at 77 K; (b) M-H loops of $CH_3NH_3PbCl_3$ grown by ITC and EA diffused AVC method taken at 100 K. 74

3.7 M-H loops of $CH_3NH_3PbBr_3$ grown by ITC, STC, DCM and EA diffused AVC method taken at 100 K and 300 K. 75

3.8 (a) X-ray powder diffraction patterns (black) of as-synthesized $CH_3NH_3PbCl_3$ obtained at room temperature with the refinement patterns (red) using the Pm-3m structure superimposed on it. Inset shows the XRD pattern from the top surface of $CH_3NH_3PbCl_3$ single crystal. (b) Temperature dependence of specific heat of $CH_3NH_3PbCl_3$, where different crystallographic phases are indicated and image of the single crystal is plotted as an inset. 80

3.9 (a) Image of $CH_3NH_3PbCl_3$ single crystal mounted on Hampton cryoloop for single crystal XRD measurement. (b) Image of diffraction spots of $CH_3NH_3PbCl_3$ single crystal suggesting the crystalline quality of the sample. 82

3.10 Comparative optical properties of $CH_3NH_3PbCl_3$ single crystal: (a) Room temperature optical absorption spectra; (b) Temperature-dependent photoluminescent spectra and inset shows the variation of peak positions with temperature; (c) temperature dependent data of integrated intensity in cubic phase; (d) valence band spectra, (e) (d) schematic energy level diagram; (f) (e) Time-correlated single-photon counting (TCSPC) spectra. 84

3.11 Current density-Voltage (J-V) response of $CH_3NH_3PbCl_3$ single crystal exhibiting three different regions obtained from the log J versus log V plot. Regions correspond to linear ohmic regime ($J \propto V$, red line), trap filling limit regime ($J \propto V^{n>3}$, blue line) and Child's regime ($J \propto V^2$, green line). 86

4.1 X-ray diffraction pattern of (a) $CH_3NH_3PbI_3$ collected at three different temperatures 100 K, 250 K and 375 K, (b) $CH_3NH_3PbBr_3$ collected at 100 K, 200 K and 300 K. Solid dots/ plus sign represents the experimental data, solid lines denote the Rietveld refined patterns while the dotted lines represents the difference between the two. Crystal structure corresponding to the three temperatures is also plotted. Inset shows heat capacity of corresponding samples where different crystallographic phases with temperature are indicated. 94

4.2 Lattice parameters and phase transitions of $CH_3NH_3PbI_3$ and $CH_3NH_3PbBr_3$. Lattice parameters refined from the synchrotron X-ray diffraction scans of (a) $CH_3NH_3PbI_3$ and (b) $CH_3NH_3PbBr_3$. Fits to the cubic lattice parameter (red solid line) and the average tetragonal lattice parameter (= $2a_{tet} + c_{tet})/3$ (red solid line), were used to determine the linear coefficients of thermal expansion. Variation of (c) axial and (d) equatorial bond angles of $CH_3NH_3PbI_3$ and $CH_3NH_3PbBr_3$. The arrows indicate the crystallographic phase transition temperature. Temperature dependence of the Tetragonal distortion from XRD data fit to a power law $((c-a)/a \sim (T_c - T)^{2\beta})$ to identify the cubic-tetragonal phase transition of (e) $CH_3NH_3PbI_3$ and (f) $CH_3NH_3PbBr_3$. (g) Visualization of axial (X1) and equatorial (X2) halide atoms in the PbX_6 octahedra. 98

4.3 XAFS spectrum showing the pre-edge, XANES and EXAFS regions of (a) $CH_3NH_3PbI_3$ and (b) $CH_3NH_3PbBr_3$ samples. Magnitude of Fourier transforms of k^3-weighted EXAFS data at Pb-L_3 edge acquired at 80 K (black open circle) and 305 K (blue open circle) for (c) $CH_3NH_3PbI_3$ and (d) $CH_3NH_3PbBr_3$ along with corresponding fitting superimposed on it (red solid line). Corresponding back-transformed spectra in k-space (open circles) along with fitting are plotted in inset. 101

4.4 Thermal variations of average (a,c) Lead-axial Halide (X1) and (b,d) Lead-equatorial Halide (X2) bond lengths of (a,b) $CH_3NH_3PbI_3$ and (c,d) $CH_3NH_3PbBr_3$ samples obtained from both EXAFS (solid circle) and XRD (open circle) analysis. Temperature dependence of variation of Debye waller factor (σ^2) of different Pb-X correlations of (e) $CH_3NH_3PbI_3$ and (f) $CH_3NH_3PbBr_3$. The solid lines represent the fitting using Einstein model (Equation 4.2). Vertical dashed line corresponds to the structural phase transitions as marked in the figure. 103

4.5 Crystal structure of $CsPbBr_3$ in (a) Orthorhombic phase, (b) Tetragonal phase and (c) Cubic phase obtained from single crystal X-ray diffraction. (d) Variation of pseudocubic lattice parameter of $CsPbBr_3$ with temperature. 105

4.6 (a) XAFS spectrum showing the pre-edge, XANES and EXAFS regions of $CsPbBr_3$. (b) Magnitude of Fourier transforms of k^3-weighted EXAFS data at Pb-L_3 edge acquired at 80 K (black open circle) and 305 K (blue open circle) for $CsPbBr_3$, along with corresponding fitting superimposed on it (red solid line). Corresponding backtransformed spectra in k-space (open circles) along with fitting are plotted in inset. (c) Thermal variations of average Pb-Br1 (axial) and Pb-Br2 (equatorial) bond lengths of $CsPbBr_3$ obtained from both EXAFS (solid circle) and XRD (open circle) analysis. Vertical dashed line corresponds to the structural phase transitions as marked in the figure. Temperature dependence of 108 variation of Debye waller factor (σ^2) of different Pb-Br (axial and equatorial) correlations of $CsPbBr_3$. The solid lines represent the fitting using Einstein model (Equation 4.2).

5.1 (a) Absorption spectra of $CH_3NH_3PbBr_3$ at room temperature. Temperature-dependent photoluminescence (PL) spectra of (b) $CH_3NH_3PbBr_3$ thin film on FTO substrate, (c) $CH_3NH_3PbBr_3$ single crystals. Dotted lines and arrows are guid to the eye highlighting the blue and red shift of the PL peak with temperature. The inset shows the variations of peak positions of each samples as a function of temperature. (d) Temperature dependent data of integrated intensity in cubic, tetragonal and orthorhombic phase of $CH_3NH_3PbBr_3$. Solid red lines are fitted as explained in the text. 117

5.2 (a) Absorption spectra of $CH(NH_2)_2PbBr_3$ and $CsPbBr_3$ at room temperature. Temperature-dependent photoluminescence (PL) spectra of (b) $CH(NH_2)_2PbBr_3$ and (c) $CsPbBr_3$ single crystals. Dotted lines and arrows are guid to the eye highlighting the blue and red shift of the PL peak with temperature. The inset shows the variations of peak positions of each samples as a function of temperature. 121

5.3 (a) Different orientations of the organic molecule (CH_3NH_3) inside the $PbBr_6$ octahedra used for calculation. (b) The change in the energy as a function of the rotation (in the ac plane) angle of the molecule. The angle θ is shown in the inset. (c) The optimized structure for the two minimum energy configurations where the C-N axis makes an angle of ~ 12^0 (configuration A) and ~ 28^0 (configuration B) with the (101) direction. (d) Conduction band for these two minima (A and B), (e-f) Valence band corresponding to these two minima (A and B) shows an energy shift of 13.7 meV. (g) Simulated high temperature behavior of the Valence band corresponding to these two minima (A and B), which shows an energy shift of 10.30 meV. 123

5.4 Temperature-dependent photoluminescence (PL) spectra of (a) $CH_3NH_3PbCl_3$ and (b) $CH_3NH_3PbI_3$ single crystals. Dotted lines and arrows are guid to the eye highlighting the blue and red shift of the PL peak with temperature. The inset shows the variations of peak positions of each samples as a function of temperature. 125

5.5 Temperature dependent data of integrated intensity and FWHM in tetragonal (a,b) and orthorhombic (c,d) phase of $CH_3NH_3PbI_3$ respectively. Temperature dependent data of integrated intensity of (e) $CH(NH_2)_2PbBr_3$ and (g) $CsPbBr_3$. Solid lines are fittings as explained in the text. 126

5.6 Room temperature Raman Spectra of $CH_3NH_3PbI_3$ 129

5.7 Single crystal X-ray diffraction to identify the planes of $CH_3NH_3PbBr_3$ single crystal. (b-d) Steady state and (e-g) time resolve photoluminescence (PL) of $CH_3NH_3PbBr_3$ single crystal at 77 K. Light 131 is incident along (10-1) (b, e), (101) (c, f) and (010) (d, g) planes of the crystal and emission spectra are recorded along (010), (10-1) and (101) planes.

5.8 Crystal orientation dependent PL of $CH_3NH_3PbBr_3$ (a) Schematic, (b-c) steady state, (d-e) Time-resolve, (b,d) positive θ and (c,e) negative θ direction, (f-g) variation of life time of peak-1 and 2 with rotation angle. 132

5.9 Photoemission Spectra of $CH_3NH_3PbI_3$, $CH_3NH_3PbBr_3$ and $CH_3NH_3PbCl_3$ samples collected at room temperature. (a) Wide scan (b) I 3d core level (c) Br 3p core level (d) Br 3p core level. 140

5.10 Measured (a) Pb 4f core level (b) Pb 5d core level (e) Pb 4p core level and (f) valence-band spectra of $CH_3NH_3PbI_3$, $CH_3NH_3PbBr_3$ and $CH_3NH_3PbCl_3$ samples collected at room temperature. Enlarged spectra of (c) Pb 4f (d) Pb 5d levels shows a noticeable shift between $CH_3NH_3PbI_3$ and $CH_3NH_3PbCl_3$ as indicated in the figure. 142

5.11 Image of (a) $CH_3NH_3PbBr_3$ and (b) $CH_3NH_3PbCl_3$ crystals grown using the antisolvent vapor-assisted crystallization (ASVAC) method at room temperature. (c) Cubic crystal structure of $CH_3NH_3PbX_3$ (X=Br, Cl) used for calculations. (d) X-ray diffraction of $CH_3NH_3PbX_3$ (X=Br, Cl) crystals on which ARPES experiment was performed. (e) Surface Brillouin zone of the cubic structure. 143

5.12 Experimental angle integrated valence band spectra (20, 31 and 40 eV) compared to calculated total DOS for $CH_3NH_3PbBr_3$ and $CH_3NH_3PbCl_3$. Inset to the figure shows all valence band spectra (with different photon energies) normalized and plotted in the same figure for comparison (b). Calculated total and orbital projected density of states for (c) $CH_3NH_3PbBr_3$ and (d) $CH_3NH_3PbCl_3$. The delta-function peaks come from the C and N atoms of the CH_3NH_3 molecule. 145

5.13 Electronic band structure of (a,c) $CH_3NH_3PbCl_3$ and (b,d) $CH_3NH_3PbBr_3$. (a,b) Experimental data obtained from angle-resolved photoemission spectroscopy (ARPES), acquired at a photon energy of 37 eV; (c,d) Calculated band structure data. 147

5.14 The charge density plot of $CH_3NH_3PbCl_3$ at (a) X point, (b) Γ point and (c) M point. (d) Schematic representation of *s* - *p*-hybridization in hybrid perovskites. 149

5.15 Calculated band structure of (a) $CsPbCl_3$ and (b) $CH_3NH_3PbCl_3$; Inset shows the zoomed view near to Γ point. 150

5.16 Calculated band structure of (a), (b) $CH_3NH_3PbCl_3$ (without and with spin-orbit coupling (SOC)) and (c), (d) $CsPbCl_3$ (without and with SOC). 151

5.17 (a-h) Constant energy contour of the electronic structure in the plane at different binding energies marked in the figure. Corresponding energy cut from theoretical spectra of (i-j) $CH_3NH_3PbCl_3$ and (k-l) $CsPbCl_3$ are shown below. 152

5.18 Effect of SOC and the resulting Rashba effect on constant energy contour curves (Schematic). (a) In the presence of SOC, valence band (VB) splits into two spin-split bands and corresponding contours at different energies. (b) Without SOC, a doubly spin-degenerate band with a single maximum is expected. 153

5.19 Dispersion of ABC band of (a) $CH_3NH_3PbCl_3$ and (A′B′C′) of (b) $CH_3NH_3PbBr_3$ single crystal. The red line denote parabolic fit of these bands. 155

6.1 X-ray diffraction (XRD) patterns of $CH_3NH_3Pb(I_{1-x}Br_x)_3$ (x=0.15, 0.24, 0.27) powders (a) and thin films (b) collected at room temperature (300 K). Temperature dependent XRD patterns of x = 0.24 shown for some selective temperatures: 100, 200, 250 and 300 K across the crystallographic phase transition (c). SEM images of the perovskite films on FTO glass prepared by the solution prepared from single crystals of $MAPb(_{I0:76}Br_{0:24})_3$ (d) and $MAI+MABr+PbI_2$ (e). 164

6.2 Temperature dependent photoluminescence (PL) spectra of $CH_3NH_3Pb(I_{1-x}Br_x)_3$ thin films for a) x = 0.15, b) x = 0.24, and c) x = 0.27; Spectra are shifted vertically and are normalized for help in viewing. Inset shows the temperature dependence of emission peak positions. 166

6.3 (a) Schematics of the experiment protocol for studying temperature dependence of photo-induced phase separation (PS). Temperature dependent PL spectra of (b) x= 0.15; (c) x= 0.24; and (d) x= 0.27 thin films collected after 0 s and 4 hrs of light soaking time, represented by black and red sold lines. Here the spectra taken at different temperatures are shifted vertically and are normalized for help in viewing. 169

6.4 Schematic temperature−Br concentration phase diagram indicating ground/ mixed state, stable state and photoinduced demixed states. 171

6.5 Evolution of PL spectra at 225 K in the presence (a, c) and absence (b, d) of light for the compositions as marked in the figure. Inset shows integrated intensity of peak 1 and peak 2 as a function of time. Evolution of PL peak intensity at 225 K by varying the (e) excitation light wavelength and (f) light intensity/power (λ = 325 nm). 173

6.6 Lifetime measurement of peak 1 corresponding to 716 nm (black dots) and photo-excited peak 2 (746 nm) (blue dots) with corresponding exponential fit (red solid line) for x = 0.24 sample. Inset shows comparison of life time measurements spectra of peak 2 at 225 K and 275 K with corresponding fit. 175

6.7 Photoinduced polaron trapping and corresponding energy scales associated with phase separation. Here yellow and blue spheres represent I and Br, respectively, the red and white pill shapes represent CH_3NH_3 and lead atoms are represented by gray circles. 176

7.1 A comparison of perovskite efficiency progress with other kinds of photovoltaic (PV) devices. Abbreviation used in the figure are: OPV, organic photovoltaic; EPFL, École polytechnique fédérale de Lausanne; IAPP, Institut für Angewandte Photophysik; KRICT, Korean Research Institute of Chemical Technology; NIMS, National Institute for Materials Science; SKKU, Sungkyunkwan University; UCLA, University of California, Los Angeles; UCSB, University of California, Santa Barbara. 181

7.2 Schematic diagram of the (a) cell architecture and (b) energy levels of different layers. (c-d) Representative figure of solar cell made by us. (e) Schematic diagram of the perovskite absorber deposition process using antisolvent vapor diffusion technique. 185

7.3 SEM images of the perovskite films (a) as-deposited, (b) DCM-diffused, (c-d) EA diffused. (e) XRD patterns and (f) EDS of the perovskite films diffused by EA and DCM antisolvents. 186

7.4 (a) UV-visible absorption spectra, (b) Photoluminescence (PL) spectra and (c) Valence band XPS spectra of EA diffused $CH_3NH_3PbI_3$ thin film. Energy level diagram of EA diffused $CH_3NH_3PbI_3$ film is shown in inset of (b). 188

7.5 (a) Effects of different antisolvents (DCM and EA) on the photovoltaic device performance in ambient atmosphere. (b) Device performance of EA diffused perovskite film prepared inside the glove box. 190

8.1 Schematic diagram of the important findings of the present work. 195

8.2 Schematic diagram of (a) Tandem solar cell, (b) Field Effect Transistor (FET) and (c) Phototransistor 198

8.3 Illustration of photovoltaic and photothermal pyro-thermoelectric device 200

List of Table

1.1 Calculated and estimated tolerance factor (t_G) and octahedral factor (μ) for 12 halide perovskites. 11

1.2 Crystal system and transition temperatures of halide perovskites. 12

3.1 Crystallographic parameters of $CH_3NH_3PbCl_3$ obtained from Rietveld refinement of powder XRD. 81

3.2 Crystallographic parameters of obtained from single crystal XRD refinement. 82

4.1 Crystallographic Parameters of $CH_3NH_3PbI_3$ obtained from Rietveld refinement. 96

4.2 Crystallographic Parameters of $CH_3NH_3PbBr_3$ obtained from Rietveld refinement. 97

4.3 Crystallographic parameters of $CsPbBr_3$ samples obtained from single crystal XRD refinement at three different temperatures, T= 150 K, 360 K and 425 K. 106

5.1 Photoionization cross-section 146

6.1 Crystallographic parameters of $MAPb(I_{1-x}Br_x)_3$ (MA = CH_3NH_3; x = 0.15, 0.24, 0.27) samples obtained from single crystal XRD refinement. 165

7.1 Summary of Solar Cell Device Performance (in ambient conditions) 189

Chapter 1

Introduction

This chapter presents an overview of photovoltaics and a brief history of organic-inorganic hybrid perovskite solar cells along with their device architectures and the working mechanism. A short description of some important physical properties like crystal structure, phase transition, effective mass, optical band gap engineering, electron-phonon coupling, excitonic emission, dielectric property and ferroelectricity of the organic-inorganic hybrid perovskite is also discussed.

1.1 Preamble

World relies on fossil fuels (coal, petroleum and natural gas *etc.*) for most of its energy requirements, which unfortunately are fast depleting. Due to ever-increasing demand of energy for growth, development and sustainability, we are heading towards a global energy crisis. Search for alternative and renewable energy sources like wind, rain, tides, waves, geothermal heat, converting biomass to energy, solar energy *etc.* has hence gained momentum [1,2] and has become one of the frontier area of research for alternative energy sources. Among various renewable energy sources, solar power has several advantages over others. A total of 174 PW solar energy approaches earth, but only 89 PW is absorbed by the land and oceans, and the rest is reflected out in space by the atmosphere. It was also reported that one hour of sunlight on Earth would be sufficient to supply enough energy for an entire year, and a land covered with 850,000 km^2 of photovoltaic panels working at 10% efficiency and with a capacity factor of 20% would meet all the present world's energy demand [2, 3]. Solar cells/photovoltaic cells are able to harvest energy from the sun into usable energy (electricity) and therefore offer the possibility to meet humankind's ever-increasing energy demands. The Solar energy sector of India has a very good opportunity to harness solar energy for plenty of applications, as India receives a sufficient and continuous supply of solar radiation throughout the calendar [4].

1.1.1 Basic Physics of Solar cells

A solar cell is a semiconducting device which converts solar energy into electricity and the process is known as the photovoltaic effect [3, 5, 6]. In fact, electric current or voltage is created across such a device if light shines on the same. Spectral distribution of radiation, the capacity of light absorption, choice of suitable electron and hole transport materials are the key factors behind this process. When the energy of incident photons is greater than the bandgap of the absorber material, charge carriers (electrons and holes) are generated in the material [6]. However, electron-hole pairs created in this process exist for a time scale equal to the minority carrier lifetime and thereafter they recombine. Thus, they should be separated and collected before their recombination takes place. For this purpose, electron transport layer (conduction band of this level is closer to the absorber conduction band)

and hole transport layer (valence band of this level is closer to the absorber valence band) are deposited to form p-i-n junction. Thus, a careful choice of electron and hole transport materials are needed for efficient solar cells [3]. Spectral radiance of Sun under different air mass (AM) condition and schematic p-n junction solar cell are presented in Figure 1.1 (a) and 1.1 (b), respectively.

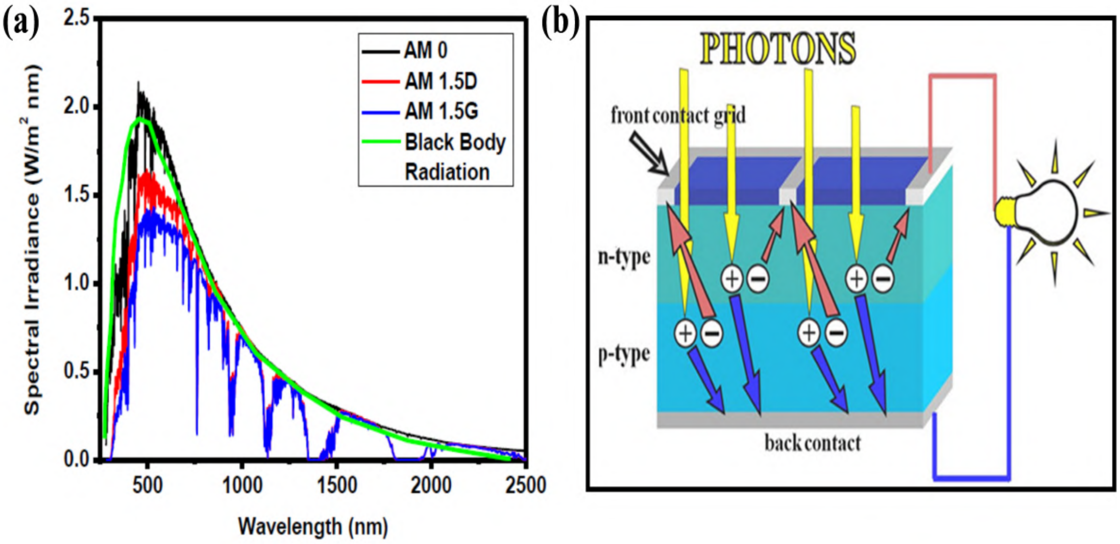

Figure 1.1: (a) Solar spectrum and spectral flux density as a function of incident photon wavelength, (b) Schematic depiction of p-n junction solar cell. (Data from ASTM) [http://rredc.nrel.gov/solar/spectra/am1.5/ASTMG173/ASTMG173.html]

1.1.2 Solar Cell Characteristics

The basic parameter of a solar cell is the power conversion efficiency (PCE) which can be measured from I-V characteristics under simulated AM1.5 G (1 Sun) illumination of intensity 100 mW/cm^2. Typical I-V curve is shown in Figure 1.2, from which the following parameters are determined [6].

1.1.2.1 Short-circuit current (I_{sc})

When the load resistance across the electrodes of the solar cell is ideally zero and the circuit is a short circuit, then a maximum current is measured through it and defined as the short circuit current. In general, it is presented in the form of the short-circuit current density (J_{sc}) defined as the ratio of the short circuit photocurrent to the active cell area.

1.1.2.2 Open-circuit Voltage (V_{oc})

When no power is derived from the solar cell across the load, a maximum voltage is measured across the electrodes of the solar cell and defined as the open-circuit voltage.

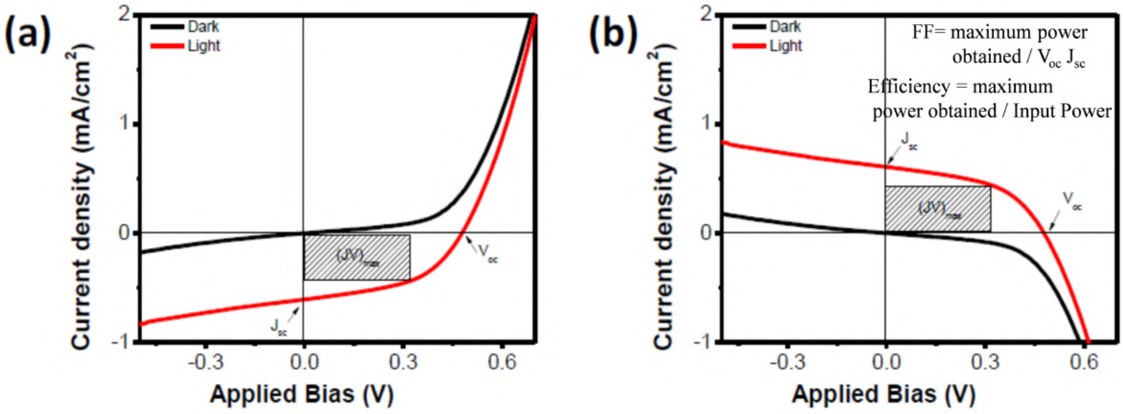

Figure 1.2: (a) Current density-Applied bias (J-V) characteristics of the solar cell under dark and 1 Sun illumination, (b) Universal way of representing the J-V data, obtained by changing the sign of photocurrent. This usually done as power generated by the device is positive.

1.1.2.3 Fill Factor (FF)

At a particular point in the J-V curve, the power obtained by the device is maximum. Ideally, the power generated across the solar cell should be equal to the product of open-circuit voltage and short-circuit current. Thus, the fill factor is defined as the ratio of the maximum power obtained to the product of open-circuit voltage and short-circuit current, which is defined as:

$$FF = \frac{P_{max}}{I_{sc}V_{oc}} = \frac{I_{max}V_{max}}{I_{sc}V_{oc}} \tag{1.1}$$

where I_{max} and V_{max} represent the current and voltage corresponding to the maximal power point.

1.1.2.4 Efficiency

The efficiency of the solar cell is defined as the percentage ratio of maximum power obtained per unit area to the input power per unit area. In standard condition, the power conversion efficiency (η) is calculated under AM 1.5G standard input light intensity of 100 mW/cm^2.

$$\eta = \frac{P_{max}}{P_{in}} = \frac{(J_{sc} * V_{oc} * FF)}{P_{in} V_{oc}} \tag{1.2}$$

1.1.3 Solar Cell Generations

Research on the photovoltaic cell started in 1959 in Bell Labs and with the subsequent developments, various types of solar cells have emerged. The evolution of various solar cells along with their efficiencies are summarized in Figure 1.3 (taken from NREL solar efficiency chart). From the figure, it is evident that different solar cell technologies have emerged over a period of time, which can be classified into four generations.

1.1.3.1 First generation solar cells

First generation photovoltaic cells are the dominant technologies in the commercial production of solar cells, accounting for more than 86% of the solar cell market. These cells are typically made using single crystalline Si (current efficiency ~27.6%), GaAs (current efficiency ~28.8%) and multi-junctions (current efficiency ~43%) [7]. Irrespective of high efficiencies of these single and multi-junction solar cells, high capital cost and limitation in large-scale production restrict their commercialization.

1.1.3.2 Second generation solar cells

The second generation solar cells are based on the thin film technology, where the material cost is believed to be reduced due to less quantity of the material used. In addition, thin film solar materials can be deposited onto large surfaces which is beneficial for volume production (*i.e.*, high throughput). The materials used for this thin film solar cells include, amorphous silicon (a-Si; current efficiency ~13%), cadmium telluride (CdTe; present efficiency ~22.1%), copper indium gallium diselenide (CIGS; current efficiency ~22.6%) *etc.* Most of these materials have much higher absorption coefficient than Si, and therefore, required an effective thickness of the film is < 1 μm thick, which is 300 times less than single crystal Si solar cells [8].

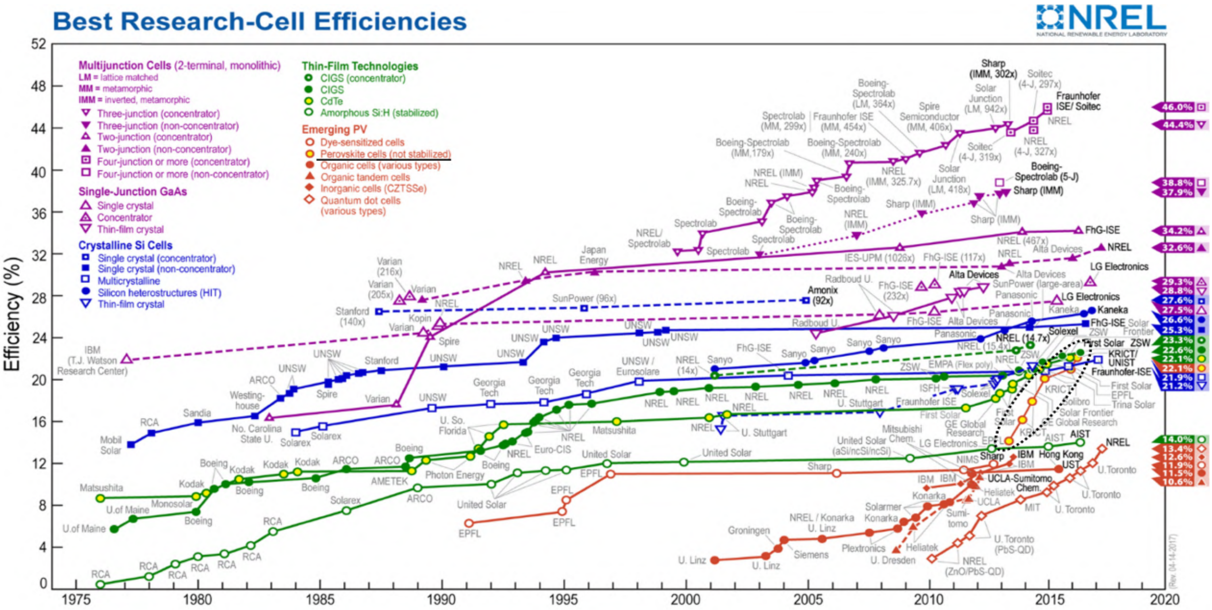

Figure 1.3: Timeline of the highest efficiencies in various solar cell technologies. Black dotted curve in the figure shows the rapid development in efficiency of hybrid perovskite solar cell.
[https://www.nrel.gov/pv/ Photovoltaic Research, Accessed: 4 May 2017, (2017).]

1.1.3.3 Third generation solar cells

Third generation solar cells were developed to overcome the limitations of first (flexibility and large area production) and second (moderately low efficiency and employment of hazardous cadmium material) generation solar cells. Briefly, third generation solar cells are fabricated by using organic semiconductor as an absorber material. Small molecules (efficiency upto 12%) and polymers (efficiency upto 10%) are good candidates for single junction and tandem structure. Dye-sensitized solar cells (DSSC), introduced by Gratzel and O'Regan in 1991 have emerged as a low-cost solar cell and become one of the most efficient (current efficiency 11.9%) candidate in third generation solar cell [9]. Quantum dot solar cells employing semiconductor with tunable bandgap (by changing quantum dot size), have attained efficiencies of ∼10%. Low efficiency restrict its commercialization. Thus, search is on to find a solar cell material which is easy to fabricate and have various tunable parameters to increase the efficiency.

1.1.3.4 Fourth generation solar cells

Combining the rigid inorganic framework with soft organic material, organic-inorganic hybrid perovskites have emerged (in recent years) as one of the most promising solution processed solar cell materials with power conversion efficiency as large as 22.1% [10]. These materials also have shown their prominence as light-emitting diode (LED), field-effect transistor (FET), spontaneous laser *etc.*) [11, 12].

1.2 Objective and Scope of the Thesis

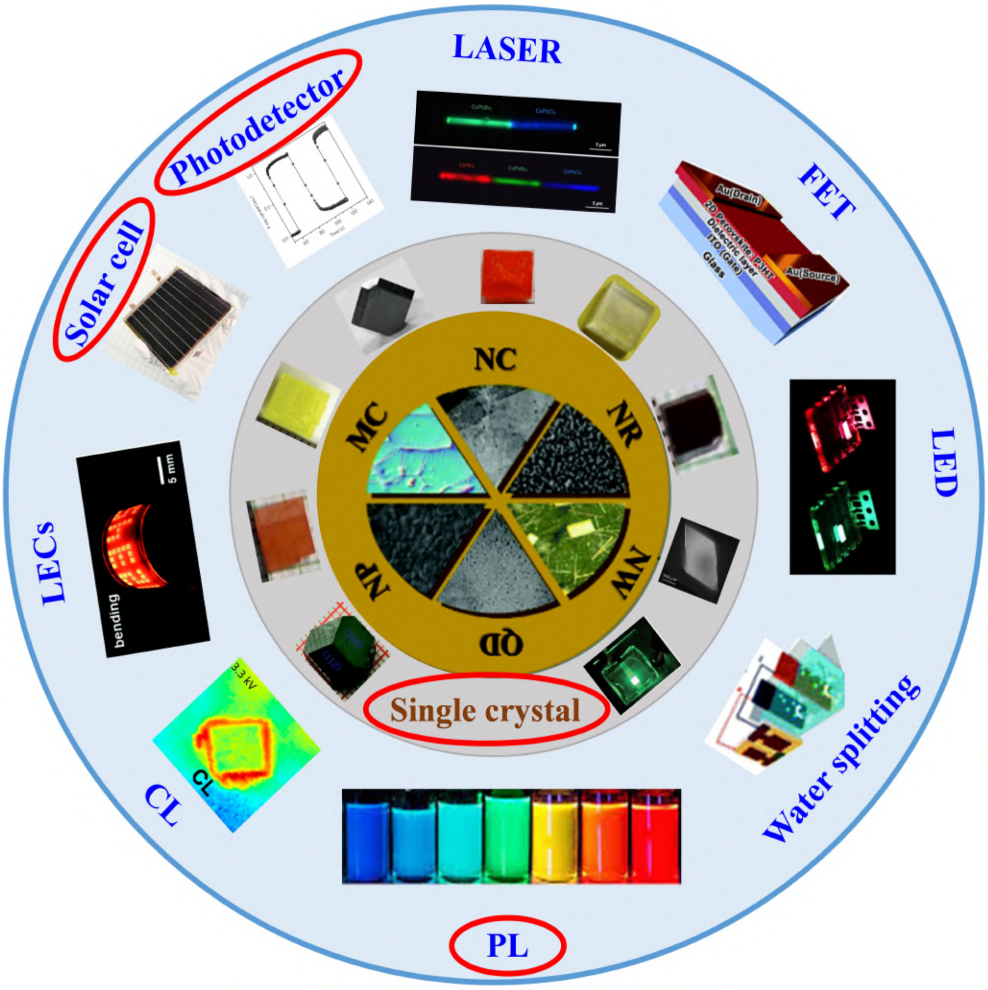

Figure 1.4: Overview of organic-inorganic hybrid perovskite and their applications. Highlighted topics are focused in this thesis.

This thesis deals with structural and spectroscopic investigations of organic-inorganic hybrid perovskites, a light absorbing material, which has shown considerable potential to be used as a solar cell material and next-generation lighting and display material (include LASER, LED, FET, Photodetector, cathodoluminescence *etc.*). The general motivation behind the research is to study the electronic and optical properties and related phenomena, in terms of fundamental understanding as well as from the application point of view (Figure 1.4). Furthermore, to achieve better device performance, the role of disorder, defect, phase separation, effective approach to synthesize high quality defect free single crystals, *etc.* need to be carefully investigated.

1.3 Overview of Organic-Inorganic Hybrid Perovskites

Any materials which have the crystal structure of titanium calcium oxide ($CaTiO_3$), is known as the Perovskite structure and is named by the Russian mineralogist Lev Aleksevich von Perrovski (1839) [13]. These compounds have stoichiometry of ABX_3 three-dimensional structure; where “A” is the larger cation, “B” is the smaller cation and “X” is the anion. Each unit cell of ABX_3 crystal comprises of corner sharing BX_6 octahedra, with the “A” moiety cubo-octahedral cavity. The ideal perovskite structure is a cubic lattice with cations “A” and “B” at the center and corner of the cube, respectively and “X” anions at the face centers. A particular aspect of perovskites is their ability to incorporate most of the elements of the periodic table in “A” and “B” sites due to their capacity to accommodate various structural distortions. Further, external parameters like temperature, pressure and chemical compositions can also tune such distortions, which results in various physical properties. Structural distortion in perovskites is governed by Goldschimdt’s tolerance factor (t_G) rule defined as [14]

$$t_G = \frac{r_A + r_X}{\sqrt{2}(r_B + r_X)} \tag{1.3}$$

where, r_A, r_B and r_X are the average ionic radii of elements “A”, “B” and “X” respectively, present in the system. When t_G is between 0.9 and 1.0, the perovskite will be in cubic structure and orthorhombic if $0.75 < t_G < 0.9$; whereas the compound adopts a hexagonal structure if $t_G < 0.75$. Further, the octahedral factor (μ) is defined as the ratio

r_B/r_X. These structural distortions are associated with three main features with respect to the parent cubic structure: (i) polar cation displacements, (ii) Rotation (tilting) of BO_6 octahedra and (iii) octahedral distortion. As a consequence, perovskite-type structures leading to a wide variety of applications like ferroelectricity, piezoelectricity, thermoelectricity, superconductivity, magnetoresistivity, photoconductivity, catalysis, solar cells, to name a few [15].

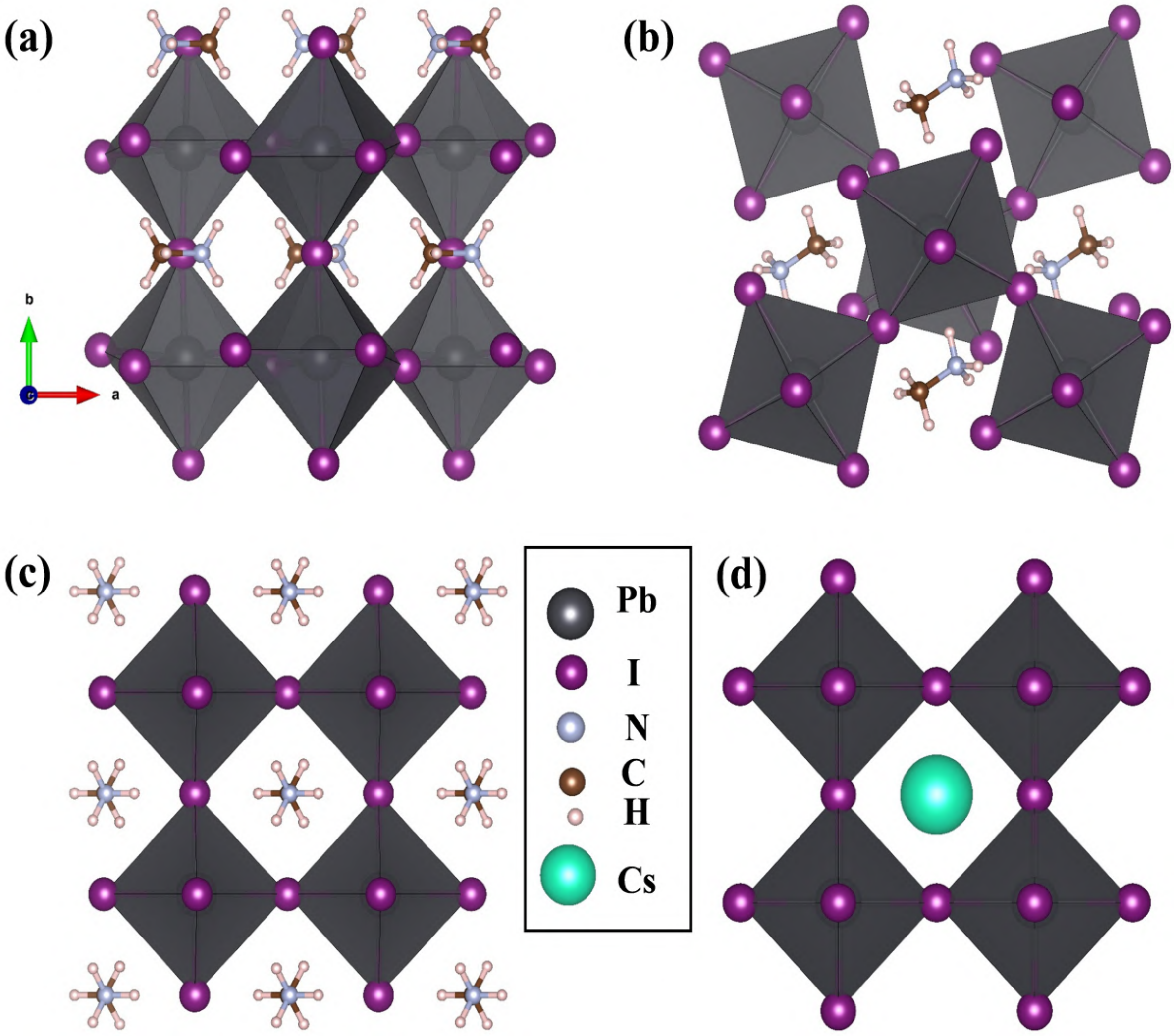

Figure 1.5: Crystal structure of $CH_3NH_3PbI_3$ in (a) Orthorhombic phase, (b) Tetragonal phase and (c) Cubic phase; (d) Cubic $CsPbI_3$.

In case of organic-inorganic hybrid perovskites, halides are found at the "X"-site anion instead of oxygen, while monovalent and bivalent cations occupy the "A" and "B" sites, respectively as opposed to the bivalent and tetravalent cations in “A” and “B” sites of oxide perovskites. Halide perovskites were first reported by Moller in 1958 for cesium lead halides [16]. Further, it was also observed that small organic molecules with effective radii less than 260 pm (methylammonium, formamidinium, hydrazinium, hydroxylammonium *etc.*) can also accommodate inside the lead halide octahedrons. The very first report on organic-inorganic hybrid perovskite was made by Dieter Weber in 1978, who synthesized $CH_3NH_3PbX_3$ (X= I, Br, Cl) [17]. Following this, layered 2D perovskite systems (commonly, $(R\text{-}NH_3)_2MX_4$) came into the forefront wherein extended inorganic lead halide framework is separated by large organo-ammonium cations [18]. The resurgent hybrid perovskite was initiated by the introduction of three-dimension (3D) hybrid perovskites ($CH_3NH_3PbI_3$ and $CH_3NH_3PbBr_3$) as an absorber in mesoporous solar cells in 2009 by Miyasaka *et al.* [19]. Since then researchers across the globe have used them as an absorber material in solar cell and achieved 22.1% efficiency [10]. The excellent electronic properties like low bandgap [20], high optical absorption coefficient [11], long charge carrier diffusion length [21], large mobilities [22] make them attractive candidates for light emitting device [11, 20], field-effect transistor [23] and laser [12] *etc.* As a solution processed high-quality semiconductors, the hybrid perovskites hold great potential to revolutionize the next generation optoelectronics [24].

1.3.1 Crystal Structure

For the organic-inorganic hybrid perovskites of present interest, “A”-sites in the generic ABX_3 formula is universally occupied by organic groups, such as methylammonium ($CH_3NH_3{}^+$; r_A = 0.18 nm), ethylammonium ($CH_3CH_2NH_3{}^+$; r_A = 0.23 nm) and formamidinium ($NH_2CH{=}NH_2{}^+$; r_A = 0.21 nm) and largest group-I inorganic ion Cs^+ (r_A = 0.167 nm) [25]. Further, anion “X” is a halogen, generally iodine (I^-; r_X = 0.220 nm), although Bromine (Br^-; r_X = 0.196 nm) and chlorine (Cl^-; r_X = 0.181 nm) are also commonly used, usually in mixed halide perovskite. For efficient solar cells, cation “B” has universally been lead (Pb^{2+}; r_B = 0.119 nm); tin (Sn^{2+}; r_B = 0.110 nm) form perovskite compounds with lower bandgaps(theoretically ideal), but lower stability (Sn^{4+} is the favorable oxidation state of Sn) hinders its usage [25, 26]. Calculated and estimated

Table 1.1: Calculated and estimated tolerance factor (t_G) and octahedral factor (μ) for 12 halide perovskites.

sample	t_G	μ
$CH_3NH_3PbI_3$	0.834	0.541
$CH_3NH_3PbBr_3$	0.844	0.607
$CH_3NH_3PbCl_3$	0.851	0.657
$CH_3NH_3SnI_3$	0.857	0.5
$CH_3NH_3SnBr_3$	0.869	0.561
$CH_3NH_3SnCl_3$	0.877	0.608
$CH(NH_2)_2PbI_3$	0.897	0.541
$CH(NH_2)_2PbBr_3$	0.911	0.607
$CH(NH_2)_2PbCl_3$	0.921	0.657
$CsPbI_3$	0.807	0.541
$CsPbBr_3$	0.815	0.607
$CsPbCl_3$	0.820	0.657

t_G and μ factors for a wide range of hybrid perovskites are tabulated in Table 1.1.

1.3.1.1 Phase Transition

Another interesting aspect of the crystal structure of halide perovskite is the structural flexibility of organic cation. Taking $CH_3NH_3PbI_3$ as an example, the disorder-order transition of $CH_3NH_3^+$ cation is believed to trigger the phase transition with the decrease of temperature [27]. At high temperature $CH_3NH_3PbI_3$ takes a cubic structure (space group: $Pm\bar{3}m$; Z=1) [28]. Since $CH_3NH_3^+$ has a lower symmetry of C_{3v}, the orientation of $CH_3NH_3^+$ ion should be disordered to satisfy the O_h symmetry [29]. As the temperature is lowered, tetragonal and orthorhombic phases are realized by an accompanying ordering of methylammonium ion. Structural transition from cubic to tetragonal phase occurs due to the reorientation of $CH_3NH_3^+$ ion, as observed by NMR studies where lowering the number of disorder states of $CH_3NH_3^+$ was observed from 24 in the cubic phase to 8 in tetragonal phase [30]. Below a critical temperature (tetragonal-orthorhombic phase transition), the $CH_3NH_3^+$ molecule is frozen (only 1 degree of freedom) and the symmetry of $CH_3NH_3PbI_3$ become orthorhombic [28, 31]. Similar crystallographic phase transition can be realized with replacing I by Br and Cl [31]. Crystallographic phase transition temperatures of hybrid halide perovskites are tabulated in Table 1.2 [31–33].

Table 1.2: Crystal system and transition temperatures of halide perovskites.

$sample$	$Cubic \rightarrow Tetragonal(K)$	$Tetragonal \rightarrow Orthorhombic(K)$
$CH_3NH_3PbI_3$	330.8	161.8
$CH_3NH_3PbBr_3$	236.1	149.8
$CH_3NH_3PbCl_3$	177.2	171.5
$CH_3NH_3PbI_{3-x}Br_x$ (x=0.5)	275	148
$CH(NH_2)_2PbBr_3$	238	150
$CsPbBr_3$	403	385

Apart from temperature dependent crystallographic phase transition, organic-inorganic hybrid perovskites also undergo amorphization under pressure. A reversible pressure induced crystallographic phase transition (cubic to orthorhombic) is observed at 0.3 GPa and 1.8 GPa for $CH_3NH_3PbI_3$ and $CH_3NH_3PbBr_3$, respectively [34]. This phase transition can slightly increase the band gap due to symmetry lowering and octahedra tilting. On further compression, both the samples exhibit a reversible pressure-induced amorphization above 4 GPa, which significantly affect its photovoltaic properties.

1.3.1.2 Defects

It is well known that trap state density and charge transport properties are two key parameters determining the high crystalline quality of a single crystalline semiconducting material and proper knowledge of the behavior of native defects is essential for the successful application in any semiconductor and optoelectronic devices. It is observed that vacancies, self-interstitials, and antisites can have deleterious effects on the performance of a laser, LED and photodetector. Thus, to enhance device performance, we need to understand the origin of defects [35]. For $CH_3NH_3PbI_3$, shallow energy levels are created due to point defects with low formation energy values, whereas for point defects deep levels arise with high formation energies [36]. Among all intrinsic point defects in $CH_3NH_3PbI_3$: CH_3NH_3, Pb, and I vacancies (V_{MA}, V_{Pb}, V_I), CH_3NH_3, Pb, and I interstitials (MA_i, Pb_i, I_i), CH_3NH_3 on Pb and Pb on CH_3NH_3 cation substitutions (MA_{Pb}, Pb_{MA}) and four antisite substitutions: CH_3NH_3 on I (MA_I), Pb on I (Pb_I), I on CH_3NH_3 (I_{MA}), and I on Pb (I_{Pb}); only five defects (I_{MA}, I_{Pb}, Pb_i, MA_I, and Pb_I) generate deep levels [37]. Further, it was also observed that $CH_3NH_3PbI_3$ exhibits an intrinsic ambipolar self-doping behavior where the electrical conductivity can be tuned from p-type to n-type via controlling the growth conditions. However, $CH_3NH_3PbBr_3$ exhibits a unipolar self-doping behavior and demonstrates preferential p-type conductivity if synthesized under thermal equilibrium growth conditions. It is seen that there are only four defects, *i.e.*, Pb_i, Pb_{Br}, Br_{MA}, and Br_{Pb} that produce deep levels in the bandgap of $CH_3NH_3PbBr_3$ [38]. $CH_3NH_3PbCl_3$ exhibits a compensated self-doping behavior due to its large bandgap [36]. Calculated transition energy levels of donor-like and acceptor-like point defects in $CH_3NH_3PbI_3$ and $CH_3NH_3PbBr_3$ are presented in Figure 1.6.

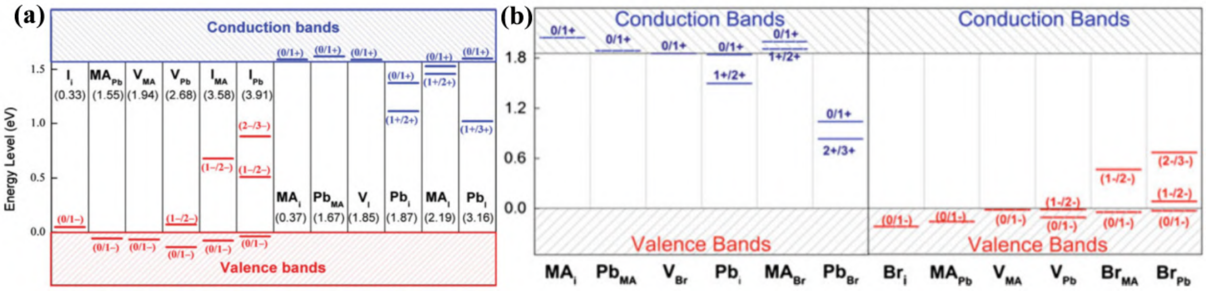

Figure 1.6: Calculated transition energy levels of donor-like and acceptor-like point defects in (a) $CH_3NH_3PbI_3$ and (b) $CH_3NH_3PbBr_3$.
[From (a) Adv. Mater., 26, 4653 (2014), (b) Appl. Phys. Lett., 106, 103902 (2015).]

1.3.2 Electronic Structure

The electronic structure can be investigated experimentally using ultraviolet photoelectron spectroscopy (UPS) [39, 40], x-ray photoelectron spectroscopy (XPS) [27], inverse photoemission spectroscopy (IPES) [40], angle-resolved photoemission spectroscopy (ARPES), *etc.* [41] while theoretically can be reproduced using density functional theory (DFT) calculations [42].

The band structure of $CH_3NH_3PbI_3$ exhibits a direct bandgap of 1.6 eV at the R point [42, 43]. Calculated band structure suggests conduction band minima (CBM) is dominated by the Pb-*p* orbital, whereas the valence band maxima (VBM) is constituted by I-*p* states mixed with a small amount of Pb-*s* states [35], which is consistent with the UPS results [39, 40]. The optical transition of $CH_3NH_3PbI_3$ thus relies on a direct bandgap *p*-*p* transition, leading to a strong optical absorption coefficient. Strong *s*-*p* antibonding enhances the dispersion of the upper valence bands, which results in small effective masses of electrons (m_e^*) and holes (m_h^*) [44]. Further, it is believed that the role of $CH_3NH_3^+$ cation is to maintain the overall charge symmetry and dictate the crystal structure of the system [42, 43]. However, recently it was reported that $CH_3NH_3^+$ cation has an indirect impact on the shape and orbital composition of the band edges [45, 46]. The molecular orientation of $CH_3NH_3^+$ cation can distorts the PbI_6 octahedra and affects the cell size and bonding of Pb-I, which modulates the density of states near the band edges [45–47]. Other halide perovskites also possess similar ways of electronic band structure [42].

1.3.2.1 Effective Mass

From band theory of solids, we know that the motion of an electron in a crystal is not free and it has to traverse through a periodic potential, hence effective mass approach is used for simplicity. In general, the value of effective mass depends on the purpose of which it is used and can vary depending on a number of factors. In general, effective mass of electron (m_e^*) and holes (m_h^*) can be represented as:

$$\frac{1}{m_e^*} = \frac{1}{\hbar^2}\frac{\partial^2 E_c}{\partial k^2} \; for\ electrons \tag{1.4}$$

$$\frac{1}{m_h^*} = \frac{1}{\hbar^2}\frac{\partial^2 E_v}{\partial k^2} \; for\ holes \tag{1.5}$$

where E_c and E_v are the conduction and valence band edges respectively; k is the wavevector and $\hbar$ is the Planck constant. For $CH_3NH_3PbI_3$, calculated m_e^* and m_h^* are found to be 0.35 m_0 and 0.31 m_0 respectively without considering spin-orbit coupling (SOC), while this value reduces to 0.18 m_0 and 0.21 m_0 respectively if SOC is considered [22,48]. Thus, proper estimation of appropriate effective masses are essential for development of hybrid perovskite as a channel material in high-speed field effect transistor and other optoelectronic applications.

1.3.3 Optical Properties

Absorption and photoluminescence (PL) spectra provides information about optical bandgap, excitonic binding energy, and nature of phonon interaction *etc.* of any semiconducting system [49]. Absorption edge and PL peak is differed by several nanometers via stock's and anti-stoke's shift. Spectral width of the emission peak (full width at half maxima) is a good indicator of the density of traps and morphological disorder. Evolution of PL intensity with time, *i.e.*, the PL decay dynamics, give a measure of the lifetime of photocarriers within the semiconductor [50]. Single or multiple decay functions represent the time dynamics of different recombination pathways.

Organic-inorganic hybrid perovskites are direct bandgap semiconductor and the direct transition produces large absorption coefficients of the order of 10^4-10^5 cm^{-1}. In the case of perovskite thin films, the optical properties of perovskites are dramatically affected by the quality, composition and morphology of the film [51]. Sizes of the halide anions (X = I, Br, Cl) affects the electronic band structure of the system. Large anion like iodine based materials show a smaller bandgap and corresponding absorption edge is at 780 nm [27]; whereas substituting iodine with smaller bromine (chlorine) anion shifts the absorption edge to 535 nm (408 nm) for CH_3NH_3 based perovskite system [52,53]. A systematic blue shift of the PL emission peak is observed with the increase of Br concentration in mixed halide perovskite of the type $CH_3NH_3Pb(I_{1-x}Br_x)_3$ [54]. Further, replacing CH_3NH_3 with $CH(NH_2)_2$ red shifts the absorption spectra by 40 nm, which makes $CH(NH_2)_2PbI_3$ more suitable for high-performance solar cell applications [32]. Intermediated solid solutions of $CH_3NH_3Sn_{1-x}Pb_xI_3$ with x= 0.25 and 0.5 exhibit the smallest bandgap of 1.17 eV [55].

Irrespective of bandgap tuning, fundamental understanding of absorption and PL spectra are essential to study the basic photophysical properties of hybrid perovskite. In spite of several optical investigations performed at different temperatures, there have been a lot of ambiguities in the data as well as its interpretations, especially observation of multiple peaks in the photoluminescence (PL) spectrum of organic-inorganic hybrid perovskites [56–59]. Literature reports excitonic emission [56], tetragonal inclusion in orthorhombic phase [57], order-disorder transition [58], surface-bulk effects [59] are responsible for these multiple PL emissions. Thus, in this thesis we have extensively discussed the origin of dual emission in methylammonium lead bromide perovskite from both theoretical and experimental points of view.

1.3.3.1 Excitons

Exciton is a bound state of an electron and the associated hole, which are attracted to each other by the electrostatic Coulomb force and exists in insulator, semiconductor, and in some liquids [60]. Therefore, such a bound electron-hole pair no longer represents two independent quasi-particles and their internal energy is less than the bandgap (E_g). Thus, an exciton is a quasi-particle which represent the lowest electronic excitation in a semiconductor [61]. There exist three types of excitons: (a) *Frenkel exciton* or a small-radius exciton. These excitons are localized at a specific atom or molecule and they move throughout the crystal by hopping mechanism. They occur in molecular crystals [62]. (b) *Charge transfer exciton* occurs in ionic crystals. When an electron transfer from lattice anion to nearest cation, thereby creating a maximum of the electron charge density. Thus, charge transfer exciton has larger radius than that of Frenkel exciton [63]. (c) *Wannier exciton* or large-radius exciton. Electron and hole are separated over many unit cells and due to delocalized wavefunction, exciton can move freely inside the crystal. Thus, these quasi-particles are known as free exciton and occur mainly in semiconductor [64]. The dispersion curve of exciton can be represented as:

$$E(K) = E_g - E_X + \frac{\hbar^2 K^2}{2(m_e + m_h)} = E_g - E_X + \frac{\hbar^2 K^2}{2m_{exc}} \tag{1.6}$$

where E_g, E_X and m_{exc} are the bandgap, exciton binding energy and total or effective (m_e+m_h) exciton mass.

Determination of the branching fraction between excitons-free carriers and the exciton binding energy are one of the key areas of investigation for organic-inorganic hybrid perovskites [65–68]. Many recent articles have shown that the exciton binding energy of $CH_3NH_3PbI_3$ is extremely low (few millielectron volts only) using a variety of techniques including electroabsorption [65], transient absorption [66], temperature dependent absorption [67] and PL spectroscopy [68]; and free carrier generation occurs upon light absorption at room temperature. However, morphology, crystalline nature and particle size (for nanocrystals) have also been shown to impact the exciton binding energy of hybrid perovskites [69]. The exciton binding energy has been shown to increase following the iodine to bromine to chlorine progression [70]. As the exciton binding energy greatly impacts the excited state population and is a factor in the dominating recombination pathway, research on exciton binding energy of hybrid perovskite become essential.

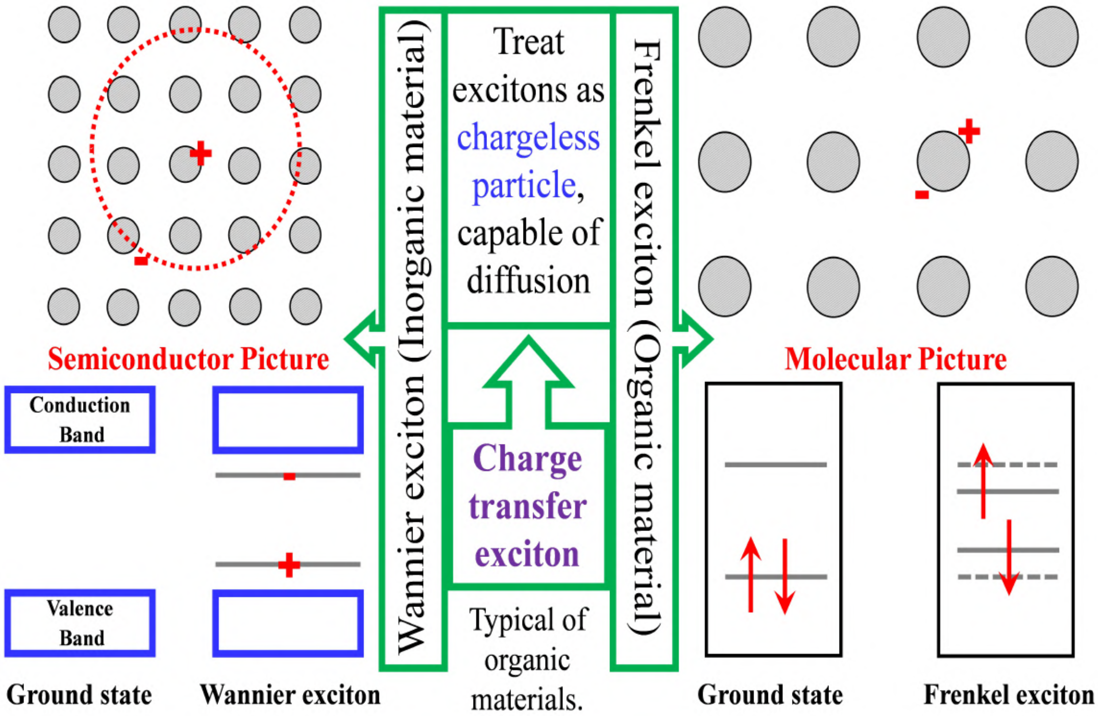

Figure 1.7: Schematic representation of Wannier, Frenkel and Charge transfer excitons.

1.3.3.2 Polarons

In case of ionic or highly polar crystals, where the Coulomb interaction between a conduction electron and the lattice ions results in a strong electron-phonon coupling, electron is always surrounded by a cloud of virtual phonons. The cloud of virtual phonons corresponds physically to the electron pulling nearby positive ions towards it and pushing nearby negative ions away. The electron and its virtual phonons, taken together, can be treated as a new composite particle, called a polaron [71]. (In particular, the above describes an electron polaron; the hole polaron is defined analogously) [72].

In case of mixed halide perovskites, it is predicted that small clusters enriched with one halide species get localized near the grain boundaries after prolonged illumination and this photogenerated charge carriers and their accompanying lattice distortion create polarons [73]. In this thesis work, we experimentally confirmed that photoinduced nanoscale phase separation is mediated through the strain generated by the polaron and provide a rather convincing support of the theoretical Molecular Dynamics (MD) simulations both in the absence and presence of hole polarons.

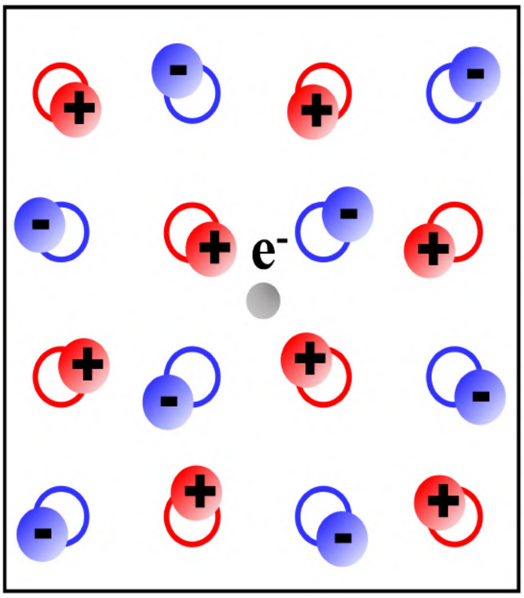

Figure 1.8: Schematic representation of Polaron.

1.3.4 Electrical Properties

Proper knowledge of a material's electrical properties, which include charge carrier mobility, diffusion length and recombination time scale, *etc.* are essential for fabricating optoelectronic devices. Space charge limited current (SCLC) is one of the effective approaches to measure mobility, diffusion length and trap density of hybrid perovskites [74]. Due to the advancement in fabrication techniques, the diffusion length of hybrid perovskite has increased from 1 μm to ~10 μm in about 3 years [21, 32, 75, 76]. This improvement reflects the progress that has been recently made in producing samples with better structural order and morphology [76]. Further, it is also observed that the diffusion length has a strong dependence on the grain size of the film and more than 1 μm diffusion length have been achieved by realizing films with an average grain size of 2 μm. The highest measured diffusion length (10 μm) are found in perovskite single crystals [32].
Carrier mobility of hybrid perovskite has also been improved over the years and exhibits morphology dependence. Mobilities exceeding 10 $\mathrm{cm^2V^{-1}s^{-1}}$ have been measured in perovskite films [75] and above 100 $\mathrm{cm^2V^{-1}s^{-1}}$ in perovskite single crystals [32]. Further, it is also observed that the mobility (and also diffusion length) does not exhibit a strong dependence on the material composition.

1.3.4.1 Dielectric Properties

The dielectric constant (relative permittivity) is a complex number given by: $\varepsilon = \varepsilon'$ - ε'', where the real part ε' is the charge storage ability and the imaginary part ε'' is the energy loss. For $CH_3NH_3PbI_3$, a small ε' is obtained ($\varepsilon' = 6.5$ in experiment [77], while 5.6 to 6.5 in calculation [78]) at optical frequency and only electronic polarization takes part in dielectric process. With the decrease of frequency, ionic polarization and dipolar polarization (contribution from $CH_3NH_3^+$ dipoles) leading to an enhanced ε' (ε'_{low} $\sim$ 60 at 100 KHz) [79]. This large dielectric constant facilitates the screening effect of Coulombic attraction between photoexcited electron-hole pairs (excitons), so that they can be separated easily.

1.3.4.2 Ferroelectricity

Based on the non-centrosymmetric crystal structure in tetragonal and orthorhombic phases, ferroelectricity was proposed for hybrid perovskites [80]. It is also believed that ferroelectricity may give rise to hysteresis observed in current-voltage (I-V) curves [81]. However, observation of ferroelectricity in hybrid perovskite is not well justified from polarization-electric field (P-E) hysteresis loop [82] and second harmonic generation experiments [83]. Despite the above controversies, it is of great interest to study the order-disorder transition of hybrid perovskites due to $CH_3NH_3^+$ orientation inside the PbX_6 octahedra.

1.4 Device Configuration

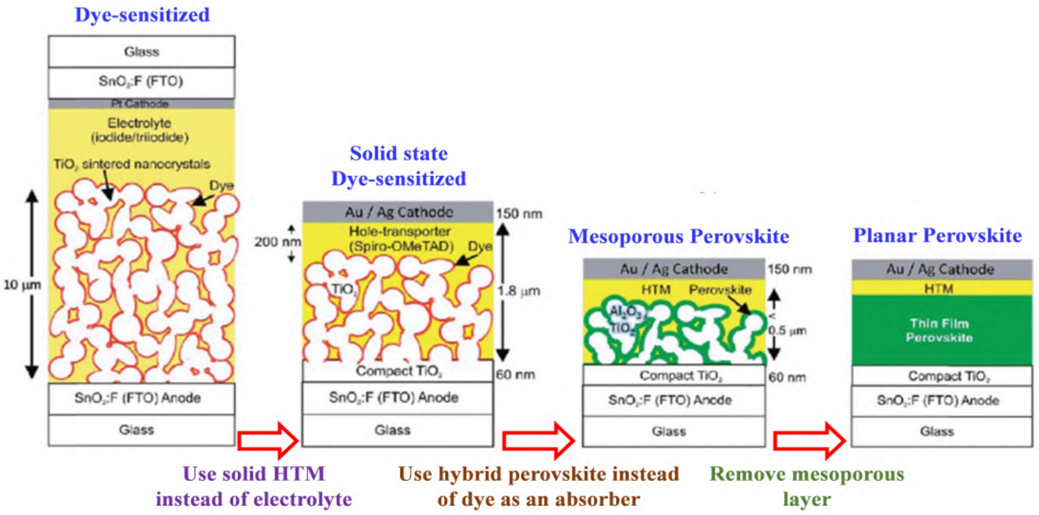

Figure 1.9: Evolution of Organic-inorganic hybrid perovskite solar cell technology starting from the electrolyte-based mesoscopic Dye-sensitized solar cells (DSSC) and solid state (ss) DSSC

[Taken from J. Mater. Chem. A, 2016,4, 6693-6713]

Evolution of perovskite solar cell from mesoscopic DSSCs are depicted in Figure 1.9. Initially, iodine-based liquid electrolyte in Dye-sensitized solar cells (DSSC) was replaced by hybrid perovskite and 3.8% PCE was achieved by Miyasaka and co-workers [19]. Subsequently, Snaith *et al.* could increase the PCE to 9.7% by using spiro-MeOTAD as solid-state hole transport materials (HTM) [84]. By using a double layer of mesoporous

TiO_2, Han *et al.* reported a PCE of 12.8% and more than 1000 hours stability in ambient condition under sunlight [85]. In all these devices, the perovskite was either deposited on high temperature processed mesoporous TiO_2 or Al_2O_3 [86]. In 2013, a regular planar structure (solution processed TiO_2 as an electron transport layer (ETL)) was employed by Snaith *et al.* and 15.4% PCE was recorded [87]. A range of new deposition techniques and even higher efficiencies were reported in 2014. A reverse-scan efficiency of 19.3% was claimed by Yang Yang at UCLA using the planar thin-film architecture and Yttrium-doped TiO_2 as an ETL [88]. In November 2014, researchers from KRICT achieved a PCE of 20.1% by using FAI solution during spin coating of $CH_3NH_3PbI_3$ thin film [89]. As of March 2017, researchers from KRICT and UNIST hold the highest certified record for a single-junction perovskite solar cell with 22.1% using the solid solution of $MA_{1-x}FA_xPbI_{1-y}Br_y$ [10]. Large ambipolar carrier diffusion lengths of hybrid perovskite enablem them to use in both p-i-n or n-i-p devices with performances comparable to its mesoporous counterparts. The unprecedented rise of perovskite-related research is due to the large number of favorable attributes of hybrid perovskites, to name a few:

- High absorption coefficient in visible and near-infrared region [11].
- Long and balanced electron and hole mobility [22, 48].
- High carrier diffusion length [21, 32, 75, 76].
- Facile bandgap tuning by varying the composition as well as dimensionality [54].
- Easy solution processing synthesized technique [90].
- Superior properties like flexibility, semitransparency, and vivid colors [91, 92].
- High photoluminescence quantum yield [93].
- High defect tolerance and low surface recombination velocity [94, 95].

1.5 Challenges concerning Hybrid Perovskites

Organic-inorganic hybrid halide solar cells are considered as next generation solar cell material with large prospects of enhancing PCE. For device applications continuous research efforts are essential to produce large-area perovskite solar cells. Key parameters for advancing a photovoltaic technology from laboratory-scale fabrication to industrial-scale applications are, (i) low cost, (ii) large area, (iii) high throughput, (iv) high solar-to-energy PCE, (v) reproducibility, (vi) cost performance, (vii) long lifetime, and (viii) low toxicity (or environmental impact). Long term stability in air and sunlight, replacement of toxic lead in hybrid perovskites and reproducible thin film synthesis procedure are one of the major challenges [96, 97].

1.6 Organization of Thesis

The various chapters of the thesis are briefly described below:
In **Chapter 2** we discuss the various experimental and theoretical techniques used in this thesis work. This include sample synthesis techniques: Inverse Temperature Crystallization method (ITC), Solution Temperature Lowering method (STL), Anti-solvent Vapor Assisted Crystallization method (AVC) and Solvent Evaporation at room temperature method (SERT) and various characterization tools such as powder and single crystal x-ray diffraction (XRD), heat capacity, scanning electron microscopy (SEM), extended x-ray absorption fine structure (EXAFS) study, UV-Visible absorption spectroscopy, photoluminescence (PL), photoelectron spectroscopy (XPS and UPS), Raman spectroscopy, *etc.* We also discuss first-principles density functional theory (DFT) based calculations to study the structural, electronic and optical properties of hybrid perovskites and demonstrate power conversion efficiency (PCE) of solar cell devices made by us.

Chapter 3 is divided into two parts. In the first part, we discuss multiple approachs to synthesize high-quality defect free single crystals of $CH_3NH_3PbBr_3$ via STL, ITC and AVC method and compared their optical properties. A broad inter-band emission peak was observed for crystals grown at high temperatures (in ITC and STL) and low boiling point (dichloromethane) AVC method, whereas it was absent in high boiling point (Ethyl acetate) AVC method. Time-resolved spectroscopy and dc magnetization studies confirmed that defect-assisted extrinsic self-trapping is dominant over the intrinsic self-trapping process in the case of sample synthesized by ITC, STL and DCM diffused AVC method. Comparison of formation energy calculations with the experimentally obtained energy levels confirmed that excess Pb in interstitial positions are predominantly responsible for the extrinsic self-trapping process. In the second part, we have presented a completely new route to synthesize high-quality defect free $CH_3NH_3PbCl_3$ crystals through proper selection of the Dimethyl sulfoxide (DMSO) and gamma-Butyrolactone (GBL) solution, which allowed crystallization due to solvent evaporation at room temperature (SERT). Further, structural, electronic, optical and electrical properties of the as grown crystals were carried out and various physical parameters (phase transition temperatures, band structure, exciton binding energy, carrier mobility, trap density and diffusion length) were determined. Low defect concentration (as seen from optical and charge transport points of view) and longer diffusion length indicate that these crystals are promising candidates to work as an active component in visible-blind UV detector. We hope, these two synthesis procedures (EA diffused AVC and SERT) will provide a breakthrough for the deployment of $CH_3NH_3PbBr_3$ and $CH_3NH_3PbCl_3$ single crystals in practical applications. We have used these crystals for detailed structural and spectroscopic characterization in following chapters.

In **Chapter 4** we discuss crystal structures and structural phase transitions of hybrid perovskites using XRD and EXAFS measurements. At 330.8 K (236.1 K), the high temperature cubic phase transforms to body centered tetragonal phase for $CH_3NH_3PbI_3$ ($CH_3NH_3PbBr_3$). Variation of lattice and order parameters, tetragonal distortion and linear expansion coefficients clearly indicate that it is a first order phase transition and rule out the possibility of phase coexistence. Upon cooling further, all the tetragonal phases transformed into a low temperature orthorhombic phase at around 161.8 K (149.8 K), again via a first-order phase transition. Nonpolar or centrosymmetric space group in all three phases rules out the possibility of ferroelectricity or second harmonic generation in this system. Further, variation of bond-length and bond-angle of $CH_3NH_3PbX_3$ (X= I, Br) clearly demonstrates octahedral distortion near the phase transition temperatures, which is absent in $CsPbBr_3$. Based upon these results, we discuss the impact of the structural phase transitions upon photovoltaic performance of organic-inorganic hybrid perovskite based solar cells.

Chapter 5 also consists of two parts. In the first part, we discuss detailed investigations on optical properties of solid solutions of $APbX_3$ (A=MA, FA, Cs and X=I, Br, Cl) using room temperature UV-Visible absorption and temperature dependent PL studies and theoretical calculations to understand the role of methylammonium cation orientation in band structure. Variation of optical bandgap; excitonic binding energy and exciton-phonon interaction with temperature in all three crystallographic phases are discussed in this chapter. Further, dual emission is observed for $CH_3NH_3PbBr_3$ and $CH(NH_2)_2PbBr_3$ systems, whereas single emission is observed for $CsPbBr_3$. We thus speculate that $CH_3NH_3^+$ orientation inside the $PbBr_6$ octahedra is responsible for this dual emission, which is also confirmed by first-principle DFT calculations and MD simulations. We also report observations of face dependent steady-state and time-resolved PL studies in single crystal samples of $CH_3NH_3PbBr_3$ in orthorhombic phase. Second part of the chapter contains detail photoemission studies (XPS and UPS) of hybrid perovskites. XPS spectra of different constituent core level elements of hybrid perovskites were also recorded to identify spin-orbit splitting and oxidation states of these elements. Further, angle-integrated, angle-resolved photoemission spectroscopy and density functional theory were used to investigate the electronic structure and valence band dispersion of hybrid perovskites. The experimental band structure shows a good agreement with the ab-initio calculations. These results suggest that the top of the valence band arise due to formation of bonding-antibonding levels because of the Pb-Cl/Br interaction. Further, highly reproducible dispersive feature of the valence band and constant energy cuts reveal binding energies of Brillouin zone boundaries ($\overline{M}, \overline{X}$) are higher than that of zone center ($\overline{\Gamma}$). Hole effective mass and carrier mobility were also determined along $\overline{\Gamma}$ - $\overline{M}$ and $\overline{\Gamma}$ - $\overline{X}$ direction which shows good consistency with other observations.

It is observed that, mixed halide perovskite undergoes a reversible complex dynamic phenomenon namely ‘photoinduced phase separation’ into low bandgap I-rich and high bandgap Br-rich domains under continuous illumination. Thus in **Chapter 6** we show that photoinduced phase separation occurs only in a narrow temperature range (190 K to 275 K) and above a particular bromine (x>0.2) concentration of $CH_3NH_3Pb(I_{1-x}Br_x)_3$

using temperature dependent photoluminescence studies. It is also observed that continuous illumination creates polaronic strain at the grain boundary and stimulates the formation of iodide and bromine rich clusters. Longer carrier lifetime of photo-induced state confirm the presence of strong electron-phonon interaction (polaronic effect).

In **Chapter 7** we discuss the fabrication of mesoporous 'methylammonium lead iodide' solar cells and the effect of antisolvent in morphology and power conversion efficiency (PCEs). Solar cells based on hybrid perovskite $CH_3NH_3PbI_3$ as an absorber in FTO/ compact TiO_2/ Mesoporous TiO_2/ $CH_3NH_3PbI_3$/ Spiro-OMeTAD/Au geometry were deposited using spin-coating technique. Thereafter, high (DCM) and low (EA) boiling point antisolvents were diffused to the $CH_3NH_3PbI_3$ films and a new morphology (microrods) were evolved for the case of EA treated films. Further, we also observed that due to better morphology of the mesoporous films, EA diffused films exhibit better fill factor and results in 32% power conversion efficiency enhancement than the DCM diffused (5.8%) and as-deposited films (5.6%).

Summary and future plans of the present thesis work are discussed in **Chapter 8**.

Chapter 2

Experimental and Theoretical Methodologies

This chapter presents a brief overview of the experimental methods used for synthesizing single crystalline and thin-film samples and their characterizations. Single crystalline samples of organic-inorganic hybrid perovskites were synthesized via wet chemical route and x-ray diffraction (XRD) technique was used to confirm phase purity and determine their crystal structure. Thereafter, samples were characterized using extended x-ray absorption fine structure (EXAFS) study, UV-Visible absorption spectroscopy, photoluminescence (PL), photoelectron spectroscopy (XPS and UPS), Raman spectroscopy etc. In addition, we also performed first-principles density functional theory based calculations to study the structural and electronic properties of this system.

2.1 Introduction

This chapter deals with the details of experimental techniques that are employed to synthesize single crystals and thin films of organic-inorganic hybrid perovskites of the type $APbX_3$ ("A" = CH_3NH_3, $NH_2CH{=}NH_2$, Cs; "X" = I, Br, Cl or mixtures of them) and to characterize them through various techniques. Single crystals of organic-inorganic and all inorganic hybrid perovskites were grown using four different wet chemical methods (Inverse Temperature Crystallization method, Solution Temperature Lowering method, Anti-solvent Vapor Assisted Crystallization method and Room temperature Solvent Evaporation method). Further, growth of hybrid perovskite thin films and solar cell module on Fluorine doped Titanium oxide (FTO) substrate using spin-coating technique is also presented. These single crystals and thin films are characterized via powder and single crystal x-ray diffraction (XRD), heat capacity, scanning electron microscopy (SEM), extended x-ray absorption fine structure (EXAFS) study, UV-Visible absorption spectroscopy, photoluminescence (PL), photoelectron spectroscopy (XPS and UPS), Raman spectroscopy *etc.* In addition, first-principles density functional theory based calculations were also performed to correlate the experimentally observed structural and electronic properties of hybrid perovskites. Following these, power conversion efficiency (PCE) of solar cell devices made by us were studied by I-V measurements.

2.2 Sample Synthesis

2.2.1 Single Crystal Growth

A material can be transferred into the single crystal by slow and gradual solidification of its fluid form (melt, solution or vapor phase). Crystal growth is a first order phase transition in which the atoms or molecules of the material lose their random character gradually in uniform manner and achieve a long-range order in the form of crystalline solid. It is a two step process which involves nucleation in the first step, and growth of the crystal through mass transport in the second step. To date, all reported hybrid perovskite crystals have been prepared from solution phase. Generally, crystals will form by slowly reducing the solubility of the target samples in a precursor solution. To synthesize perovskite single crystals four strategies have been adopted to modulate solubility of the sample: (a) Cooling HX-based solutions (use HI, HBr and HCl as solvent); (b) heating N,N-dimethylformamide (DMF)/γ-butyrolactone (GBL)/dimethyl sulfoxide (DMSO) based solutions; (c) add an antisolvent; (d) evaporate the solvent.

2.2.1.1 Solution Temperature Lowering (STL) method

Supersaturation is the driving force of crystallization from solution; therefore, determining the cause of crystallization is synonymous with determining the mechanism by which a solution reaches its solubility limit. Typically, saturation concentration is presented as a function of temperature to define the solubility of a material in solution. Materials, which have moderate/low solubility at room temperature and have considerable variation of solubility with temperature, can be grown easily using this method. The perovskite solubility in a HX-based solvent decreases with the lowering of solution temperature. Following this basic principle, cooling the precursor can produce well bordered, rectangular shaped, highly transparent, high-quality hybrid perovskite single crystals within two-three days. Briefly, cooling a concentrated aqueous solution of HX acid, Pb^{2+} and $CH_3NH_3{}^+$ from 100^0C to room temperature allows to obtain $CH_3NH_3PbX_3$ (X=I, Br, Cl) single crystals [17, 27, 28]. However, the final temperature of $MAPbI_3$ should be above 40^0C, otherwise, colorless $(CH_3NH_3)_4PbI_6.2H_2O$ will be formed [28]. Crystals grown by STL method have many advantages (reduced structural imperfections, variety of morphologies and polymorphic forms) over other methods, whereas slow growth rate and the probability of solvent inclusion are the main disadvantages of this process. In this thesis work, STL method is employed to synthesize single crystals of $CH_3NH_3PbI_3$ and $CH_3NH_3PbBr_3$.

2.2.1.2 Inverse Temperature Crystallization (ITC) method

Inverse solubility, which is presented as the temperature dependence of the saturation point, exists when the saturation concentration decreases with the increase of temperature. Figure 2.1 shows that the solubility of $CH_3NH_3PbI_3$ in GBL and $CH_3NH_3PbBr_3$ in DMF drops significantly as the solution temperature was increased from 60 to 100^0C and the highest concentration of $CH_3NH_3PbX_3$ in the solution can be controlled by adjusting the temperature [98]. During the heating of the saturated precursor solution, perovskite

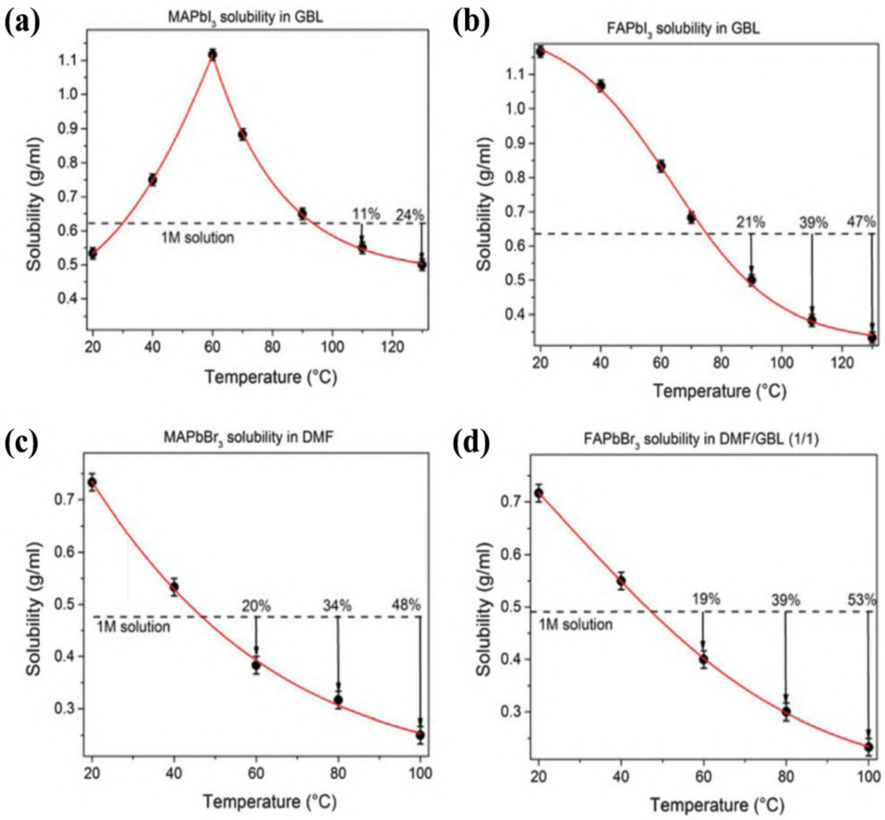

Figure 2.1: Temperature-dependent solubility of (A) $CH_3NH_3PbI_3$ in GBL and (B)$CH(NH_2)_2PbI_3$ in GBL, (C) $CH_3NH_3PbBr_3$ in DMF, and (D) $CH(NH_2)_2PbBr_3$ in DMF : GBL (1 : 1 v/v).
[Taken from: Chem. Commun., 2015,51, 17658-17661]

crystals will precipitate at the bottom of the solution since the precursor concentration is larger than that the solubility allows. This method quickly produce high-quality 5 mm sized perovskite crystals within 3-4 hours [32, 99, 100]. Briefly, PbX_2 and CH_3NH_3X were dissolved in DMF/GBL/DMSO solvent at room temperature and large perovskite crystals can be quickly produced by maintaining the precursor solution at a higher temperature (80^0C to 100^0C) for 3-4 hours. Liu *et al.* grew the largest single crystals of $CH_3NH_3PbI_3$ so far (two-inch) using this method [101]. Because of the faster growth rate ($\sim$1mm^3/hr), this method can be adopted for commercial purposes, whereas, structural imperfection and solvent corrosion might arise due to high growth temperature which deteriorates the crystalline quality of these perovskites. In this thesis work, ITC method is employed to synthesize single crystals of $CH_3NH_3PbX_3$ (X=I, Br, Cl and mixtures of them), $CH(NH_2)_2PbBr_3$ and $CsPbBr_3$.

2.2.1.3 Antisolvent Vapor-assisted Crystallization (AVC) method

Anti-solvent vapor-assisted crystallization method is used to grow materials that are highly soluble in a good solvent, but have poor solubility in other solvents. As an example, hybrid halide perovskites show good solubility in DMF, GBL and DMSO, while they are sparingly soluble in Ethylacetate (EA), Dichloromethane (DCM), benzene, diethylether *etc.* The antisolvent could accelerate the crystallization of perovskite by reducing the precursor solubility [41, 58, 102–104]. Briefly, PbX_2 and CH_3NH_3X powders were dissolved in DMF/GBL/DMSO solvent at room temperature and this precursor solution is kept in an antisolvent environment. Vapor of antisolvent will diffuse into the precursor solution and results high-quality hybrid halide perovskite crystals within 2-4 weeks. As this process can be carried out at ambient temperature, it would demand less energy than above two methods and this crystallization technique is really important for thermally sensitive samples, mostly where organic groups are present. Furthermore, the presence of antisolvent changes the solvent activity of the solution which has more profound effect on the morphology and polymorphic form than that of ITC and STL methods, whereas, use of additional raw material (*i.e.*, antisolvent) might create problems in the purity of crystals and may also enhance the capital cost. In this thesis work, EA and DCM were used as an antisolvent to synthesize single crystals of $CH_3NH_3PbX_3$ (X=I, Br, Cl and mixtures of them).

2.2.1.4 Solvent evaporation at Room Temperature (SERT) method

As we know, slow solvent evaporation method is one of the simple and traditional methods to obtain single crystals in the solution growth process, and most of the organic crystals were synthesized using this method. In this method, supersaturation is achieved by evaporating the solvent at room temperature. As the vapor pressure of the solvent in the solution is higher than that of solute; solvent evaporates more rapidly and the solution becomes supersaturated to grow single crystals. Aromatic ((benzylammonium)$_2$PbCl$_4$) [105] and aliphatic ($(CH_3NH_3)_2Pb(SCN)_2I_2$) [106] 2D perovskite crystals were synthesized by Liao *et al.* and Daub *et al.* respectively following this method. In this thesis work, we have demonstrated a new route to synthesize $CH_3NH_3PbCl_3$ single crystals at room

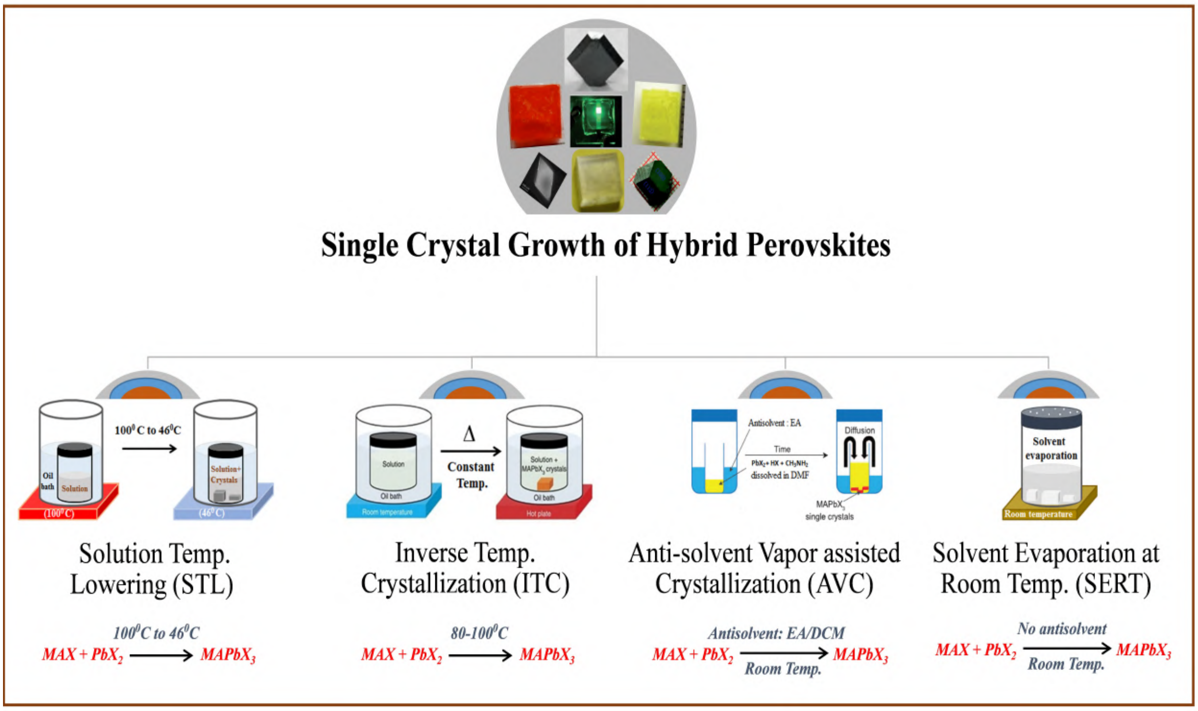

Figure 2.2: Schematic representation of single crystal growth of organic-inorganic hybrid perovskite via different techniques.

temperature. To achieve our goal, a mixture of Dimethyl sulfoxide (DMSO) and gamma-Butyrolactone (GBL) (1:1 volume ratio) were used as a solvent in which $PbCl_2$ and CH_3NH_3Cl were dissolved, and the precursor solution was kept at room temperature without any disturbance. It was observed that $CH_3NH_3PbCl_3$ is highly soluble in DMSO and sparingly soluble in GBL. Further, GBL (204^0C) has a higher boiling point than DMSO (189^0C). Thus, DMSO vaporizes much faster than GBL at room temperature, and steers to have more antisolvent contained reaction mixture condition, eventually leading to the growth of rectangular shaped ($8.3 \times 5.1 \times 1$ mm), highly transparent, colorless and high-quality $CH_3NH_3PbCl_3$ single crystals within four weeks. SERT is a traditional method to obtain single crystals of most organic compounds from solution where no extra solvent is required and demand less energy than other methods. However, longer synthesis time make it less competitive than all other single crystal growth techniques.

2.2.2 Thin Film Growth

Thin film deposition is a major key to the fabrication of photovoltaic and optoelectronic devices. Large scale efforts are put in to improve the quality of the deposited film as it can enhance the efficiency of the created devices [8]. Advancements in thin film deposition techniques have also helped in understanding the role of morphology and underlying physics and chemistry of thin films. Thin film deposition techniques can be classified into two broad categories: (a) Physical deposition, which includes Molecular Beam Epitaxy (MBE), sputtering (dc/rf), Physical Vapor Deposition (PVD), e-beam/thermal evaporator, Pulsed Laser Deposition (PLD) *etc.*, and (b) Chemical deposition, which include Chemical Bath Deposition (CBD), Spin-coating, Dip-coating, Chemical Vapor Deposition (CVD), Plasma enhanced CVD (PECVD), Atomic Layer Deposition (ALD) *etc.*. In this thesis, both physical (thermal evaporator) and chemical (spin-coating) techniques have been used to synthesize hybrid lead halide perovskites.

2.2.2.1 Thermal Evaporator

Thermal evaporation is the vaporization of a material by heating it to a temperature so that vapor pressure becomes appreciable and atoms or molecules are lost from the surface into vacuum and deposited on the target substrate. It involves the following steps: (i)conversion of deposited material into vapor by resistive heating, (ii)transport of vapors from source to target substrate (high vacuum increases the mean free path of the molecules), (iii)vapor condensation on the substrate, (iv)formation of thin film. In this thesis work, thermal evaporation technique (Figure 2.3(a)) is employed to deposit gold (Au) film of 80 nm thick on single crystals and thin films of hybrid lead halide for transport measurements.

2.2.2.2 Spin-coating

Spin coating is a thin film deposition technique by which uniform films can be deposited on flat substrates. Usually, a small amount of coating material is applied on the substrate which is at rest. After that, the substrate is rotated at a high speed to spread the coating material by centrifugal force. Spinning speed, viscosity and concentration of the solution

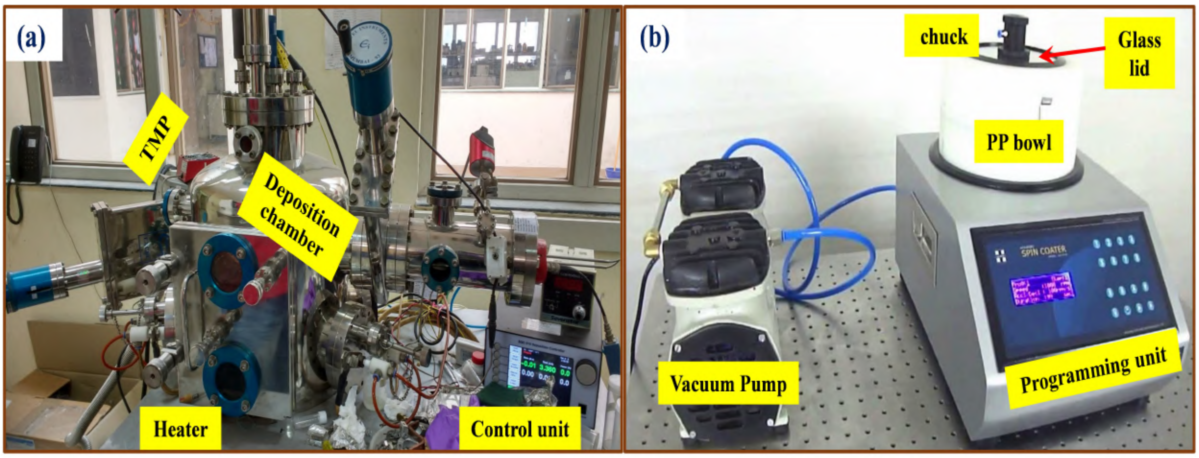

Figure 2.3: Thin Film growth systems used for the work in this thesis: (a) High vacuum coating unit (Thermal evaporator), (b) Spin-coating unit.

controls the thickness of thin film. Thin films of mixed halide perovskites to identify the role of temperature in photoinduced phase separation and pure halides for the solar cell device fabrication were employed using spin-coating technique (Figure 2.3(b)).

2.3 X-ray diffraction and Rietveld refinement

X-ray diffraction (XRD) technique is used to characterize the crystallographic structure, phase purity, crystallite site (grain size), degree of crystallinity, lattice parameter and site-specific order/disorder of the polycrystalline samples. Since the wavelength of X-rays (0.1-10 Å)are comparable to the interatomic spacing of materials, the waves diffract and the scattered waves contain information of the atoms and their arrangement in materials [107]. The use of diffraction of waves from periodic arrangement of atoms in solid to determine the crystal structure was first introduced by Von Laue in 1912, developed by Bragg in 1913 and now it is a well-developed technique [108]. When high energetic electrons (produced by thermionic emission) collide with a metal target within a sealed tube which is in vacuum, X-rays are generated. The X-rays are collimated and directed towards the powder sample, which consists of various lattice planes in every possible orientation. The incident ray gets scattered elastically from different atoms arranged periodically in lattice planes and the interfered beam is collected by scintillation detector which converted it into a voltage pulse to display the spectrum of intensity *vs*. angle of incidence in the computer.

The constructive interference is favored when the path difference of scattered x-rays is an integral multiple of the phase difference and it is expressed by the Bragg condition [109] given by $2dsin\theta = n\lambda$; where d is the inter-planer spacing of the diffracted planes, θ denotes the diffraction angle, n is an integer and λ, the wavelength of the incident X-ray beam. The schematic representation of x-ray diffraction process is shown in Figure 2.4(a).

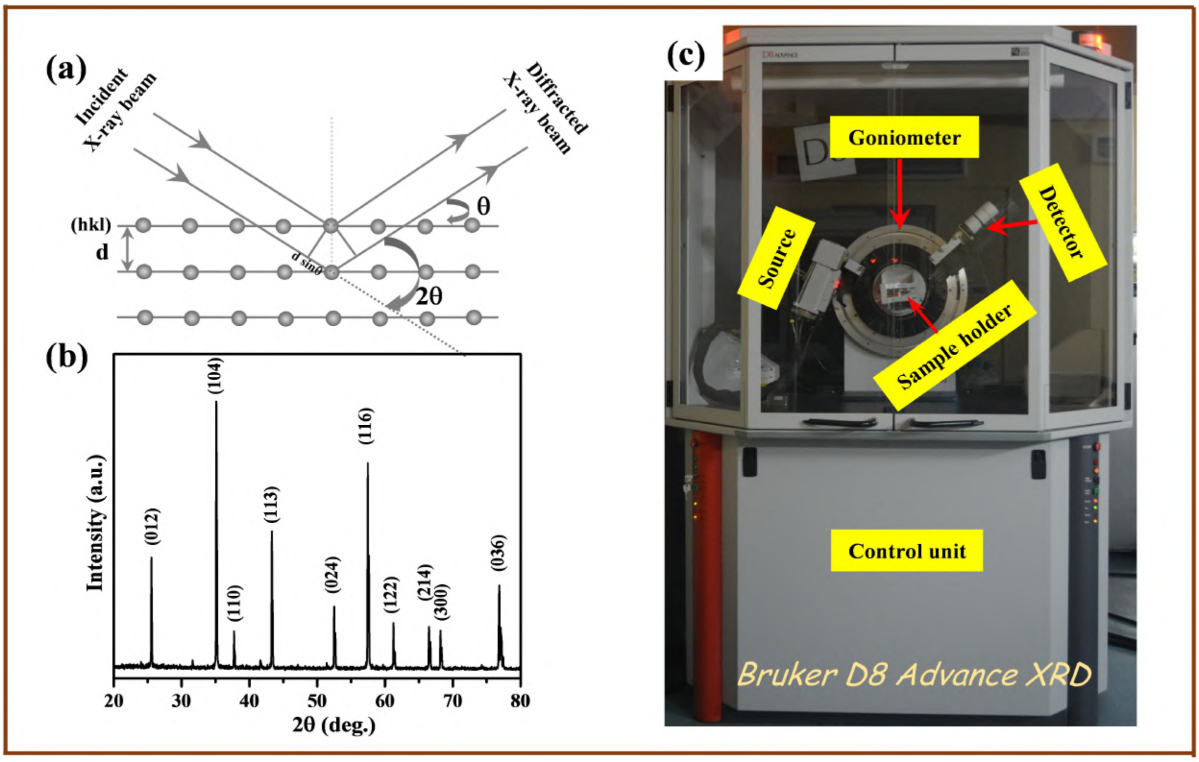

Figure 2.4: (a) Schematic representation of x-ray diffraction from the parallel planes of the periodic crystal lattice. (b) X-ray diffraction pattern of corundum (standard sample) collected in our lab; peak indices are also marked. (c) X-ray diffraction set-up at Institute of Physics, Bhubaneswar.

The intensity distribution of the scattered wave or distribution pattern is the fingerprint of the crystalline solid and is directly related to the amplitude of the structure factor $| F_{hkl} |$. The intensity of the diffracted beam is given by $I_{hkl} = | F_{hkl} |^2$, where $| F_{hkl} |$ can be represented as,

$$F_{hkl} = \sum_{n=1}^{N} g^n t^n(s) e^{2\pi i(hu_n + kv_n + lw_n)} \tag{2.1}$$

Here, g^n is the population factor of nth atom, $t^n(s)$ is the temperature factor, f^n is the atomic scattering factor and (u, v, w) are the fractional coordinates of nth atom in the unit cell. Further, lattice parameters (a, b, c) of a unit cell are related to the inter-planer distance *via* miller indices (h, k, l) as given by $\frac{1}{d^2} = \frac{h^2}{a^2} + \frac{k^2}{b^2} + \frac{l^2}{c^2}$. In addition, some external factors may also affect the position, intensity and width of the diffracted peak, such as lattice strain, orientation of molecules, particle size and instrument parameters [110].

A Bruker D8 diffractometer (Figure 2.4 (c)) in Bragg-Brentano geometry with Cu K_α (λ = 1.54184 Å) radiation has been used for the powder diffraction studies presented in this thesis. The X-ray source is operated at a voltage of 40kV and the diffracted X-rays are collected by a sodium iodide (NaI) scintillation detector. While performing the measurements, a Ni filter was used to eliminate Cu K$_\beta$ lines. X-ray diffraction pattern of corundum (standard sample) collected in our lab is shown in Figure 2.4 (b).
Temperature-dependent XRD measurements were carried out at the XRD1 beamline at ELETTRA synchrotron radiation facility using photons of wavelength 0.85507 Å.
Further, single crystal XRD data of hybrid halide perovskites were acquired using an Oxford Xcalibur (Mova) diffractometer at Indian Institute of Science, Bengaluru. In order to perform this measurement, crystals were mounted on a Hampton cryo-loop on an Oxford Xcalibur (Mova) diffractometer equipped with an EOS CCD detector using Mo K_α radiation (= 0.71073 Å). Data collection, data reduction and numerical absorption corrections were performed using the programs present in the CrysAlisPro software suite [111]. Crystal structures were refined by using SHELXL-97 [112] program present in WinGX suit [113].

Rietveld refinement

Rietveld refinement method was first introduced by Dutch crystallographer Hugo Rietveld in 1969 [114]. It is a least square fit method to match the observed X-ray pattern with the theoretically calculated diffraction pattern. The theoretical diffraction is generated by considering the initial structural parameters like Wyckoff positions, lattice constants, anisotropic parameters, peak shape parameters, asymmetry parameters and instrument parameters such as peak shape and background. Over the refinement cycles, the difference between experimental and theoretical pattern are minimized by statistical approach.

Mathematically, the calculated intensity (y_{cal}) can be represented as

$$y_i^{cal} = s\sum_k L_k \mid F_k \mid^2 \phi(2\theta_i - 2\theta_k)P_k A + y_i^{bkg} \tag{2.2}$$

where s, L_k, F_k ϕ, P_k, A and y^{bkg} are scaling factor, Lorentz-polarization factor, structure factor, peak-function, preferred orientation factors, absorption factor and background intensity, respectively. Difference function $\Delta Y = \sum_i w_i(y_i^{obs} - y_i^{cal})$, where w_i=$1/\sigma_i^2$ (σ_i^2 is the standard deviation) is statical weighing factor and y_i^{obs} and y_i^{cal} are observed and calculated intensity, respectively for the i^{th} data point. The quality of the refinement can be evaluated from the reliability parameters, which are expressed in terms of R-factors such as profile factor (R_p), weighted profile factor (R_{wp}), expected weighted profile factor (R_{exp}) and goodness of fit indicator (χ^2).

$$R_p = \frac{\sum_{i=1}^n \mid y_i^{obs} - y_i^{cal} \mid}{\sum_{i=1}^n y_i^{obs}} \tag{2.3}$$

$$R_{wp} = \sqrt{\frac{\sum_{i=1}^n w_i \mid y_i^{obs} - y_i^{cal} \mid^2}{\sum_{i=1}^n w_i {y_i^{obs}}^2}} \tag{2.4}$$

$$R_{exp} = \sqrt{\frac{n-p}{\sum_{i=1}^n w_i {y_i^{obs}}^2}} \tag{2.5}$$

$$\chi^2 = \frac{R_{wp}}{R_{exp}} \tag{2.6}$$

where, n-p is the number of degrees of freedom. R_p provides the information of the difference between the observed and calculated intensity points, R_{wp} contains weighted profile which gives more accurate difference between the observed and calculated intensity peaks rather than considering the background intensity. R_{exp} is calculated based on the number of data points (n) in the profile and number of variable parameters (p) used in the refinement procedure. It should be noted that n should be always greater than p.

The lower values of χ^2 and R-factors suggest a good profile fit to the data. The Rietveld refinement of powder XRD data presented in this thesis is carried out using FULLPROF software [115].

2.4 Physical Property Measurement System - PPMS Evercool-II

Physical Property Measurement System (PPMS) is a versatile instrument offering the options for measuring a large variety of physical properties and Evercool-II is a cryocooler based system which condenses helium gas to liquid helium using cold head by Joule-Thomson effect. The basic setup consists of dewar, sample chamber, superconducting magnet, cryocooler unit, power source and a lock-in amplifier. Dewar contains liquid helium and creates super-insulation to minimize helium consumption. This system contains one outer layer which isolates the sample chamber from liquid helium bath. Two concentric tubes (inner vacuum tube and sample chamber) separated by a sealed and evacuated region, prevent heat exchange between the sample chamber and helium bath and the region between them is known as cooling annulus which helps to cool or warm the sample uniformly. A superconducting solenoid, composed of a niobium-titanium alloy embedded in copper is immersed in liquid helium inside the dewar which help to ramp the magnetic field in the system. Cryocooler unit is composed of a cold head and compressor. Cold head is a closed-cycle, Gifford-McMahon style cryo-refrigerator which uses high-purity helium as the working gas and an indoor control unit, outdoor compressor and heat exchanger help to supply high-pressure and oil-free helium gas to cold head. Machine is controlled by sophisticated user friendly software (MultiVu), which provides easy control over the environmental conditions during the experiment. Most of the experimental options can be operated in a wide range of temperature (1.9 - 400 K) and magnetic field (±9 T) [116]. Various physical properties of materials like specific heat, resistivity, DC and AC electrical transport, thermal conductivity, Seebeck coefficient, hall measurement, DC magnetization, AC susceptibility *etc.* can be extracted using this machine. The PPMS EverCool-II system of our lab is shown in Figure 2.5(a). In this thesis work, we have used heat capacity and VSM (for DC magnetization measurements) options extensively (Figure 2.5(b-e)) .

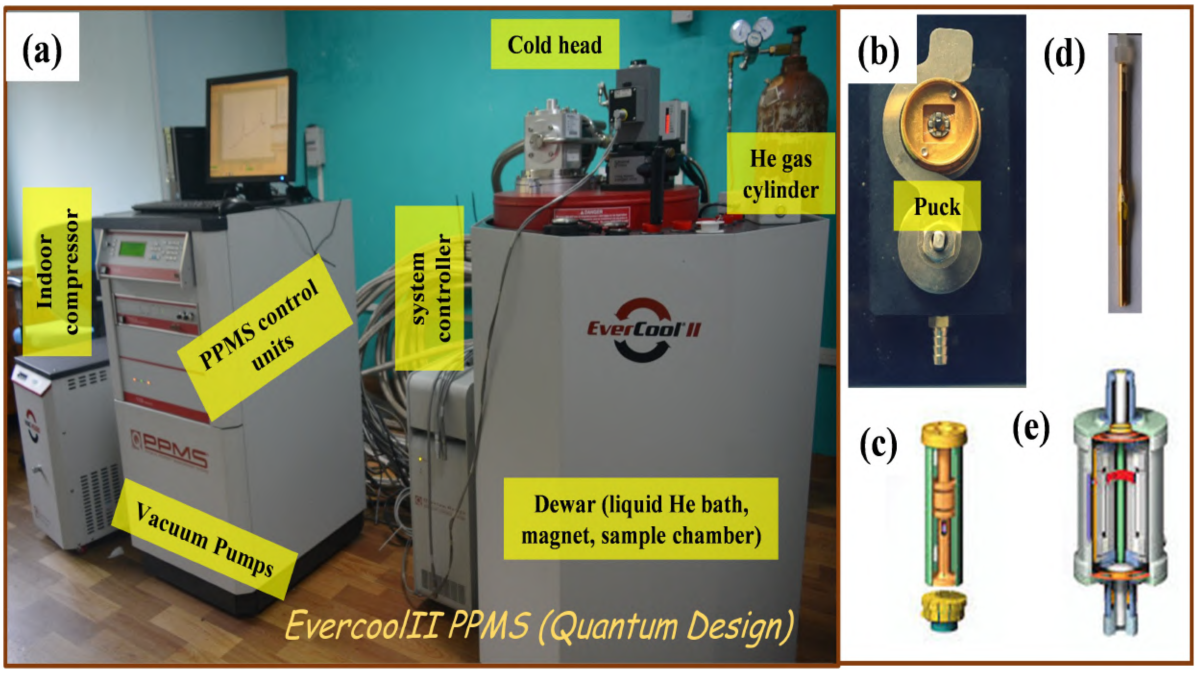

Figure 2.5: (a) PPMS Evercool-II set up at Institute of Physics, Bhubaneswar., (b) The sample holder used for heat capacity measurements in PPMS, (c) Vibrating-sample magnetometer (VSM) pick-up coil, (d) sample holder, (e) VSM head/motor used for DC magnetization measurements in PPMS.

2.4.1 Heat capacity

As heat capacity measurement determines the thermodynamic behavior of the sample, it is a good tool to identify the order and nature of any phase transition which may be structural, magnetic or electrical. PPMS apparatus utilizes the two-tau relaxation method for the specific heat measurements. The relaxation calorimeter consist of a 3×3 mm^2 alumina platform connected to the puck by eight thin sapphire wires. The Cernox thermometer (Lakeshore) and a RuO thin film heater are attached to the bottom side of the platform and sample is attached to the platform using a small amount of Apiezon N (for measurements below room temperature) or H (For measurements above room temperature) grease. The sample puck is then sealed with a cap which acts as a radiation shield and placed inside the sample chamber under high vacuum ($< 10^{-3}$ mbar). Further, the heat capacity measurement is performed using ac relaxation technique. During the measurement, platform is heated above the reservoir temperature and then relax. Decay can be described by two exponential components, depending on thermal link between sample and the platform and the value of specific heat can be obtained from data fitting [117]. Mathematically,

$$C_{platform}\frac{dT_p}{dt} = P(t) - K_w\Big(T_p(t) - T_b\Big) - K_g\Big(T_s(t) - T_p(t)\Big) \tag{2.7}$$

$$C_{sample}\frac{dT_s}{dt} = -K_g\Big(T_s(t) - T_p(t)\Big) \tag{2.8}$$

Where, $C_{platform}$ and C_{sample} are the heat capacities of the platform and sample, respectively. $P(t)$, K_w, K_g, T_p, T_s and T_b are heat power, thermal conductivity of supporting wires, thermal conductivity of grease, platform temperature, sample temperature and thermal bath temperature, respectively. Heat capacity of the sample can be extracted after subtracting the addenda contribution (contribution from sample stage and grease) from the total measured value.

In this thesis work, temperature dependent heat capacity of hybrid halide perovskites were performed to identify the order, nature and accurate temperature of crystallographic phase transitions.

2.4.2 DC Magnetic measurement system - PPMS-VSM

Basic magnetic characteristics of our samples were carried out in the PPMS apparatus using the VSM (Vibrating Sample Magnetometer) option. Faraday's law of induction is the basic principle of dc magnetization measurement using VSM. Primarily, VSM consists of a linear motor transport (VSM head) to oscillate the sample and sample oscillates near the detection (pickup) coil which produces an alternating magnetic flux in the detection coils and current is produced in response to magnetic flux. Finally, the magnetization of the sample is deduced by fitting the measured flux profile to that expected for a point dipole [118]. The frequency of oscillation is ∼40 Hz and amplitude is normally ∼2 mm (could be ranged from 0.5 mm to 5 mm). This setup provides very fast DC magnetization measurement with very good sensitivity (10^{-6} emu). In present thesis work, we performed temperature dependence of magnetization (M vs T) and isothermal magnetization (M vs H) measurements on various samples using PPMS-VSM, to understand the magnetic properties of the materials.

2.5 Scanning Electron Microscopy-SEM

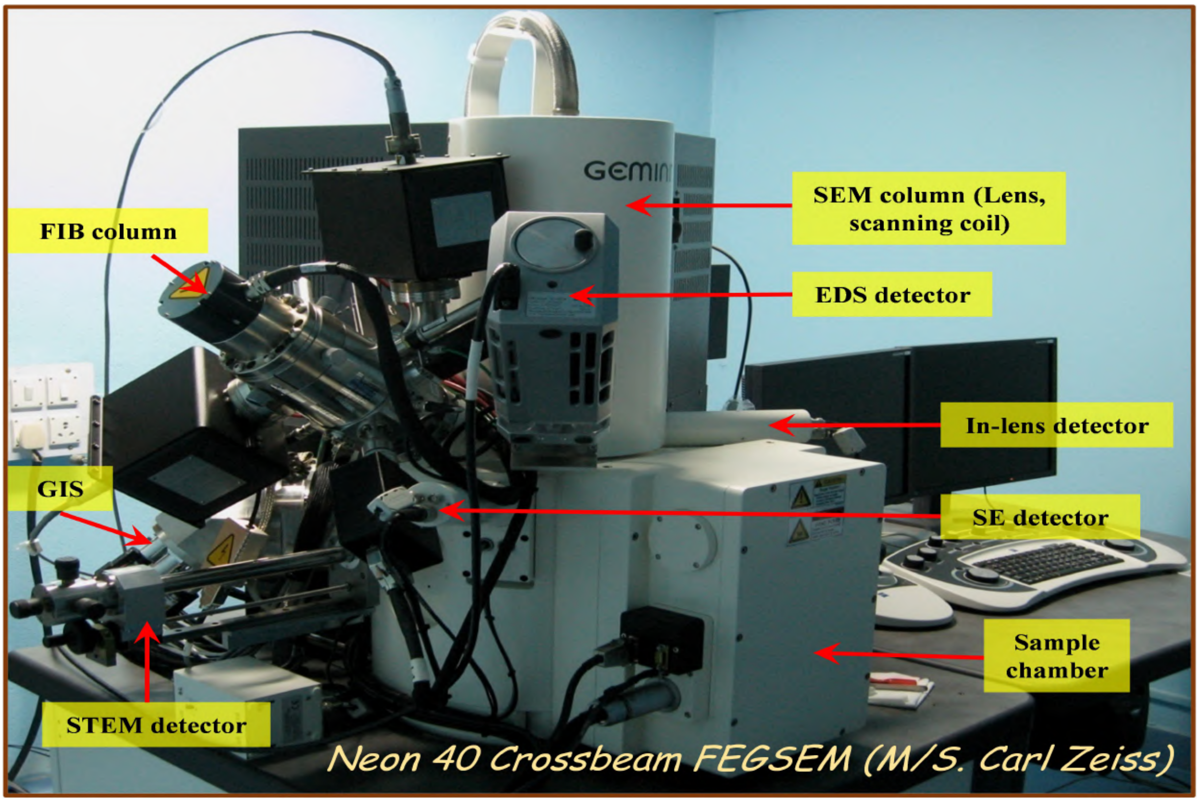

Figure 2.6: FIB-SEM crossbeam system at Institute of Physics, Bhubaneswar.

In scanning electron microscopy (SEM), a finely focused electron beam is scanned in vacuum over the sample surface. The novelty of SEM lies in its capability of producing 10-1,00,000 times magnified, three dimensional-like image of surface features of length scale starting from micrometer down to nanometre scale [119]. When energetic electrons incident on a sample, various elastic and inelastic scattering events take place which includes backscattering of electrons, production of characteristic x-rays, emission of secondary electrons *etc.* In the most standard imaging mode, secondary electrons are used, which produce topographic contrast with high resolution and large depth of field. Secondary electron coefficient strongly depends on the electron beam energy; at lower energies, they are generated closer to the surface and have higher escape possibility. Whereas, at higher electron beam energies, number of secondary electron increases and they are excited deeper in the specimen. Further, secondary electron yield depends on the surface gradient and increases with the increasing tilt angle. Thus, secondary electrons provide an important mechanism for the surface topographic imaging through SEM. The main components of SEM are: (a) electron column containing an electron gun, (b) demagnification system, consisting of two or more electromagnetic lenses for focussing the electrons from electron gun to the sample in vacuum, (c) Everhart-Thornley (E-T) detector to detect the electron signals in the SEM, which consist of a scintillator, an optical guide and a photomultiplier tube, (d) Computer display and electronic control units [120]. For the studies presented in this thesis, a Carl-Zeiss-make SEM (Figure 2.6) was used with a probe current up to 100 nA and acceleration voltage ranging from 0.2 to 30 kV.

2.6 Optical Spectroscopy

Spectroscopy is basically the measurement of the interaction between material and electromagnetic radiation. The spectrum of electromagnetic radiation ranges from long-wavelength radio waves to high energy gamma rays through microwaves, infrared waves, visible light rays, ultraviolet waves and X-rays. The types of spectroscopy can be distinguished by the nature of interaction between the energy of electromagnetic radiation and the material. These interactions include: (a) Absorption Spectroscopy, (b) Emission Spectroscopy, (c) Elastic Scattering, (d) Inelastic Scattering. In this thesis work, we have extensively used UV-Visible-NIR Spectroscopy, Photoluminescence Spectroscopy and Raman Spectroscopy to identify the absorption, emission and scattering (inelastic) properties of the hybrid halide perovskites.

2.6.1 Ultraviolet-visible-near infrared (UV-Vis-NIR) Spectroscopy

Transmission/absorption spectroscopy is carried out using UV-Visible-NIR spectrometer to probe the optical quality of single crystals, powders and thin films and find out its optical band gap and the absorption levels introduced by dopants or impurities. Here, the ratio of light intensity passing through the sample (I), to the light intensity without passes through the sample (I_0) is known as transmittance and can be expressed as (%T), whereas absorbance (A) can be represented as, A= -log(T/100) [121, 122]. In the present work, transmission/absorption measurements were carried out in the range from 200 nm to 1100 nm using a Shimadzu (Model:UV 3101PC) make ultraviolet-visible-near infrared (UV-Vis-NIR) spectrophotometer and the schematic diagram is shown in Figure 2.7.

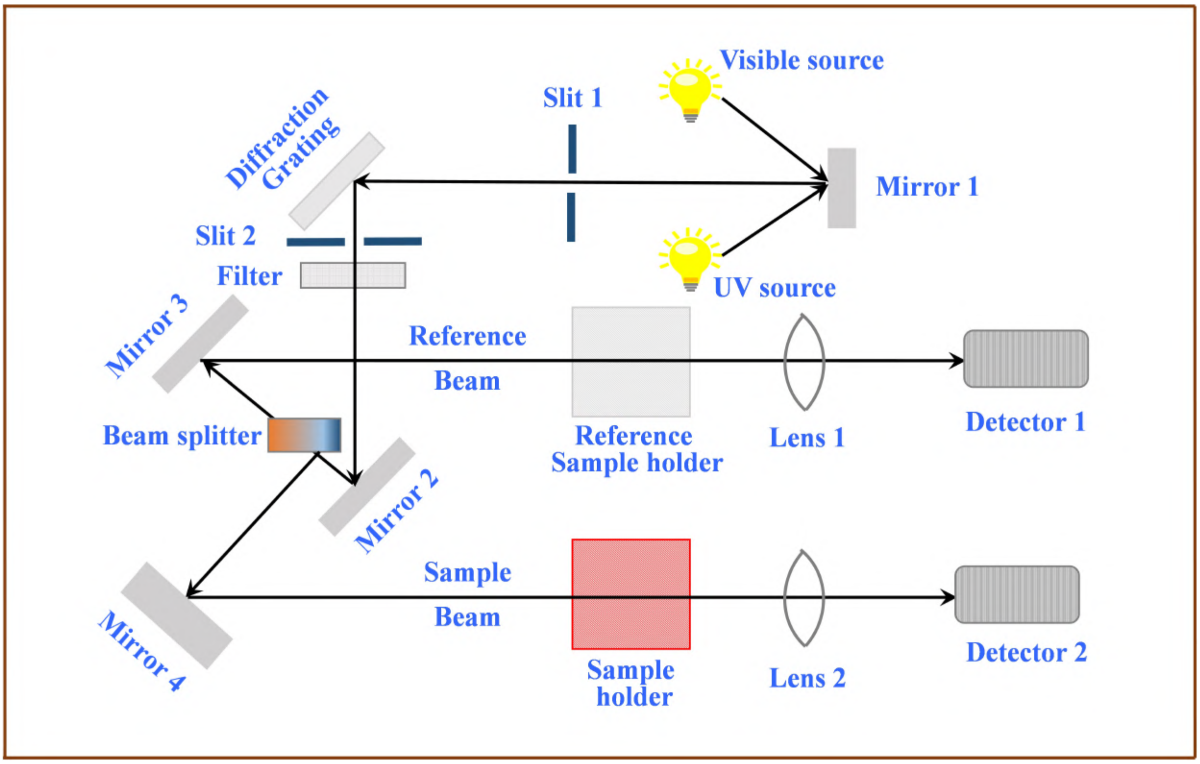

Figure 2.7: Schematic representation of UV-Vis-NIR spectrophotometer.

2.6.2 Photoluminescence (PL) Spectroscopy

Photoluminescence (PL) phenomenon is a consequence of radiative recombination of electron-hole pair between different electronic bands, caused by an external optical excitation [123–125]. In this process, when bandgap of the host material (E_g) is less than the incident optical excitation ($\hbar\omega_i$), electrons and holes of finite momenta (k) are ejected into conduction and valence bands, respectively. Once the electrons and holes are injected into respective bands, the excited electrons undergo the relaxation of energy by emitting phonons of very short life-time ~100fs and accumulate at the bottom of the conduction band, as shown by the cascade lines of Figure 2.8 (a), and finally by emitting photons, the annihilation of electron-hole pairs occur through the electronic transitions from the minima of conduction band to the maxima of valance band [126]. Figure 2.8(a) represents schematic energy band diagram of a direct bandgap semiconductor. In a direct band gap semiconductor, optical transitions are governed by the dipole selection rules. During PL process, some other electronic transitions like free and bound excitonic emission, donor-acceptor-pair (DAP) transition also take place depending on the population strength and lifetimes of the respective states, irrespective of band to band direct transitions. Further, various midgap defect states like native point defects, impurity or interstitial can also be identified using PL spectroscopy. The intensity of direct band to band electronic transitions (near band edge emission) is expressed as:

$$I(\hbar\omega) = \sqrt{\hbar\omega - E_g}\left(\exp\frac{-(\hbar\omega - E_g)}{K_B T}\right) \tag{2.9}$$

Here the first term $\sqrt{\hbar\omega - E_g}$ arises from the density of states of the band to band transition and the second term denotes the Boltzmann statistics of the electrons and holes [124, 125].

Using this technique, a sample is excited by photons (generally in UV range) and the emitted spectrum of the sample can be detected and recorded via different modes, excitation and emission spectrum and luminescence decay lifetime. Emission spectrum is the wavelength distribution of an emission measured at a constant excitation wavelength and excitation spectrum is the dependence of emission intensity, measured at a single emission wavelength by scanning the excitation wavelength. With a pulsed excitation source and a fast detector, PL spectrometer can also record the lifetime of the sample. Photoluminescence decay of any specimen is a measurement where the variation of lu-

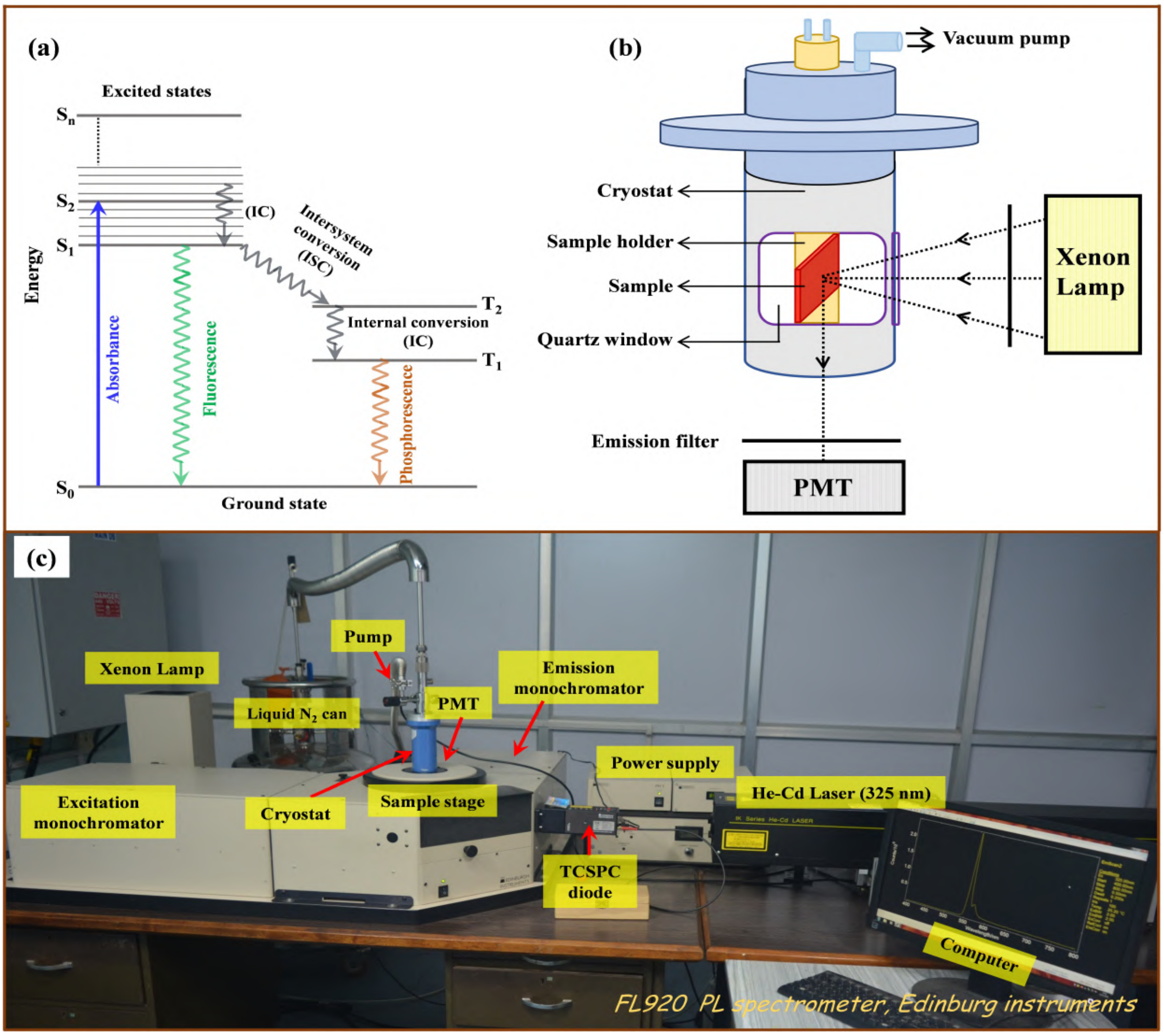

Figure 2.8: (a) Jablonski diagram shows the possible relaxation processes in a molecule after the molecule has absorbed a photon; (b) Schematic representation of cryostat for performing temperature-dependent photoluminescence (PL) measurement; (c) PL spectrometer at Institute of Physics, Bhubaneswar.

minescence signal is recorded as a function of time at fixed wavelength. In the present work, PL studies were performed over the wavelength range from 200 to 800 nm and temperature range of 77 K to 400 K using Edinburgh fluorescence spectrometer (Model FLP920). The schematic of this instrument is shown in Figure 2.8(c). The spectrometer comprises of an excitation source, excitation monochromator, sample chamber, emission monochromator and detector. As an excitation source, 150 Watt Xenon lamp, 325 nm He-Cd Laser and 375 nm pulsed diode laser were used for recording emission spectrum and decay times of hybrid perovskites. A spectral bandwidth of 1 nm was selected for both excitation and emission monochromators. Xenon lamp produces a broad spectrum of high intensity radiation in the UV-Vis-NIR range which is focused to the entrance slit of the excitation monochromator and a specific excitation wavelength with a bandwidth is selected by the monochromator passed through an iris (so that the intensity can be controlled) and then focused onto the sample. Further, a part of luminescence from the sample is collected by a lens system and focused to the emission monochromator which selects a wavelength having a bandwidth of this emission and the light is then focused to the photomultiplier tube (PMT) for recording. Usually, emission and excitation spectra were recorded in the reflection geometry by positioning the sample at an angle of 45^0 to the excitation beam. For low-temperature measurements, sample was mounted on Oxford Instruments OptistatDN cryostat (vacuum $\sim$4.3 $\times$ 10^{-3} mbar) and fit to the FLS920 as shown in Figure 2.8(b).

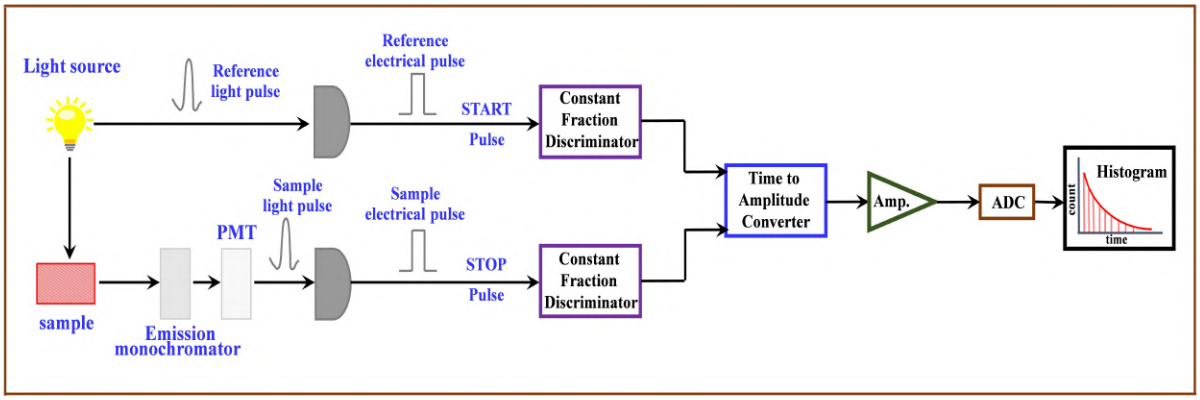

Figure 2.9: Schematic representation of Time-Correlated Single Photon Counting (TC-SPC) Technique.

The lifetime measurement was carried out in this system based on Time Correlated Single Photon Counting (TCSPC) Technique which requires an excitation source with high repetitive pulse output and the schematic of this technique is presented in Figure 2.9. Generally, the probability to detect one photon in one signal period is much less than one for the low-level high repetition rate signals and a significantly high number (several thousand or even million times per second) of single photons are processed for the resulting fluorescence life-time measurement. TCSPC electronics can be compared to two fast stopwatches with two inputs, in which the clock is commended by the START signal pulse and stopped by the STOP signal pulse. The time elapsed for one START-STOP sequence is represented by an increase of a memory value in a histogram, in which the channels on the x axis represent the time [127, 128]. Millions of START-STOP sequences can be measured in a short time using a high repetitive light source and the resulting histogram-counts versus channels represent the fluorescence intensity versus time plot in the computer screen [128]. In this work, lifetime measurement of pure and mixed halide hybrid perovskites are performed using TCSPC technique and a pulsed diode laser of wavelength 375 nm is used as an excitation source.

2.6.3 Raman spectroscopy

Raman spectroscopy is a powerful tool to observe vibrational, rotational and other low-frequency modes in a system and is commonly used as a fingerprint by which molecules can be identified. The basic principle of this spectroscopic technique is based on Raman effect, where monochromatic light scattered inelastically from molecule, which was discovered by Sir C. V. Raman and K. S. Krishnan [129, 130]. For the spontaneous Raman effect, the molecule is excited from the ground state to a virtual energy state, and then relax to a vibrational excited state, which results **Stokes Raman Scattering line** and if the molecule is already in vibrational excited state, then it generates **anti-stokes Raman scattering lines** (Figure 2.10(a)). Generally, Stokes Raman light is used in measurement as it has more intensity than the anti-Stokes, however, both give the same vibrational information of the compound.

Upon interaction with the sample molecule, electric field ($\overrightarrow{E}$) induces electric dipole moment $\overrightarrow{P} = \alpha\overrightarrow{E}$, which is responsible for molecular deformation and the spectral modes can only be observed when there is a change in polarizability (α) of the molecule during the scattering process. Intensity of inelastically scattered light is,

$$I_S = I_0 L \left(\frac{d\alpha}{dq}\right)^2 \left(\frac{1}{\lambda}\right)^4 \tag{2.10}$$

Here, λ is wavelength of the monochromatic source, $(\frac{d\alpha}{dq})$ is change in polarizability, I_0 and

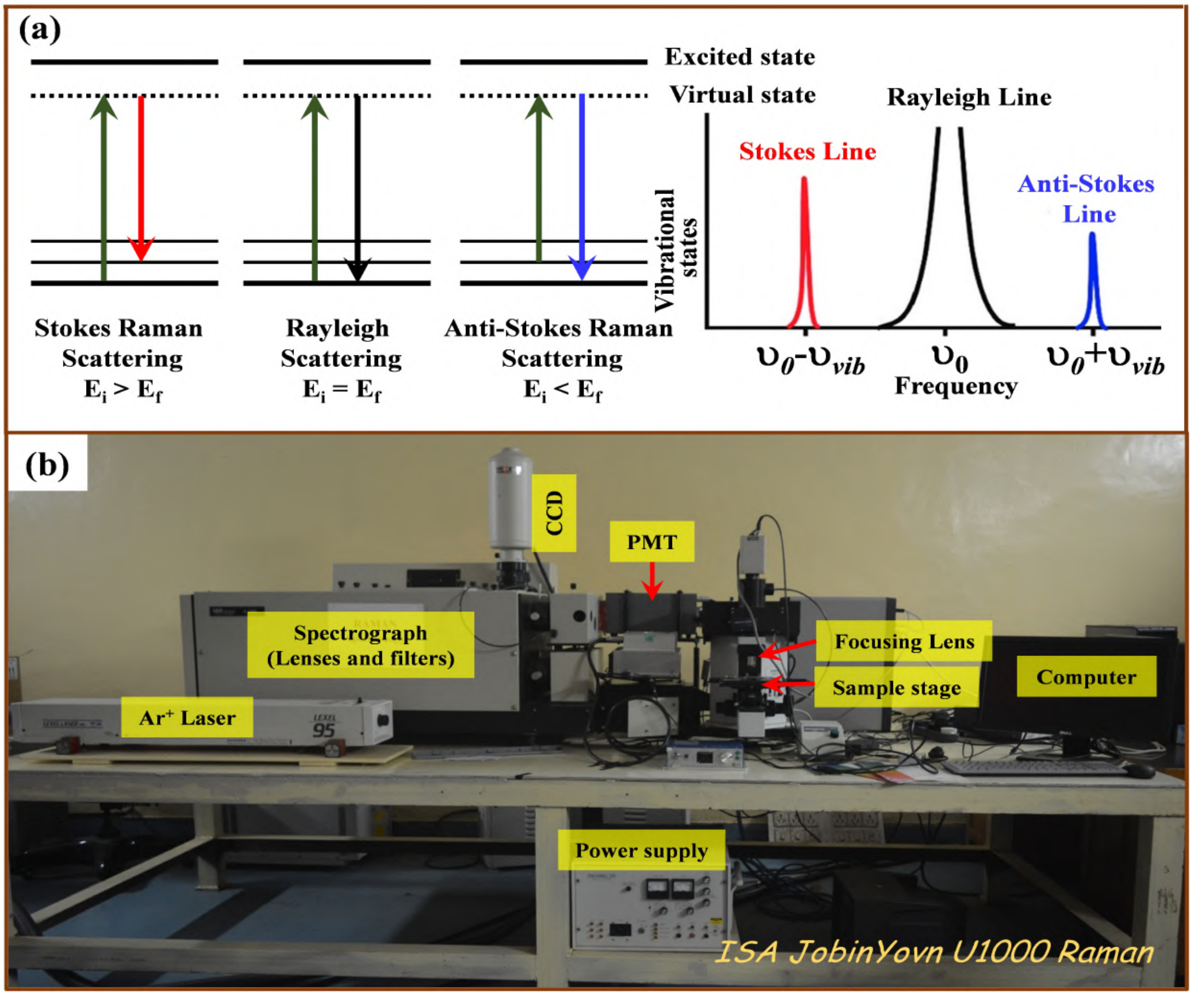

Figure 2.10: (a) Mechanism of Raman Scattering effect when molecule exposed to LASER light; (b) Raman spectrometer at Institute of Physics, Bhubaneswar.

L are the intensities of incident light and sample optical path, respectively. For lattice vibrations in a crystalline solid, the typical Raman shift is of the order 100-1000 cm^{-1}, and the lifetime of scattering is $\tau < 10^{-14}$ sec. [124]

In order to capture Raman spectrum, the sample is illuminated with a laser beam and the scattered radiation from the illuminated spot is collected with a lens and sent through a monochromator. Further, elastic Rayleigh scattered radiation is filtered out, while the rest of the collected light is dispersed onto a CCD detector by different filters present in the system. In the present thesis, the vibrational properties of hybrid halide perovskites were measured using a JobinYovn U1000 Raman spectrometer available in IOP with 514.5

nm excitation of an Ar^+ laser. Spectra were collected in the back scattering configuration using a thermoelectrically cooled CCD camera as the detector. A long working distance 50× objective with a numerical aperture of 0.45 was used for the spectral acquisition (Figure 2.10(b)).

2.7 Electrical measurements

The electrical properties of semiconductors, such as current-voltage characteristics and resistivity, are commonly performed for their practical applications. The current-density versus voltage (J-V) curves of solar cells are recorded with a computer controlled Keithley 2400 in air under simulated AM 1.5 solar spectrum provided by Newport solar simulator. The characteristic parameter such as scan rate, scan-direction and pre-treatment are reported in the corresponding chapter.

Figure 2.11: Newport solar simulator for device characterization.

The space charge limited current (SCLC) measurement was performed using Keithley 2410 source-meter in the dark, under vacuum at room temperature [74].

2.8 Photoemission Spectroscopy

The technique of photoelectron spectroscopy (PES) has emerged as one of the most widely used and versatile tools for materials characterization, especially in surface-related areas [131]. Almost all branches of physics, chemistry and materials science use this technique for the proper understanding of electronic structure of materials. Irrespective of providing direct information about the electronic structure, this technique is more popular for its unique elemental sensitivity which allows to determine the accurate chemical composition of materials. This technique has added an extra advantage over other spectroscopy techniques like scanning tunneling spectroscopy, which cannot provide any information concerning the chemical composition responsible for the specific electronic structure [132]. The basic concept of this phenomena is the photoelectric effect which was discovered by A. Einstein in 1905 [133]. When a photon of energy $h\nu$ impinges on a sample and the photon energy is sufficiently high, it can knock out an electron from its bound state. These outgoing electrons are known as photoelectrons and their kinetic energy (KE) can be measured using an electrostatic analyzer. Figure 2.12(a) represents the schematic picture of this process.

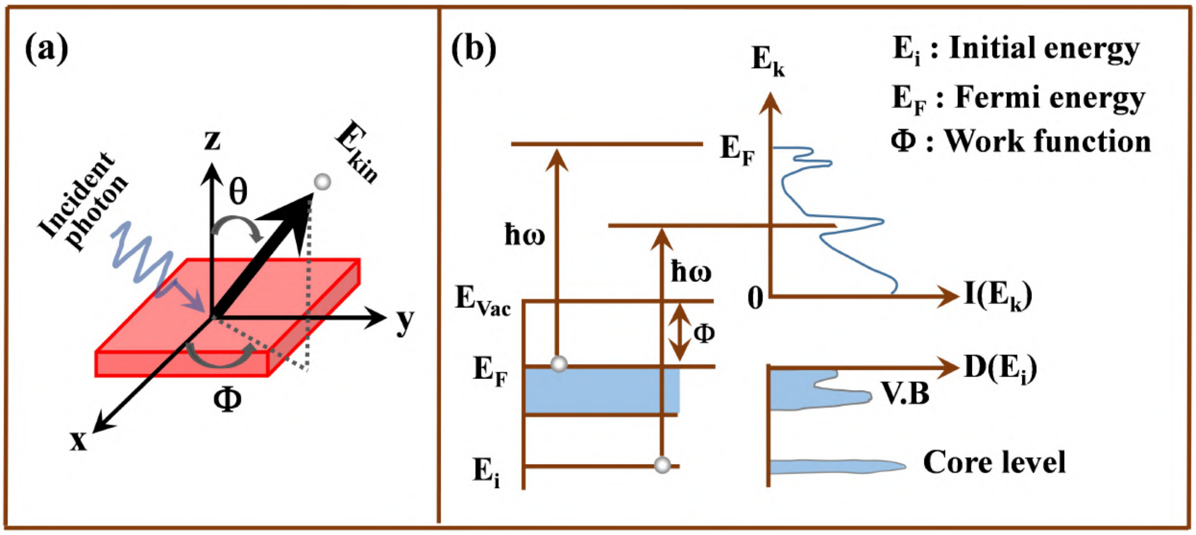

Figure 2.12: (a) A schematic representation of photoemission experiment where the characteristics of photoelectrons are defined by its kinetic energy (E_{kin}) and momentum ($\mathbf{p}$). The value of momentum is determined from the polar angles (θ and ϕ) of emission; (b) An intuitive representation to describe the energy level profile inside the solid and resulting photoemission spectra.

The kinetic energy of emitted photoelectrons are represented by the following relation:

$$E_{kin} = h\nu - \mid E_B \mid - \phi \tag{2.11}$$

where, E_{kin} is the kinetic energy of photoelectron, $h\nu$ is the incident photon energy, E_B is the binding energy of electron inside the solid and ϕ is the work function (energy required for an electron to escape from the solid at E_F). Schematic energy level diagram is presented in Figure 2.12(b).

In addition to energy, momentum is also conserved in the photoemission process:

$$k_i + k_{h\nu} = k_f \tag{2.12}$$

where k_i and k_f are the reduced initial and final wavevectors inside the solid and $k_{h\nu}$ is the wave vector of incident photon. For low energy photon, $k_{h\nu}$ can be neglected as compared to the crystal momentum in the first Brillouin zone, which makes $k_i = k_f$ and final Bloch function can be written as:

$$k_f = k + G = K \tag{2.13}$$

where final crystal momentum in the reduced Brillouin zone is denoted by k and G is the reciprocal lattice vector arising from the periodicity of lattice. As the photoexcited electrons are free outside the solid, (k+G) component can be replaced by the wave vector of traveling free electron (K) [134]. However, due to surface discontinuity in the sample, only the parallel component of momentum to the sample surface is conserved and is represented by:

$$k_{i||} = k_{||} + G_{||} = K_{||} \tag{2.14}$$

where, $k_{i||}$, $k_{||}$, $G_{||}$ and $K_{||}$ are the surface parallel components of the reduced initial(k_i), final (k_f) wave vectors, reciprocal lattice vector (G) and external photoelectron wave vector (K), respectively. The value of K can be determined from the measured photoelectron kinetic energy on the basis of free electron model:

$$K = \frac{\sqrt{2m_e E_{KE}}}{\hbar} \tag{2.15}$$

Cartesian component of K can be obtained from the polar(θ) and azimuthal(ϕ) angles of emission defined in the experimental geometry

$$K_{||x} = \frac{\sqrt{2m_e E_{KE}}}{\hbar} sin\theta cos\phi \tag{2.16}$$

$$K_{||y} = \frac{\sqrt{2m_e E_{KE}}}{\hbar} sin\theta sin\phi \tag{2.17}$$

$$K_{||z} = \frac{\sqrt{2m_e E_{KE}}}{\hbar} cos\theta \tag{2.18}$$

Once $K_{||x}$ and $K_{||y}$ are known, parallel component of initial state crystal momentum ($K_{i||}$) can be extracted using equation 2.14.

Incident photon energy classifies photoemission spectroscopy into two broad categories: (a) X-ray Photoemission Spectroscopy (XPS) and Ultraviolet Photoemission Spectroscopy (UPS).

2.8.1 X-ray Photoelectron Spectroscopy (XPS)

In the case of XPS, photon source lies in the X-ray regime (100-2000 eV) and probe the core levels in solids determining elemental compositions, concentrations and oxidation states of the materials. In the present thesis, the XPS experiments were performed using a PHI 5000 Versaprobe II scanning XPS microprobe manufactured by UL-VAC PHI, USA and the schematic of the system setup is shown in Figure 2.13. The base pressure of the main chamber is maintained at 4 × 10^{-10} torr. The system consists of load-lock and analysis chambers with various sources (AlK_α and MgK_α for probing core levels and HeI and HeII for valence levels) integrated into it. A FIG-5CE 5 kV floating argon ion gun is attached to the analysis chamber that could be operated between 5 eV and 5 keV range. This is designated to perform three different tasks: (i) sputter cleaning to remove the surface contamination, (ii) depth profiling and (iii) charge neutralization. A fully automated, five-axis (X, Y, Z, Θ and tilt) sample stage with compucentric zalar rotation and eucentric tilt compensation which can handle sample platens with 25 and 60 mm diameter is available. The hemispherical electron analyzer is composed of two concentric hemispheres with a mean diameter of 280 mm, which are surrounded by a magnetic shield optimized for energy resolution and high angular acceptance lens optimized for small-area XPS sensitivity. Finally, a unique multi-channel detector (MCD) and fast electronics are used for rapid data acquisition and maximum sensitivity [135].

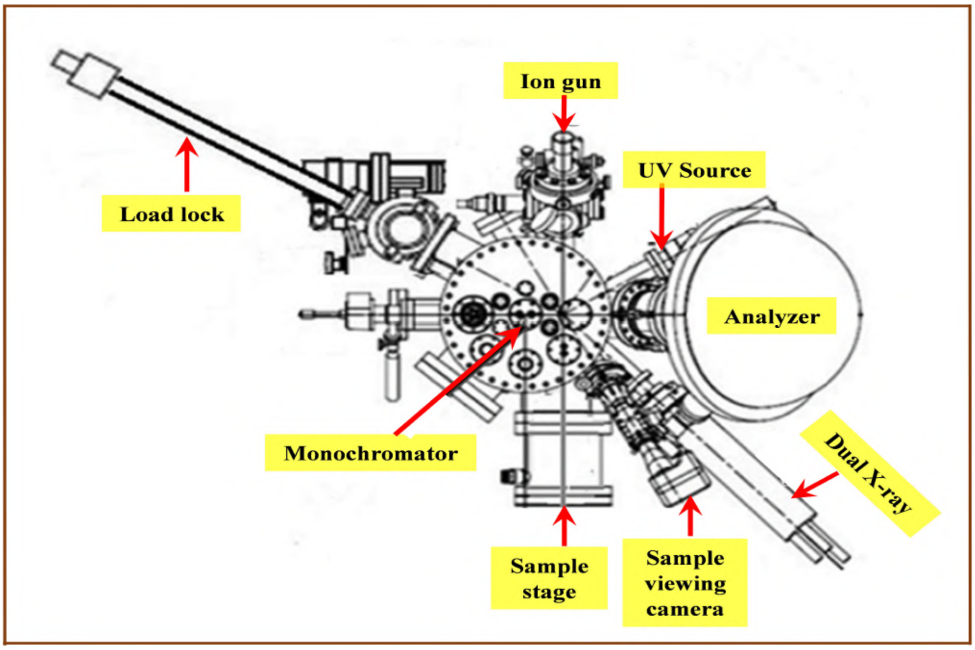

Figure 2.13: Schematic representation of x-ray photoelectron spectrometer. [Taken from: Curr. Sci., 2013, 105(8), 1056-1060]

2.8.2 Ultraviolet Photoemission Spectroscopy (UPS)

The energy range of the incident photon is in the UV regime (4-100 eV) in case of UPS and hence probe valence energy levels and chemical bonding. Lower photon energy in the case of UPS results in a higher probability of interaction with the valence electrons and is more sensitive to the valence bands. UPS is divided into two broad categories depending on the geometry, one is angle integrated photoemission and the other is angle resolved photoemission [136]. When the solid angle of detection is large (close to 2π), the momentum information is blurred by the integration over all the outgoing wave vectors and is known as angle integrated photoemission. These measurements were performed on the polycrystalline samples and yield joint density of states. In the case of angle-resolved photoemission, the solid angle of detection is small (<2 deg) which allows exploitation of k-conservation by detection in a narrow k-interval. Take off angles of emitted photoelectrons are taken care of either by an analyzer with pin hole entrance aperture and data are recorded point by point by moving the analyzer or by a more advanced analyzer with channel plate. From the energy and angular distribution of the emitted electrons, the energy versus momentum information of the crystal (band dispersion) can be determined and this “band mapping” is a powerful probe for the electronic structure identification of crystalline materials. Angle resolved photoemission data can be directly compared with the calculated band structure which enhances the understanding of the electronic structure of solids [134]. Further, position of the valence band maxima in reciprocal space can be visualized instructively by plotting the photoemission results in a different way. Irrespective of keeping the emission angle of ejected electrons fixed and scanning its kinetic energy, keep the photoelectron energy constant and measure its intensity as a function of the emission direction over the entire Brillouin zone. Further, the emission angle was translated into the in-plane wave vector $k_{||}$ and the occupancy of states at a particular energy in reciprocal space was mapped and termed as constant energy contour (CEC) [137, 138]. This is a very useful technique to measure Fermi surface in metals and valence band maxima in semiconductors. Angle-integrated and angle-resolved photoemission data of hybrid perovskites presented in this thesis were recorded in “The Band Dispersion and Electron-Phonon coupling (BaDElPh) beamline”, Elettra-Sincrotrone, Trieste, Italy.

2.9 Extended X-ray Absorption Fine Structure (EXAFS)

X-ray absorption spectroscopy (XAS) is a widely used technique to study the local geometrical environment of the elements present in the systems as well as for studying the conduction band via the electron excitations. This technique uses synchrotron x-ray source where there is a possibility to tune the photon energy using monochromator and high brilliance [139]. In this technique, one electron is excited to one of the unoccupied state using a tunable photon source and the extent of photon absorption can be monitored directly by measuring the incident and the transmitted photons. When the incident x-ray energy exceeds the binding energy of core-shell electrons, they absorb the energy either to land in the higher energy empty shells to give pre-edge feature in the absorption or in case of larger energy, the electron is emitted as free electron giving a huge change in the absorption coefficient called absorption edge, and the interaction of emitted photoelectron with the surrounding atoms results post edge features in the absorption coefficient. Depending on particles detected, XAS can be categorized into two modes: (a) Total Fluorescence Yield (TFY) mode: emitted photons are detected to extract information and (b) Total Electron Yield (TEY) mode: emitted electrons are detected to obtain information about the unoccupied part. As the absorption process involves the transition of electrons from a core level to the unoccupied part, the various features in the spectrum can be characterized by appropriate selection rules ($\Delta l = \pm 1$, $\Delta s = 0$). Thus, this technique provides information about the site and momentum projected spectral functions. A typical x-ray absorption spectrum for $CH_3NH_3PbI_3$ at Pb L_3-edge is shown in Figure 2.14(b).

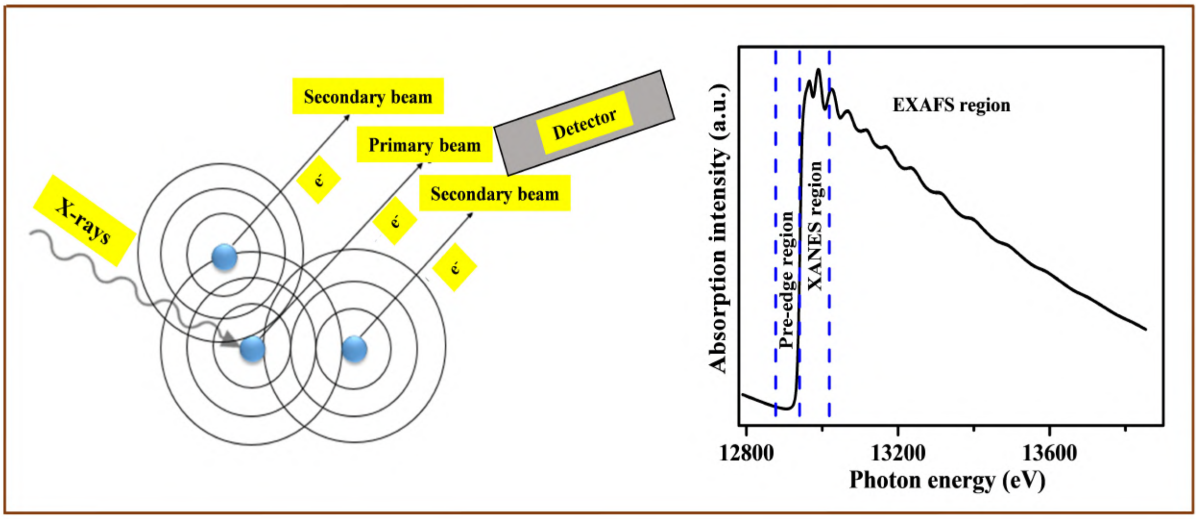

Figure 2.14: (a) Schematic representation of EXAFS process; (b) XAFS spectrum of $CH_3NH_3PbI_3$ showing the pre-edge, XANES and EXAFS regions.

Depending on the scanned energy window around the absorption edge, X-ray absorption spectroscopy is named as X-ray Absorption Near Edge Structure (XANES) and

Extended X-ray Absorption Fine Structure (EXAFS) providing significant information about the absorbing atom. XANES is the characteristic of valence and chemical environment of element, arises from various complex effects such as many-body interactions, multiple scatterings, band structures, distortion of the excited state wavefunction by the Coulomb field and many more, which exists between 5 eV and 100 eV above the absorption edge [140]. oxidation states or the proportion of oxidation states in case of mixed state samples can be determined using this technique. Local geometry like tetrahedral and octahedral can also be distinguished by comparing the results with the known standards. The oscillatory variation of the x-ray absorption as a function of photon energy beyond the absorption edge (upto 1000 eV) is known as EXAFS. In EXAFS, the emitted photoelectrons from the core shell of the sample are scattered by the surrounding atoms and these scattered electrons can constructively or destructively interfere with the outgoing photoelectron wave to give modulations in the absorption coefficient. Co-ordination number, bond lengths, thermal Debye-Waller factors *etc.* can be extracted from EXAFS data analysis.

The incident (I_0) and transmitted (I_t) photon intensities were recorded and the energy dependence of absorption coefficient can be written as, $\mu(E) = log(I_0/I_t)$. Thereafter, a smooth pre-edge function was subtracted from $\mu(E)$ to get rid of instrumental background, and a threshold energy (E_0) was identified from the derivative of $\mu(E)$. Further, a smooth post-edge background function ($\mu_0(E)$) was identified, which represent absorption of an isolated atom, and EXAFS function can be defined as,

$$\chi(E) = \frac{\mu(E) - \mu_0(E)}{\Delta\mu_0(E)} \tag{2.19}$$

where $\Delta\mu_0(E)$ is the measured jump in the absorption at the threshold energy (E_0). As EXAFS is best understood in terms of the wave behavior of the photoelectron created in the absorption process, it is essential to convert the x-ray energy to the wavevector (k) and is defined as, $k = \sqrt{\frac{2m}{\hbar^2}(E - E_0)}$, where m is the electron mass. Equation 2.19 can be expressed as a function of the photoelectron wavevector k as following,

$$\chi(k) = \sum_j N_j S_i(k) F_j(K) e^{-2\sigma_j^2 k^2} e^{-2r_j/\lambda_j(k)} \frac{sin(2kr_j + \phi_{ij}(k))}{kr_j^2} \tag{2.20}$$

where $F_j(k)$ is the backscattering amplitude from each of the neighboring atoms (N_j) of the jth type. σ_j and r_j denote Debye-Waller factor and distance between neighboring atoms which account thermal vibration (assuming harmonic vibration) and static disorder of the sample. $\phi_{ij}(k)$ is the total phase shift experienced by the photoelectron. e^{-2r_j/λ_j} represent the inelastic losses in the scattering process (due to neighboring atoms and the medium in between) with electron mean free path λ_j. $S_i(k)$ is the amplitude reduction factor due to many-body effects such as shake up/down processes at the central atom denoted by j. Hence each EXAFS wave is determined by the backscattering amplitude $N_jF_j(k)$, modified by the reduction factors $S_i(k)$, $e^{-2\sigma_j^2k^2}$ and e^{-2r_j/λ_j} and the $1/kr_j^2$ distance dependence, and the sinusoidal oscillation is a function of interatomic distance ($2kr_j$) and the phase shift $\phi_{ij}(k)$. While the amplitude function depends only on the type of the backscatters, the phase function contains contributions from both the absorber and the backscatter [141].

In the present thesis work, temperature dependent (30 K - 300 K) EXAFS studies were carried out on the P65 beam-line at Petra III, “Deutsches Elektronen-Synchrotron” (DESY), Germany. In order to perform this experiment, powder sample of appropriate weight, estimated to obtain a reasonable edge jump was taken in powder form and mixed thoroughly with cellulose powder to obtain total weight of 100 mg and homogeneous pellets of 15 mm diameter was prepared using a hydraulic press. Finally, fitting of the experimental data to theoretical EXAFS functions was performed using various applets of Demeter Program [142].

2.10 Theoretical methodology

Density Functional Theory (DFT) is one of the most powerful and widely used ab-initio methods for the calculation of ground state properties of metals, semiconductors and insulators, which deals with the interactions among large number of particles [143]. We know that, one should solve the Schrodinger equation to understand the physical and chemical behavior of a system;

$$\hat{H}\Psi = E\Psi \tag{2.21}$$

where $\hat{H}$, Ψ and E denotes the Hamiltonian, wave function and energy eigenvalue of the system. Hamiltonian can be written as:

$$\hat{H} = -\frac{\hbar^2}{2m_e}\sum_{i=1}^{N}\nabla_i^2 - \frac{\hbar^2}{2}\sum_{I=1}^{N_I}\frac{\nabla_I^2}{M_I} + k\sum_{i<j}^{N}\frac{e^2}{\mid r_i - r_j \mid} + k\sum_{I<J}^{N_I}\frac{Z_I Z_J e^2}{\mid R_I - R_J \mid} - k\sum_{i,I}^{N,N_I}\frac{Z_I e^2}{\mid r_i - R_I \mid} \tag{2.22}$$

Individual right hand terms represent: (i) Kinetic energy of nuclei, (ii) Kinetic energy of electrons, (iii) Interaction between electrons themselves, (iv) Interaction between nuclei themselves, (v) Interaction between electrons and nuclei, respectively. In equation 2.22, $\hbar$ and k = $\frac{1}{4\pi\epsilon_0}$ are Planck constant and Coulomb's constant; r_i and R_I are positions of electrons and nuclei; m_e and M_I are masses of electrons and nuclei; e and $Z_I e$ are charges of electrons and nuclei; N and N_I are number of electrons and nuclei in the system, respectively. As nuclei are much heavier than electrons, we can freeze them at fixed positions and assume the electrons to be in instantaneous equilibrium with them. In short, the nuclei are assumed to be at rest with respect to the electrons and become "external" to the electron cloud. This is known as **Born-Oppenheimer** (BO) approximation and the Hamiltonian can be written as:

$$\hat{H} = -\frac{\hbar^2}{2m_e}\sum_{i=1}^{N}\nabla_i^2 + \frac{1}{4\pi\epsilon_0}\sum_{i<j}^{N}\frac{e^2}{\mid r_i - r_j \mid} - \frac{1}{4\pi\epsilon_0}\sum_{i,I}^{N,N_I}\frac{Z_I e^2}{\mid r_i - R_I \mid} \tag{2.23}$$

The quantum mechanical approach to solve this many-body problem involves specification of external potential, calculation of wave function and observables by taking the expectation value of operators with this wave function. The early attempts to solve the many body problem started with the free electron model (FEM), which works well for metals. Thereafter, Hartree and Hartree-Fock approaches came and finally, the Thomas-Fermi model was developed, which is assumed as a very early form of DFT since it uses the electron charge density as the basic variable instead of the wave function. Then, Hohenberg and Kohn [144] proposed the density functional theory (HK-DFT) in 1964, which is based on the two theorems: (i) The ground state properties of a many-electron system are uniquely determined by an electron density which depends on three spatial coordinates, through the use of the functionals of electron density, (ii) An energy functional should be defined, which is minimum at the correct ground state. Due to the absence of exchange-correlation (XC) terms, HK-DFT lacked in accuracy. In 1965, Kohn-Sham formulated the DFT theory (KS-DFT) including the XC terms [145]. In the KS-DFT approximation, the many-body problem of interacting electrons in a static external potential is treated as a system of non-interacting electrons moving in an effective potential. However, as XC term is in general unknown, its correct modeling are difficult within the framework of KS-DFT. The most widely accepted approximations are the local density approximation (LDA) and generalized gradient approximation (GGA) to incorporate the XC interactions. LDA is basically based on the uniform electron gas model, which can predict good result only when electron density varies slowly with space. The XC energy in the LDA approximation is given by:

$$E_{xc}^{LDA}[n] = \int n(\mathbf{r})\epsilon_{xc}[n(\mathbf{r})]d\mathbf{r} \tag{2.24}$$

where $\epsilon_{xc}[n]$ is the exchange-correlation energy per particle of a homogeneous gas of interacting electron density $n(\mathbf{r})$. Under this approximation, it is assumed that the charge density $n(\mathbf{r})$ varies smoothly with respect to $\mathbf{r}$. However, in most of the practical systems, we must take care of the significant spacial variation of electron density. Thus, GGA has emerged as a promising attempt, in which exchange functional depends on the gradient $\mid \nabla_n \mid$ of the electron density. This inclusion of $\mid \nabla_n \mid$ introduces a few nonlocality to the previous LDA functional as well as remove some of the self-interaction present in the LDA. Valence wavefunctions tend to have rapid oscillations near ion cores due to the requirement that they be orthogonal to core states and the oscillatory behavior in the core regions, requires a very large set of plane waves, or equivalently a very fine grid, to be described correctly. In order to solve this problem, ultrasoft [146] and projector augmented wave (PAW) [147, 148] are used as a pseudopotential, in which the collective system of nuclei and core electrons are described by an effective, much smoother potential. Due to smaller radial cutoffs (core radii), PAW potentials are more accurate than the ultrasoft pseudopotentials. GGA of Perdew-Burke-Ernzerhof (PBE) parameterization for the XC potential is the most widely used functional in the first-principle DFT calculations; however, it overestimates lattice parameters. In order to obtain better values of lattice constant and accurate equilibrium properties of solids, PBE-sol functional has been proposed.

Theoretical calculations of the structural, electronic and spectroscopic properties of this thesis work is based on DFT, using GGA with PBE parameterization for the XC potential along with the PAW method as implemented in the Vienna ab-initio simulation package (VASP) [149–151]. A Gamma-centred k-point mesh of $8 \times 8 \times 8$ was used for reciprocal space integration and a plane wave basis set energy cutoff of 600 eV was considered in the calculations. Correction to the K-S DFT energy due to van der Waals interactions was included within the method of Tkatchenko and Scheffler (DFT-TS) implemented in VASP. The results were found to be well converged with considered lattice parameters. The internal coordinates were then optimized until the forces on the atoms were less than 10^{-3} eV/Å. Density of states and band structure calculations were then performed on the optimized structure for the organic-inorganic hybrid perovskites.

2.11 Summary

This chapter highlights experimental approaches used for the growth and characterization of hybrid organic-inorganic and all-inorganic lead halide perovskites. Different wet-chemical approaches were used for the synthesis of single crystals and spin-coating technique was employed for thin film growth. Structural characterization of these samples were carried out using XRD, PPMS, EXAFS and FESEM techniques; whereas UV-Vis absorption, photoluminescence, Raman scattering, XPS and ARUPS were used for spectroscopic characterization. First-principle DFT calculations were performed to correlate the experimentally observed structural and electronic properties. Following these, power conversion efficiency (PCE) of solar cell devices made by us were derived from current density-voltage plots using AM1.5 solar simulator.

Chapter 3

Optimization of Single Crystal Growth

This chapter consists of two sections, in the first section a comparative study on structural and optical properties of $CH_3NH_3PbBr_3$ *single crystals grown via four different techniques (ITC, STL, high and low boiling point AVC method) is discussed. An inter-band broad emission was identified for crystals grown at high temperatures (ITC and STL) and low boiling point (dichloromethane) AVC method, whereas it was absent in high boiling point (Ethyl acetate) AVC method. Furthermore, a comparison of formation energy calculations with the experimentally obtained energy levels suggests that excess Pb atoms in interstitial positions are predominantly responsible for the extrinsic self-trapping process. In the second part of this chapter, we report the synthesis of high quality, defect free 3D perovskite single crystals of* $CH_3NH_3PbCl_3$ *using solvent evaporation at room temperature (SERT) for the first time and detailed evolution of its structural, optical and electrical properties are discussed. Observation of low trap density, high carrier mobility and long diffusion length make the obtained crystals suitable for high efficient visible-blind UV photodetector and other optoelectronic devices.*

3.1 Defects and its Engineering in Methylammonium Lead Bromide

3.1.1 Introduction

It is well known that trap state density and charge transport properties are two key parameters determining the high crystalline quality of a single crystalline semiconducting material, and proper knowledge of the behavior of native defects has been essential for the successful applications of any semiconductor into devices [152–154]. Luminescence efficiency, electrical conductance, minority carrier lifetime and other key aspects of device performance is dependent on the presence of native point defects such as vacancies, self-interstitials and antisites [153]. It is observed that vacancies, self-interstitials, and antisites have deleterious effects on the performance of a laser, LED and photodetector [154]. Thus, to enhance device performance, we need to understand the origin of defect and engineer the same for optimal results.

However, it has remained challenging to obtain defect-free large single crystals of hybrid perovskites due to their rapid growth rates, despite sustained attempts in this direction. Crystal growth of organic-inorganic metal halide perovskites was first reported by Weber in 1978 using solution temperature lowering (STL) method [17]. Alternatively, lot of groups have adopted this method directly, with little modifications (Using methylammonium halide instead of methylammonium and hydrohalide acid), to synthesize pyramidal, cuboid or rhombohedral shaped single crystals of methylammonium lead halides within two to three days [27, 28]. Crystals grown by STL method have many advantages (reduced structural imperfections, variety of morphologies and polymorphic forms) over the other methods, whereas slow growth rate and the probability of solvent inclusion in the sample are the main disadvantages of this process. Very recently, two more crystallization techniques have been adopted to synthesize metal halide perovskites, (i) inverse temperature crystallization (ITC) and (ii) antisolvent vapor assisted crystallization (AVC). As the solute solubility of hybrid perovskite in solvent decreases rapidly with increasing temperature (retrograde solubility) [98], shape-controlled high quality single crystals of $CH_3NH_3PbX_3$ and $CH(NH_2)_2PbX_3$ (X=I, Br, Cl) can be synthesized using

ITC method by maintaining the precursor solution at higher temperature (80^0c to 100^0c) for 3-4 hrs [32, 54, 99, 100]. Liu *et al.* grew the largest single crystals of $CH_3NH_3PbX_3$ so far (two-inch) using this method [101]. Because of faster growth rate ($\sim$ 1mm^3/hr), this method can be adopted for commercial purposes, whereas, structural imperfection and solvent corrosion might arise due to high growth temperature which deteriorates the crystalline quality of these perovskites. Around the same time, D. Shi *et al.* proposed a strategy to synthesize single crystals of metal halide perovskite using anti-solvent vapor assisted crystallization (AVC) method [102]. This method is used to synthesize the materials which are highly soluble in a solvent (good solvent) but have poor solubility in other solvents (antisolvent) and diffusion of suitable antisolvent vapor into the precursor solution results in high-quality crystals [90, 155]. Thereafter, great effort has been implemented to synthesize single crystals of perovskites using AVC method where toluene and dichloromethane (DCM) have been used as an antisolvent [41, 58, 103, 104]. This room temperature crystallization technique is really important for thermally sensitive samples, mostly where organic groups are present. Furthermore, the presence of antisolvent changes the solvent activity of the solution which has a more profound effect on the morphology and polymorphic form than that of ITC and STL methods, whereas, use of additional raw material (*i.e.*, antisolvent) might create problems in the purity of crystals and also enhance the capital cost. Hence, among these three crystallization techniques, ITC and AVC are popular among the perovskite community because perfect cuboid sized single crystals can be formed. Though several groups have synthesized single crystals of metal halide perovskite using above three methods and characterized them in their own suitable way. However, there is no comparative study available in the literature, focusing on the crystallographic and spectroscopic point of view to engineering defect states of crystals grown by above three crystallization techniques.

In this work, a comparative study of heat capacity, room temperature powder XRD, room temperature absorbance and temperature-dependent photoluminescence (PL) on single crystals of $CH_3NH_3PbBr_3$ synthesized by STL, ITC, dichloromethane (DCM) and Ethylacetate (EA) diffused AVC method has been carried out. Absorbance and PL results indicate the presence of deep level defect state between valence and conduction bands in case of crystals synthesized by STL, ITC and DCM diffused AVC methods; which is absent in crystals grown in the EA antisolvent environment. Such broadband white light emission has been observed upon near ultraviolet excitation at room temperature for two-dimensional lead-halide perovskites and it was proposed that self-trapped excitons (STE) are responsible for this [156–158]. Further, we know that, intrinsic-self-trapped excitons (i-STE) are transient defects which form in the excited state and photogenerated carriers are stabilized through strong electron-phonon coupling, whereas extrinsic-self-trapped excitons (e-STE) are permanent material defects (vacancies, interstitials *etc.*) [159]. Presence of optical absorption in the below gap energy region, observation of broadband emission upon below-gap excitation and signature of paramagnetic behavior indicate e-STE / permanent lattice defects might be responsible for this broadband emission. A comparison of formation energy calculations with the experimentally obtained energy levels suggest that excess Pb atoms in interstitial positions are predominantly responsible for the extrinsic self-trapping process.

3.1.2 Experimental Details

3.1.2.1 Sample Preparation methods

Synthesis of CH_3NH_3Br- Methylammonium bromide precursor (CH_3NH_3Br) was synthesized by reacting methylammonium (CH_3NH_2) with slight excess hydrobromide acid (HBr) and the mixture was stirred for two hours in an ice bath. The resulting solution was evaporated using a rotary evaporator until white microcrystals were formed. These microcrystals of CH_3NH_3Br were washed three times in diethyl ether and dried [54] and were kept in vacuum for further use.

Method-1: Inverse Temperature Crystallization (ITC) method- In general, solubility of a solution increases as the temperature is increased. However, Bakr *et al.* have shown that solubility of $CH_3NH_3PbBr_3$ dissolved in dimethylformamide (DMF) decreases at 80^0C (detailed in section 2.2.1.2) [98]. Thus, we used 10 ml N, N dimethylformamide (DMF) as solvent in which 0.367 gm lead (II) bromide ($PbBr_2$; 1 mM) and 0.111 gm methylammonium bromide (CH_3NH_3Br; 1 mM) were dissolved and this precursor solution was kept at 80^0C. After 3 hrs nice orange colored single crystals of $CH_3NH_3PbBr_3$ grew.

Method-2: Solution temperature lowering (STL) method- In this method the obtained precursor solution (by disolving equimolar $PbBr_2$ and CH_3NH_3Br in DMF as mentioned in the above section) was cooled down from 100^0C to room temperature over 20 hrs as reported earlier (detailed in section 2.2.1.1) [27, 28]. This is the most common and traditional way to synthesize $CH_3NH_3PbBr_3$ perovskite single crystals. It is also observed that crystallization increases at around 80^0C.

Anti-solvent vapor assisted Crystallization (AVC) method- Rather than above mentioned two high-temperature crystal growth techniques we have tried to grow single crystals of $CH_3NH_3PbBr_3$ perovskite at room temperature. It is well known that solubility of a compound in one solvent (good solvent) decreases due to slow incorporation of another solvent (bad solvent) in which the solute is not soluble (an anti-solvent). This can be done in two way; one is by direct contact between the saturated solution and the anti-solvent (“layering”) and other is by allowing the vapors of the anti-solvent to slowly diffuse into a saturated solution. In this method, Ethyl acetate (EA) and dichloromethane (DCM) vapors are used to reduce the solubility of the solute (detailed in section 2.2.1.3).

Method-3: Ethyl acetate (EA) diffusion- In this method, a vial containing $CH_3NH_3PbBr_3$ precursor solution (same as method-1) was kept in EA environment. With slow diffusion of EA into the solution, nice orange crystals were grown within 7-8 days.

Method-4: Dichloromethane (DCM) diffusion- In order to visualize the effect of low boiling point antisolvent in crystallization, a low boiling point solvent like DCM is used. In this method, the precursor solution (same as method-1) filled vial kept in DCM environment and orange crystals were grown within 2-3 days.

3.1.2.2 Experimental techniques

X-ray powder diffraction of all samples were collected by Bruker D8 Advance diffractometer using CuK_α radiation (λ= 1.34 Å) to confirm phase purity. Temperature dependence of specific heat were recorded using Physical property measurement System (PPMS) Evercool II, from Quantum design, USA. Heat capacity measurements were performed in the temperature range between 70 K and 300 K. The optical absorption spectra at room temperature was measured using an ultraviolet-visible-near-infrared (UV-Vis-NIR) spectrophotometer (Shimadzu, 3101PC) in the wavelength range of 400-800 nm. Temperature-dependent photoluminescence (PL) spectra were recorded in the temperature range 77 K to 300 K using FL920 spectrometer from Edinburg instruments with an excitation energy of 325 nm. Time-resolved PL experiment was performed on the same FL 920 spectrometer by means of time correlated single photon counting (TCSPC) method using a pulsed diode laser. For both the measurements samples were mounted on a copper plate in a Oxford-cryostat and cooled by liquid nitrogen. Magnetization measurement were performed using VSM mounted on PPMS, from Quantum design, USA.

3.1.3 Results and Discussion

3.1.3.1 structural Studies

Powder X-ray diffraction (XRD) and heat capacity measurements were performed on samples made by four different methods as mentioned before to assess their structure and phase purity (Figure 3.1). Figure 3.1(a) shows that all samples are highly crystalline in nature, diffraction peaks of all four samples appear at same 2θ position, (indexed in the Figure 3.1 (a)), which matches well with $CH_3NH_3PbBr_3$ perovskite with cubic phase structure ($Pm\bar{3}m$ space group) [99]. Previous reports suggest that depending on crystal growth techniques $CH_3NH_3PbI_3$ [160] and $CsPbI_3$ [161] can crystallizes in cubic phase irrespective of their conventional tetragonal and orthorhombic phases respectively at room temperature. It is hence important to identify the crystallographic phase of all the synthesized compounds at room temperature as well as their phase transition temperatures, for which temperature dependent heat capacity measurements were performed (Figure 3.1(b)). A decrease of temperature from 280 K to 70 K results a decrease in the heat capacity with sharp anomalies at 236.9 K, 154.6 K and 149.3 K, indicating a change in internal energies arising from the crystallographic phase transitions. A comparison with previous reports suggest that all four samples undergo a crystallographic phase transition from cubic to tetragonal (I), tetragonal (I) to tetragonal (II) and tetragonal (II) to orthorhombic at 236.9 K, 154.6 K and 149.3 K respectively [17, 162]. Detailed structural analysis of $CH_3NH_3PbBr_3$ is discussed in chapter 4. Hence, it can be concluded that all four samples grown by three different synthesis methods are identical from the structural point of view.

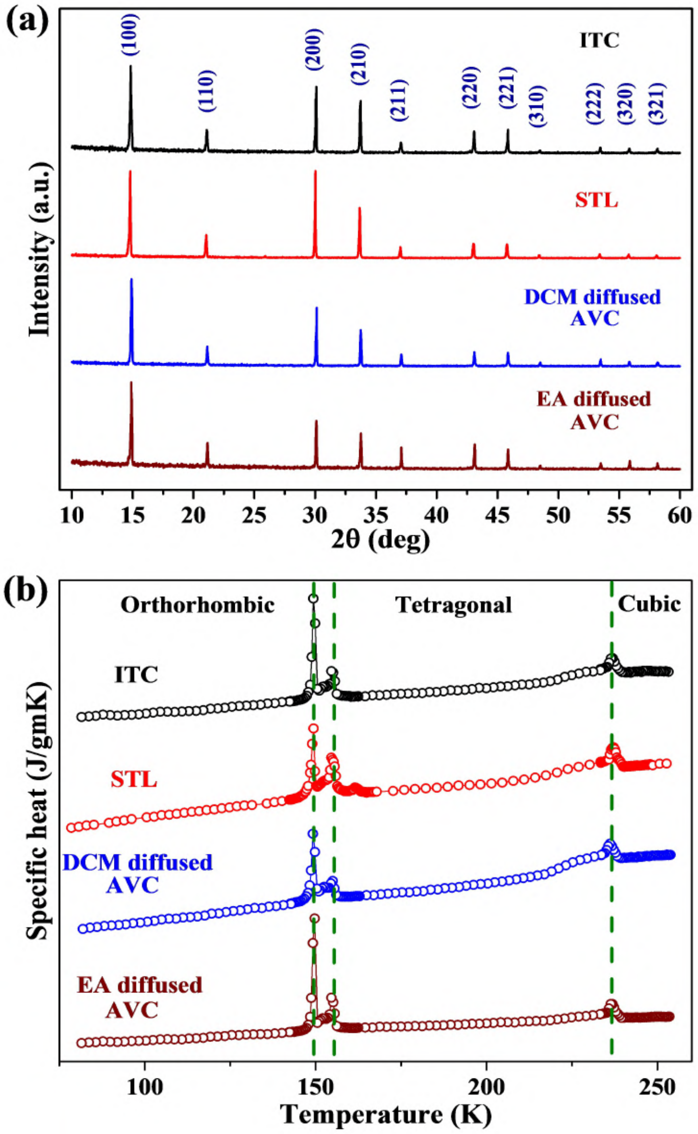

Figure 3.1: (a) Room temperature powder X-ray diffraction patterns and (b) heat capacity of $CH_3NH_3PbBr_3$ grown by ITC, STC, DCM and EA diffused AVC method.

3.1.3.2 Optical Studies

Optical properties of $CH_3NH_3PbBr_3$ samples synthesized by above four different techniques are investigated using steady-state absorption and PL studies. Figure 3.2 depicts the room temperature UV-Visible absorption spectra of four $CH_3NH_3PbBr_3$ samples synthesized via ITC, DCM diffused AVC, STL and EA diffused AVC techniques. Each spectrum was acquired from a pellet (diameter of 10 mm) made by crushing equal amount (120 mg) of single crystals of $CH_3NH_3PbBr_3$, which consist of three broad features: a

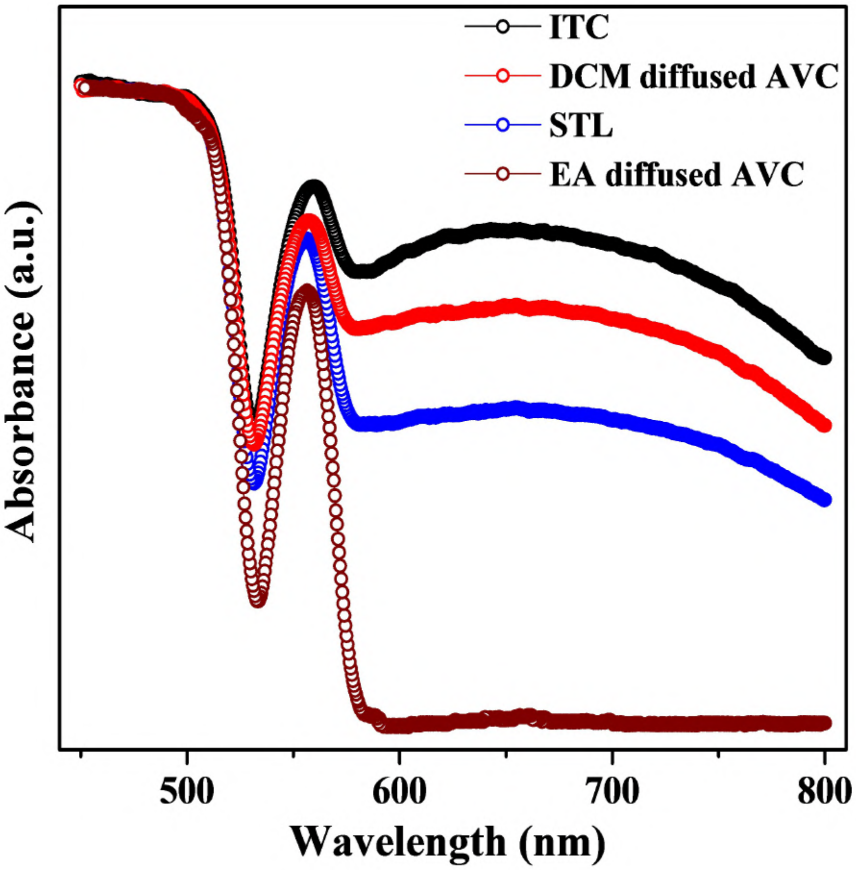

Figure 3.2: Room temperature UV-VIS absorbance spectra of four $CH_3NH_3PbBr_3$ samples grown by ITC, STC and AVC (DCM and EA diffused) method.

sub-bandgap absorption feature at low energy (800 to 600 nm), followed by a strong and sharp peak at around 556 nm (2.23 eV) followed by band-edge transitions which starts from about 506 nm (2.45 eV) which is consistent with the previous report [20]. Steeper band edges of $CH_3NH_3PbBr_3$ suggest that it is a direct bandgap semiconductor with ordered nature. Apart from dual transitions at 506 nm and 556 nm, a broad hump between 600 nm and 750 nm is observed for samples synthesized by ITC, STL and DCM diffused AVC method and the relative absorbance of this broad band is maximum for samples grown by ITC method, followed by DCM diffused AVC and STL method. In contrast, no broad absorbance peak (between 600 and 750 nm) is observed in sample grown by EA diffused AVC method. Thus, the question is what is the origin of this broad feature in absorption spectra of $CH_3NH_3PbBr_3$. We hence performed detailed temperature-dependent PL measurements to address this issue.

Figure 3.3(a) shows steady-state photoluminescence (PL) of sample grown by ITC method over temperature range from 77 K to 300 K. At 77 K, three PL emission peaks were observed (i) Peak-1 at 543.5 nm, (ii) peak-2 at 561 nm and (iii) peak-3 at 649 nm, which is consistent with the previous reports [163]. It was observed that relative intensity and full width at half maxima (FWHM) of peak-3 is high and broad compared to peak-1 and 2. Peak-1 is blue shifted, while peak-2 is red shifted continuously with increasing temperature, reaching 529.5 nm and 573.5 nm, respectively, at room temperature (300 K). Observation of such dual emission peaks and their temperature evolution were consistent with literature reports [163, 164]. Integrated intensity and full width at half maxima (FWHM) of peak 1 and peak 2 change in regular manner for all four samples. Origin of this dual transition will be discussed in details in chapter-5 [47, 165]. Irrespective of these dual emission peaks, another peak (peak 3) is observed at 650 nm whose intensity and FWHM reduces drastically in the temperature range 77 K to 140 K and almost vanishes above 160 K. Further, temperature dependent steady-state PL spectra of the samples grown by STL and DCM diffused AVC methods were carried out, as depicted in Figure 3.3 (b) and (c), respectively. Similar to the previous case, peak-1 is blue shifted from 540 nm (77 K) to 525 nm (300 K) and 541.5 nm (77 K) to 527 nm (300 K), respectively. Also, peak-2 is red shifted from 556.5 nm (77 K) to 570 nm (300 K) and 558 nm (77 K) to 571.5 nm (300 K) in the respective cases. Apart from these, an additional peak (peak 3) was observed at 651 nm and 660 nm, respectively, for the two samples which are red-shifted with the increase of temperature from 77 K to 140 K and vanishes above 160 K.

Further, it is also observed that the relative intensity of peak-3 with respect to peak-1 is maximum for the sample grown by ITC method and minimum for the sample grown by STL method, consistent with the UV-Visible absorbance studies. Looking at the position and FWHM of peak 3 in the energy level diagram, we believe that intermediate defect/ trap states are responsible for this interband feature and might originate due to rapid growth rate at high temperature and fast diffusion by low boiling point solvent (DCM). Similar observation of deep level trap states is also present in the UV-Visible absorbance study of the corresponding samples. Further study on existence and behavior of peak-3

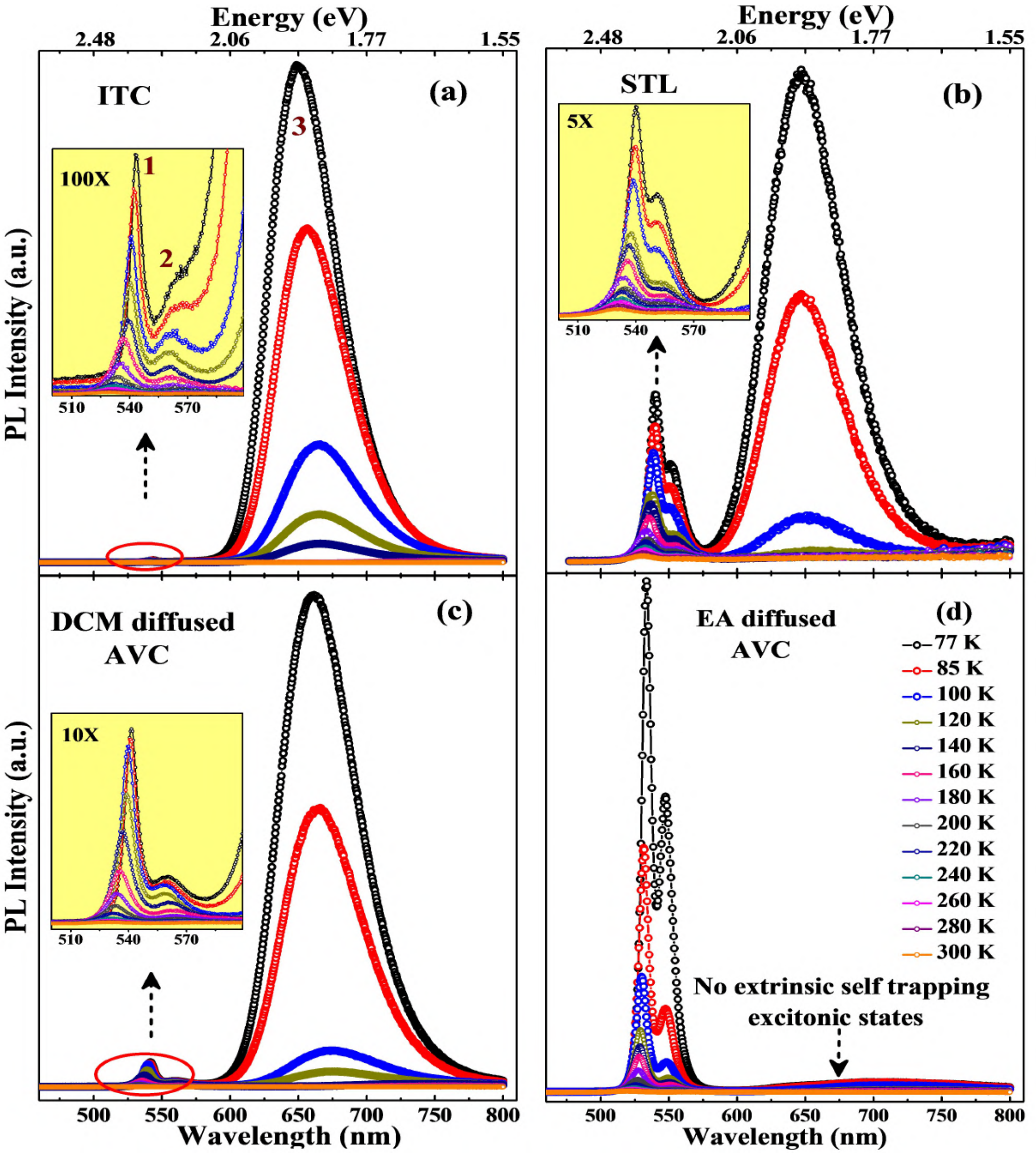

Figure 3.3: Temperature dependent photoluminescence spectra of $CH_3NH_3PbBr_3$ grown by (a) ITC, (b) STC, (c) DCM diffused and (d) EA diffused AVC method. Inset shows the variation of first two peaks with temperature.

of samples grown at room temperature by high boiling point antisolvent diffusion (EA) treatment where growth rate is relatively lower was interesting. Surprisingly, no peaks were observed around 650 nm, but only peak-1 and peak-2 at 533.5 nm and 549.5 nm were observed at 77 K, which were blue and red-shifted to 519 nm and 563 nm at 300

K, respectively. Thus, in conclusion, broadband (peak-3) is observed when the sample was synthesized by ITC, STL and DCM diffused AVC method, with the relative intensity being maximum for ITC and minimum for STL, while no broadband (peak-3) is observed for sample grown by EA diffusion.

The broad emission/absorption in the midgap region in defect free semiconductors and insulators is best described in terms of an intrinsic self-trapping of electron and excitons (STEs). Additionally, it has been suggested that the presence of defects/ impurity atoms in the crystal can add further inhomogeneity to the excited-state potential surface, leading to escalation of the broad midgap emission response [159]. According to literature reports, STEs as well as carrier traped permanent lattice defects are responsible for such broadband white light emission in two dimensional hybrid perovskites ($(N-MEDA)[PbBr_4]$ (N-MEDA = N1-methyl ethane-1,2-diammonium) and $(EDBE)[PbX_4]$ (EDBE = 2,2 (ethylenedioxy)bis(ethylammonium); X = Cl and Br)) [156–158]. Absence of interband PL intensity in sample synthesized via EA diffused AVC technique and dominance of peak 3 compared to peak 1 at low temperature (190 K) for other three samples suggested the observation of STEs or permanent lattice defects in this sample. Further, careful observation of present data reveals that excitonic peak positions (peak 1 and 2) show a redshift of 41-45 meV for ITC, 32-35 meV for DCM diffused AVC and 27-28 meV for STL method grown sample compared to EA diffused AVC sample throughout the temperature region. This result indicate that the local configurations of trap states and electronic properties are quite sensitive to their charge states introduced by the permanent lattice defects or e-STEs. It must be noted that the shifting of valence band maxima (VBM) or conduction band minima (CBM) due to the introduction of defects is consistent with previous literature reports [166].

For further clarification, time-correlated single photon counting (TCSPC) of peak-1 and peak-3 on sample prepared by ITC method were performed and presented in Figure 3.4. The time difference between peak-3 and peak-1 is evident. The lifetime of the energy levels responsible for peak-1 and peak-2 (not shown here) are relatively small (ns range), while, that of peak-3 is in μs range/order confirming a different origin of peak-3.

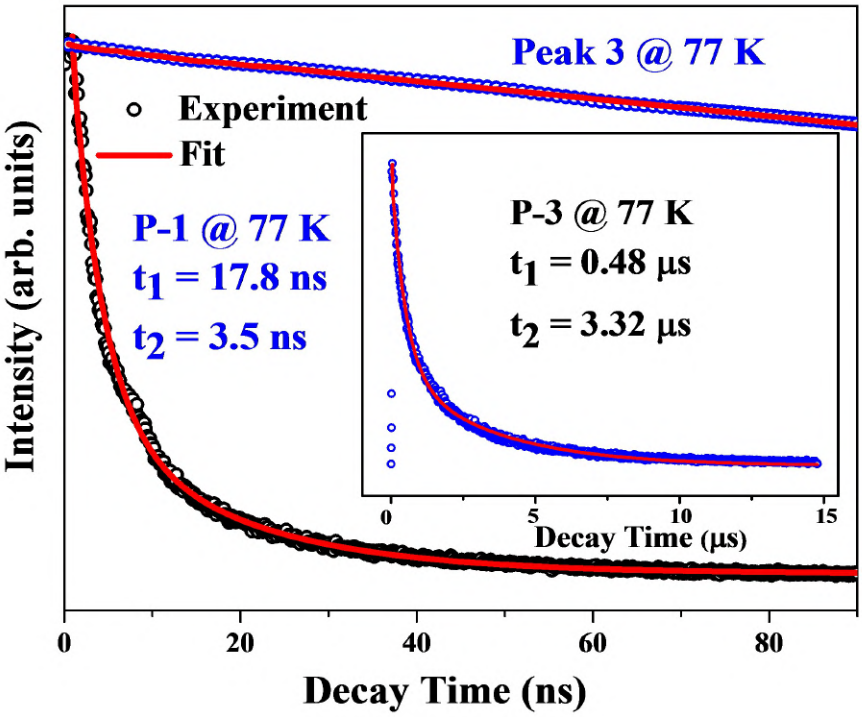

Figure 3.4: Time correlated single photon counting (TCSPC) data corresponding to 650 nm and 531 nm (Inset) emission peaks at 77 K of $CH_3NH_3PbBr_3$ grown by ITC method. Hollow dots represents the experimental data and solid lines denote the biexponential fitting of the data.

Recombination lifetime of $CH_3NH_3PbBr_3$ was determined by measuring PL decay at the emission peak wavelengths and the curves are fitted with the biexponential function of time (t) given by-

$$I(t) = I_1 exp\frac{-t_1}{\tau_1} + I_2 exp\frac{-t_2}{\tau_2} \tag{3.1}$$

where τ_i is the decay time and I_i is the weight factor of each decay channel. Fitting yielded biexponential decay (surface and bulk recombination) confirms the energy level associated with peak-1 has lifetime around 17.8 ns with 59.32% weight% and 3.5 ns with 40.68% weight%, whereas, lifetime of energy levels associated with peak-3 is 0.48 μsec with 57.12% weight% and 3.32 μsec with 42.88% weight%, suggesting that the origin of transition responsible for emission of peak-3 is completely different than that of peak-1 (electronic band to band transition). To understand the origin of broad midgap states in this system, a reinvestigation of possible defect states of $CH_3NH_3PbBr_3$ was required.

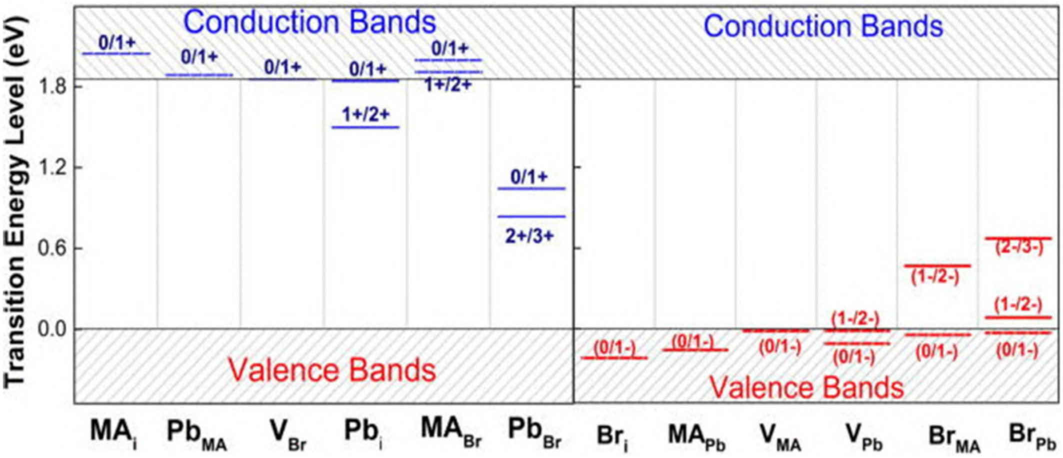

Figure 3.5: Calculated transition energy levels of intrinsic point defects in $CH_3NH_3PbBr_3$. (Taken from: Appl. Phys. Lett. 106, 103902 (2015).)

Depending on the location of the energy states in band diagram, defect states might be shallow or deep level. Shallow defects have energy levels within few tens of meV from respective band edges, whereas deep level defects reside within the middle third of the bandgap. In other way one can associate deep levels with highly localized wave functions, whereas shallow level wave functions are as extended as the far-reaching coulomb potential [36, 37]. According to this definition, it is observed that almost all dominant defects in $CH_3NH_3PbBr_3$ are shallow levels except only four deep level defects as shown in Figure 3.5. List of all possible point defects of $CH_3NH_3PbBr_3$ are- (i) CH_3NH_3 (MA), Pb, Br vacancies (V_{MA}, V_{Pb}, V_{Br}), (ii) MA, Pb, Br interstitial (MA_i, Pb_i, Br_i), (iii) MA on Pb (MA_{Pb}) and Pb on MA (Pb_{MA}) cation substitution and (iv) MA on Br (MA_{Br}), Pb on Br (Pb_{Br}), Br on MA (Br_{MA}), Br on Pb (Br_{Pb}) antisite substitutions. Formation energy calculation reveals that MA_i, Pb_{MA}, V_{Br} and MA_{Br} are shallow donors whereas Br_i, MA_{Pb}, V_{MA}, V_{Pb} are shallow acceptors which are not responsible to show the observed midgap defect states. Remaining four defects Pb_i, Pb_{Br}, Br_{MA} and Br_{Pb} produce deep levels in the bandgap of $CH_3NH_3PbBr_3$ [38]. Further, it is also observed that Pb_i and Pb_{Br} levels are situated nearer to the conduction band, whereas, Br_{MA}, Br_{Pb}, exist closer to the valence band, and are responsible for the interband transition. In order to identify whether Pb or halides are responsible for these broadband feature in UV-Visible absorption and PL spectra, further experiments were carried out by substituting Br ion site with Cl. For this purpose single crystals of $CH_3NH_3PbCl_3$ were synthesized via ITC and EA diffused AVC method and steady-state PL at 77 K of both the samples were acquired (Figure 3.6 (a)). Similar to $CH_3NH_3PbBr_3$, dual emission is also observed at 403 nm and 410.5 nm for both the samples (ITC and EA diffused AVC of $CH_3NH_3PbCl_3$) which also originated due to methylammonium orientation inside $PbCl_6$ octahedra as discussed above. Apart from this, an additional peak at 641.5 nm is observed for sample synthesized by ITC method, thereby confirming that halogen atoms don't participate in deep level defect formation in metal halide perovskite crystals. These experimental observations suggest that point defects due to self-doping of Pb atoms are responsible for the creation of the midgap defect states in samples synthesized by ITC, STL and DCM diffused AVC method. However, formation energy calculations also predict that unipolar self-doping of Pb at interstitial positions can create interband defect states. This result is receprocated by a recent report on optical absorption from density functional theory (DFT) studies where absorption related to Pb defects appeared at 650 nm for the case of $CH_3NH_3PbI_3$ [167].

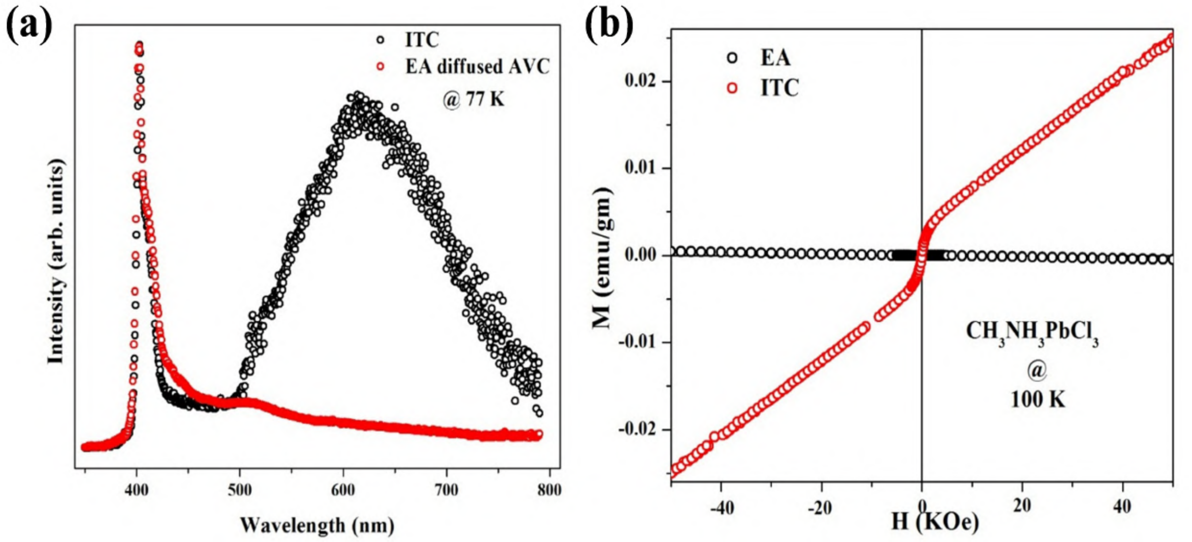

Figure 3.6: (a) Photoluminescence spectra of $CH_3NH_3PbCl_3$ grown by ITC and EA diffused AVC method at 77 K; (b) M-H loops of $CH_3NH_3PbCl_3$ grown by ITC and EA diffused AVC method taken at 100 K.

3.1.3.3 Magnetic Studies

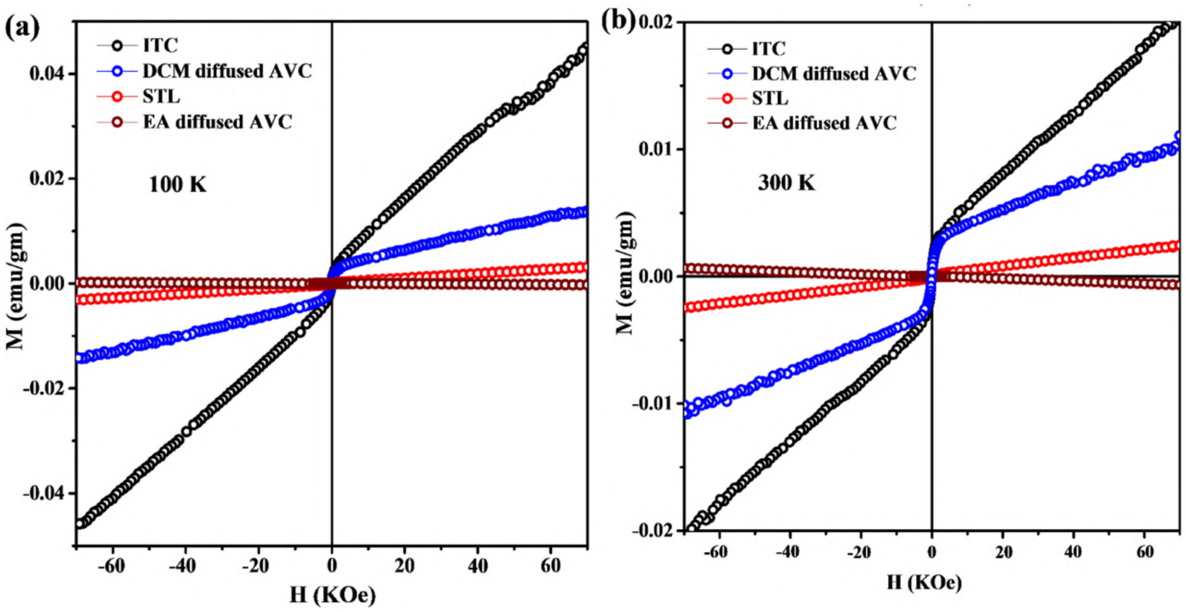

Figure 3.7: M-H loops of $CH_3NH_3PbBr_3$ grown by ITC, STC, DCM and EA diffused AVC method taken at 100 K and 300 K.

Defect states of methylammonium lead halide samples can result in uncompensated spins of Pb to align in the applied magnetic field direction like in Mn-doped $CH_3NH_3PbBr_3$ micro-rods [168]. Hence, M-H behavior of all $CH_3NH_3PbBr_3$ samples were acquired at 100 K and 300 K, which are presented in Figure 3.7 (a) and 3.7 (b) respectively. A careful inspection of the M-H loop at 100 K and 300 K suggests that $CH_3NH_3PbBr_3$ crystals synthesized by EA diffused AVC method is diamagnetic in nature with susceptibility $\chi = -4.43 \times 10^{-9}$ which is consistent with the literature reports [77, 168, 169]. Other three samples synthesized by STL, DCM diffused AVC and ITC method show paramagnetic behavior with small ambiguity at low magnetic field. It is interesting to observe that magnetization is maximum for sample grown by ITC method (0.045 emu/gm), followed by DCM diffused AVC method (0.014 emu/gm) and STL method (0.003 emu/gm) at 100 K at a particular magnetic field (70 KOe). Similar behavior of magnetization was observed at 300 K for all samples as shown in Figure 3.7 (b). M-H measurements were also performed on $CH_3NH_3PbCl_3$ crystals grown by ITC and EA diffused AVC method and similar behavior was observed, as shown in Figure 3.6 (b). This result revealed magnetization increases depending on the number of uncompensated Pb atoms in interstitial positions, consistent with conclusions from PL results. Reproducibility of the above observation was confirmed by performing magnetization measurements on all samples multiple times and synthesized in multiple batches. Defect induced magnetism in predominantly diamagnetic samples have been observed in graphite [170], graphene [171], ZnO [172] and TiO_2 [173]. Our PL and magnetic measurements hence suggests that Pb related defects contribute to the broad peak around the midgap state and the number of interstitial Pb atoms are higher in case of ITC method, minimum in STL method and almost negligible for the case of the sample grown by EA diffused AVC method.

3.1.4 Conclusion

Systematic and in-depth comparative study of the structural, optical and magnetic properties of $CH_3NH_3PbBr_3$ grown by ITC, STL, DCM and EA diffused AVC method were performed through powder XRD, heat capacity, room temperature UV-VIS and temperature dependent PL spectroscopy as well as M-H studies. Identical powder XRD patterns and heat capacity confirm the phase purity and the presence of three crystallographic phase transitions in all four samples synthesized by different techniques. However, the presence of a broad band between 600nm and 700 nm was observed in the room temperature absorption and temperature dependent PL studies in case of samples grown by ITC, STL and DCM diffused AVC method which was absent in the sample grown by EA diffused AVC method. Time-resolved PL study confirm that the lifetime associated with this broad band is three orders of magnitude higher ($\sim \mu$s) than that of band edge transitions ($\sim$ ns). A comparison with the formation energy calculations confirmed that excess Pb in interstitial positions create defect levels for the samples whose growth rate is high. This observation was also confirmed by dc magnetization studies. Thus, a novel approach to synthesize defect-free crystals is put forth, which will be useful to fabricate optoelectronic devices using metal halide perovskite single crystals.

3.2 Growth of $CH_3NH_3PbCl_3$ Single Crystals by Solvent Evaporation

3.2.1 Introduction

We know that $CH_3NH_3PbCl_3$ is one of the less extensively investigated materials for photovoltaic and optoelectronic applications due to its low power conversion efficiency (PCE) compared with that of other halide perovskites [29, 100, 162, 174–176]. However, $CH_3NH_3PbCl_3$ is found to be a good candidate for visible-blind UV detector because of its large band gap and limited absorption of the solar spectrum [100, 175]. Hence, it is essential to synthesis high-quality, well-shaped and defect-free single crystals of $CH_3NH_3PbCl_3$ and have proper understanding of its photophysical properties for its use in optoelectronic devices which include photovoltaic devices [10], LEDs [11], photodetectors [177], X-ray and gamma-ray detectors [178] *etc.* Till now, literature reports only two methods to synthesize single crystals of $CH_3NH_3PbCl_3$; one is solution temperature lowering method (STL) [29, 162] and other by inverse temperature crystallization method (ITC) [100, 175]. The single crystals of hybrid perovskites grown by the above two methods are not necessarily defect-free crystals; the crystals grown by antisolvent vapor assisted crystallization (AVC) method are defect-free single crystals (as discussed in previous section of this chapter) [102], however, the use of an additional solvent can create impurity and also enhance capital cost. An alternate method is the solvent evaporation method, which is a traditional method to obtain single crystals of most organic compounds from solution where no extra solvent is required. Aromatic and aliphatic 2D perovskite crystals were synthesized by Liao *et al.* and Daub *et al.* respectively following this method. Liao *et al.* evaporated N, N-dimethylformamide (DMF) at 90^0C to synthesize hybrid perovskite analogs (benzyl ammonium)$_2$PbCl$_4$ single crystals using this method and studied its crystal structure [105]; whereas, Daub *et al.* synthesized black colored $MA_2Pb(SCN)_2I_2$ single crystals (where I^- was partially substituted by SCN^- ion) via dissolving a stoichiometric molar ratio of $Pb(SCN)_2$ and MAI in DMF [106]; followed by slow evaporation at room temperature.

In this work, we have demonstrated a new route to synthesize $CH_3NH_3PbCl_3$ single crystals at room temperature without adding antisolvent. To achieve our goal, a mixture of Dimethyl sulfoxide (DMSO) and gamma-Butyrolactone (GBL) (1:1 volume ratio) were used as a solvent in which lead (II) chloride ($PbCl_2$) and methylammonium chloride (MACl) were dissolved and the precursor solution was kept at room temperature without any disturbance. $CH_3NH_3PbCl_3$ is highly soluble in DMSO and sparingly soluble in GBL. Further, GBL (204^0C) has higher boiling point than DMSO (189^0C). Thus, DMSO vaporizes much faster than GBL at room temperature, and steers to have more anti-solvent contained reaction mixture condition, eventually leading to the growth of rectangular shaped (8.3 X 5.1 X 1 mm), highly transparent, colorless and high-quality $CH_3NH_3PbCl_3$ single crystals within four weeks. Further, phase stability, lattice parameter and phase transition temperatures of the grown crystals were investigated through heat capacity and X-ray diffraction (XRD), both single crystal and powder XRD, measurements. Detailed analysis of the optical and charge transport properties of the as-synthesized sample was carried out using UV-Visible absorbance study, temperature dependent steady-state photoluminescence (PL) and I-V characteristics. Further, we have explored optical and electrical properties to estimate energy band levels, exciton binding energy, lifetime, carrier mobility and diffusion length which are essential parameters for understanding the possible utilization of this material in practical applications.

3.2.2 Experimental Details

3.2.2.1 Growth of $CH_3NH_3PbCl_3$ Single Crystals:-

Single crystals of CH_3NH_3Cl were synthesized by reacting CH_3NH_2 and HCl in molar ratio of 1.2:1. HCl was added dropwise into CH_3NH_2 in a flask under nitrogen atmosphere in an ice bath and stirred for 3 hrs; the resulting solution was evaporated at 60^0C in a rotary evaporator to remove the unreacted solvent and white crystals of CH_3NH_3Cl were obtained. Further, 2.78 gm $PbCl_2$ (1 M), 0.67 gm CH_3NH_3Cl (1 M) were dissolved in a mixture of DMSO (5 ml) and GBL (5 ml) (1:1 volume ratio) and this precursor solution was kept at room temperature without any disturbance. Due to solvent evaporation, rectangular shaped, highly transparent, colorless and high-quality $CH_3NH_3PbCl_3$ single crystals were grown within two weeks. Keeping the same chemical environment for two more weeks resulted in the growth of larger crystals of (8.3 mm × 5.1 mm × 1 mm) size.

3.2.2.2 Characterizations and Measurements:-

Powder X-ray diffraction (XRD) measurement of the as-grown sample was carried out with a Bruker D8 Advance diffractometer using Cu K_α radiation to confirm 3D perovskite phase of the sample. Furthermore, a detailed and high resolution structural investigation of the single crystals were carried out at XRD1 beamline at Elettra Synchrotron Light Source, Trieste, Italy using a wavelength of λ= 0.96864 Å, to confirm their phase purity, and Rietveld refinement was performed using Fullprof software to identify the lattice constants. Single crystal XRD measurements were performed on an Oxford Xcalibur (Mova) diffractometer equipped with an EOS CCD detector using Mo K_α radiation (λ = 0.71073 Å). Data collection, data reduction and numerical absorption corrections were performed using the programs present in the CrysAlisPro software suite [111]. Crystal structures were refined by using SHELXL-97 [112] program present in the WinGX suite [113]. To illustrate the temperature-dependent phase transition and identify accurate phase transition temperatures, heat capacity measurement of $CH_3NH_3PbCl_3$ was recorded in the physical Property Measurement System (PPMS) Evercool II, from Quantum Design, USA. Measurements were performed in the temperature range between 100 K and 280 K with a 0.5 K point density in the region of interest. Temperature-dependent steady-state and time-dependent photoluminescence (PL) measurements of this sample were acquired using FL920 spectrometer from Edinburg instrument in the temperature range 100 K to 300 K. For this measurement, pellets made from grounded crystal was mounted on a copper plate in a cryostat (Oxford, UK) and cooled to 100 K using liquid nitrogen. Xenon lamp with 325 nm was used as the excitation source for steady-state measurements. To determine current-voltage characteristics of the $CH_3NH_3PbCl_3$ crystals ($8 \times 5 \times 0.4$ mm^3), hole only devices were obtained by vapor deposition of 80 nm gold electrodes on both sides. The space charge limited current (SCLC) measurement was performed using Keithley source-meter in the dark, under vacuum at room temperature.

3.2.3 Results and Discussion

3.2.3.1 Structural Studies

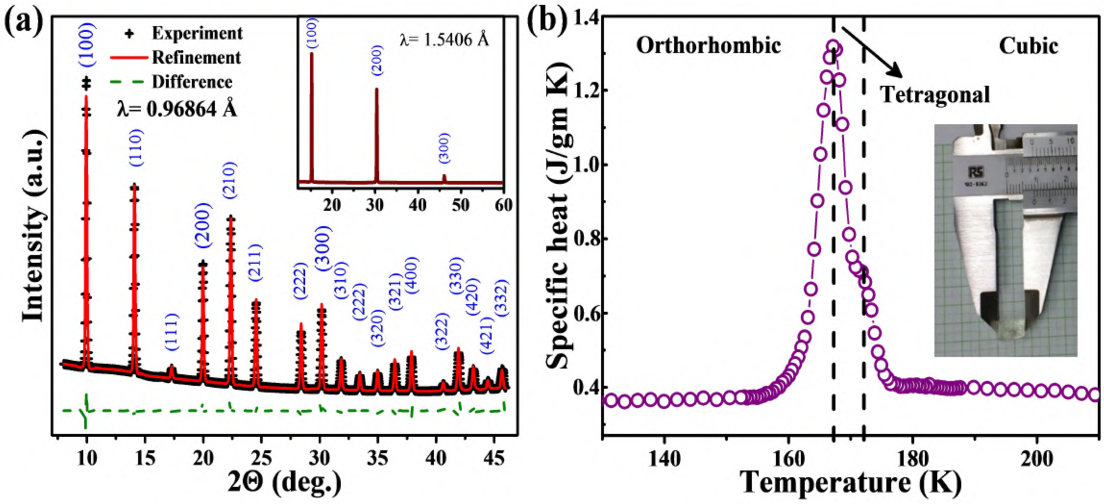

Figure 3.8: (a) X-ray powder diffraction patterns (black) of as-synthesized $CH_3NH_3PbCl_3$ obtained at room temperature with the refinement patterns (red) using the P$m\bar{3}m$ structure superimposed on it. Inset shows the XRD pattern from the top surface of $CH_3NH_3PbCl_3$ single crystal. (b) Temperature dependence of specific heat of $CH_3NH_3PbCl_3$, where different crystallographic phases are indicated and image of the single crystal is plotted as an inset.

Figure 3.8(a) depicts synchrotron powder X-ray diffraction (XRD) pattern of $CH_3NH_3PbCl_3$ acquired at room temperature along with the corresponding Rietveld refined data using P$m\bar{3}m$ space group superimposed on it. The reasonably small values of reliability parameters ($R_w \sim 0.091$, $R_{exp} \sim 0.045$ and $\chi^2 \sim 6.26$) indicate good quality of fitting (Table-3.1) with lattice parameter of a = 5.6834 Å, which is consistent with the literature reports [100]. XRD pattern recorded from the top surface of the crystal is depicted in the inset of Figure 3.8(a). The appearance of only (100) hkl reflections and its higher orders confirms single crystalline nature of our sample. The refinement of single crystal X-ray diffraction and some random snap-shots during measurement are presented in Table 3.2 and Figure 3.9, respectively. Refined single crystal structure data from our single crystal sample is accepted in the Cambridge Crystallographic Data Centre (CCDC) data base with no: CCDC 1872901. Organic-inorganic hybrid perovskites also exhibit crystallographic phase transitions from cubic to tetragonal to orthorhombic phases with decrease of temperature due to the reduction of MA orientation inside the $PbCl_6$ octahedra [27]. This can be traced from heat capacity measurements performed on $CH_3NH_3PbCl_3$ single crystal as depicted in Figure 3.8(b) which shows anomalies at 172.39 K and 167.02 K related to crystallographic phase transition from cubic to tetragonal and tetragonal to orthorhombic phase, respectively [17, 162].

Table 3.1: Crystallographic parameters of $CH_3NH_3PbCl_3$ obtained from Rietveld refinement of powder XRD.

Crystal system		Cubic
Temperature		300 K
Space group		P$m\bar{3}m$
Z		1
Unit cell dimension	a = b = c	5.6834 Å
	$\alpha = \beta = \gamma$	90^0
Atom coordinates (x,y,z,B_{iso})	Pb	(0,0,0,0.85)
	Cl	(0,0.076,0.5,0.108)
	C	(0.394,0.394,0.5,0.491)
	N	(0.414,0.414,0.5,0.235)
R factor	R_w	0.091
	R_{exp}	0.045
	χ^2	6.26

3.2.3.2 Optical Studies

Figure 3.10 (a) demonstrates the optical absorption spectrum acquired from a pellet made by crushing the $CH_3NH_3PbCl_3$ single crystal at room temperature which consists of three features; (a) ultralow sub-bandgap absorption tail at higher wavelength; (b) strong peak at 411 nm (3.02 eV) and (c) band to band transition around 393 nm (3.15 eV), similar to the results on $CH_3NH_3PbCl_3$ films observed by Kumawat *et al.* [20]. For further understanding, systematic temperature-dependent PL studies were carried out on the same $CH_3NH_3PbCl_3$ sample between 100 K and 300 K and the outcome of these measurements are summarized in Figure 3.10(b). Intensities of all the spectra are normalized and vertically translated for a clearer view. Temperature-dependent PL spectra displayed dual

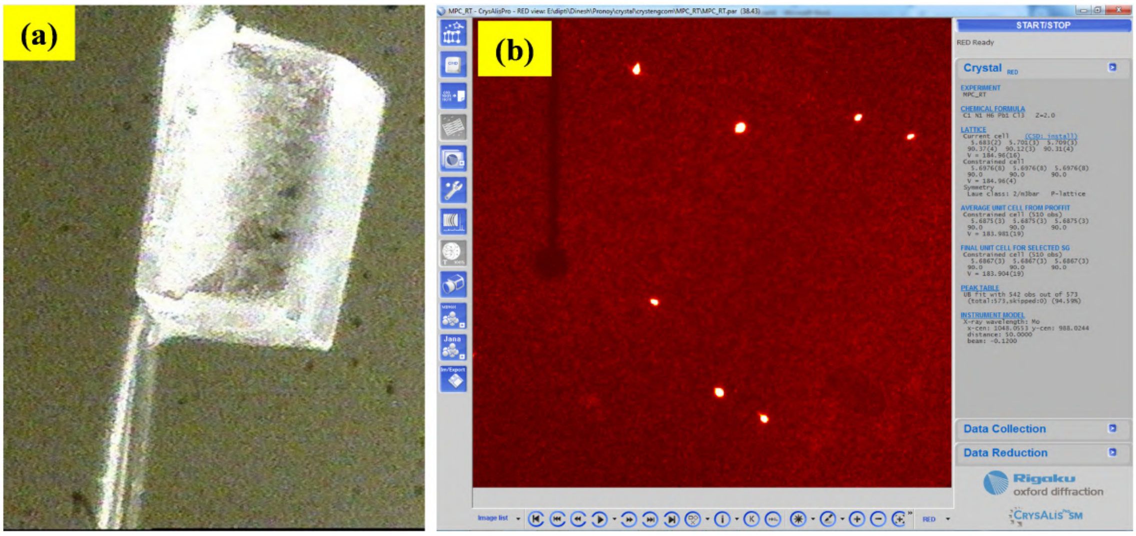

```
RED Ready

EXPERIMENT
 MPC_RT

CHEMICAL FORMULA
 C1 N1 H6 Pb1 Cl3   Z=2.0

LATTICE
 Current cell     (CSD: install)
   5.683(2)  5.701(3)  5.709(3)
  90.37(4)  90.12(3)  90.31(4)
  V = 184.96(16)
 Constrained cell
   5.6976(8)  5.6976(8)  5.6976(8)
  90.0       90.0       90.0
  V = 184.96(4)
 Symmetry
  Laue class: 2/m3bar   P-lattice

AVERAGE UNIT CELL FROM PROFFIT
 Constrained cell (510 obs)
   5.6875(3)  5.6875(3)  5.6875(3)
  90.0       90.0       90.0
  V = 183.981(19)

FINAL UNIT CELL FOR SELECTED SG
 Constrained cell (510 obs)
   5.6867(3)  5.6867(3)  5.6867(3)
  90.0       90.0       90.0
  V = 183.904(19)

PEAK TABLE
 UB fit with 542 obs out of 573
  (total:573,skipped:0) (94.59%)

INSTRUMENT MODEL
 X-ray wavelength: Mo
  x-cen: 1048.0553 y-cen: 988.0244
  distance: 50.0000
  beam: -0.1200
```

Figure 3.9: (a) Image of $CH_3NH_3PbCl_3$ single crystal mounted on Hampton cryoloop for single crystal XRD measurement. (b) Image of diffraction spots of $CH_3NH_3PbCl_3$ single crystal suggesting the crystalline quality of the sample.

Table 3.2: Crystallographic parameters of obtained from single crystal XRD refinement.

Formula	$CH_3NH_3PbCl_3$
Formula weight	345.61
Temperature	298 K
Color	Colorless
Radiation	MoK$_\alpha$
Wavelength	0.7107 Å
Crystal system	Cubic
Space group	$Pm\bar{3}m$
Unit cell dimension (a)	5.6867(3) Å
Volume	183.90(3)Å^3
Z	1
$R[F^2 > 2\sigma^2(F^2)]$	0.0347
$wR_2(F^2)$	0.0665
GooF (S)	1.270

emission peaks in the temperature range from 100 K to 300 K, which is consistent with the PL spectra obtained from one of its sister compounds $CH_3NH_3PbBr_3$ [163,164]. Peak positions of the two emission peaks at 100 K: 402 nm (peak 1; 3.08 eV) and 410.5 nm (peak 2; 3.02 eV) gradually vary with temperature as shown in the inset of Figure 3.10(b) with strong divergence in peak position observed at 175 K which is close to the crystallographic phase transition temperature. The observation of dual emission in PL spectra of $CH_3NH_3PbCl_3$ is consistent with the other organic-inorganic lead halide perovskites ($CH_3NH_3PbBr_3$) which might be arising from excitonic emission [163] or the coexistence of MA-ordered and MA-disordered domains in the sample [164]. Detailed discussion on the origin of dual emission of $CH_3NH_3PbBr_3$ is discussed in chapter 5. Eventhough the blue shifting behavior of peak-1 is inconsistent with the convensional semiconducting materials like Si [179], GaN [180], GaAs [181] *etc.*, this feature in hybrid perovskites can be explained by the Varshni model where the temperature coefficient of band gap (dE_g/dT) can be expressed as [182]:

$$\left(\frac{dE_g}{dT}\right)_p = \left(\frac{dE_g}{dT}\right)_v + \left(\frac{dE_g}{dln(v)}\right)_T \left(\frac{dln(v)}{dT}\right)_p \tag{3.2}$$

Here, the first term $\left(\frac{dE_g}{dT}\right)_v$ indicates electron-phonon coupling, which represents a decrease in band gap with an increase in temperature, and the second term is the lattice dilation term, which causes the increase in band gap as temperature increases. It is suggested that the blue shifting nature of PL peak in hybrid perovskites arises because of valence band maxima stabilization due to lattice dilation with an increase in temperature [164].

Further, exciton binding energy can also be extracted from the temperature dependence of integrated PL intensities. For $CH_3NH_3PbCl_3$, cubic phase is stable above 177.2 K; exciton binding energy was estimated in this phase. Temperature dependence of the integrated intensity of peak 1 in cubic phase is plotted in Figure 3.10(c) which can be fitted using following formula [27]:

$$I(t) = \frac{I_0}{1 + exp(-\frac{E_B}{K_B T})} \tag{3.3}$$

Here, I_0, E_B and K_B are zero temperature intensity, exciton binding energy and Boltzmann constant, respectively. Fitting yields the exciton binding energy value to be 105.21 meV, which is consistent with theoretical estimation of 106 meV [70].

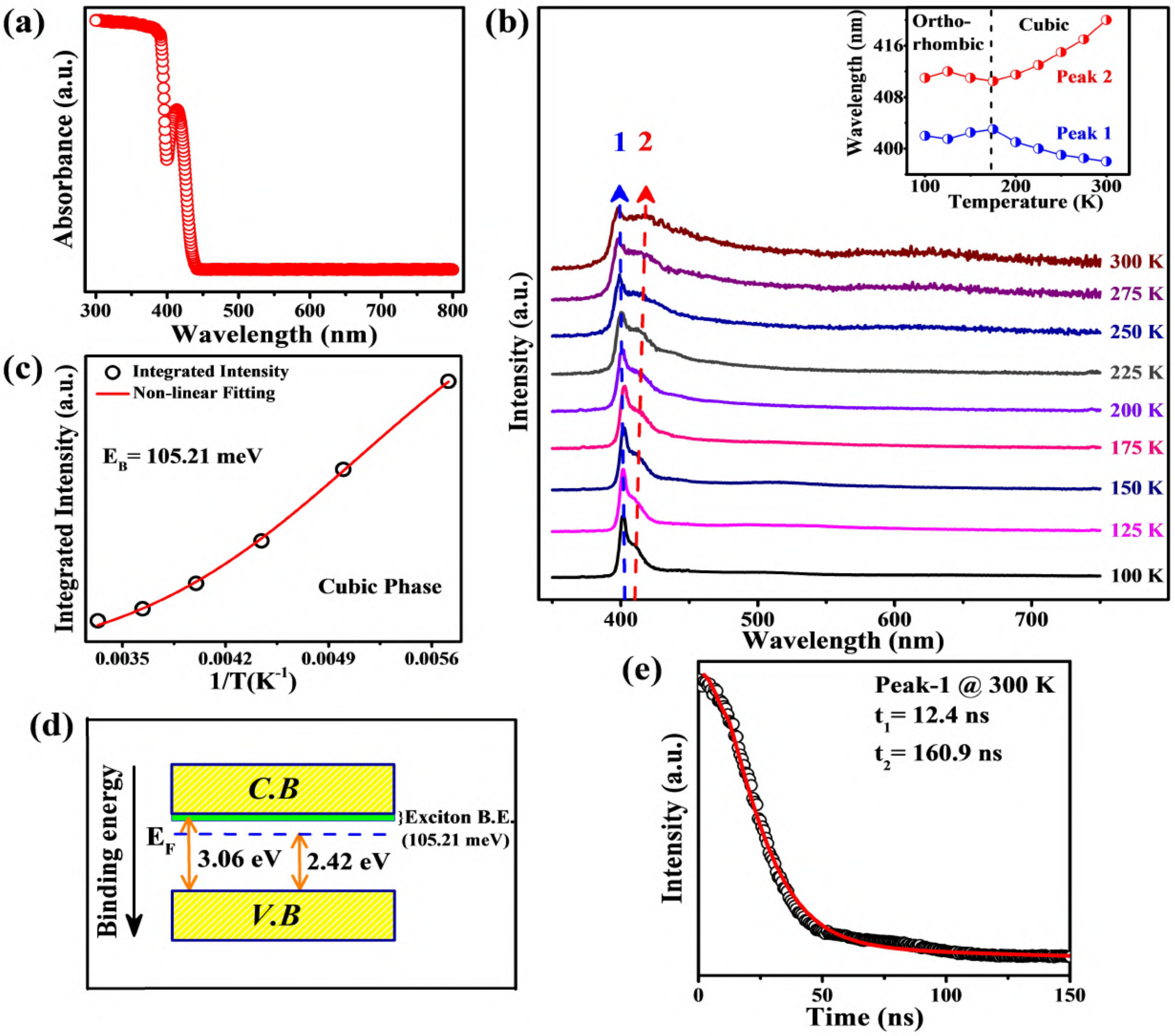

Figure 3.10: Comparative optical properties of $CH_3NH_3PbCl_3$ single crystal: (a) Room temperature optical absorption spectra; (b) Temperature-dependent photoluminescent spectra and inset shows the variation of peak positions with temperature; (c) temperature dependent data of integrated intensity in cubic phase; (d) valence band spectra, (e) (d) schematic energy level diagram; (f) (e) Time-correlated single-photon counting (TCSPC) spectra.

Schematic energy level diagram (Figure 3.10(d)) of Fermi energy (E_F), bottom of conduction band (CB) and top of valence band (VB) was constructed using room temperature PL studies (band gap of 3.11 eV) and linear interpolation of VB spectra (detail in chapter 5). A proper understanding of this energy level diagram is essential for the efficient fabrication of a visible-blind UV detector and solar cell device.

Excited-state lifetime and recombination dynamics (peak-1) of $CH_3NH_3PbCl_3$ were investigated by time-correlated single photon counting (TCSPC) method by using a pulsed laser of 375 nm excitation (Figure 3.10(e)). The obtained TCSPC spectra could be fitted using biexponential fit with two different decay times of 12.4 ns and 160.9 ns suggesting fast and slow carrier recombination times, respectively, which could be assigned as surface and bulk recombination [100]. These carrier life times are useful in extracting diffusion lengths of the charge carriers in the sample as explained below.

3.2.3.3 Transport Measurement

For estimating the potential of $CH_3NH_3PbCl_3$ sample in optoelectronic applications, charge transport experiment was also carried out on the same system. Hole mobility was extracted from dark current density-voltage (J-V) characteristics, following standard space-charge limited current (SCLC) model, in which 400 µm thick $CH_3NH_3PbCl_3$ single crystal was sandwiched between two 80 nm thick gold (Au) electrodes. Here, J-V curve showed Mott-Gurney's power law dependence as shown in Figure 3.11. For lower bias voltages (<0.16 V), $CH_3NH_3PbCl_3$ showed ohmic behavior ($I \propto V$) with electrical conductivity (σ) of 7.11 × 10-9 $\Omega^{-1}m^{-1}$, whereas for bias voltages between 0.16 V and 4.5 V, a sharp rise of current ($I \propto V^{n>3}$) was observed, which can be identified as the trap filling process [183]. The voltage at which all the traps are filled by the charge carriers (trap filled limited voltage, V_{TFL}) can be determined using following trap density relation [100,183]:

$$V_{TFL} = \frac{en_tL^2}{2\epsilon\epsilon_0} \tag{3.4}$$

where ϵ(23.9) [29,100] and ϵ_0 are dielectric constants of $CH_3NH_3PbCl_3$ and vacuum, respectively, e is the elementary charge and L (400 μm) is the thickness of the crystal. Using V_{TFL}= 0.16 V, trap density (n_t) was estimated to be 2.645×10^9 cm^{-3}. This value of trap density is one order of magnitude lower than that obtained from single crystal grown by inverse temperature crystallization method [100] and seven orders of magnitude lower than that of its thin-film counterpart [184].

Further, for the voltage region above 4.5 V, *i.e.*, in trap free space charge limit region (child region), dark current has a quadratic dependence on voltage and can be expressed as:

$$J_D = \frac{9\epsilon\epsilon_0\mu V_b^2}{8L^3} \tag{3.5}$$

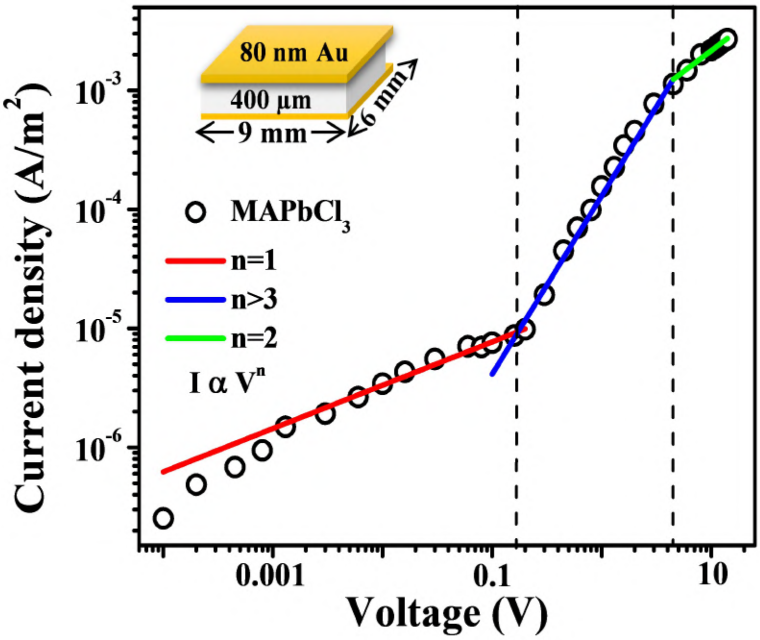

Figure 3.11: Current density-Voltage (J-V) response of $CH_3NH_3PbCl_3$ single crystal exhibiting three different regions obtained from the log J versus log V plot. Regions correspond to linear ohmic regime (J $\propto$ V, red line), trap filling limit regime (J $\propto$ $V^{n>3}$, blue line) and Child's regime (J $\propto$ V^2, green line).

where, J_D, V_b and μ are current density, applied voltage and hole mobility, respectively. Using equation 3.5, hole mobility (μ) and free charge carrier density ($n_c = \sigma/e\mu$) were found to be 14.7 $cm^2V^{-1}S^{-1}$ and 3.02×10^7 cm^{-3}. By combining the values of μ obtained from SCLC and carrier lifetime (T_r) from TCSPC method, carrier diffusion length (L_D) can be determined by the following equation:

$$L_D = \sqrt{\frac{K_B T \mu T_r}{e}} \tag{3.6}$$

Two values of diffusion lengths were obtained: (a) 2.47 μm using longer recombination time (160.9 ns) and (b) 0.68 μm for small recombination time (12.4 ns), which can be ascribed as bulk and surface recombination of $CH_3NH_3PbCl_3$ crystals, respectively. Though these extracted values of diffusion lengths are comparable with that of a single crystal of $CH_3NH_3PbCl_3$ grown by ITC method [100], samples grown by solvent evaporation method (at room temperature) result in lower values of trap charge density, suggesting that the new method of sample synthesis proposed in this work results in relatively defect free samples which can find direct application in visible blind UV detector.

3.2.4 Conclusion

In summary, we have presented a completely new route to synthesize high-quality $CH_3NH_3PbCl_3$ crystals through proper selection of the DMSO-GBL solution, which allowed crystallization due to solvent evaporation at room temperature. A detailed evaluation of structural, optical and electrical properties of the single crystal were carried out and various parameters like crystallographic phase transition temperatures, exciton binding energy and transport parameters, such as electrical conductivity, carrier mobility, trap density and diffusion length were determined. Low defect concentration (as seen from optical and charge transport points of view) and longer diffusion length indicate that these hybrid perovskite crystals are promising candidates to work as an active component in visible-blind UV detector. We hope, this room temperature growth mechanism will provide a breakthrough for the deployment of $CH_3NH_3PbCl_3$ crystals in practical applications.

Chapter 4

Structural Investigations of Hybrid Perovskites

In this chapter we will discuss crystal structures and structural phase transitions of hybrid perovskites using XRD and EXAFS measurements. Temperature dependent synchrotron powder x-ray diffraction studies along with heat capacity measurements revealed crystallographic phase transition from cubic to tetragonal to orthorhombic phase with the decrease of temperature. Further, preferred symmetry of hybrid perovskites is found to be centrosymmetric rather than non-centrosymmetric, supporting the non-polar nature of the system and rules out the possibility of ferroelectricity. Variation of lattice and order parameters, tetragonal distortion and linear expansion coefficients clearly indicate that crystallographic phase transition is first order and rule out the possibility of phase coexistence. Variation of bond-length and bond-angle of $CH_3NH_3PbX_3$ *(X= I, Br) suggests octahedral distortion near the phase transition temperatures, which is absent in* $CsPbBr_3$*. Based upon these results, we discuss the impact of the structural phase transitions upon photovoltaic performance of organic-inorganic hybrid perovskite-based solar cells.*

4.1 Introduction

The origin of the surprisingly high efficiencies exhibited by solar cells and optoelectronic devices fabricated with organic-inorganic hybrid perovskites remains a subject of widespread research interest [10]. These materials also combine the advantages of low cost starting materials [90, 92] and high throughput, [93] and low-tech fabrication techniques compared to traditional silicon and III-V photovoltaic (PV) devices [7,8,185], which holds great promise for decreasing the cost of solar energy.

It is essential to understand the crystal structure of organic-inorganic hybrid perovskites, characterized by structural phase transitions, considerable static or dynamic disorder, various defects like lead cation, halogen anion or organic cation vacancy or interstitial, to understand the underlying physics behind its high efficiency and accelerate the search for new solar cell materials. The structure of organic-inorganic hybrid perovskite is far more complicated than the conventional solar cell absorbers like, Si, CIGS, CdTe *etc.*, where an asymmetric and positively charged organic unit, methylammonium ion ($CH_3NH_3^+$), with a permanent dipole, is located at the center of a lead halide cage [17, 29, 162]. These perovskite materials crystallizes in orthorhombic phase at low temperature and have high/room-temperature cubic phase depending on halide ion, with an intermediate tetragonal phase, which is relevant to its photovoltaic properties [162]. At low temperature this system is in orthorhombic perovskite structure where the methylammonium ($CH_3NH_3^+$) dipoles order in an antiferroelectric arrangement [186, 187]; however, the behavior of this dipole and their possible roles in determining the structural chemistry and material properties in high temperature tetragonal and cubic phase is still developing [83, 188]. It is also suggested that the halogen ions exhibit disorder; i.e., PbX_6 tetrahedron is distorted in cubic phase [28, 80]. Such a wide range of distortions, including polar distortions, has fueled the possibility of ferroelectricity in this system [189]. Alternate claims regarding the crystallographic structure of hybrid perovskite in tetragonal phase suggests it is in polar $I4cm$ [80] as well as centrosymmetric $I4/mcm$ [28] space group for this system. Hence we perform careful high resolution temperature dependent synchrotron X-ray diffraction measurements and Rietveld refinement to understand the crystal structure of hybrid perovskites and identified that preferred symmetry of hybrid perovskites is centrosymmetric rather than non-centrosymmetric. Spatial anisotropy and selective ionic bonding of $CH_3NH_3^+$ ions with the halide atoms of the inorganic cage influence the bond-length and bond-angle distributions, and consequently, the structural features of the crystal [190–192]. Despite nearly identical crystal structure observed by powder x-ray diffraction, the local coordination environment reveals deviations in the octahedral Lead-Halide distances observed in X-ray pair distribution function (PDF) analysis due to anharmonic lattice dynamic and is modeled as rotational distortion of the PbX_6 octahedra [193,194]. Tyson *et al.* [194] also indicated a large degree of anharmonicity in the PbX_6 octahedra and speculate that the halide atoms can move considerably within the lattice at very low cost in energy using x-ray absorption fine structure (XAFS) measurements. It is also argued that the softness of the lattice which underlies the high anharmonicity, enable deformation of the lattice in response to the defect but limits its extension to a very small region of space yielding a material with resilient high carrier mobility in the presence of defects [167, 169, 195–197]. Thus, we believe that careful comparative investigations of local structure environment is essential for this system where permanent dipole ($CH_3NH_3^+$) is present in one case, and $CH_3NH_3^+$ is replaced by monopolar, symmetric Cs^+ ion in other case. Therefore, a comparison of the Lead-Halide bond angle variation with temperature of $CH_3NH_3PbBr_3$ and $CsPbBr_3$ is expected to make the contribution from the dipoles obvious.

In this chapter, we have discussed detailed temperature dependent synchrotron powder x-ray diffraction studies along with heat capacity measurements to identify the crystallographic phase transitions with temperature of $CH_3NH_3PbX_3$ (X= I, Br). We have also extracted lattice parameters, tetragonal distortion, thermal expansion coefficient, bond-length and bond-angles as they play crucial role in phase transitions. Additionally, we have systematically studied the changes in the local structure around Pb atom in $CH_3NH_3PbX_3$ (X= I, Br) and $CsPbBr_3$ using temperature dependent extended x-ray absorption fine structure (EXAFS) studies.

4.2 Experimental Details

4.2.1 Sample synthesis

Single crystal Samples of $CH_3NH_3PbI_3$, $CH_3NH_3PbBr_3$ and $CsPbBr_3$ were synthesized by the antisolvent vapor assisted crystallization (AVC) method as reported elsewhere [41, 58, 103, 104]. Rectangular shaped, defect free, smooth surfaced, high-quality single crystals were obtained at room temperature using this method (as reported in section 2.2.1.3 and 3.1.2.1). Synthesis involves the addition of antisolvent (a liquid miscible with the precursor solvent) to reduce the solubility of the solute in order to achieve supersaturation. For this purpose, 4.61 gm (1 M) lead (II) iodide (PbI_2) and 1.59 gm (1 M) methylammonium iodide (MAI) were dissolved in 10 ml Gamma-butylacetone (GBL) and keep this precursor in ethyl acetate (100 ml) environment at 50^0C. Due to slow diffusion of ethyl acetate into the solution, high quality, well-bordered rectangular shaped black $CH_3NH_3PbI_3$ single crystals were formed. Similarly, 3.67 gm lead(II) bromide ($PbBr_2$) + 1.11 gm methylammonium bromide (MABr) were dissolved in 10 ml N,N dimethylformamide (DMF) for the synthesis of $CH_3NH_3PbBr_3$. For this case, the precursor is kept in ethyl acetate at room temperature. For the synthesis of $CsPbBr_3$ single crystals, 3.67 gm (1 M) $PbBr_2$ and 3.19 gm (1.5 M) CsBr were dissolved in 10 ml dimethyl sulfoxide (DMSO) and kept in methyl alcohol (MeOH) environment to form pure $CsPbBr_3$ single crystals within 3-10 days [198].

4.2.2 Experimental techniques

Phase purity of the samples were confirmed by powder x-ray diffraction (XRD) measurements as performed in Bruker D8 Advanced x-ray diffractometer using Cu K_α ($\lambda = 1.5406$ Å) radiation. Detailed temperature dependent XRD measurements of $CH_3NH_3PbX_3$ (X= I, Br) samples were carried out at the XRD1 beamline at the ELETTRA synchrotron radiation facility using photons with a wavelength of 0.85507 Å. Rietveld refinements of the diffraction patterns were performed using FULLPROF package. In order to perform temperature dependent single crystal XRD of $CsPbBr_3$ samples, crystals were mounted on a Hampton cryoloop on an Oxford Xcalibur (Mova) diffractometer equipped with an EOS CCD detector using Mo K_α ($\lambda = 0.71073$ Å) radiation. Data collection, data reduction and numerical absorption corrections were performed using the programs present in the CrysAlisPro software suite. Crystal structures were refined by using SHELXL-97 program present in WinGX suit. Temperature dependent EXAFS measurements were performed at P-65 beamline at PETRA-III synchrotron source, DESY, Hamburg, Germany. In order to perform this experiment, powder sample of appropriate weight, estimated to obtain a reasonable edge jump was taken in powder form and mixed thoroughly with cellulose powder to obtain total weight of 100 mg and homogeneous pellets of 15 mm diameter was prepared using a hydraulic press. The incident (I_0) and transmitted (I_t) photon intensities were recorded simultaneously using ionization chambers filled with appropriate gases at Pb L3 (13.035 keV) edge of $CH_3NH_3PbI_3$, $CH_3NH_3PbBr_3$ and $CsPbBr_3$ samples. Knowing I_0 and I_t, energy dependence of absorption coefficient ($\mu(E)$) can be written as, $\mu(E) = log(I_0/I_t)$. Thereafter, a smooth pre-edge function was subtracted from $\mu(E)$ to get rid of instrumental background and a threshold energy (E_0) was identified from derivative of $\mu(E)$ using the ATHENA software. Further, a smooth post-edge background function ($\mu_0(E)$) was identified which represent absorption of an isolated atom and EXAFS function can be defined as, $\chi(E) = \frac{\mu(E)-\mu_0(E)}{\Delta\mu_0(E)}$; where $\Delta\mu_0(E)$ is the measured jump in the absorption at the threshold energy (E_0). As EXAFS is best understood in terms of the wavevector (k), EXAFS function is also convoluted to $\chi(k)$ and magnitude of Fourier transform of k^2 weighted $\chi(k)$ is here represented as $|\chi(R)|$ [141]. Thereafter, the fitting of the EXAFS spectrum with a specific theoretical model obtained from basic crystallographic information was carried out using the ARTEMIS software. The software computes the theoretical spectrum from the given model using the ATOMS and FEFF6 programs [142].

4.3 Results and Discussions

4.3.1 Structural Studies: Global

$CH_3NH_3PbX_3$ (X= I, Br, Cl) crystallizes in cubic perovskite structure at high temperature, having Goldschimdts tolerance factor, $t_G = \frac{r_A+r_X}{\sqrt{2}(r_B+r_X)}$ = 0.834 ($CH_3NH_3PbI_3$), 0.844 ($CH_3NH_3PbBr_3$), 0.851 ($CH_3NH_3PbCl_3$), 0.911 ($CH(NH_2)_2PbBr_3$) and 0.815 ($CsPbBr_3$)

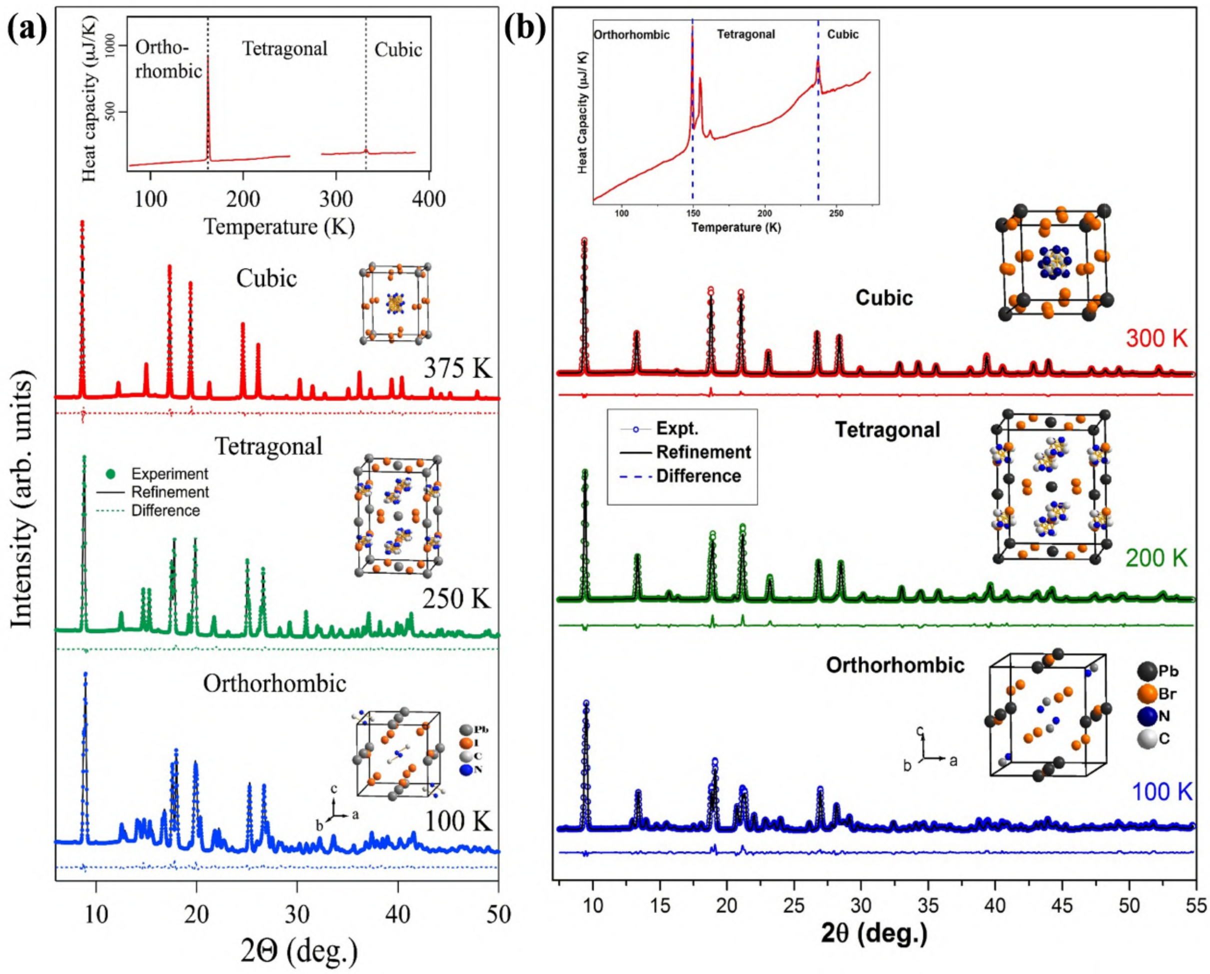

Figure 4.1: X-ray diffraction pattern of (a) $\mathrm{CH_3NH_3PbI_3}$ collected at three different temperatures 100 K, 250 K and 375 K, (b) $\mathrm{CH_3NH_3PbBr_3}$ collected at 100 K, 200 K and 300 K. Solid dots/ plus sign represents the experimental data, solid lines denote the Rietveld refined patterns while the dotted lines represents the difference between the two. Crystal structure corresponding to the three temperatures is also plotted. Inset shows heat capacity of corresponding samples where different crystallographic phases with temperature are indicated.

[199]. In case of hybrid perovskite structure, one unit cell is composed by eight octahedral sites ($\mathrm{BX_6}$) and the cation "A" is situated between each octahedra as shown in Figure 1.5. Here the cite, "A", represents the organic cation $(\mathrm{CH_3NH_3})^+$; $(\mathrm{CH(NH_2)_2}{}^+$ or Cs^+ and "B" is Pb^{2+}, while the anion, "X", is the halide ion (I^-, Br^- or Cl^-) [200, 201]. This group of hybrid perovskites exhibit crystallographic phase transition with temperature. High resolution X-ray diffraction patterns of $\mathrm{CH_3NH_3PbI_3}$ ($\mathrm{CH_3NH_3PbBr_3}$) were recorded at three different temperatures *viz*. 100 K, 250 K and 375 K (100 K, 200 K and 300 K) as shown

in Figure 4.1 (a) (4.1 (b)). Rietveld refinement of the patterns was performed (Figure 4.1 (a) and (b)) and the resulting parameters are summarized in Table 4.1 (4.2). The refined parameters confirms the existence of orthorhombic, tetragonal and cubic phases at 100 K, 250 K and 375 K (100 K, 200 K and 300 K) respectively, thereby confirming the crystallographic phase transition with temperature in $CH_3NH_3PbI_3$ ($CH_3NH_3PbBr_3$) [27,83,162]. At 375 K (300 K) $CH_3NH_3PbI_3$ ($CH_3NH_3PbBr_3$) crystallises in cubic $Pm\bar{3}m$ space group with a lattice parameter of $\sim$ 6.339 Å($\sim$ 5.930 Å). Cubic structure contains only one formula unit (Z = 1); hence the non-centrosymmetric methylammonium ion $(CH_3NH_3)^+$ must be randomly oriented to satisfy the O_h symmetry [27]. As the temperature is lowered, tetragonal and orthorhombic phases are realised with an accompanying ordering of methylammonium ion [30]. At $\sim$ 250 K ($\sim$ 200 K) $CH_3NH_3PbI_3$ ($CH_3NH_3PbBr_3$) crystallises in tetragonal phase ($I4/mcm$) with lattice parameters a = 8.875 Å, c = 12.732 Å(a = 8.332 Å, c = 11.867 Å), where $a_{tetragonal} = \sqrt{2}a_{cubic}$). Structural transition from cubic to tetragonal phase occurs due to the reorientation of $(CH_3NH_3)^+$, as observed by NMR studies where lowering of the number of disordered states of $(CH_3NH_3)^+$ was observed from 24 in cubic phase to 8 in tetragonal phase [30]. This molecular ordering is completed in the orthorhombic phase such that at 100 K $CH_3NH_3PbI_3$ ($CH_3NH_3PbBr_3$) forms in orthorhombic $Pnma$ space group with lattice parameters a = 8.865 Å, b = 12.617 Å, c = 8.584 Å(a = 7.966 Å, b = 11.839 Å, and c = 8.570 Å), which are consistent with previous reports [27,28,83,162]. These structural transitions are depicted fairly well in the heat capacity measurements, plotted as inset to Figure 4.1 (a) (4.1 (b)), which shows two sharp anomalies at temperatures 330.8 K and 161.8 K (236.1 K and 149.8 K) for $CH_3NH_3PbI_3$ ($CH_3NH_3PbBr_3$) corresponding to the crystallographic phase transitions from cubic to tetragonal and from tetragonal to orthorhombic phases, respectively.

Some reports suggest that $CH_3NH_3PbX_3$ (X=I, Br) crystallizes in non-centrosymmetric space groups such as $I4cm$ [80] and $Pna2_1$ [29] for tetragonal and orthorhombic phases, respectively, based on which ferroelectricity was proposed [82]. Subsequently, Sharada *et al.* [83] also tried to observe second harmonic generation (SHG) in $CH_3NH_3PbI_3$ perovskite crystal. However, their SHG signal (if any) was well below detectable limit and signal to noise ratio was very poor in both ground and excited states, strongly indica-

Table 4.1: Crystallographic Parameters of $CH_3NH_3PbI_3$ obtained from Rietveld refinement.

Crystal System	Orthorhombic	Tetragonal	Cubic
Temperature	100K	250K	375K
Space group	P*nma*	I4/*mcm*	Pm$\bar{3}$m
Unit cell dimensions	a(Å) = 8.865	a(Å) = 8.875	a(Å) = 6.339
	$\alpha = 90°$	$\alpha = 90°$	$\alpha = 90°$
	b(Å) = 12.617	b(Å) = 8.875	b(Å) = 6.339
	$\beta = 90°$	$\beta = 90°$	$\beta = 90°$
	c(Å) = 8.584	c(Å) = 12.732	c(Å) = 6.339
	$\gamma = 90°$	$\gamma = 90°$	$\gamma = 90°$
Z	4	4	1
Atom Coordinates			
Pb	(0.5, 0, 0)	(0, 0, 0)	(0, 0, 0)
I(1)	(0.489, 0.25, -0.053)	(0.207, -0.292, 0)	(0, 0.072, 0.5)
I(2)	(0.197, 0.018, 0.191)	(0, 0, 0.25)	
C	(0.915, 0.25, 0.066)	(0.549, -0.052, 0.279)	(0.574, 0.574, 0.5)
N	(0.937, 0.75, 0.021)	(0.423, 0.048, 0.211)	(0.379, 0.379, 0.5)
R-factors			
R	0.042	0.036	0.024
R_{wp}	0.114	0.080	0.074
R_p	0.098	0.080	0.076

tive of a nonpolar or centrosymmetric structure. We also performed refinements in the above non-centrosymmetric space groups. R factors obtained for refinement in I4*cm* space group are $R_p = 0.123$, $R_{wp} = 0.205$, R = 0.159 ($R_p = 0.117$, $R_{wp} = 0.208$, R = 0.145), whereas the refinement was really bad for P*na*2_1 space group where R = 0.282 (R = 0.267) was obtained for $CH_3NH_3PbI_3$ ($CH_3NH_3PbBr_3$). In comparison to these refine-

Table 4.2: Crystallographic Parameters of $CH_3NH_3PbBr_3$ obtained from Rietveld refinement.

Crystal System	Orthorhombic	Tetragonal	Cubic
Temperature	100K	200K	300K
Space group	P*nma*	I4/*mcm*	$\mathrm{Pm\bar{3}m}$
Unit cell dimensions	a(Å) = 7.966	a(Å) = 8.332	a(Å) = 5.930
	$\alpha = 90°$	$\alpha = 90°$	$\alpha = 90°$
	b(Å) = 11.839	b(Å) = 8.332	b(Å) = 5.930
	$\beta = 90°$	$\beta = 90°$	$\beta = 90°$
	c(Å) = 8.570	c(Å) = 11.867	c(Å) = 5.930
	$\gamma = 90°$	$\gamma = 90°$	$\gamma = 90°$
Z	4	4	1
Atom Coordinates			
Pb	(0.5, 0, 0)	(0, 0, 0)	(0, 0, 0)
Br(1)	(0.531, 0.25, -0.023)	(0.227, -0.282, 0)	(0, 0.071, 0.5)
Br(2)	(0.213, 0.022, 0.217)	(0, 0, 0.25)	
C	(0.946, 0.25, 0.101)	(0.576, -0.072, 0.286)	(0.427, 0.427, 0.5)
N	(0.968, 0.75, 0.065)	(0.453, 0.045, 0.201)	(0.375, 0.375, 0.5)
R-factors			
R	0.052	0.032	0.024
R_{wp}	0.116	0.088	0.061
R_p	0.107	0.082	0.059

ment outputs, those for the centrosymmetric space groups I4/*mcm* and P*nam* produced far better results, as depicted in Table 4.1 (Table 4.2). Our results hence contradict the non-centrosymmetric nature of the crystal structure and supports the non-observance of ferroelectric response in $CH_3NH_3PbI_3$ ($CH_3NH_3PbBr_3$).

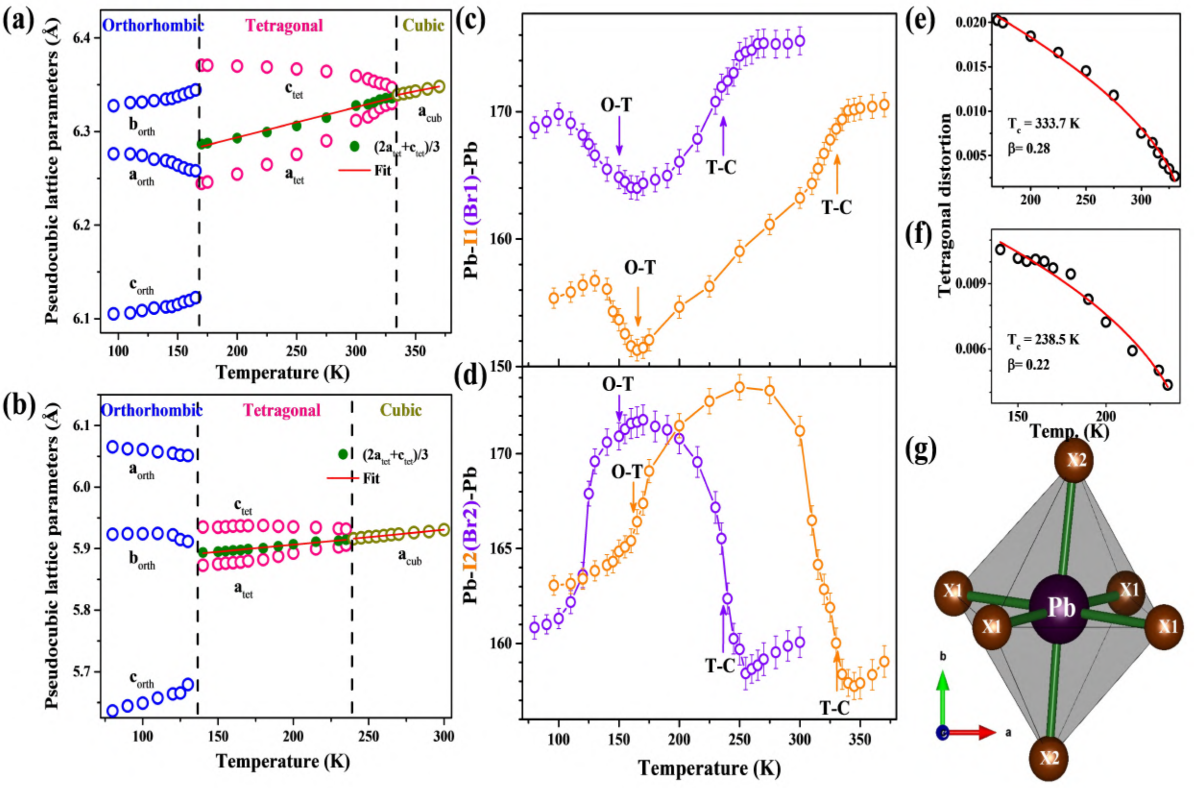

Figure 4.2: Lattice parameters and phase transitions of $CH_3NH_3PbI_3$ and $CH_3NH_3PbBr_3$. Lattice parameters refined from the synchrotron X-ray diffraction scans of (a) $CH_3NH_3PbI_3$ and (b) $CH_3NH_3PbBr_3$. Fits to the cubic lattice parameter (red solid line) and the average tetragonal lattice parameter (= $2a_{tet} + c_{tet})/3$ (red solid line), were used to determine the linear coefficients of thermal expansion. Variation of (c) axial and (d) equatorial bond angles of $CH_3NH_3PbI_3$ and $CH_3NH_3PbBr_3$. The arrows indicate the crystallographic phase transition temperature. Temperature dependence of the Tetragonal distortion from XRD data fit to a power law ((c—a)/a ∼ $(Tc- T)^{2\beta}$) to identify the cubic-tetragonal phase transition of (e) $CH_3NH_3PbI_3$ and (f) $CH_3NH_3PbBr_3$. (g) Visualization of axial (X1) and equatorial (X2) halide atoms in the PbX_6 octahedra.

Rietveld refined parameters of temperature dependent synchrotron XRD of $CH_3NH_3PbI_3$ and $CH_3NH_3PbBr_3$ confirm the existence of orthorhombic (Pnma), tetragonal (I4/mcm) and cubic (P$m\bar{3}m$) phases for both the samples and the unit cell parameters are plotted in figure 4.2 (a) and 4.2 (b), respectively. Refined unit cell parameters (blue open circle in figure 4.2 (a) and 4.2 (b)) of $CH_3NH_3PbI_3$ and $CH_3NH_3PbBr_3$ in orthorhombic phase are consistent with the previous reports and negative coefficient of thermal expansion was observed for ‘a’ and positive coefficient for both ‘b’ and ‘c’, whereas total volume expansion is positive (not shown) [28, 201]. Further, decomposition of 100 K XRD data with ISODISTORT [202] showed the major displacement in the orthorhombic structure to be pure octahedral tilts, which in Glazer's notation are given by $a^-b^+a^-$ [203]. Variation of Pb-I/ Pb-Br bond lengths (Figure 4.4 (a) and (b)/ Figure 4.4 (c) and (d)) and Pb-I-Pb/ Pb-Br-Pb bond angles (Figure 4.2 (c) and (d)) with temperature in orthorhombic phase were also extracted from refined XRD data and the role of octahedral tilt towards the variation of bond lengths are discussed later. When the sample temperature is above 149.8 K (160 K), $CH_3NH_3PbI_3$ ($CH_3NH_3PbBr_3$) crystallizes in tetragonal phase (I4/*mcm*) and the refined lattice parameters (pink open circles) are consistent with the literature reports [27, 28, 176, 201]. Average tetragonal lattice parameter ($=(2a_{tet}+c_{tet})/3$) were used to extract the linear coefficient of thermal expansion and the values are 3.23×10^{-4} K^{-1} and 2.5×10^{-4} K^{-1} for $CH_3NH_3PbI_3$ and $CH_3NH_3PbBr_3$, respectively. In order to extract order parameter of tetragonal-cubic phase transition, tetragonal strain was extracted from the lattice parameters [201, 204]:

$$(c-a)/a \sim Q^2 \sim (T_c - T)^{2\beta} \tag{4.1}$$

where Q, T_c and β are order parameter, phase transition temperature and critical exponent. Fitting yielded the values of T_c and β are 333.7 K and 0.28 (238.5 K and 0.22) for $CH_3NH_3PbI_3$ ($CH_3NH_3PbBr_3$) as shown in Figure 4.2 (e) (Figure 4.2 (f)) and this transition temperature is consistent with the specific heat values and literature reports [17, 27, 162]. We know that synchrotron based powder X-ray diffraction allowed a more detailed examination of phase compositions across the phase transitions, and also provided the temperature dependence of the order parameter associated with each transition. However, they are not sensitive to the positions of the organic cations, X-rays will only provide information about the heavier PbX_6 octahedra. Temperature dependent variation of Pb-I/ Pb-Br bond lengths (Figure 4.4 (a) and (b)/ Figure 4.4 (c) and (d)) and Pb-I-Pb/ Pb-Br-Pb bond angles (Figure 4.2 (c) and (d)) with temperature was also extracted in the tetragonal phase and detailed discussion is emphasized next section of this chapter. Further, when the sample temperature is above the critical temperature of tetragonal-cubic phase transition, they transformed to cubic phase (P$m\bar{3}m$). Variation of lattice parameters of $CH_3NH_3PbI_3$ ($CH_3NH_3PbBr_3$) with temperature in cubic phase, extracted from XRD results are presented in Figure 4.2 (a) (Figure 4.2 (b)) (Dark yellow open circles). Extracted values of linear coefficient of thermal expansion in cubic phase are 2.52×10^{-4} K^{-1} and 2.31×10^{-4} K^{-1} for $CH_3NH_3PbI_3$ and $CH_3NH_3PbBr_3$, respectively, which are consistent with literature reports [201]. As before, we have also extracted variation of Pb-I/ Pb-Br bond lengths (Figure 4.4 (a) and (b)/ Figure 4.4 (c) and (d)) and Pb-I-Pb/ Pb-Br-Pb bond angles (Figure 4.2 (c) and (d)) with temperature in the cubic phase. The temperature dependent variation of the bond angles of $CH_3NH_3PbI_3$ and $CH_3NH_3PbBr_3$ with temperature are shown in Figure 4.2 (c) and (d). With decreasing temperature, the axial angle (pb-I1-Pb/ Pb-Br1-Pb) decreases upto tetragonal-orthorhombic transition and then increases; whereas the equatorial angle (pb-I2-Pb/ Pb-Br2-Pb) decreases till cubic-tetragonal transition temperature, then increases nearly upto tetragonal-orthorhombic transition and again decreases. The overall behavior of axial and equatorial angle for both the hybrid lead halide perovskites are same with anomaly around the crystallographic phase transition. This suggests that there exist distortions in the octahedra probably associated with off-center displacements of halogen due to CH_3NH_3 orientation.

4.3.2 Structural Studies: Local

Based on X-ray diffraction studies, it is found that PbX_6 octahedra exhibits distortions due to off-center displacements of halogen atoms, which might arise because of CH_3NH_3 orientation [190, 191]. For better understanding, temperature dependent extended x-ray absorption fine structure (EXAFS) measurement were performed. It is a powerful technique which provides information on the local structure around atoms. It provides valuable information about the structural peculiarities and allows us to verify different structural models. Figure 4.3 (a) and (b) show the X-ray absorption spectra of $CH_3NH_3PbI_3$ and $CH_3NH_3PbBr_3$ samples from the Pb L_3 edge and corresponding pre-edge, X-ray Absorption Near-edge Structure (XANES) and EXAFS region are marked in the figure. In this technique, the absorption of X-ray radiation in resonance with an atomic absorption

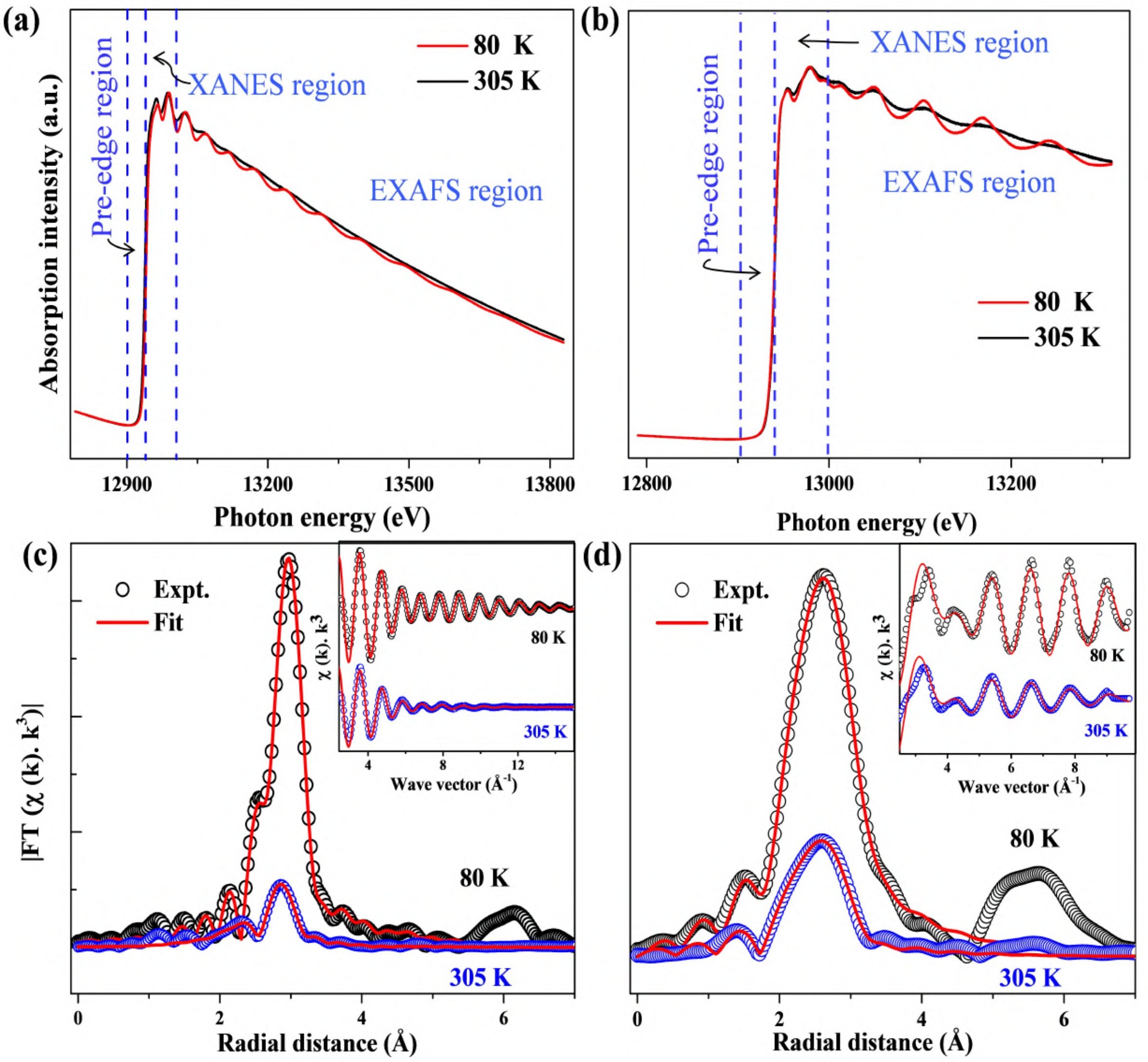

Figure 4.3: XAFS spectrum showing the pre-edge, XANES and EXAFS regions of (a) $CH_3NH_3PbI_3$ and (b) $CH_3NH_3PbBr_3$ samples. Magnitude of Fourier transforms of k^3-weighted EXAFS data at Pb-L_3 edge acquired at 80 K (black open circle) and 305 K (blue open circle) for (c) $CH_3NH_3PbI_3$ and (d) $CH_3NH_3PbBr_3$, along with corresponding fitting superimposed on it (red solid line). Corresponding back-transformed spectra in k-space (open circles) along with fitting are plotted in inset.

edge yields information about the local environment surrounding the absorbing atom. This resonance is responsible for the damped oscillatory behavior of XAS spectra in EXAFS region [195, 196]. 1st derivative of absorption intensity results threshold energy of $CH_3NH_3PbI_3$ ($\sim$ 12.94 keV). Further, pre and post edge correction of the x-ray absorption spectrum reveals pre and post edges are located at ± 100 eV from the threshold energy.

Thereafter, the magnitude of Fourier transforms of k^3-weighted EXAFS data ($|\chi(R)|$) at Pb-L$_3$ edges acquired at 80 K and 305 K for $CH_3NH_3PbI_3$ and $CH_3NH_3PbBr_3$ samples are presented in Figure 4.3 (c) and 4.3 (d), respectively, along with corresponding fitting superimposed on it. The corresponding back-transferred spectra along with fitting are shown in inset of Figure 4.3 (c) and 4.3 (d), respectively. The scattering contribution for atomic shells were derived considering the centrosymmetric space groups (P$m\bar{3}m$, I4/mcm and Pnam) and fitting resulted in R-factor $\sim$ 0.003 for $CH_3NH_3PbI_3$ and $\sim$ 0.005 for $CH_3NH_3PbBr_3$ throughout the measured temperature range. For $CH_3NH_3PbI_3$, fits were confined to the k range of 3 < k < 13 Å^{-1} and R range of 1.5 < R < 5 Å, and for $CH_3NH_3PbBr_3$ k range was set to 3 < k < 9 Å^{-1} and R range as 1.2 < R < 4.5 Å, respectively. In this region, Pb-L$_3$ edge is contributed by three halide (I/Br) subshell with four axial halide (I1/Br1) atoms and two equatorial halide (I2/Br2) atoms. Best fit and significant result is obtained by considering equatorial atoms into two subshells with one atoms each, which is consistent with previous reports [195,196]. During fitting procedure, co-ordination number was fixed, while bond-length and mean square relative displacement (MSRD) or Debye waller factor [σ^2 = <(r - <r>)^2>] were used as free variables. It is seen that Debye waller factor [σ^2 = <(r - <r>)^2>] for short (I2′/ Br2′) and long (I2″/ Br2″) (Figure 4.4 (e) and (f)) Lead-Halide equatorial bonds are highly correlated, therefore we choose single σ^2 for them and different one for Lead-Halide axial bonds.

Temperature dependence of σ^2 for all the shells were fitted with Einstein model which consider the bond vibrations as harmonic oscillations with a single effective frequency proportional to Einstein temperature, θ_E, as given by the following relation [205]:

$$\sigma^2(T) = \sigma_0^2(T) + \left(\frac{\hbar^2}{2\mu k_B \theta_E}\right) coth\left(\frac{\theta_E}{2T}\right) \tag{4.2}$$

where σ_0^2 is the static contribution, μ is the bond-pair reduced mass and T is the temperature in Kelvin. Relative stiffness of the bond-pair is characterized by the Einstein temperature θ_E. Fitting of temperature dependence of σ^2 using Einstein model for Lead-Halide bond correlation of $CH_3NH_3PbI_3$ and $CH_3NH_3PbBr_3$ are shown in Figure 4.4 (a) and 4.4 (b), respectively. Fitting yields $\sigma^2 \sim 0.0021$ (~ 0.0056) and $\theta_E \sim 186$ K ($\sim$ 128 K) for Lead-axial Halide bonds and $\sigma^2 \sim 0.0013$ (~ 0.0034) and $\theta_E \sim 539$

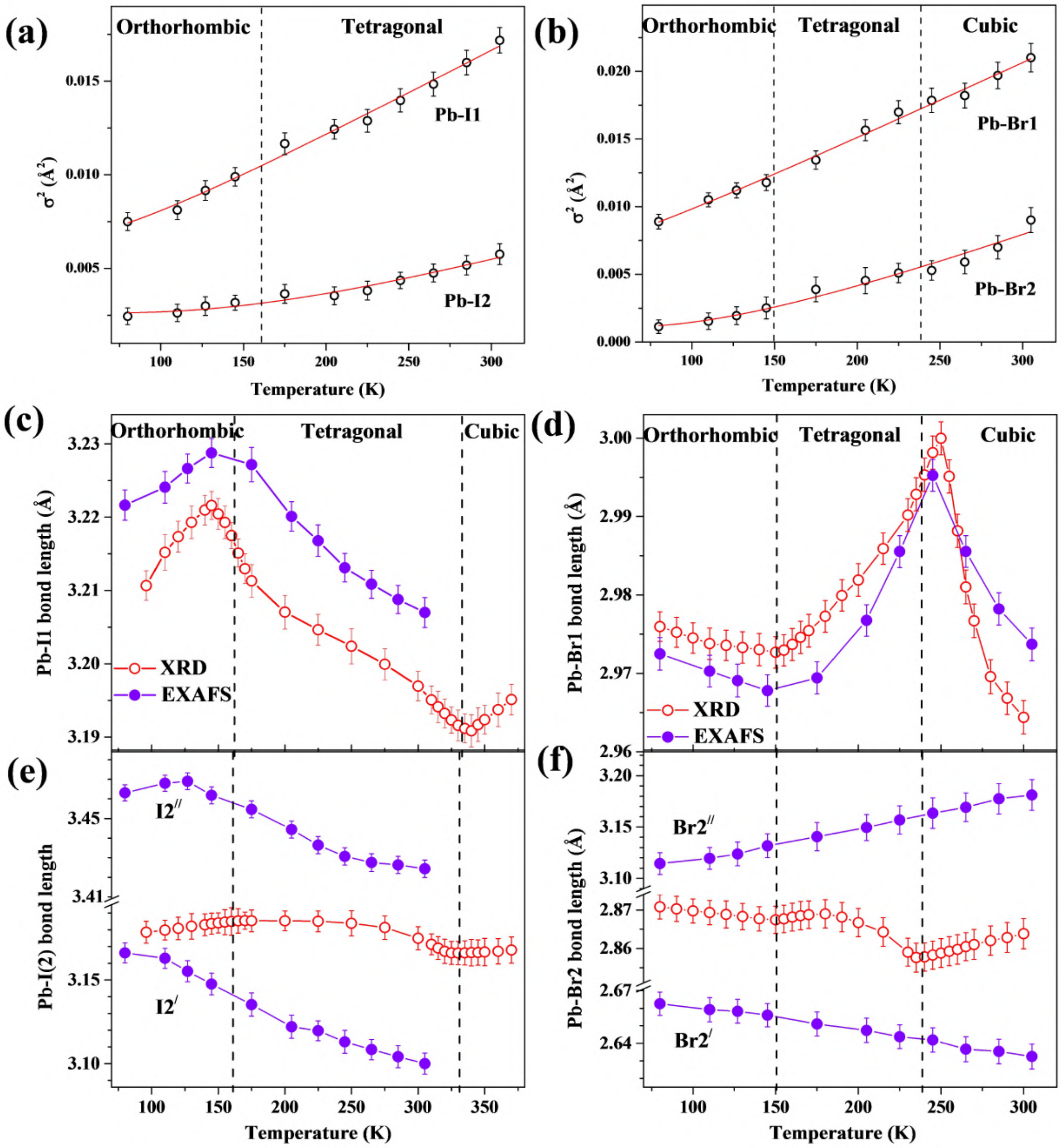

Figure 4.4: Thermal variations of average (a,c) Lead-axial Halide (X1) and (b,d) Lead-equatorial Halide (X2) bond lengths of (a,b) $CH_3NH_3PbI_3$ and (c,d) $CH_3NH_3PbBr_3$ samples obtained from both EXAFS (solid circle) and XRD (open circle) analysis. Temperature dependence of variation of Debye waller factor (σ^2) of different Pb-X correlations of (e) $CH_3NH_3PbI_3$ and (f) $CH_3NH_3PbBr_3$. The solid lines represent the fitting using Einstein model (Equation 4.1). Vertical dashed line corresponds to the structural phase transitions as marked in the figure.

K ($\sim$ 375 K) for Lead-equatorial Halide bonds of $CH_3NH_3PbI_3$ ($CH_3NH_3PbBr_3$). The large value of θ_E indicates the rigidness of PbX_6 octahedra. The relatively low values of θ_E of Pb-I1/Br1 subshells compared to Pb-I2/Br2 suggest that the Lead-axial Halide bonds are weaker than Lead-equatorial Halide bonds. Furthermore, there is deviation of σ^2 from the expected behavior in the region near to the crystallographic phase transition temperatures, suggesting the presence of structural anomalies.

For further understanding, we extracted various bond lengths from EXAFS fitting and Rietveld refinement of XRD pattern. The thermal variation of Lead-axial Halide (Pb-I1 and Pb-Br1) bonds obtained from EXAFS and XRD analysis are shown in Figure 4.4 (c) and 4.4 (d), respectively. Pb-Br1 bonds obtained from EXAFS analysis match reasonably well with that extracted from the Rietveld refinement of XRD, whereas, Pb-I1 bond obtained from EXAFS fitting is longer by $\sim$ 0.01 Å, than that determined from XRD. Discrepancies between EXAFS and XRD result may arise from either physical or fictitious effects. The systematic errors in the EXAFS data analysis may originate from the correlation between distances and energy scale parameters. Further, discrepancies can be possible due to the differences between local and long-range structure as reported in the literature. Both Pb-I1 and Pb-Br1 bonds exhibit anomalous behavior around the crystallographic phase transition as shown in Figure 4.4 (c) and (d). Further, the temperature dependent variation of short (I2′/ Br2′) and long (I2″/ Br2″) Lead-Halide equatorial bond length obtained from EXAFS and that of average Lead-Halide equatorial bond length obtained from XRD are shown is Figure 4.4 (e) and (f). As Einstein temperature (θ_E) of this Lead-equatorial Halide bonds are greater than that of Lead-axial Halide bonds, bonds are rigid and has less variation, though some anomaly appears at the transition temperatures. We believe that such anomalous behavior in both Lead-axial Halide and Lead-equatorial Halide bonds of $CH_3NH_3PbI_3$ and $CH_3NH_3PbBr_3$ arise due to orientation of CH_3NH_3 molecule which result into PbX_6 octahedral distortion.

To test our hypothesis, we performed temperature dependent XRD and EXAFS measurements on $CsPbBr_3$ sample where orientationally active CH_3NH_3 ion (dipole) is replaced by the monopolar Cs^+ ion with no dipole on it. Therefore, a comparison of the behavior of Lead-Halide bond lengths of $CH_3NH_3PbBr_3$ and $CsPbBr_3$ is expected

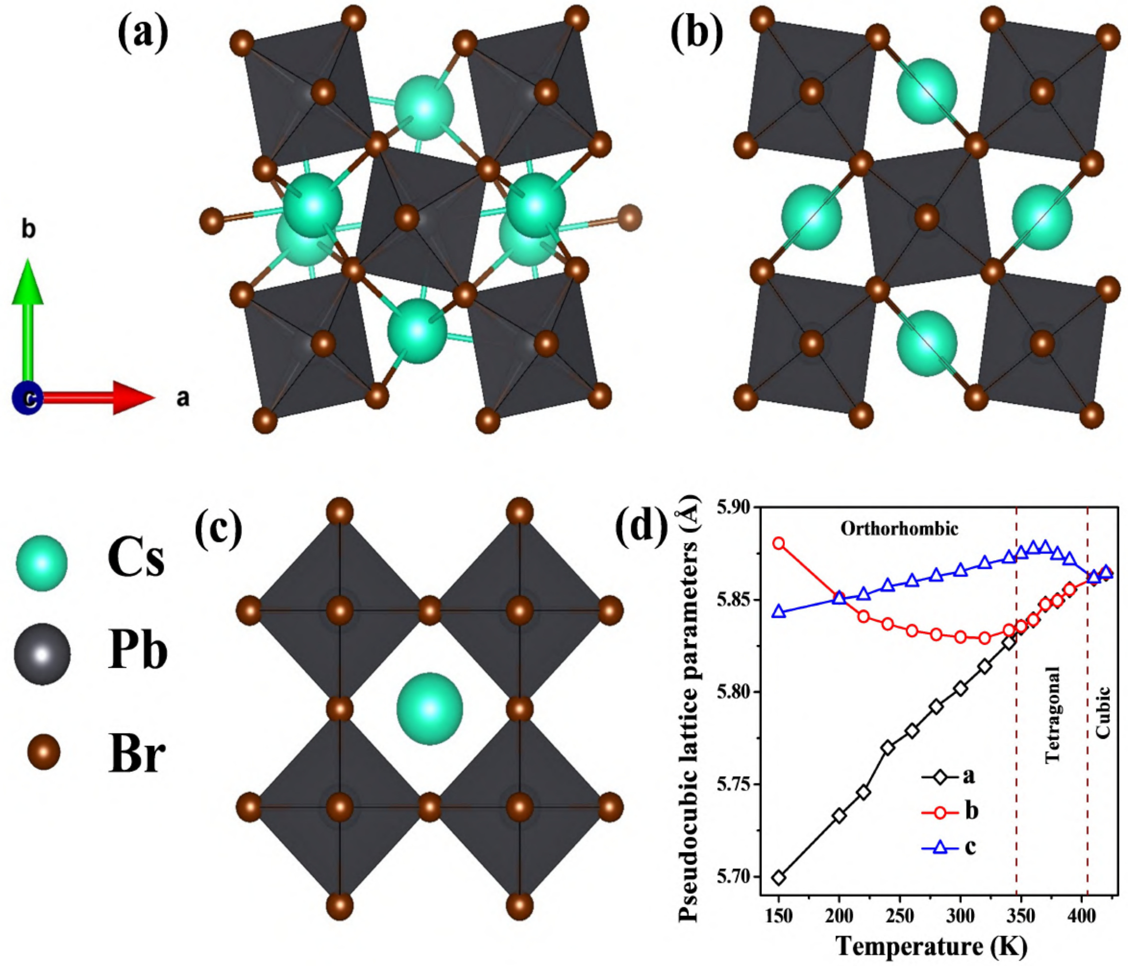

Figure 4.5: Crystal structure of $CsPbBr_3$ in (a) Orthorhombic phase, (b) Tetragonal phase and (c) Cubic phase obtained from single crystal X-ray diffraction. (d) Variation of pseudocubic lattice parameter of $CsPbBr_3$ with temperature.

to make a statement about the orientation of CH_3NH_3 dipoles and its effect. Temperature dependent single crystal XRD of $CsPbBr_3$ were recorded between 150 K and 425 K and representative crystal structure and crystallographic parameters obtained from single crystal XRD refinement at three different temperatures, *viz.* 150 K, 360 K and 425 K are presented in Figure 4.5 (a-c) and Table 4.3. The refined parameters confirm the existence of orthorhombic, tetragonal and cubic phases at 150 K, 360 K and 425 K, respectively, thereby confirming the temperature dependent crystallographic phase transition in the system. $CsPbBr_3$ crystallizes in cubic $Pm\bar{3}m$ space group with a lattice parameter of 5.8844 Å, at 425 K. As the temperature is lowered below 405 K, tetragonal

Table 4.3: Crystallographic parameters of $CsPbBr_3$ samples obtained from single crystal XRD refinement at three different temperatures, T= 150 K , 360 K and 425 K.

Crystal system	Orthorhombic	Tetragonal	Cubic
Temperature (K)	150	360	425
Color	Orange	Orange	Orange
Crystal form	Cuboid	Cuboid	Cuboid
Crystal size (mm)	0.12 × 0.1 × 0.04	0.12 × 0.1 × 0.04	0.12 × 0.1 × 0.04
Formula weight	579.83	579.83	579.83
Radiation	MoK_α	MoK_α	MoK_α
Wavelength (Å)	0.7107	0.7107	0.7107
Space group	$Pbnm$	$I4/mcm$	$Pm\bar{3}m$
Unit cell dimensions			
a (Å)	8.0601(1)	8.2577(6)	5.8844(4)
b (Å)	8.3163(1)	8.2577(6)	5.8844(4)
c (Å)	11.686(2)	11.7548(7)	5.8844(4)
$\alpha = \beta = \gamma$	90°	90°	90°
Volume ($Å^3$)	783.3(3)	400.78(8)	203.75(4)
Z	4	2	1
Atom Coordinates			
Pb1	(0.5, 0.5, 0)	(0, 0, 0)	(0, 0, 0)
Br1	(0.437, 0.506, 0.25)	(0, 0, 0.5)	(0, 0, 0)
Br2	(0.802, 0.701, 0.033)	(0.285, 0.215, 0)	
Cs1	(0.984, 0.443, 0.25)	(0, 0.5, 0.5)	(0.5, 0.5, 0.5)
θ range (^{0})	3.487, 30.116	3.466, 30.317	3.462, 29.381
Measured Reflns.	2257	1106	235
Unique Reflns.	1067	331	78
No. of parameters	28	12	5
$R[F^2 > 2\sigma^2(F^2)]$, $wR_2(F^2)$	0.0880, 0.2317	0.0700, 0.1834	0.0581, 0.1371
GooF (S)	1.073	1.143	1.149

phase with space group I4/*mcm* is realized and lattice parameters at 360 K are, a = b = 8.2577 Å and c = 11.7548 Å, (a = $\sqrt{2}$ a$_{cubic}$). Further, when the temperature is below 360 K, $CsPbBr_3$ crystallizes in orthorhombic phase (P*bnm*) and lattice parameter at 150 K are a = 8.0601 Å, b = 8.3163 Å and c = 11.686 Å which are consistent with literature reports [206,207]. Temperature dependent crystallographic phase transitions of $CsPbBr_3$ are caused by successive condensation of zone boundary phonon modes related to rotational motions of $PbBr_6$ octahedra [206]. As a result of it, physical character of chemical bond, such as bond length, bond angle in different motion mode changes with temperature. Refined unit cell parameters ('a', 'b' and 'c') of $CsPbBr_3$ in orthorhombic, tetragonal and cubic phase are presented in Figure 4.5 (d). Negative coefficient of thermal expansion was observed for 'b' ('c') and positive coefficient for both 'a' and 'c' ('a' and 'b') in orthorhombic (tetragonal) phase, whereas thermal expansion of all parameters are positive in cubic phase, as shown in Figure 4.5 (d).

Figure 4.6 (a) shows the X-ray absorption spectra of $CsPbBr_3$ samples from the Pb L3 (13.035 keV) edge and corresponding pre-edge, X-ray Absorption Near-edge Structure (XANES) and EXAFS region are marked in the figure. The magnitude of Fourier transform of k^3-weighted EXAFS data ($|\chi(R)|$) and back-transformed spectra in k space at Pb-L3 edge acquired at 80 K and 305 K for $CsPbBr_3$ are depicted in Figure 4.6 (b) and inset of Figure 4.6 (b), respectively, along with corresponding fitting superimposed on it. The scattering contributions were derived considering P*bnm* crystal structure and the EXAFS data fit well throughout the entire (measured) temperature range with R-factor of ~ 0.008. Fits were confined to the k range of $3 < k < 9$ Å^{-1} and R range of 1 < R < 5 Å. From fitting it was found that the Bromide shell is originated from two subshell with four and two atoms from axial and equatorial positions as shown in Figure 4.2 (g), whereas a single Cs shell is considered with two atoms. Two σ^2 parameters were used; one for both Lead-axial Bromide and Lead-equatorial Bromide bonds and other for Pb-Cs bond and the thermal variation of Pb-Br bond is fitted using Eq. 4.2 and presented in Figure 4.6 (d). From the fitting, it is found $\sigma_0^2 \sim 0.0058$ and $\theta_E \sim 270$ K for Pb-Br1/Br2 bond distribution. Relatively low values of θ_E for $CsPbBr_3$ Lead-equatorial Bromide bond compared to $CH_3NH_3PbBr_3$ indicate that $PbBr_6$ octahedra of $CsPbBr_3$ are not rigid enough

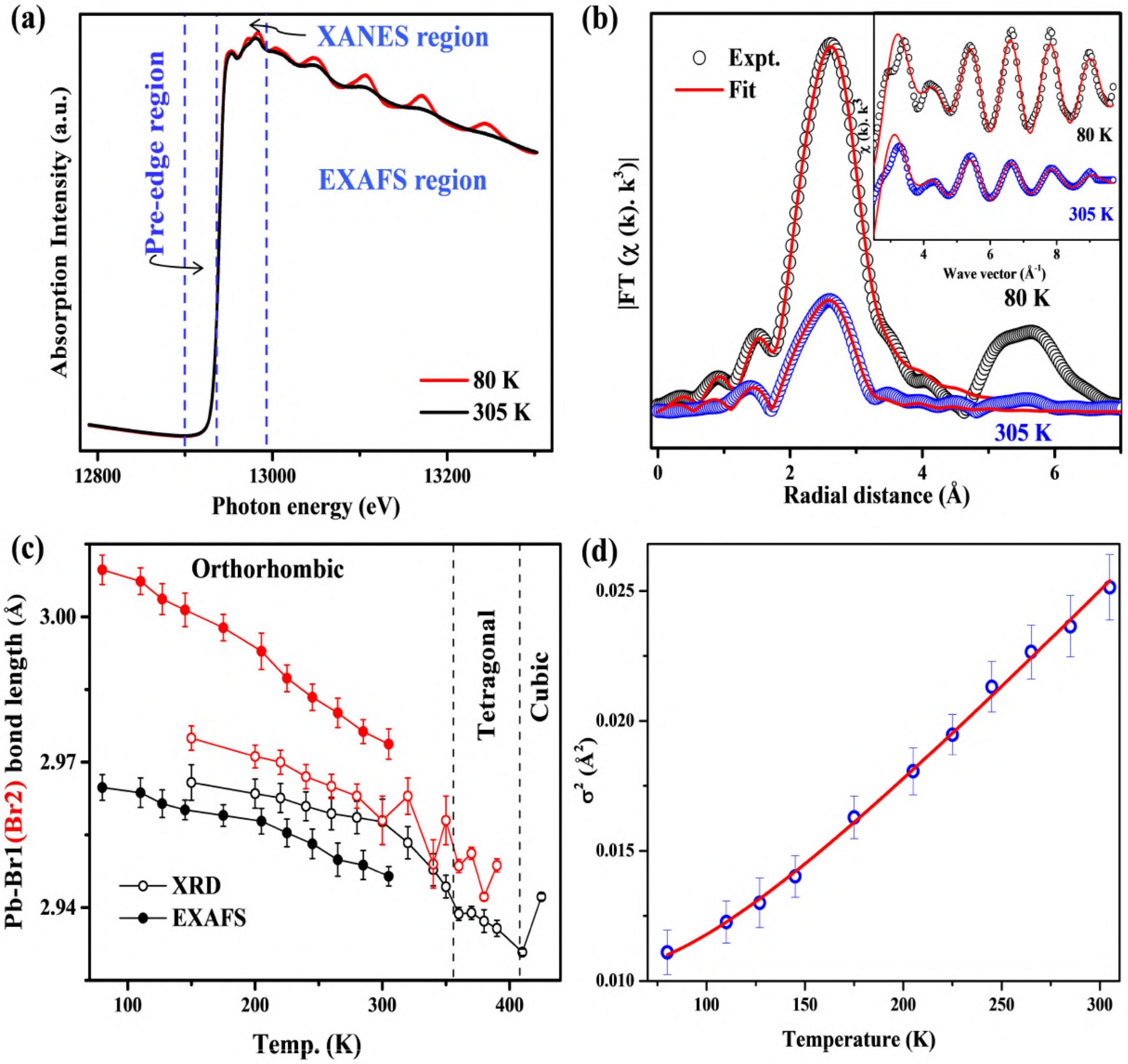

Figure 4.6: (a) XAFS spectrum showing the pre-edge, XANES and EXAFS regions of $CsPbBr_3$. (b) Magnitude of Fourier transforms of k^3-weighted EXAFS data at Pb-L_3 edge acquired at 80 K (black open circle) and 305 K (blue open circle) for $CsPbBr_3$, along with corresponding fitting superimposed on it (red solid line). Corresponding back-transformed spectra in k-space (open circles) along with fitting are plotted in inset. (c) Thermal variations of average Pb-Br1 (axial) and Pb-Br2 (equatorial)bond lengths of $CsPbBr_3$ obtained from both EXAFS (solid circle) and XRD (open circle) analysis. Vertical dashed line corresponds to the structural phase transitions as marked in the figure. Temperature dependence of variation of Debye waller factor (σ^2) of different Pb-Br (axial and equatorial) correlations of $CsPbBr_3$. The solid lines represent the fitting using Einstein model (Equation 4.2).

like $PbBr_6$ octahedra of $CH_3NH_3PbBr_3$. Further, various bond lengths were extracted from EXAFS fitting and Rietveld refinement of XRD pattern. The thermal variation of

Lead-axial Bromide (Pb-Br1) bonds obtained from EXAFS and XRD analysis are shown in Figure 4.6 (c). Pb-Br1 bonds obtained from EXAFS analysis match reasonably well with that extracted from the Rietveld refinement of XRD, whereas, Pb-Br2 bond obtained from EXAFS fitting is shorter by $\sim$ 0.03 Å, than that determined from XRD. Both the bonds contracts with the increase of temperature and no significant anomaly is observed around phase transitions, indicating octahedral distortion is absent here.

The above studies indicate the distortion in the structure is associated with the Halide displacement due to CH_3NH_3 orientation inside the PbX_6, which is absent for the case of symmetric $CsPbBr_3$ system. The distortion is dominated at the axial Halide bonds than equatorial ones.

4.4 Conclusion

Rietveld refinement of high resolution temperature dependent synchrotron X-ray diffraction data clearly demonstrate that the preferred symmetry of $CH_3NH_3PbX_3$ (X= I, Br, Cl) is found to be centrosymmetric in all three phases, *viz.*, orthorhombic, tetragonal and cubic phases, and contradicts some previous observations of noncentrosymmetric space group. Above-mentioned structural phase transitions were also captured by heat capacity measurements. Variation of lattice parameters, tetragonal distortion and linear expansion coefficients clearly indicate that it is a first order phase transition and rule out the possibility of phase coexistence in this system. Further, detailed EXAFS and XRD studies corroborate the distortion in the structure is associated with the Halide displacement due to CH_3NH_3 orientation inside the PbX_6, which is absent for the case of symmetric $CsPbBr_3$ system. We believe that our temperature dependent structural studies of hybrid perovskites will provide significant insight to design more stable and efficient solar cell and optoelectronic devices, as these devices will be exposed to significant temperature changes.

Chapter 5

Spectroscopic Investigations of Hybrid Perovskites

This chapter is divided into two parts. In the first part, a detailed evaluation of optical spectroscopy (UV-Visible absorption, photoluminescence and Raman) of hybrid perovskite of the type $APbX_3$ *("A" =* CH_3NH_3*,* $CH(NH_2)_2$ *and Cs; "X" = I, Br and Cl) were carried out and various parameters like exciton binding energy, exciton-phonon interaction and electron-phonon coupling constant were determined. We believe that* CH_3NH_3 *orientation and* PbX_6 *octahedral distortion are responsible for dual emission and optical anisotropy of hybrid perovskite system. In the second part, detailed electronic structures of* $CH_3NH_3PbX_3$ *("X" = I, Br and Cl) are addressed using a combination of angle-integrated, angle-resolved photoemission spectroscopy and calculations using density functional theory (DFT), to extract information about the top of the valence band of this system.*

5.1 Band Gap Engineering and Dual Emission of Hybrid Perovskites

5.1.1 Introduction

Hybrid organic-inorganic halide perovskites of the type $APbX_3$ (where “A” = CH_3NH_3, $CH(NH_2)_2$, Cs; “X” = I, Br, Cl and mixtures of them) have generated a surge of attention to the researchers in the last five years due to their impressive performance in solar cell applications [10, 90] and optoelectronic devices [11, 12, 24]. Research activities in this field have mostly been focused on increasing the efficiency of the solar cells by engineering morphology [208], interfaces [209], solvents, *etc.* [88, 90, 210, 211] Nevertheless, higher efficiencies cannot be achieved without a deeper understanding of the fundamental properties of the absorber material, which is still evolving for this newly found class of material. However, in this work, we take a closer look at the optical properties of organic-inorganic hybrid perovskites.

Recently, it was observed that intrinsic nature of the optoelectronic properties of polycrystalline thin films are overshadowed by the micro- and/or nanostructure quality and non-crystalline domains. On the contrary, absence of grain boundaries and non-crystalline domains in single crystals makes them an ideal platform for studying the intrinsic material and optical properties of organic-inorganic hybrid perovskite, and therefore help to improve the power conversion efficiency of perovskite solar cells [212–214]. Thus, low-temperature understanding of photophysical properties of hybrid perovskite single crystals are essential as the additional thermal complexity is minimized.

Inspite of several spectroscopic investigations performed at low temperatures, there have been a lot of ambiguities in the data as well as its interpretations, especially observation of multiple peaks in the photoluminescence (PL) spectrum of organic-inorganic hybrid perovskites. For *eg.*, Xing *et al.* [56] observed three emission peaks for $CH_3NH_3PbI_3$ at low temperatures which they assigned to bound (815 and 782 nm) and free (746 nm) exciton emission, whereas Kong *et al.* [215] attributed them to a donor-acceptor pair (782 nm) and free-exciton transitions. Similarly, Fang *et al.* [216] ascribed the two peaks; low and high-energy emission peaks at low temperature, to free and bound excitons, respectively. Panzer *et al.* [217] and Wehrenfennig *et al.* [57] concluded the presence of tetragonal inclusions in the orthorhombic phase at low temperature are responsible for dual transitions. Many of these hypotheses have not been confirmed theoretically and are insufficient to explain the complete phenomenology behind the origin of dual/multiple emissions in hybrid perovskites. Almost in all temperature dependent PL reports it was observed that one or two new emission peak arises other than the band edge transition in orthorhombic phase, however, only band edge transition exist in tetragonal and cubic phase for thin films of organic-inorganic hybrid perovskites [56, 57, 163, 164, 215–217].

In this work, the temperature dependence of the bandgap was explored in $APbX_3$ (“A” = CH_3NH_3, $CH(NH_2)_2$ and Cs; “X” = I, Br, Cl) using UV-Vis absorption and steady-state photoluminescence (PL) spectroscopy. Optical spectroscopic measurement of hybrid perovskite revels that the bandgap can be tuned from blue to red region of visible spectra by changing the halide composition from Cl to Br to I and the corresponding bandgap at room temperature are 405 nm, 532 nm and 785 nm, respectively. The observed bandgap changes upon halide substitution are influenced by the electronic states of the anion. Further, it was claimed that, the “A” site substitution doesnot directly contribute to the frontier electronic structure, but it has some indirect influences like lattice contraction, structural distortion and physical or chemical strain *etc.* [218–221] Further, the temperature dependent steady state PL studies of above samples help us to estimate the exciton binding energy as well as the exciton-phonon interaction and optical phonon energy.

Above studies (both absorption and PL) revealed the presence of a well-defined second peak throughout the temperature region for $CH_3NH_3PbBr_3$ and $CH(NH_2)_2PbBr_3$, whereas $CsPbBr_3$ exhibited a single emission peak indicating the role of organic cation (*i.e.* “A” site) in the origin of second peak. Detailed density functional theory (DFT) calculations and classical molecular dynamics (MD) simulations were carried out to identify the molecular origin of the experimental observation. Recently, it was realized that hydrogen bonding between an organic “A”-cation and the halide frame plays a significant role in stabilizing octahedral tilts of the halide frame [222]. Hydrogen attached to nitrogen (H-N) can come closer to Br atom due to CH_3NH_3 (MA) orientation inside the octahedra and octahedral distortion occurs [47]. Thus, to understand the favorable orientations of MA inside the octahedral cage, it was allowed to rotate in the ac plane and 12 and 28-degree rotations were found to be favorable ones for which energy minimization occurs with separation of 6 meV. While calculating electronic structure using these two energy minima, conduction band minima (CBM) coincides with each other and a small shift of 13.7 meV was observed in valence band maxima (VBM). We believe that this separation in VBM is responsible for dual emission in organic-inorganic lead halide perovskites. We also performed face dependent PL measurements on single crystal samples of $CH_3NH_3PbBr_3$. The anisotropic optical (PL) property of the crystal is depicted by comparing the steady state and time-resolve PL results on (101), (010) and $(10\bar{1})$ planes of $CH_3NH_3PbBr_3$ at 77 K.

5.1.2 Experimental details

5.1.2.1 Sample synthesis

Single crystal Samples of $CH_3NH_3PbI_3$, $CH_3NH_3PbBr_3$, $CH_3NH_3PbCl_3$, $CH(NH_2)_2PbBr_3$ and $CsPbBr_3$ were synthesized by the antisolvent vapor assisted crystallization (AVC) method as reported elsewhere [41, 58, 103, 104]. Rectangular shaped, defect free, smooth surfaced, high-quality single crystals of $CH_3NH_3PbI_3$, $CH_3NH_3PbBr_3$, $CH_3NH_3PbCl_3$ were obtained at room temperature using this method (as reported in section-3.1.2.1 and 4.2.1). Synthesis involves the addition of antisolvent (a liquid miscible with the precursor solvent) to reduce the solubility of the solute in order to achieve supersaturation. Further, 3.67 gm lead(II) bromide ($PbBr_2$) and 1.25 gm formamidinium bromide ($CH(NH_2)_2Br$) (1M) were used for the synthesis of $CH(NH_2)_2PbBr_3$. With the slow diffusion of ethyl acetate into the solution, high quality, crack-free, millimeter-sized single crystals were grown within 2-4 days. For the synthesis of $CsPbBr_3$ single crystals, 3.67 gm (1 M) $PbBr_2$ and 3.19 gm (1.5 M) CsBr were dissolved in 10 ml dimethyl sulfoxide (DMSO) and kept in methyl alcohol (MeOH) environment to form pure $CsPbBr_3$ single crystals within 3-10 days [198].

5.1.2.2 Experimental techniques

The optical absorption spectra were measured using an ultraviolet-visible-near-infrared (UV-Vis-NIR) spectrophotometer (Shimadzu, 3101PC) in the wavelength range of 400-800 nm and temperature dependent photoluminescence measurements were carried out using FL920 spectrometer from Edinburg instruments (UK) equipped with a cryostat (Oxford, UK) and cooled by liquid nitrogen. Photoluminescence (PL) emission spectra were acquired with a monochromatic excitation energy of 325 nm (intensity $\sim$ 1.5 mW/cm^2). The crystal structure and electronic properties of the samples were also analyzed using Raman scattering studies using U1000 and T64000 micro-Raman spectrometers from Horiba at room temperature. A T64000 spectrometer was attached with Olympus microscope (focused to 5 μm size) and a charge coupled detector (CCD) with spectral resolution 0.8 cm^{-1}. The laser line of 488 nm from the Argon ion laser source, was used as excitation source for the measurements.

5.1.2.3 Computational Details

Electronic structure of the system was calculated using a projected augmented wave (PAW) [147, 148] implementation of density functional theory within Vienna ab-initio simulation package (VASP) [149–151]. Generalized gradient approximation (GGA) [223] was used for the exchange-correlation function. To predict the structural properties correctly, inclusion of nonlocal, weak van der Waals (vdW) interaction is necessary. A GGA+vdW density functional theory calculation has been found to give a reasonable estimation of the lattice parameters [224, 225]. Dispersive interactions are responsible for a significant contraction of the unit cell, correcting the overestimation in general done by GGA. Prediction of bandgap close to the experimental value is also possible due to error cancellation when the spin-orbit coupling (SOC) is not explicitly considered in the calculations [46]. DFT-D2 method of Grimme [226] was considered to introduce non-local, weak vdW interactions within the system and Monkhorst Pack k-mesh of $8 \times 6 \times 8$ was used to perform the k-space integrations. In addition to this, an energy cutoff of 400 eV was used for the kinetic energy of the plane waves included in the basis. The non-polar orthorhombic unit cell with space group symmetry Pnma was used [27, 227], both the lattice parameters and internal positions were optimized till the forces on the atoms were less than 103 eV/Å, to find the minimum energy structure [29]. The optimized lattice parameters were found to be 7.87, 11.69 and 8.46 Å; 1% smaller on average than the experimental values. The average Pb-Br bond lengths are reduced by 0.7% in the optimized structure compared to the experimental structure. Calculations were performed considering both the experimental lattice parameter values and optimized ones to see the effect of volume change as discussed in detail.

5.1.3 Results and Discussion

5.1.3.1 UV-Visible Absorption Studies of $CH_3NH_3PbBr_3$

Optical properties of Organic-inorganic hybrid perovskite were investigated using absorption and steady-state photoluminescence studies. Figure 5.1 (a) shows room temperature optical absorption spectrum for a pellet made by crushing single crystals of $CH_3NH_3PbBr_3$. Here the absorption spectra of $CH_3NH_3PbBr_3$ sample consist of three broad features; (i) a subband gap very weak absorption at low energy (800 nm to 600 nm), (ii) a strong and sharp peak at 554.5 nm and (iii) band edge transition starts from 506 nm. Steeper band edge suggest that it is ordered in nature and is a direct band gap semiconductor. Contrasting observations regarding the optical absorption spectra of this system exists in literature which include single band edge transition at 515 nm and 565 nm for thin film [228] and single crystal [99] of $CH_3NH_3PbBr_3$, respectively, whereas, absorption coefficient calculated from ellipsometry measurement on single crystal of $CH_3NH_3PbBr_3$ revealed one sharp peak at 514 nm and continuous band edge transition from 486 nm [95]. However, temperature dependent PL spectra of $CH_3NH_3PbBr_3$ thin film (Figure 5.1 (b)) shows a single emission at 536 nm (77 K) which is blue shifted to 526 nm (300 K). Hence for a better understanding, temperature-dependent photoluminescence (PL) spectroscopy investigations were performed on the same sample and results are shown in Figure 5.1 (c).

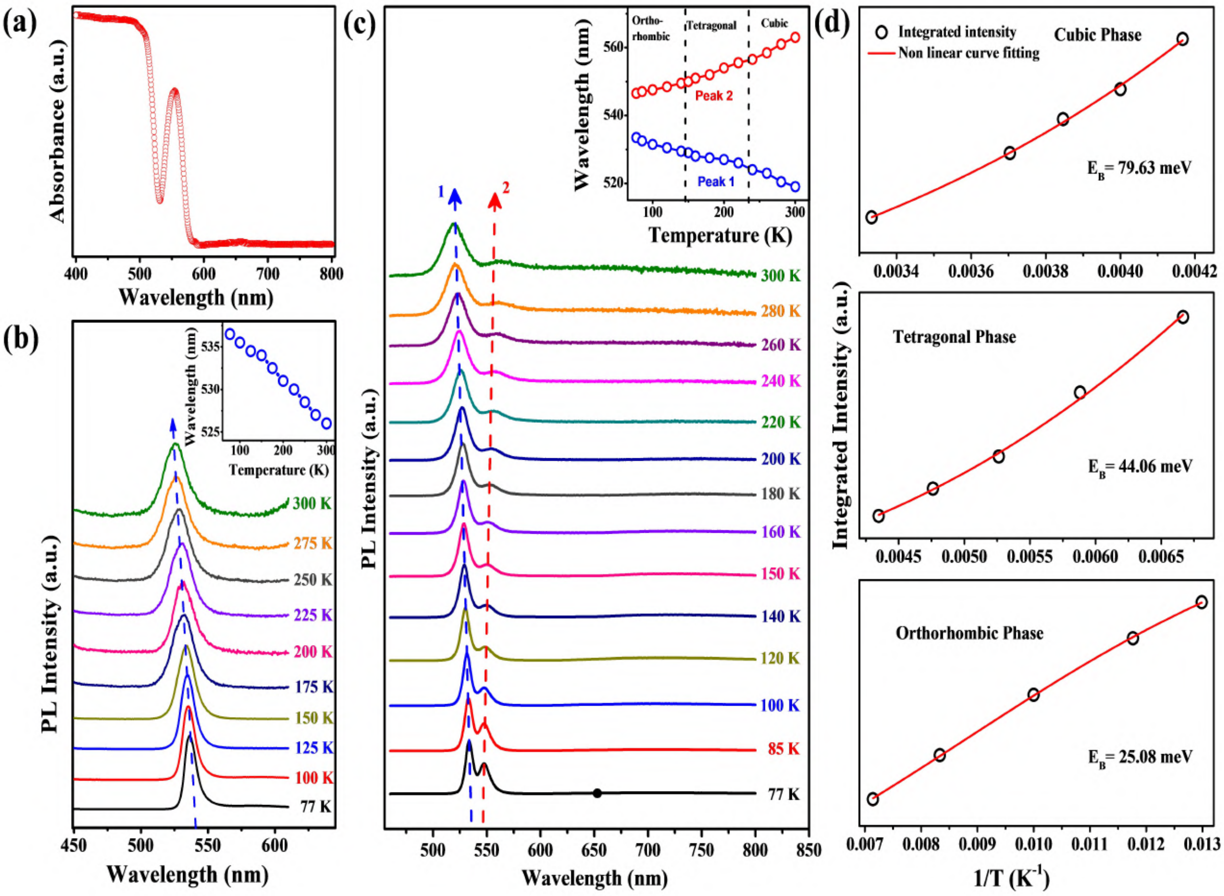

Figure 5.1: (a) Absorption spectra of $CH_3NH_3PbBr_3$ at room temperature. Temperature-dependent photoluminescence (PL) spectra of (b) $CH_3NH_3PbBr_3$ thin film on FTO substrate, (c) $CH_3NH_3PbBr_3$ single crystals. Dotted lines and arrows are guide to the eye highlighting the blue and red shift of the PL peak with temperature. The inset shows the variations of peak positions of each samples as a function of temperature. (d) Temperature dependent data of integrated intensity in cubic, tetragonal and orthorhombic phase of $CH_3NH_3PbBr_3$. Solid red lines are fitted as explained in the text.

5.1.3.2 Temperature-dependent photoluminescence (PL) Studies of $CH_3NH_3PbBr_3$

Temperature dependent photoluminescence (PL) measurements of $CH_3NH_3PbBr_3$ were carried out between 77 K and 300 K and the data are summarized in Figure 5.1 (c). Intensities of all the spectra are normalized to clarify the shift of emission peaks and spectra are shift vertically for help of view. There is a continuous evolution of the PL peak position, its full width at half-maxima (FWHM) and intensity with temperature. However, noticeable discontinuities exist across the crystallographic phase transition temperatures, as shown in the inset of Figure 5.1 (c), where the rate of change of peak position with temperature is found to be different in three crystallographic regions. Temperature dependent PL spectra displayed dual emission peaks for $CH_3NH_3PbBr_3$ throughout the temperature region and is consistent with the UV-Visible absorption results (Figure 5.1 (a)). At 77 K; two sharp PL emission peaks were observed when the sample was excited using 325 nm wavelength from a xenon lamp. The main PL emission (peak-1) was observed at 533.5 nm (2.324 eV; FWHM = 35.55 meV) followed by another emission peak (peak-2) at 547.5 nm (2.26 eV; FWHM = 56.14 meV). Here peak-1 is attributed to the band to band recombination/bandgap as reported using absorption studies [95, 99, 228], which is blue shifted with increasing temperature. At 300 K, emission peak-1 was observed at 519.5 nm (2.387 eV; FWHM = 110.74 meV), as shown in the inset of Figure 5.1 (c) [229].

This blue shifting behavior of peak-1 is inconsistent with most of the semiconducting materials, such as Si [179], GaAs [181], GaN [230], *etc.* However, blue shifting behavior of peak-1 can be explained by Varshni model where temperature coefficient of band gap (dE_g/dT) can be expressed as [176, 182, 231]:-

$$\left(\frac{dE_g}{dT}\right)_p = \left(\frac{dE_g}{dT}\right)_v + \left(\frac{dE_g}{dln(v)}\right)_T \left(\frac{dln(v)}{dT}\right)_p \tag{5.1}$$

Here the first term represents electron-phonon coupling through the deformation coupling, which represents a decrease in band gap with an increase of temperature and the second term is the lattice dilation term which causes the increase in band gap with temperature. For better understanding of blue shifting behavior of peak-1, we have taken $CH_3NH_3PbBr_3$ as a reference and revisited the temperature dependent x-ray diffraction as discussed in chapter-4. From figure 5.1 (c), estimated values of $\left(\frac{dE_g}{dT}\right)_v$ is $(3.24 \pm 0.21) \times 10^{-4}$ eV/K for orthorhombic, $(2.01 \pm 0.34) \times 10^{-4}$ eV/K for tetragonal and $(1.12 \pm 0.27) \times 10^{-4}$ eV/K for cubic phases and estimated values of volume expansion coefficient $\left(\frac{dln(v)}{dT}\right)_p$ for orthorhombic, tetragonal and cubic phases from temperature dependent XRD are $(7.925 \pm 0.312) \times 10^{-5}$ K^{-1}, $(9.532 \pm 0.241) \times 10^{-5}$ K^{-1} and $(1.125 \pm 0.137) \times 10^{-4}$ K^{-1}, respectively. Further, theoretical calculations predict a value of 2.16 eV for $\left(\frac{dE_g}{dln(v)}\right)_T$ in the cubic phase and a little higher value for the orthorhombic phase [232]. Thus it can be concluded that the second term i.e., lattice dilation term, dominates the temperature dependence of peak-1 which is responsible for blue shifting behavior.

5.1.3.3 Origin of Dual Emission of $CH_3NH_3PbBr_3$

Figure 5.1 (c) clearly indicate that a sub bandgap PL emission peak (Peak-2) exist for $CH_3NH_3PbBr_3$ samples, irrespective of bandedge transitions (peak-1), and is red-shifted with increasing temperature as shown in the inset. An earlier report on the PL emission spectra recorded on powder sample of $CH_3NH_3PbBr_3$ has shown two peak structure similar to our observations [163, 164], whereas, only peak-1 was observed for thin films of $CH_3NH_3PbBr_3$ [233] (consistent with our PL emission spectra recorded on thin film (Figure 5.1(b))) and peak-2 evolved as lasing fluence increases above the threshold value even at room temperature [163, 164]. Nanowires [234], microwires [235] and thin films [56, 217] of both iodide and bromide halide perovskites also showed such stimulated lasing behavior where the intensity of the second peak increases with laser fluences. However, peak positions were not reproducible in high fluence excitation [217] and no claims were put forward regarding the coherency of the emitted light, one of the primary requirements for lasing action. Hence the stimulated/lasing behavior could not be conclusively stated as the origin of second peak.

Further, it was observed that PL emission revealed single peak in tetragonal phase and two peaks in orthorhombic phase when temperature dependent photoluminescence was performed on thin films of $CH_3NH_3PbI_3$ [215, 217]. Similar behavior was observed by Wehrenfennig *et al.* [57] for $CH_3NH_3PbI_{3-x}Br_x$ thin film and Ibrahim Dar *et al.* [164] for thin films of $CH_3NH_3PbI_3$ and $CH_3NH_3PbBr_3$ and predicted that inclusion of tetragonal phase in the orthorhombic phase was responsible for dual emission. However, our heat capacity and temperature dependent high-resolution synchrotron XRD do not show any signatures of phase inclusion and this hypothesis has not been confirmed theoretically as well. Above studies hence reflect the state of confusion regarding the origin of the second photoexcited states.

Recently, Niesner *et al.* [58] have observed single and two-photon absorption from $CH_3NH_3PbBr_3$ single crystal after cleaving in ultrahigh vacuum, with the extracted spectra revealing a prominent direct transition at 536 nm, as well as an additional transition at 551 nm and 558 nm in the orthorhombic and tetragonal phase, respectively, with each peak accompanied by excitonic emission. To address this occurance of dual emission in closer details, exciton binding energy was extracted from the temperature dependence of the integrated intensity of peak 1 in three different phases (as plotted in Figure 5.1 (d)) using equation 5.2.

$$I(t) = \frac{I_0}{1 + exp\big(- \frac{E_B}{K_B T}\big)} \tag{5.2}$$

where I_0 is the intensity at 0 K, E_B is the binding energy, and k_B the Boltzmann constant. As expected, the PL intensity decreases with increasing temperature due to the competition of PL emission with non-radiative processes. Fitting yielded an exciton binding energy of 79.63 meV in cubic phase, which is closer to 71 meV, the binding energy value estimated from relativistic Bethe-Salpeter equation calculations (GW-BSE) [70]. With decreasing temperature, as the sample undergoes a structural phase transition at 237.1 K and 149.2 K to tetragonal and orthorhombic phases, respectively, exciton binding energies were found to be 44.06 meV and 25.08 meV, respectively. Extracted values of exciton binding energies are consistent with the literature reports [236, 237]. Above analysis suggests that excitonic peak (if different from the main peak) should appear in PL data around 79.63 meV, 44.06 meV and 25.08 meV below the main peak for cubic, tetragonal and orthorhombic phases, respectively. However, energy difference among 1st and 2nd peaks estimated from temperature-dependent PL measurements are 84-120 meV, 52-76 meV and 40-50 meV for cubic, tetragonal and orthorhombic phases, respectively. From basic physics of exciton [61–64], we know that excitonic levels should be within the the exciton binding energy, which rules out the possibility of excitonic levels as an origin of dual emission. Further, Stoke shift cannot be expected in peak-2 as excitonic levels are sharp transitions; whereas stoke shift of peak-2 (45 meV) is comparable to the band edge transition (60 meV) (peak-1) in this case. Hence, we might rule out the possibility of excitonic transitions for this case.

From the above discussions it is clear that band gap and optical properties of $CH_3NH_3PbX_3$ can be easily tuned in the entire visible range of the electromagnetic spectrum by anion exchange, however, the origin of dual/multiple emissions in hybrid perovskites can't be explained. Another way to tune the band gap and optical properties is to replace the

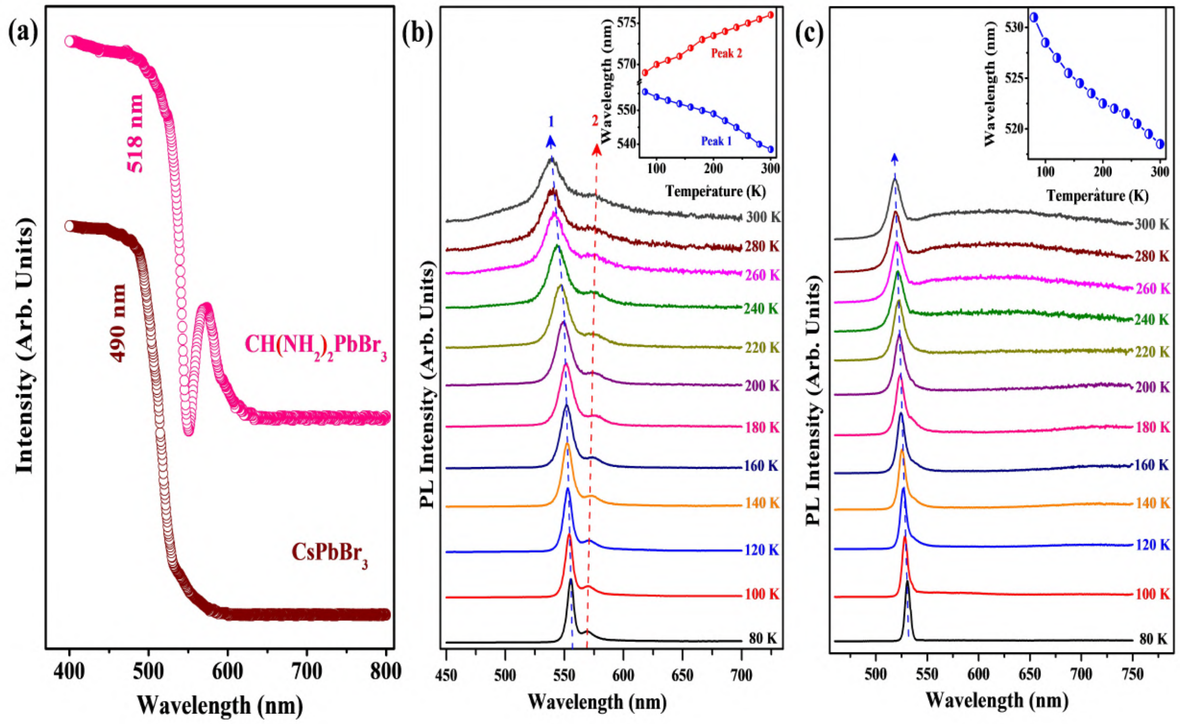

Figure 5.2: (a) Absorption spectra of $CH(NH_2)_2PbBr_3$ and $CsPbBr_3$ at room temperature. Temperature-dependent photoluminescence (PL) spectra of (b) $CH(NH_2)_2PbBr_3$ and (c) $CsPbBr_3$ single crystals. Dotted lines and arrows are guide to the eye highlighting the blue and red shift of the PL peak with temperature. The inset shows the variations of peak positions of each samples as a function of temperature.

organic cation present in the system [47, 221, 229]. For this purpose, methylammonium (MA; CH_3NH_3) was replaced by formadinium (FA; $CH(NH_2)_2$) (where two nitrogen were attached with carbon) and cesium (Cs) (where no organic groups were present) and a comparative study on optical properties of all three samples were carried out (figure 5.2 (a), (b) and (c)). Here we observed that dual emission peaks remain unaffected by changing ammonium group from methyl to formamidine in lead bromide based perovskites. However, the replacement of organic cation with inorganic cesium (Cs) cation in bromide-based perovskite surprisingly led to the disappearance of the distinct second emission peak, which implies that the origin of the dual emission is associated with the nature of the organic cation. As compared to $CH_3NH_3PbBr_3$ perovskite, $CH(NH_2)_2PbBr_3$ exhibits a narrower linewidth and lesser relative intensity of the second peak which also indicate that peak intensity and broadening are dependent on the organic cation. Further, all inorganic perovskite $CsPbBr_3$ experienced smaller linewidth than that of organic-inorganic hybrid perovskites, which confirmed organic cation played a crucial role in splitting the valence band which in turn is responsible for dual emission in organic cation based hybrid perovskites.

5.1.3.4 Theoretical Understanding

To show further insight into this issue electronic band structure calculations were performed by considering methylammonium orientation inside the inorganic octahedral (Figure 5.3 (a) and (b)). Results from $CH_3NH_3PbBr_3$ shows that there are no significant contributions from the molecule to states several electron volts below and above the Fermi energy (E_F) [35]. The valence band (VB) and conduction band (CB) are mainly contributed from Pb s; p and Br p states, as in the well-studied inorganic perovskites [238], where the cation at the "A" site of the perovskite plays an important role in determining the ensuing structure [46]. This scenario is similar to the context of the hybrid perovskites where the molecule has been found to drive the octahedral tilts. Our calculations have found that the orientation of the molecule in the inorganic cage formed by Pb and Br determines the tilt patterns, which was previously reported as a result of the dispersive interactions [46, 47]. As per recent report, replacing MA with an ion having the same ionic radii led to the vanishing of the octahedral tilts [222]. Hydrogen bonding with the anion was concluded to be responsible for the octahedral tilts in the low-temperature orthorhombic phase. Thus, the interaction between the organic molecule and inorganic cage plays an important role in determining the overall structure as well as electronic properties of the system.

Considering different orientations of the organic molecule (Figure 5.3 (a)) and relaxing the system gives rise to different octahedral distortions which are all local minima in a complex potential energy (PE) landscape. Such correlation leading to complex potential energy (PE) landscape was primarily studied for cubic systems in earlier works [46,47,239]. For each orientation of the molecule in an ideal high symmetry structure, relaxing only the molecule shows its movement along that direction of orientation to have shorter H_N-Br bond lengths. Favored orientation is determined by maximizing hydrogen bonding.

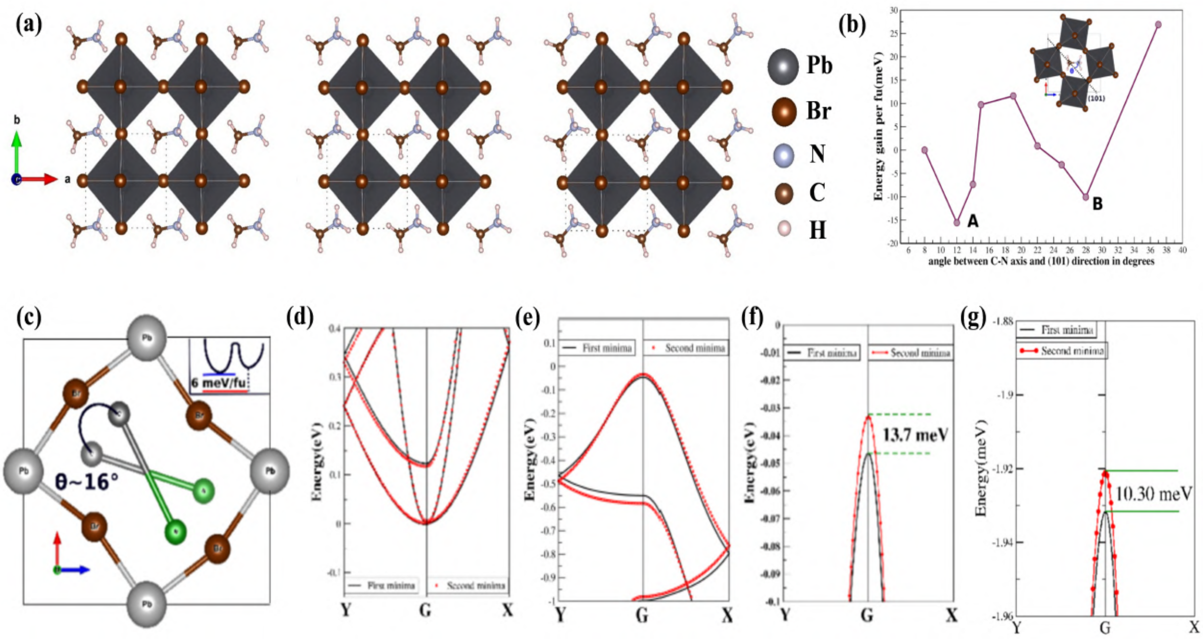

Figure 5.3: (a) Different orientations of the organic molecule (CH_3NH_3) inside the $PbBr_6$ octahedra used for calculation. (b) The change in the energy as a function of the rotation (in the ac plane) angle of the molecule. The angle θ is shown in the inset. (c) The optimized structure for the two minimum energy configurations where the C-N axis makes an angle of $\sim 12^0$ (configuration A) and $\sim 28^0$ (configuration B) with the (101) direction. (d) Conduction band for these two minima (A and B), (e-f) Valence band corresponding to these two minima (A and B) shows an energy shift of 13.7 meV. (g) Simulated high temperature behavior of the Valence band corresponding to these two minima (A and B), which shows an energy shift of 10.30 meV

Such attractive H_N-Br interactions also displace the Br ions from their ideal positions leading to octahedral tilts, when we relax the whole system (Figure 5.3 (c)). However, the octahedral tilting do not simply follow the simple prescription of short H_N-Br bonds. Hydrogen bonds together with steric effects determine the octahedral tilt pattern for any molecular orientation giving rise to a complex PE landscape as a function of different molecular orientations leading to different octahedral distortions.

Allowing for rotations of the C-N axis of the molecule in the ac plane about the b-axis leads to the a^+bc^+ (in Glazer notations) tilt pattern [203], but with different Pb-Br-Pb bond angles. Plotting the energy as a function of molecular orientation, one finds the presence of two closely spaced minima (Figure 5.3 (b)) with an energy separation of 6 meV, each having different molecular orientations and octahedral tilt (Figure 5.3 (c)). The second minima can be populated by thermal excitations (Figure 5.3 (b)). The electronic structure of the two systems are different. The conduction band minima (CBM) almost coincides with each other (Figure 5.3 (d)), however, there is a small shift in the valence band maxima (VBM) (Figure 5.3 (e)). When measured with respect to CBM of both the systems at zero energy, the difference between the two VBM is 13.7 meV (Figure 5.3 (f)) at the experimental volume. When we consider the GGA optimized volume to simulate the red shifting behavior of peak-2, the energy difference between the two minima increases to 9 meV and the band gap difference decreases to 10.30 meV (Figure 5.3 (g)) and we speculate that volume contraction is responsible for red shifting behavior of peak-2. Thus, it was hypothesized that synthesis conditions could lead to the presence of two different structures associated with the minima that we find being frozen in at different locations and could explain the presence of the two peak feature in PL experiments . Recently Motta *et al.* have revealed that orientation of CH_3NH_3 can also have a profound impact on the band structure of methylammonium lead halides [46]. Van der Waals corrected density functional theory calculations reveal that if CH_3NH_3 orients along (011) direction, $PbBr_6$ octahedra can distort and band gap can become indirect. There are not enough experimental evidence about the role of MA orientation in band gap of $CH_3NH_3PbBr_3$ though some indications exist in the form of PL spectra [240]. However, our calculation produces direct band gap for all cases as the change in orientation was not able to induce enough distortion in the inorganic network. An alternate explanation for the two peak structure in the PL that exists in the literature has been associated with the orientational disorder of the molecule which has been found in the molecular dynamics simulations at 15 K considering the orthorhombic phase [58]. However, we find that the stacking in the b-direction could lead to another source of orientational disorder. Both ferroelectrically stacked as well as antiferroelectrically stacked cases are found to be degenerate in our calculations which fails to explain 40 meV bandgap difference and so cannot explain the 2-peak feature.

5.1.3.5 Optical properties of $CH_3NH_3PbI_3$ and $CH_3NH_3PbCl_3$

Temperature dependent photoluminescence (PL) measurements of $CH_3NH_3PbCl_3$ and $CH_3NH_3PbI_3$ were carried out between 77 K and 390 K and data are summarized in Fig-

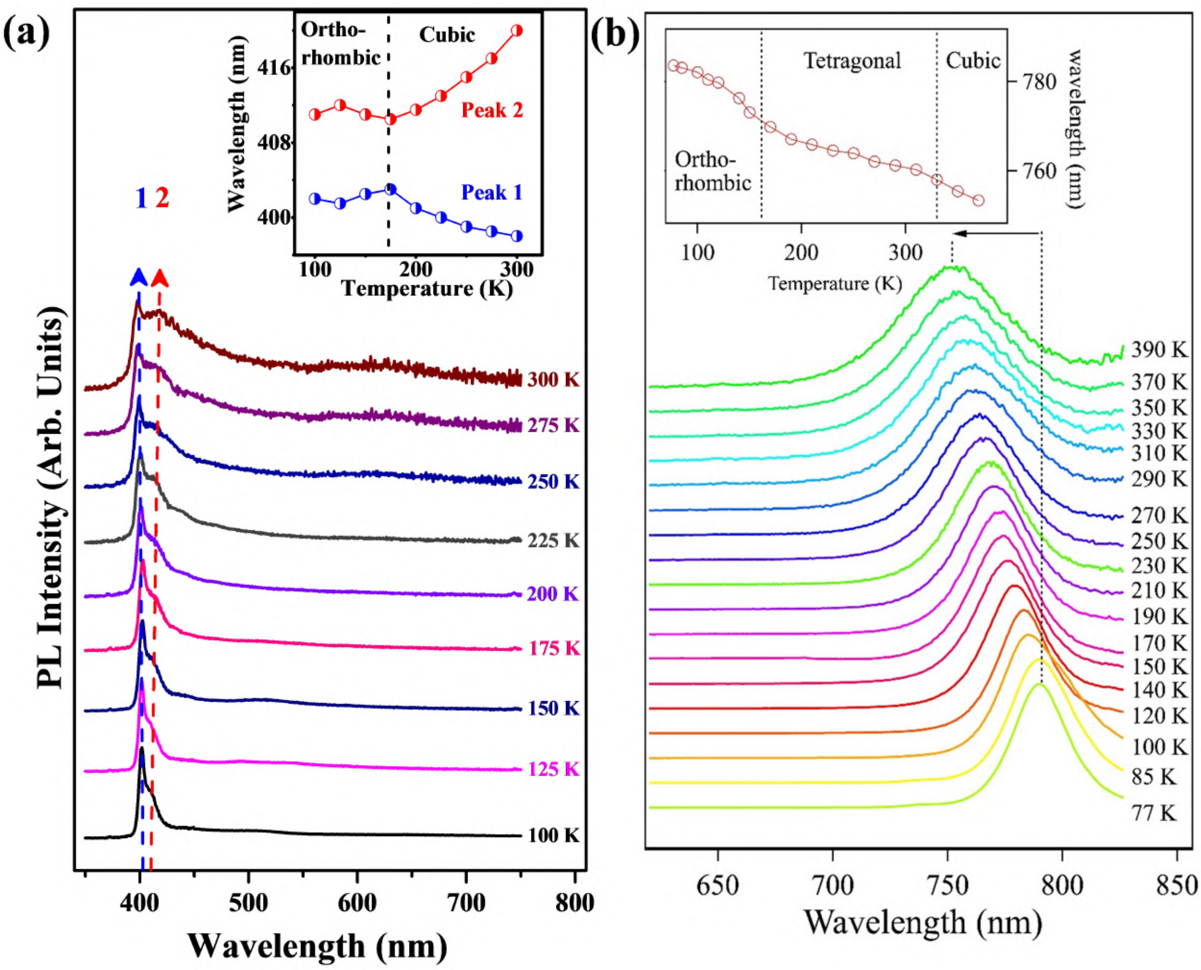

Figure 5.4: Temperature-dependent photoluminescence (PL) spectra of (a) $CH_3NH_3PbCl_3$ and (c) $CH_3NH_3PbI_3$ single crystals. Dotted lines and arrows are guide to the eye highlighting the blue and red shift of the PL peak with temperature. The inset shows the variations of peak positions of each samples as a function of temperature.

ure 5.4 (a) and (b), respectively. As before, we have shifted the PL spectra vertically and normalized the intensity for the help of view. There is a continuous evolution of the PL peak position, FWHM and intensity with temperature. However, noticeable discontinuities exist across the crystallographic phase temperatures, as shown in the inset of Figure 5.4 (a) and (b), where the rate of change of peak position with temperature is found to be different in three crystallographic regions. Figure 5.4 (a) displays steady-state PL of $CH_3NH_3PbCl_3$ over a temperature range from 100 K to 300 K. Peak positions of the two emission peaks at 100 K: 402 nm (peak 1; 3.08 eV) and 410.5 nm (peak 2; 3.02 eV) gradually vary with temperature as shown in the inset of Figure 5.4(a) with strong divergence in peak position observed at 175 K which is close to the crystallographic phase transition temperature [17, 162, 176]. Further, the observed PL peak position of $CH_3NH_3PbI_3$ at 77 K is centered at 793 nm (1.56 eV) with a line width of 55 meV (28 nm), which is blue shifted with increasing temperature, as shown by dashed lines and arrows in Figure 5.4 (b), to 752 nm (1.65 eV) with a line width of 106 meV (53 nm) at 390 K [27]. Due to limitation of detector range (restrict upto 830 nm) we are not able to catch peak-2 of $CH_3NH_3PbI_3$ [164].

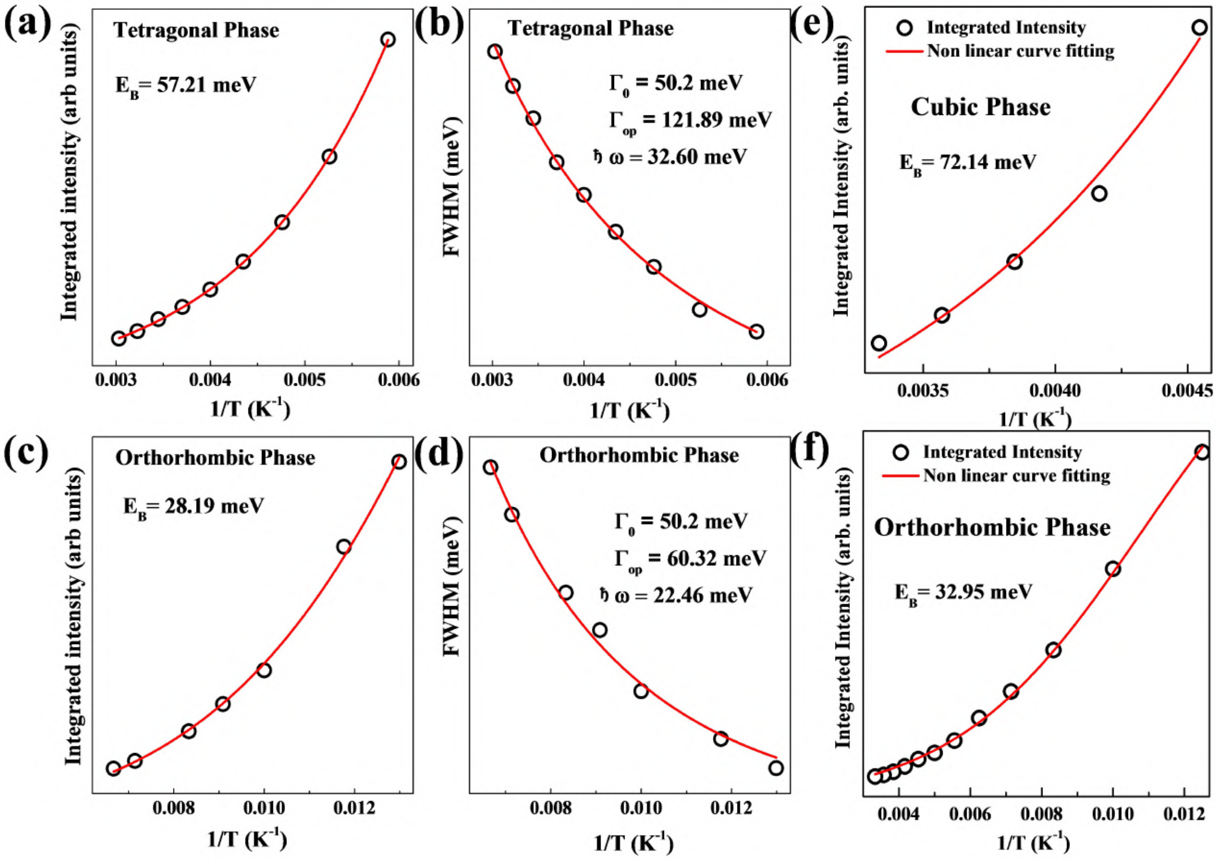

Figure 5.5: Temperature dependent data of integrated intensity and FWHM in tetragonal (a,b) and orthorhombic (c,d) phase of $CH_3NH_3PbI_3$ respectively. Temperature dependent data of integrated intensity of (e) $CH(NH_2)_2PbBr_3$ and (f) $CsPbBr_3$. Solid lines are fittings as explained in the text.

The continuous spectral evolution of the PL peak with temperature indicates that the peak should be attributed to free excitons and not to the bound excitons [67]. Further the broadening of the peak with increasing temperature can be explained by stronger exciton-phonon interaction [68]. We can extract information regarding the exciton binding energies as well as exciton-phonon interactions from the PL data as indicated in Figure 5.5. Temperature dependent free-exciton emission intensity for tetragonal and orthorhombic phases of $CH_3NH_3PbI_3$ are plotted in Figure 5.5 (a) and 5.5 (c) and that of $CH(NH_2)_2PbBr_3$ (cubic phase) and $CsPbBr_3$ (orthorhombic phase) are depicted in Figure 5.5 (e) and 5.5 (f), respectively, which can be fitted using Equation 5.2 [27, 176, 241, 242]. Fitting yielded binding energy of 57.59 meV for the tetragonal phase of $CH_3NH_3PbI_3$. Exciton binding energy was estimated to be around 50 meV at room temperature from magneto-absorption data [236], temperature dependent absorbance spectra of thin film of $CH_3NH_3PbI_3$ [67] and theoritical calculation [70]. Similarly exciton binding energy of 64.3 meV was obtained from temperature dependent PL data of a similar hybrid organometal halide perovskite system $CH_3NH_3PbI_{3-x}Cl_x$ which are consistent with our observations [68]. By fitting integrated intensity of emission peak in the temperature range 77 K to 150 K exciton binding energy of 28.19 meV was obtained in orthorhombic phase. These extracted values of exciton binding energies are consistent with the literature reports [236, 237]. Ishihara at. el. [243] and Tanaka et. al. [244] showed that exciton binding energy increases with the increase of band gap for PbX based perovskite materials which is consistent with our result. Figure 5.5 (e) and (f) displayed variation of integrated intensity with temperature from 300 K to 220 K (cubic phase) and 325 K to 77 K (orthorhombic phase), for $CH(NH_2)_2PbBr_3$ and $CsPbBr_3$, respectively, and the corresponding exciton binding energy are found to be 72.14 meV and 32.95 meV.

Since the broadening effect of PL spectra arises from exciton-phonon scattering, to understand the strength of exciton-phonon interaction, we evaluated the temperature dependent broadening of exciton emission, following the FWHM of the corresponding peak in tetragonal and orthorhombic phase of $CH_3NH_3PbI_3$, which are depicted in Figure 5.5 (b) and 5.5 (d). The expression of this relationship is given by [245, 246]:-

$$\Gamma(T) = \Gamma_0 + \sigma T + \left(\frac{\Gamma_o p}{\exp\left(\frac{\hbar\omega_p}{K_B T}\right) - 1}\right) \tag{5.3}$$

Here Γ_0, σ, Γ_{op} and hω are the zero temperature broadening parameter, the coupling strength of exciton-acoustic phonon interaction, the strength of exciton-optical phonon contribution and the energy of the optical phonon, respectively. At low enough temperatures the first term (Γ_0) is expected to be dominating. However, as the temperature is increased, contributions from acoustic and optical phonon also becomes substantial. In the tetragonal phase (160 K - 330 K) which is at relatively higher temperature, we can neglect contribution of acoustic phonon to width broadening. Accordingly, the measured FWHM data of peak were fitted using equation 5.3 with $\sigma = 0$. Figure 5.5 (b) shows the fitting and the extracted values for zero temperature broadening parameter (Γ_0) = 50.2 meV, the exciton-optical phonon contribution (Γ_{op}) = 121.89 meV and the optical phonon energy $\hbar\omega_{op} = 32.60$ meV. Similarly for orthorhombic phase we have extracted (Γ_{op}) = 60.32 meV and $\hbar\omega_{op} = 22.46$ meV. The optical phonon energy of 32.6 meV extracted for tetragonal phase (using PL data) correlates well with the observed Raman bands at 274.8 cm^{-1} as discussed in the next section. Maksimov *et al.* suggested that the electron-phonon coupling constant can also be calculated from PL spectroscopy using the following formula [27, 247]:-

$$\alpha = \left(\frac{\hbar}{2\pi K_B}\right) * Slope \tag{5.4}$$

Here ‘Slope’ refers to the slope of temperature dependent FWHM of the PL spectrum versus temperature (not shown here), which is 0.2647 $meVK^{-1}$ and K_B is the Boltzmann constant. Using equation 5.4, the electron-phonon coupling constant (α) was calculated as 0.48.

5.1.3.6 Raman Spectroscopy

The Raman spectrum acquired from single crystal $CH_3NH_3PbI_3$ at room temperature (300 K) is shown in Figure 5.6. The spectrum consists of sharp vibrational modes at 83.9 cm^{-1} and 136.3 cm^{-1} followed by broad band modes appearing at 274.8 and 350 cm^{-1}. According to Mosconi *et al.* [248], depending upon the packing of the moieties in the $CH_3NH_3PbI_3$, the crystal structure at room temperature can be classified into tetragonal-1 (the methyl ammonium (MA) moiety exhibits disordered packing) or tetragonal-2 (the

MA moiety exhibits ordered packing). Also, Quarti *et al.* [249], pointed out that the vibrational bands between 70 and 90 cm^{-1} correspond to the normal stretching modes of the Pb-I, whereas the modes in the range 200-400 cm^{-1} refer to the torsional vibrational frequencies of the organic MA cations. Therefore, the observation of 83.9 cm^{-1} mode in Raman spectra may be assigned to the normal stretching mode of the Pb-I from the tetragonal-1 phase of $CH_3NH_3PbI_3$, where the MA moiety exhibits disordered packing, as observed by X-ray diffraction. Absence of the Raman band at 94 cm^{-1} further rules out the existence of the less stable tetragonal-2 structure [27]. As MA cations, Pb atoms and Iodine atoms occupy D_{4h} sites of the tetragonal-1, the calculated liberation modes appear at 141 cm^{-1} [250]. Hence, the vibrational line observed at 136.3 cm^{-1} may be associated with the MA cation liberation modes.

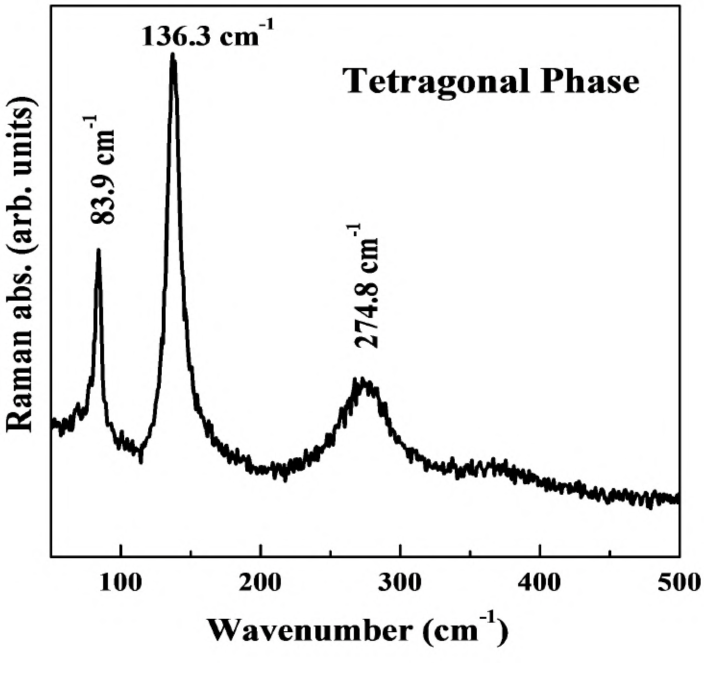

Figure 5.6: Room temperature Raman Spectra of $CH_3NH_3PbI_3$.

From theoritical calculation [249], the isolated MA cation exhibits torsional modes of vibration at 278 cm^{-1}; therefore, the Raman line observed at 274.8 cm^{-1} can be assigned to a torsional mode. The observed downshift of the vibrational line may be due to the disorder mediated anharmonic effect in MA cations. In addition, a weak and broad band is observed at 350 cm^{-1} which may be attributed to the longitudinal optical (LO) mode of the tetragonal phase of $CH_3NH_3PbI_3$. Notably, the LO mode is observed to be up-shifted by 40 cm^{-1} as compared to the previous literature report from single crystal tetragonal $CH_3NH_3PbI_3$ [251,252]. The weak, broad and up-shifted LO mode may be due to (i) the disordered structure of MA moiety in the inorganic cavity. (ii) polaron shift (i.e, the large difference between static dielectric constant(ε_0= 25) and dynamic dielectric constant(ε_∞= 6.5) causing nonhydrogenic exciton states) and (iii) electron-phonon interaction [43,77,253]. A similar polaron shift has also been observed by Proupin *et al.* [251] and the strength of the electron-phonon interaction can be understood quantitatively by the coupling constant (α), where

$$\alpha = \frac{m^* e^4}{2\hbar^2 \varepsilon^{*2} E_{LO}} \tag{5.5}$$

Where m^* is the effective mass, $\hbar$ is Planck constant, ε^* is the effective dielectric constant and E_{LO} be the LO phonon energy. Taking m_e ($0.190m_0$) and m_h ($0.225m_0$) as electron and hole masses [44,65,254], effective mass will be $\left(\frac{1}{m^*} = \frac{1}{m_e} + \frac{1}{m_h}\right)$ $0.103m_0$, where m_0 is rest mass of electron. Taking effective dielectric constant, $(\frac{1}{\varepsilon^*} = \frac{1}{\varepsilon_\infty}$ - $\frac{1}{\varepsilon_0})$ as 8.7 [188] and E_{LO} as 43.42 meV, the α has been estimated to be 0.653, which is closer to the value obtained from temperature dependent PL measurements (0.48). The modest value of the electron-phonon coupling constant opens up the possibility of increased power conversion efficiency for hybrid perovskite based solar cells and also makes it suitable as a gain medium for short-pulse lasers.

5.1.3.7 Crystal Face Dependent PL of $CH_3NH_3PbBr_3$

We know that the anisotropy of the single crystal often affects the physical properties of the materials, like hardness, magnetic properties, thermal properties, optoelectronic properties and piezoelectric properties [255–257]. In last few years, many efforts have been made to reveal the influence of structural anisotropy on the characteristics of organic-inorganic hybrid lead halide perovskites [258–260]. Anisotropy of optoelectronic and photovoltaic properties in lead halide is recently being reported [175,260–264]. Cho *et al.* [261]

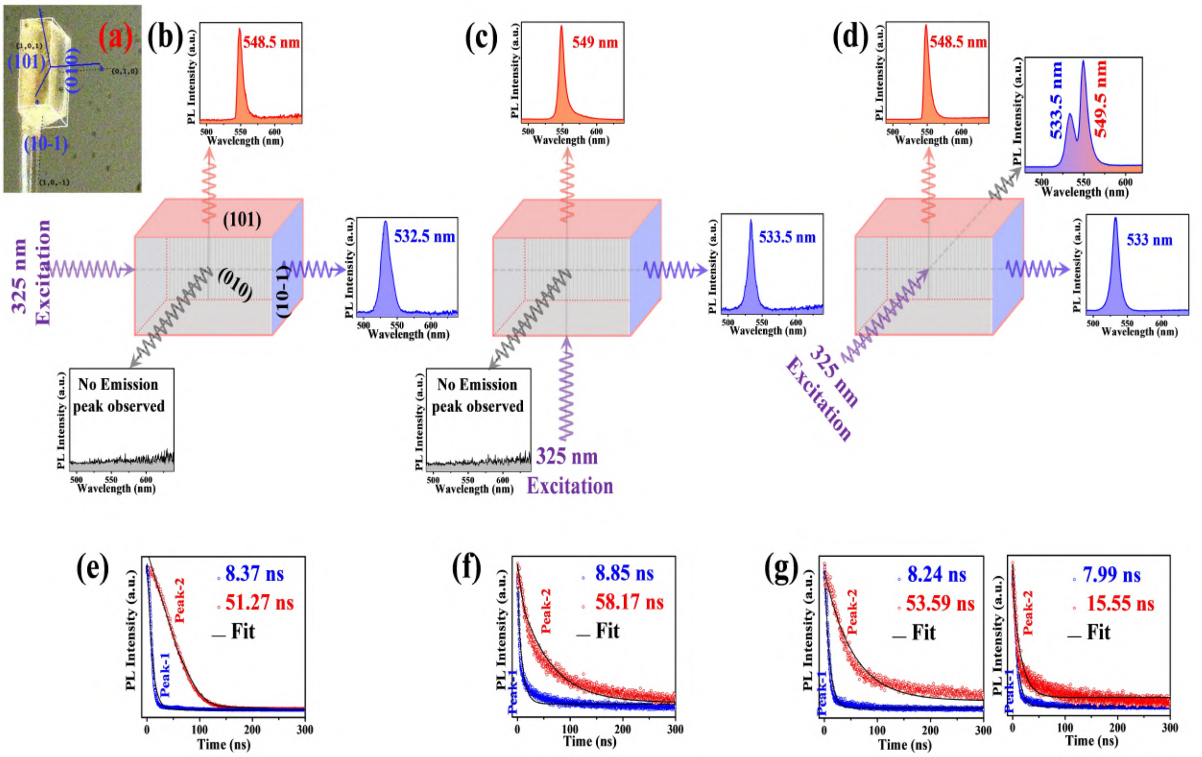

Figure 5.7: Single crystal X-ray diffraction to identify the planes of $CH_3NH_3PbBr_3$ single crystal. (b-d) Steady state and (e-g) time resolve photoluminescence (PL) of $CH_3NH_3PbBr_3$ single crystal at 77 K. Light is incident along (10$\bar{1}$) (b, e), (101) (c, f) and (010) (d, g) planes of the crystal and emission spectra are recorded along (010), (10$\bar{1}$) and (101) planes.

and Leblebici *et al.* [260] have shown that both trap state densities and photovoltaic properties in $CH_3NH_3PbI_3$ thin films are facet-dependent, suggesting crystal anisotropy plays vital roles in photovoltaic and optoelectronic properties. Motta *et al.* [265] found a significant asymmetry of the mobility that depends on the charge transport direction with respect to the molecular axis of $CH_3NH_3PbI_3$. Controllable anisotropic photon emission from the vertically aligned transition dipole moments in the film of $CsPbBr_3$ nanocubes was observed by Jurow *et al.* [264] Further, 153.33% enhancement of responsivity was reported by Zuo *et al.* for (110) plane of $CH_3NH_3PbBr_3$ single crystal compared to the (100) plane [263] and Ding *et al.* observed a 135% increased responsivity and 128% heightened external quantum efficiency (EQE) on the (112) plane of $CH_3NH_3PbI_3$ single crystal compared to that of (100) plane [262]. These results indicate that crystal anisotropy of hybrid lead halide perovskites play an important role in the photovoltaic and optoelectronic properties. However, detail study on optical anisotropy of hybrid lead halide perovskite crystals is still lacking. As we have grown very high quality large (1.5 cm × 1 cm × 0.4 cm) single crystals of $CH_3NH_3PbBr_3$, we decided to perform crystal face dependent PL to shed more light on the $PbBr_6$ octahedral distortion due to CH_3NH_3 orientation (if any). As discussed above, the effect of octahedral distortion due to CH_3NH_3 orientation on the Photoluminescence (PL) property of $CH_3NH_3PbBr_3$ is well understood in the orthorhombic phase (as CH_3NH_3 molecule has only one possible orientation), we decided to perform crystal face dependent optical experiments at 77 K. Single crystal X-ray diffraction studies at 77 K revealed the exposed crystallographic planes in orthorhombic phase are (101), (010) and $(10\bar{1})$ respectively as shown in Figure 5.7 (a). Single crystal XRD also indicate that $CH_3NH_3PbBr_3$ single crystals possess excellent crystallinity and they exhibit perfect crystalline integrity along (101), (010) and $(10\bar{1})$ facets.

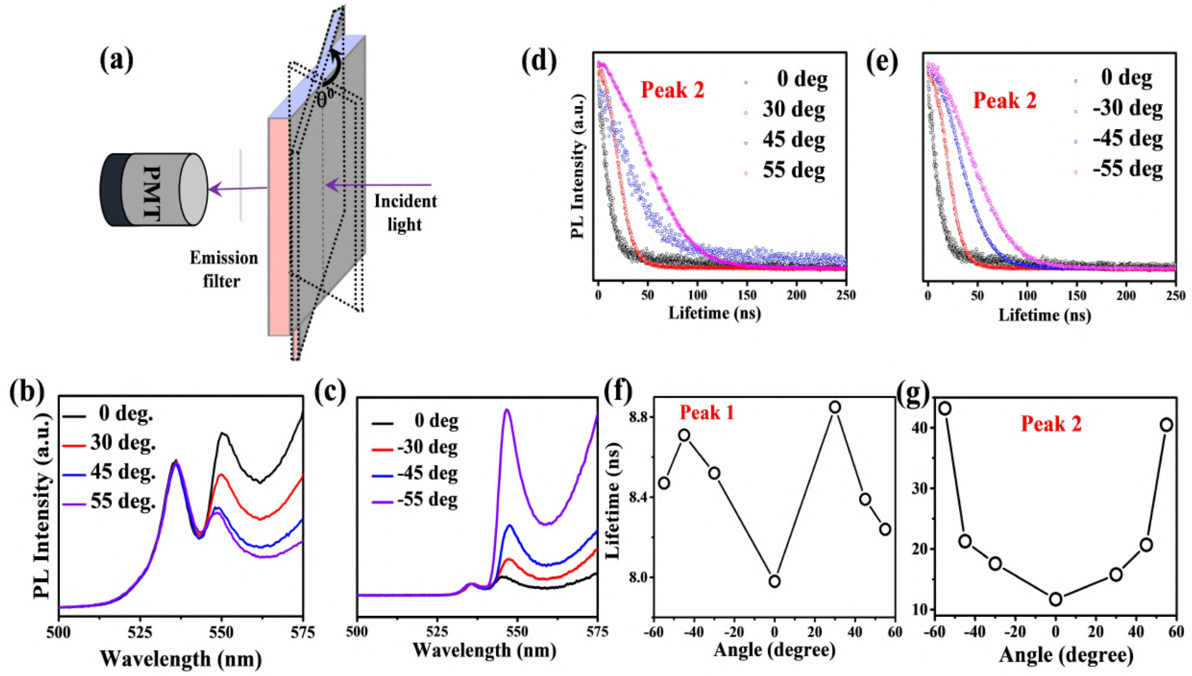

Figure 5.8: (a) Crystal orientation dependent PL of $CH_3NH_3PbBr_3$ (a) Schematic, (b-c) steady state, (d-e) Time-resolve, (b,d) crystal is oriented along positive θ and (c,e) negative θ direction, (f-g) variation of life time of peak-1 and 2 with rotation angle.

The anisotropic optical (PL) property of $CH_3NH_3PbBr_3$ single crystal is depicted by comparing the steady state and time-resolve PL results on (101), (010) and $(10\bar{1})$ planes of $CH_3NH_3PbBr_3$ at 77 K. Thus, we shine light at one crystal face and record PL emission spectra along other five different faces of the crystal. Steady state and time-resolve PL results of $CH_3NH_3PbBr_3$ are displayed in Figure 5.7 (b-d) and 5.7 (e-g), respectively. As the crystal planes of opposite faces are identical and show similar PL emission, we restrict our further discussion on three faces of the crystal. While shining light along $(10\bar{1})$ direction, PL spectra at 77 K results single emission peak at 548.5 nm along (010) direction, 532.5 nm along $(10\bar{1})$ direction and no emission peak along (010) direction. PL Peak positions (532.5 nm and 548.5 nm) are in good agreement with that of $CH_3NH_3PbBr_3$ pellet made by crushing single crystal sample (533.5 nm and 547.5 nm) as depicted in Figure 5.1 (c). Further, we also observe that only peak-1 (between 532.5 nm and 533.5 nm) is emitted along (101) plane and peak-2 (between 548.5 nm and 549 nm) along $(10\bar{1})$ plane independent of light shining direction, i.e., peak positions remain same if we shine light along $(10\bar{1})$, (101) or (010) faces of the crystal, as shown in Figure 5.7 (b), (c) and (d). However, no peak is observed along (010) plane if we shine light through $(10\bar{1})$ and (101) faces of the crystal, in contrast, both peak-1 (533.5 nm) and peak-2 (549.5 nm) are observed with varying intensity if we shine light through (010) plane and record PL emission spectra along (010) direction (opposite to the incident direction). This result opens up the debate on surface and bulk recombination of hybrid perovskites pointed by Murali *et al.* [59] To understand more, we decided to perform lifetime measurements (TCSPC method) of PL transitions (Peak-1 and 2) after shining pulsed laser light through $(10\bar{1})$ and (101) direction and observed that life time corresponding to peak-1 is around 8.3 ns and that of peak-2 is around 51.5 ns, respectively, with $\pm 6\%$ error bars. However, if we shine light along (010) direction and record lifetime spectra of peak-1 and 2 (Figure 5.7 (g)) along (010) direction (opposite to the incident direction), interesting results are observed: lifetime of peak-1 is around 7.9 ns (consistent with the lifetime of peak-1 observed along $(10\bar{1})$ directions) and that of peak-2 is around 15.5 ns (3.5 times lower than that of peak-2 observed along (101) directions).

In order to understand more, we decided to perform steady state and time resolved PL measurements by rotating the $CH_3NH_3PbBr_3$ single crystal. As (010) plane of the single crystal is larger than the other two, we decided to perform experiments on this plane of the crystal. Here we have taken the normal incident as 0^0 and rotated the crystal along right side with respect to the incident beam and denoted it by positive θ direction, while rotation along left side is represented by negative θ direction as shown in Figure 5.8 (a). Interestingly, steady state PL spectra shows that intensity of peak-2 decreases with the increase of θ along positive θ direction (Figure 5.8 (b)); and increases if we rotate it in the other direction (negative θ) (Figure 5.8 (c)), keeping the intensity of peak-1 same for both the cases. TCSPC measurement along positive and negative θ direction reveals lifetime of peak-1 is around 8.4 ns with $\pm 10\%$ error bar (Figure 5.8 (f)). However, lifetime of peak-2 is $\sim$ 15.55 ns for $\theta = 0^0$ and it increases all the way from 15.5 ns to 55.3 ns as we rotate the crystal along positive and negative θ direction as shown in Figure 5.8 (d), (e) and (g). These results clearly indicate that PL intensity and lifetime of peak-2 is dependent on crystal plane and orientation of the crystal and rules out the possibility of surface and bulk recombination as the origin of PL emission (peak-1 and 2) in hybrid perovskites [266, 267].

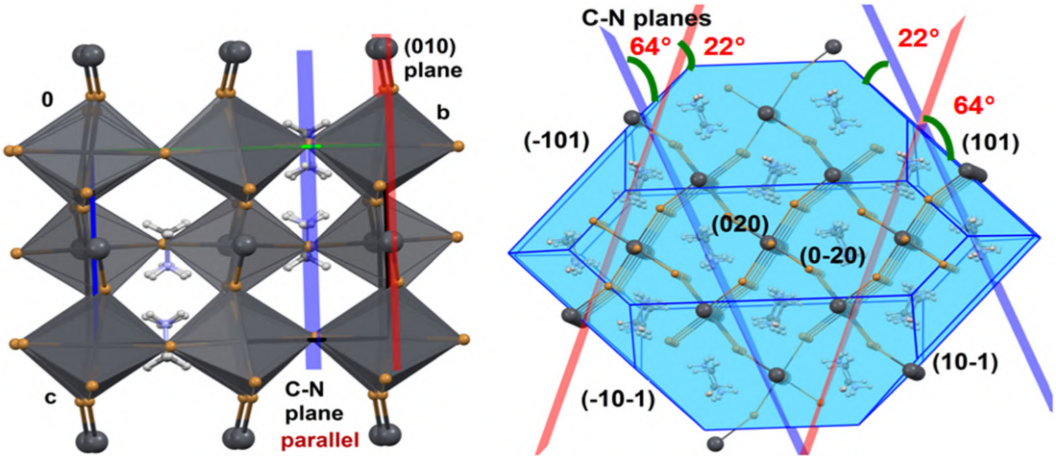

Figure 5.9: Orientation of the organic cation (C-N plane) with respect to different crystal faces in Orthorhombic phase at 100K.

To understand more, single crystal XRD of $CH_3NH_3PbBr_3$ were recorded at 100 K and representative crystal structure and C-N bond angles with respect to different crystallographic planes obtained from single crystal XRD refinement at 100 K is presented in Figure 5.9. The refined parameters confirm the existence of orthorhombic (P*nma*) phase at 100 K with a lattice parameter of a= 8.65 A, b= 8.72A and c=12.25 A. Further, phase indexing of single crystal XRD data of $CH_3NH_3PbBr_3$ confirm three faces of the crystal are (010), (10-1) and (101) and MA molecule are parallel to “a” axis in (010) plane, whereas they make two different angles (22 and 64) with respect to (10-1) and (101) crystallographic planes.

Now correlating this experimental observation with theoretical understanding, we might conclude that two different orientation of the MA molecule are responsible for the dual emission of hybrid perovskite and parallel orientation results no emission. We believe that CH_3NH_3 orientation, PbX_6 octahedral distortion or systematic halide defects might be responsible for this observation.

5.1.4 Conclusion

The optical properties of $CH_3NH_3PbCl_3$, $CH_3NH_3PbBr_3$, $CH_3NH_3PbI_3$, $CH(NH_2)_2PbBr_3$ and $CsPbBr_3$ perovskite were studied using UV-Visible absorption and temperature dependent XRD steady-state PL. Optical spectroscopic measurements of hybrid perovskite revels that the bandgap can be tuned from blue to red region of visible spectra by changing the halide composition from Cl to Br to I and the corresponding bandgap (room temperature) are 405 nm, 532 nm and 785 nm. The observed bandgap changes upon halide substitution are influenced by the electronic states of the anion. Further, it was also observed that, the “A” site substitution doesnot directly contribute to the frontier electronic structure, but it has some indirect influences. Further, Exciton binding energy, exciton-phonon interaction and electron-phonon coupling constant of hybrid perovskites are extracted from temperature dependent PL and ambient temperature Raman measurements. UV-Visible absorption spectra showed the existence of two electronic states in either valence or conduction bands of $CH_3NH_3PbCl_3$, $CH_3NH_3PbBr_3$, $CH(NH_2)_2PbBr_3$ which was further confirmed by temperature-dependent PL measurements. However, single peak is observed for the case of $CsPbBr_3$, which implies that the origin of the dual emission is associated with the nature of the organic cation. With the first-principle DFT calculations and MD simulations, we determined the experimentally observed energy difference of dual PL emission peaks is caused most likely by the octahedral distortion which arises due to molecular orientation of MA molecule. Allowing the C-N bonds to rotate in the ac plane about the b-axis, two closely spaced minima were observed and the electronic structure calculations result in two closely spaced valence band at gamma point with a separation of 13.7 meV which matches closely with the experimentally observed energy difference between the two peaks (40 meV) in orthorhombic phase. We also observe anisotropic crystal face dependent PL of $CH_3NH_3PbBr_3$.

5.2 Electronic Structure of Hybrid Perovskites

5.2.1 Introduction

Organic-inorganic halide perovskites are one of the the most widely studied class of materials in photovoltic community today due to their strong light absorption ability [11], coupled with the easiness and low cost of fabrication [90]. Further, their performance in a solar cell, with above 22.1% efficiency [10], almost to the level of commercially available silicon cells [7] has stimulated considerable interest to unravel the photo-transport and photo-physics properties of these systems [20, 54]. However, the fundamental questions concerning the electronic structure, effect of spin-orbit coupling/splitting (if any) and orientation of the organic cations, at the “A” site of the perovskite ($MAPbX_3$, where MA = methylammonium, X = Cl. Br, I) are not well understood.

In this regard, understanding the electronic structure of the constituent materials i.e. energies of the valence band maxima (VBM) and conduction band minima (CBM), nature of the density of states (DOS) and dispersive nature of the valence band along different symmetry directions of the unit cell is important. Previous studies on these systems were performed using valence band photoemission [27, 35, 103, 176, 268, 269], combined photoemission and inverse photoemission [41, 104, 270, 271], and band structure calculations [42, 43, 46, 272–279] to elucidate the electronic structure of the methylammonium lead halide perovskites. Despite these studies, the nature of lead-halogen (Pb-Cl/Br) and methylammonium-halogen (MA-Cl/Br) interactions, effect of the orientational dynamics of CH_3NH_3 (MA) ion on the electronic structure is yet to be established. The importance of a deeper understanding of these materials can be appreciated by the fact that the nature of states near the top of the valence band plays a crucial role in photo-excitation and carrier transport, which are important to the performance of optoelectronic devices synthesized from these hybrid perovskites [12, 24]. Photoelectron spectroscopy, over the years, has established itself as a unique tool for mapping out the electronic structure of the occupied density of states. Hence we performed detailed core level and valence band photoemission of hybrid perovskites and compare them with the theoretical results.

It is agreed that the organic cation (at the "A" site) do not contribute directly in the formation of valence or conduction bands, but their possible dynamics and orientation strongly influence the optoelectronic properties [35, 46, 47]. Lowering of symmetry due to orientation of organic cation i.e. changing MA orientation from (100) to (111) direction has profound effect on the electronic structure, namely the bandgap changes from direct to indirect [46]. Further, it was observed that, MA orientation inside the PbX_6 octahedra are responsible for strong frequency dependence of the relative permittivity [280], reduction of the Fröhlich e-phonon coupling of the $PbI_3{-}LO$ vibration [281] and reduction of thermal stability of hybrid perovskites [282], irrespective of structural phase transition of the system [27, 176].

Band structure calculations of hybrid perovskites are sensitive to orientational dynamics of MA ion, the choice of functional [273, 279] and the relativistic effects, i.e., Spin-Orbit Coupling (SOC) [273] and predict Rashba spin-split bands for specific orientation of MA ion [277]. However, there appears to be several controversies concerning real band structure of these compounds. One angle-resolved photoemission spectroscopy (ARPES) study reported the absence of any k-dependent spin-splitting of the bands in their room temperature experiments [41], whereas another study suggested giant splittings of 11±4 eVÅ for the high temperature cubic phases of $CH_3NH_3PbBr_3$ [103]. The nature of the Rashba spin-split states from theoretical and experimental investigations bands is also controversial. Niesner *et al.*, suggests Rashba spin-split bands at valence band maxima i.e. at M point in cubic phase and also in low temperature orthorhombic phase [103], while first-principles calculations based on density functional theory (DFT) suggests absence of any such spin-splitting at the M point [278]. Spin splitting, if any, is observed theoretically at Γ point with much lesser amplitude and considering polar nature of MA bonds. Thus, it is obvious that even the basic issues concerning the electronic structures of these series of compound have not been settled so far.

In this chapter, we present the results of the electronic structure from single crystal samples of $CH_3NH_3PbCl_3$, $CH_3NH_3PbBr_3$, $CH_3NH_3PbI_3$ using photoelectron spectroscopy (X-ray photoelectron spectroscopy (XPS), angle-integrated and angle-resolved ultra-violet photoelectron spectroscopy (UPS)) along with the first-principles band structure calculations based on density functional theory of these organic-inorganic hybrid perovskites in the cubic phase. The orbital contributions of elements in the valence band spectra were identified as hybridized Pb-s and Cl/Br-p bands by comparing photoionization cross section and projected density of states (PDOS) for each of these elements. Further, analyzing ARPES intensity map along $\overline{X} - \overline{\Gamma} - \overline{M}$ direction reveals downward dispersing bands with maxima occurring at $\overline{M}$ symmetry point and minima at the $\overline{\Gamma}$ point, which is consistent with the calculated band structure for a cubic phase. However, experimental observation of degenerate bands at $\overline{\Gamma}$ point, contrary to the theoretical results, where 9 fold degeneracy was lifted, in a periodic calculation with a specific configuration (specific orientation of MA molecule) of the disordered system (cubic system) points out at theoretical limitations in understanding electronic structure of hybrid perovskites in cubic phase. A more involved and accurate approach could be based on local density approximation method and using the coherent-potential approximation in DFT to average over the ensemble of various atomic configurations and provide an average band structure. In absence of such code (with us), we calculated band structure of $CsPbCl_3$ wherein symmetric potential exist at the center of the inorganic cage, due to presence of Cs atom and were able to reproduce the experimental ARPES intensity map to a large extend, but some discrepancies in reproducing experimental constant energy counters still persists. What is needed is a comprehensive calculations using coherent potential approximation in DFT which is beyond the scope of this study.

5.2.2 Experimental and Computational Details

High-quality single crystal samples of $CH_3NH_3PbX_3$ (X=Cl, Br) were synthesized using anti-solvent vapor-assisted crystallization (ASVAC) approach at room temperature as reported in the experimental part of the last section of this chapter [41, 58, 103, 104]. These crystals were characterized for phase purity by X-ray diffraction while Laue measurements were used for allingment of the sample for ARPES study. X-ray Photoelectron spectroscopy (XPS) measurements were performed on PHI-5000 Versaprobe II Scanning XPS Microprobe using monochromatic Al K_α radiation at room temperature. Further, crystals oriented along (100) direction (normal to the surface) were cleaved in ultrahigh vacuum (base pressure 10^{-10} mbar, to expose clean surface) and angle integrated Ultraviolet Photoelectron Spectra (UPS) were recorded at different photon energies like: 20, 31 and 40 eV while ARPES measurements were performed using a photon energy of 37 eV at room temperature. Fermi energy for all the measurements were calibrated using Cu sample holder. All UPS experiments were performed at Badelph beamline, Elettra, Trieste, Italy.

Electronic structure calculations were carried out using projected augmented wave (PAW) [147, 148] implementation of density functional theory within the Vienna ab initio simulation package (VASP) [149–151]. The generalized gradient approximation and Perdew-Burke-Ernzerhof model for the exchange-correlation potential (GGA-PBE) were used in our calculations [223]. Scalar relativistic correction (necessary for accurate representation of Pb 6s band) was also included in the calculations. A Gamma-centred k-point mesh of 8 × 8 × 8 was used for reciprocal space integration and a plane wave basis set energy cutoff of 600 eV was considered in the calculations. Correction to the Kohn-Sham DFT energy due to van der Waals interactions was included within the method of Tkatchenko and Scheffler (DFT-TS) implemented in VASP. The results were found to be well converged with the considered parameters. The experimentally observed simple cubic unit cell with $\overrightarrow{a}$ = 5.68 Å, and 5.96 Å, for $CH_3NH_3PbCl_3$ and $CH_3NH_3PbBr_3$ were used as the starting point of our calculation respectively [41, 176]. The internal coordinates were optimized until the forces on the atoms were less than 10^3 eV/Å. Density of states and band structure calculations were then performed on the optimized structure. The spin-orbit interactions were ignored in the calculations. To represent constant energy contours, 2452 k-points along Γ, M and X directions in the Brillouin zone of the crystal were used. As experiments were carried out at 300 K, where the MA molecules undergo hindered rotation and the average structure is cubic. Carrying out ab-initio electronic structure calculations for such a system is not possible at the present time. In order to confront this problem, we have performed two different T = 0 K calculations; (i) where we replace the orientationally disordered MA^+ molecular ions by spherically symmetric Cs^+ ions, preserving the cubic symmetry and (ii) by freezing the MA^+ ion orientation along a symmetry direction (we have chosen (100) direction), but keeping the unit cell cubic. The latter approximation breaks the cubic symmetry, to simulate the orientationally disordered structure we superimpose the results obtained from different equivalent broken symmetry states. These are two extreme limits and the real physics lies somewhere in between.

In addition to the above approximations, to compare the theoretical results with experimental photoemission data, we have performed energy scaling to the theoretical GGA-PBE spectra. Density of states and band structures were shifted by constant energy -2.45 eV (-1.85 eV) and stretched by a factor 1.1 (1.1) for $CH_3NH_3PbCl_3$ ($CH_3NH_3PbBr_3$) so that the quantitative agreement with experiment improves. This combined “shift and stretch” procedure is well known to be justified theoretically by a linear interpolation between self-energy and exchange-correlation potential and between Kohn–Sham eigenvalues and quasi-particle energies [283, 284]. This procedure has been used semi-empirically in the literature while making a quantitative comparison between experimental photoemission data and theoretical calculations [270].

5.2.3 Results and Discussions

5.2.3.1 X-ray Photoemission spectroscopy (XPS) Studies

An overview of the photoelectron spectra of the $CH_3NH_3PbI_3$, $CH_3NH_3PbBr_3$ and $CH_3NH_3PbCl_3$ samples, acquired using monochromatized 1486.6 eV photon energy, are Shown in Figure 5.9 (a). It contains all the expected core levels of the constituent elements of perovskites, as marked in the Figure. For further analysis, narrow scan spectra of I 3d, Br 3p, Cl2p, Pb 4f, Pb 5d and Pb 4p core levels along with the valence band were also collected and are shown in Figures 5.9 (b), 5.9 (c), 5.9 (d), 5.10 (a), 5.10 (b) and 5.10 (e), respectively, showing the quality of the sample. The I 3d core level spectrum consists of the spin-orbit split $3d_{5/2}$ and $3d_{3/2}$ components separated by 11.5 eV, which is in good agreement with the values previously reported in the literature [27, 35]. Also, the I $3d_{5/2}$ peak appears at 619.3 eV binding energy, which corresponds to I in the -1 oxidation state. The Br 3p level is broader (fwhm 2 eV) compared to I 3d level which is due to the larger lifetime

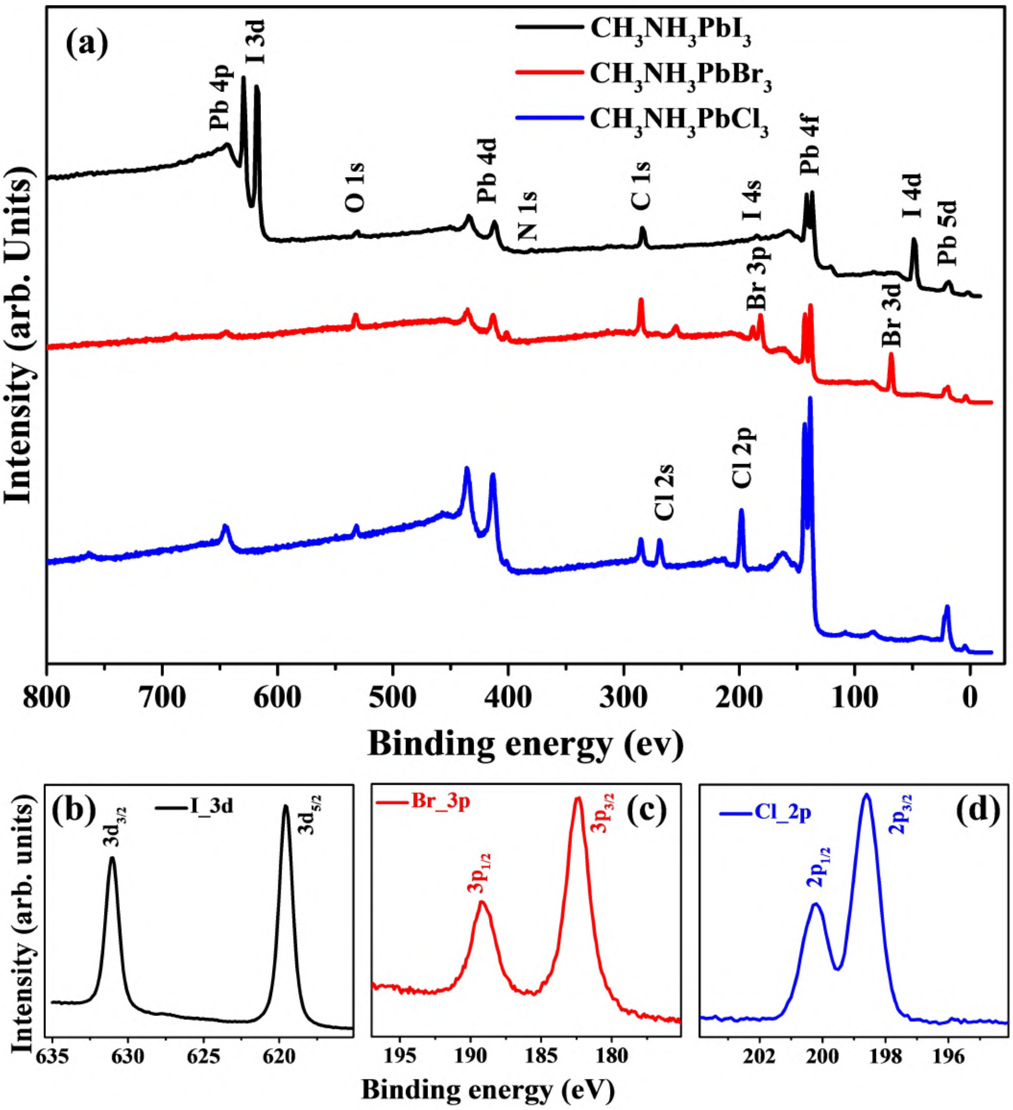

Figure 5.10: Photoemission Spectra of $CH_3NH_3PbI_3$, $CH_3NH_3PbBr_3$ and $CH_3NH_3PbCl_3$ samples collected at room temperature. (a) wide scan (b) I 3*d* core level (c) Br 3*p* core level (d) Br 3*p* core level.

broadening of Br 3*p* level. Br $3p_{3/2}$ level has a binding energy of 182.4 eV and a spin-orbit splitting to the Br $3p_{3/2}$ level of 6.7 eV (Figure 5.9 (c)), as also found in literature. The core level feature of Cl 2*p* is depicted in Figure 5.9 (d). The Cl $2p_{3/2}$ (fwhm 1.1 eV) peak appears at 198.6 eV binding energy and a splitting to the Cl $2p_{1/2}$ level of 1.6 eV.

The experimental Pb 4*f*, Pb 5*d* and Pb 4*p* signal for the $CH_3NH_3PbI_3$, $CH_3NH_3PbBr_3$ and $CH_3NH_3PbCl_3$ samples are shown in Figure 5.10 (a), 5.10 (b) and 5.10 (e), respectively. The spin orbit splitting between the Pb $4f_{7/2}$ and Pb $4f_{5/2}$, and Pb $5d_{5/2}$ and Pb

$5d_{3/2}$ lines are 4.9 eV and 2.6 eV, respectively, for all three compounds. Pb $4f_{7/2}$ peak appears at a binding energy of 138.4 eV for the $CH_3NH_3PbI_3$ sample, which corresponds Pb in Pb^{+2} state. However, in the Pb spectra there is also a contribution at lower binding energy (137.0 eV), which is assigned to metallic lead (Pb_0) [27, 35, 176]. It needs to be noted that in the first few measurements, the intensity of this metallic lead peak were negligible and its intensity increased with the exposure time confirming beam damage due to X-rays. We believe that formation of metallic lead in the sample was a result of X-ray induced damage. Thus, any studies dealing with intense X-ray beam should be performed carefully as beam damage can alter the local stoichiometric composition and hence the properties of this hybrid perovskite material [176]. However, emergence of metallic lead feature has helped us in aligning the core levels, small feature from metallic lead (Pb_0) also appears at 137.0 eV for the $CH_3NH_3PbBr_3$ and $CH_3NH_3PbCl_3$ samples. However, the Pb $4f_{7/2}$ lines appear at binding energies of 138.7 eV, 138.9 eV and 139.1 eV for $CH_3NH_3PbI_3$, $CH_3NH_3PbBr_3$ and $CH_3NH_3PbCl_3$, respectively. Thus, a clear shift in binding energy of 0.4 eV is observed between $CH_3NH_3PbI_3$ and $CH_3NH_3PbCl_3$ for the Pb $4f_{7/2}$ level as shown in Figure 5.10 (c). Similarly, Pb $5d_{5/2}$ peak appears at a binding energy of 19.8 eV, 20.0 eV and 20.4 eV for $CH_3NH_3PbI_3$, $CH_3NH_3PbBr_3$ and $CH_3NH_3PbCl_3$ samples, respectively as depicted in Figure 5.10 (b). This result clearly indicate Pb $5d_{5/2}$ of $CH_3NH_3PbCl_3$ appear at a 0.6 eV higher binding energy than that of $CH_3NH_3PbI_3$ (Figure 5.10 (d)). However, Figure 5.10 (e) indicate Pb $4p_{3/2}$ level of all three compounds appear almost in same binding energy (645.3 eV). The relative binding energy shift of the Pb $4f$ and Pb $5d$ core levels in the two perovskites ($CH_3NH_3PbI_3$ and $CH_3NH_3PbCl_3$) can be rationalized from theoretical Z+1 approximation based on a charge analysis, which tells that Pb atoms have a much larger overlap with the iodine ions than with the chlorine ions and affects the binding energy of the Pb $4f$ and Pb $5d$ core levels [35]. Further, we believe that different screening of Pb $4f$ and Pb $5d$ levels are responsible for different shifts of the levels and detailed theoretical investigation is required to pin-down this point.

Valence band spectra of the $CH_3NH_3PbI_3$, $CH_3NH_3PbBr_3$ and $CH_3NH_3PbCl_3$ samples are shown in Figure 5.10 (f). Here the main feature between 2-6 eV binding energies arises due to the nonbonding I $5p$ orbitals [35, 268], along with dominant contributions

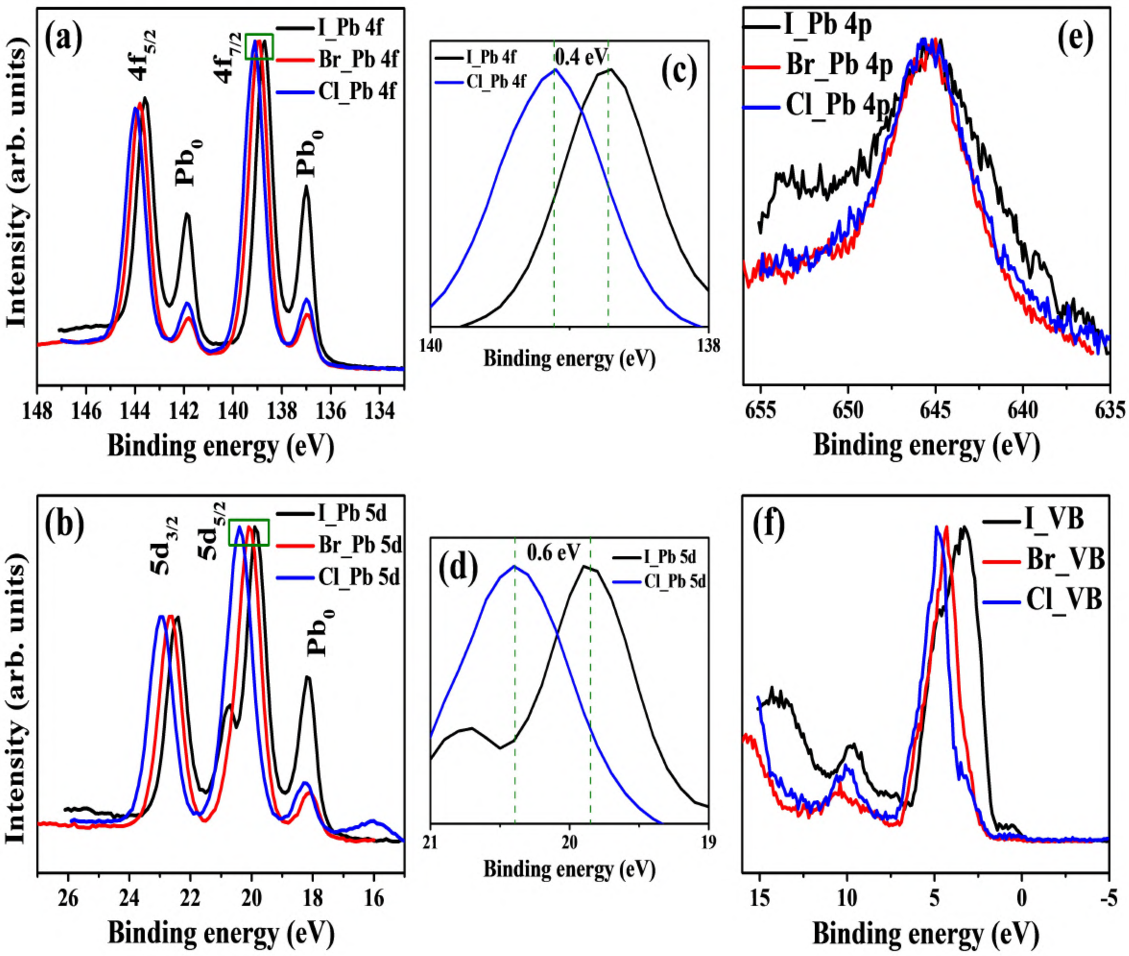

Figure 5.11: Measured (a) Pb 4*f* core level (b) Pb 5*d* core level (e) Pb 4*p* core level and (f) valence-band spectra of $CH_3NH_3PbI_3$, $CH_3NH_3PbBr_3$ and $CH_3NH_3PbCl_3$ samples collected at room temperature. Enlarged spectra of (c) Pb 4*f* (d) Pb 5*d* levels shows a noticeable shift between $CH_3NH_3PbI_3$ and $CH_3NH_3PbCl_3$ as indicated in the figure.

from anti-bonding states of Pb 6*s* and I 5*p* orbitals as well, as seen from various band structure calculations [35, 42, 272]. Energy of the top of the valence band edge (estimated from the intersection point of the linearly extrapolated experimental spectra with the base line) is obtained at 1.4 eV, 2.1 eV and 2.3 eV for $CH_3NH_3PbI_3$, $CH_3NH_3PbBr_3$ and $CH_3NH_3PbCl_3$, respectively. Detailed analysis of valence band spectra are discussed in the next section.

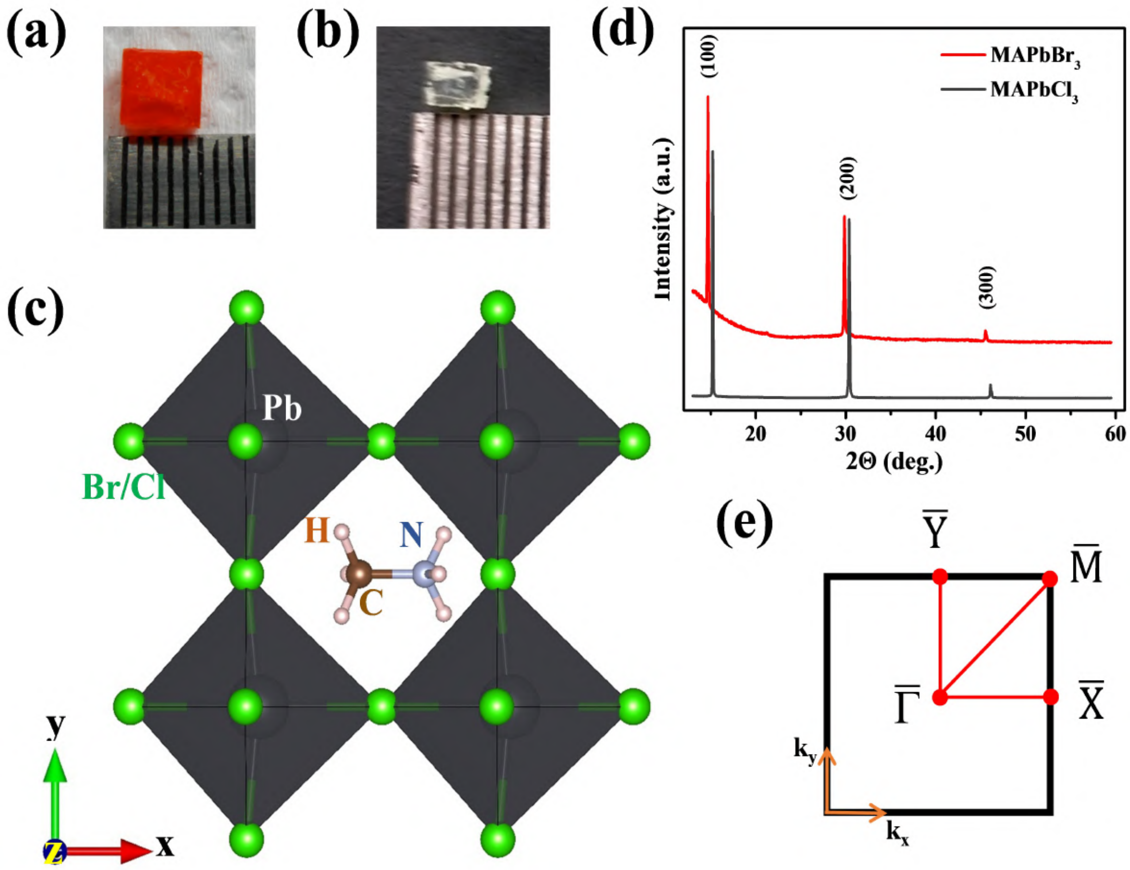

Figure 5.12: Image of (a) $CH_3NH_3PbBr_3$ and (b) $CH_3NH_3PbCl_3$ crystals grown using the antisolvent vapor-assisted crystallization (ASVAC) method at room temperature. (c) Cubic crystal structure of $CH_3NH_3PbX_3$ (X=Br, Cl) used for calculations. (d) X-ray diffraction of $CH_3NH_3PbX_3$ (X=Br, Cl) crystals on which ARPES experiment was performed. (e) Surface Brillouin zone of the cubic structure.

5.2.3.2 Ultra-violet Photoemission spectroscopy (UPS) Studies

Figure 5.11 (a) and (b) show images of the as grown samples of $CH_3NH_3PbBr_3$ and $CH_3NH_3PbCl_3$ single crystals, while figure 5.11 (c) shows the typical crystal structure of hybrid perovskite, with cubic symmetry (space group $Pm\bar{3}m$) at room temperature. Here CH_3NH_3 ion is polar and has C_{3v} symmetry, which results in a disordered cubic phase with site occupancies of $\frac{1}{4}$ for Cl/Br and $\frac{1}{12}$ for C and N [27,162]. XRD of the top surface of the crystals on which ARPES measurements were performed is depicted in figure 5.11 (d). Appearance of only (100) hkl plane and its higher order confirms (100) orientation of surface normal of the crystal. Figure 5.11 (e) represents the 2D cubic surface Brillouin zone for (100) orientation, as investigated by photoemission measurements. Due to cubic symmetry of the system $\overline{\Gamma}-\overline{X}$ and $\overline{\Gamma}-\overline{Y}$ directions are degenerate, hence, band dispersions are only recorded along $\overline{\Gamma}-\overline{X}$ and $\overline{\Gamma}-\overline{M}$ directions. Constant energy cuts were constructed by collecting photoemission intensity maps acquired over an azimuthal angular range of 45^0 in steps of 1^0 between $\overline{\Gamma}-\overline{X}$ and $\overline{\Gamma}-\overline{M}$ symmetry directions, and then symmetrizing them to get full two-dimensional contours.

5.2.3.2.1 Angle-integrated Photoemission

Angle integrated photoemission spectrum of $CH_3NH_3PbBr_3$ and $CH_3NH_3PbCl_3$ are depicted in figure 5.12 (a) with different photon energies. Valence band edges of these two compounds were extracted by extrapolating the experimental spectra with the baseline and the intersects are observed at binding energies of 2.16 and 2.48 eV for $CH_3NH_3PbBr_3$ and $CH_3NH_3PbCl_3$, respectively, i.e. top of the valence band for $CH_3NH_3PbCl_3$ is approximately 0.32 eV higher in energy than $CH_3NH_3PbBr_3$, which is in agreement with earlier reports [35, 176, 268]. Additionally, it is observed that the entire valence band spectrum including features between 8 to 10 eV for $CH_3NH_3PbBr_3$ are shifted to lower binding energy. The calculated total DOS of both the compounds are also presented in the bottom part of figure 5.12 (a). Ignoring the sharp delta-function like peaks associated with the electronic states of MA^+, and considering only the lead halide contributions to the experimental photo-electron spectrum, the Pb, Br and Cl atom projected density of states (PDOS) were analyzed and are presented in figure 5.12 (c) and (d) respectively. From the PDOS calculations, it is evident that both the halide and lead PDOS are shifted towards higher binding energies for the $CH_3NH_3PbCl_3$ perovskite (figure 5.12(c)-(d)), which is consistent with our experimental results. Different electron affinity and chemical bonding of halide ions are mostly responsible for this small binding energy shift [35].

To gain further insight into the orbitals involved in the process of hybridization, photoemitted intensity of the ejected electrons (density of states) was compared using different photon energies as shown in the Figure 5.12 (b) and is with photoionization cross-section (table 5.1). Increase of band edge intensity (feature A and A′) with incident photon energy (hν) and comparing the same with photo ionization cross-section as shown in Table 5.1 reveals that Pb-*s* state has significant contribution at the valence band edge, while the halogen *p* states make dominant contributions at B and B′. PDOS calculations are

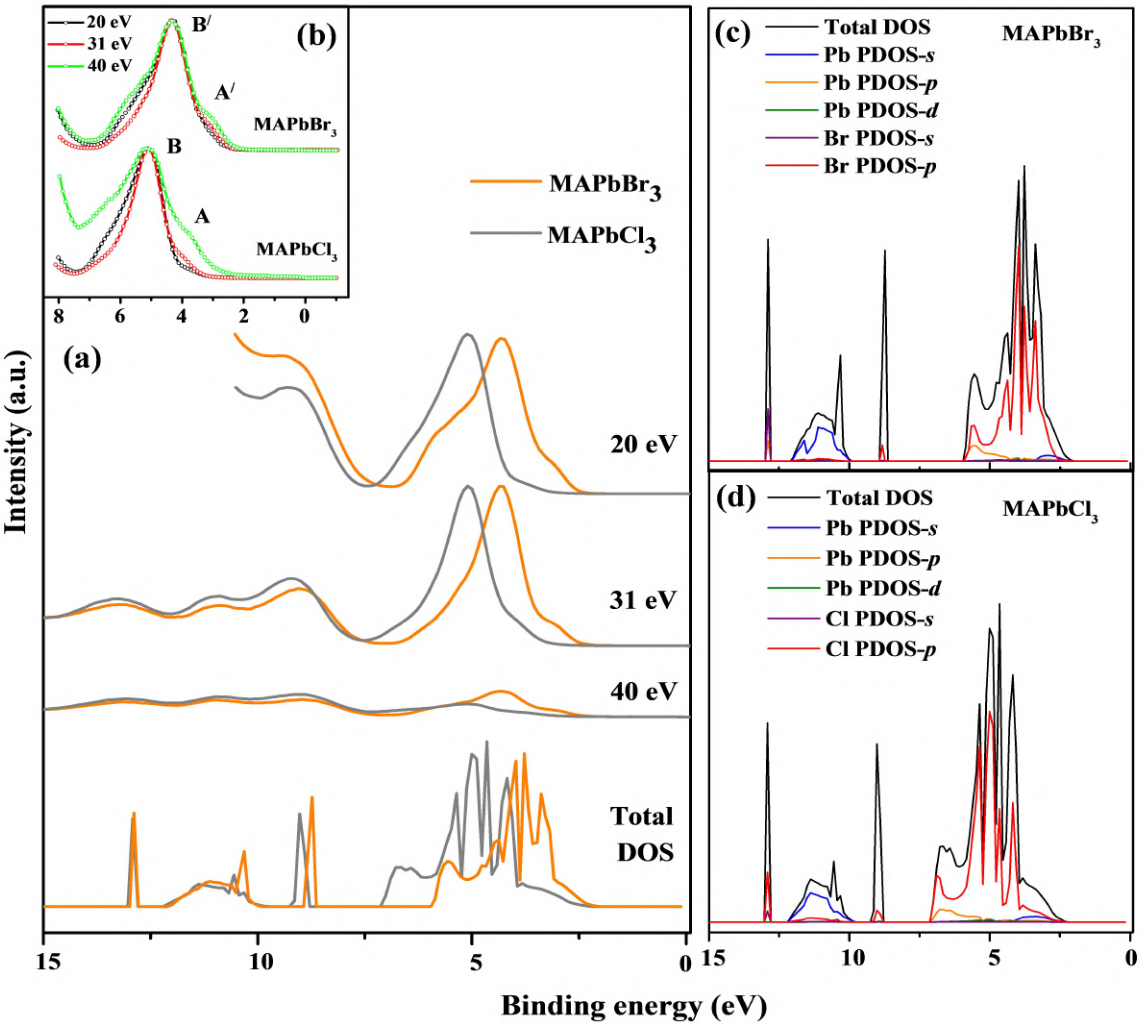

Figure 5.13: Experimental angle integrated valence band spectra (20, 31 and 40 eV) compared to calculated total DOS for $CH_3NH_3PbBr_3$ and $CH_3NH_3PbCl_3$. Inset to the figure shows all valence band spectra (with different photon energies) normalized and plotted in the same figure for comparison (b). Calculated total and orbital projected density of states for (c) $CH_3NH_3PbBr_3$ and (d) $CH_3NH_3PbCl_3$. The delta-function peaks come from the C and N atoms of the CH_3NH_3 molecule.

verified by the experimental findings and reveals that the major contributions to valence band arise from the Cl 3*p* or Br 4*p* orbitals, while contribution from Pb 6*s* orbital are also significant. This can be attributed to the covalency between the Pb-Br/Cl present in these systems as will be discussed later. Major contribution of the Pb-*s* states is also found well below 9 eV from the Fermi level, which can be understood in terms of bonding-antibonding levels resulting from Pb 6*s*-Br/Cl *p* hybridization. The bonding levels formed in this case are deep below the Fermi level (at $\sim$ 9 eV binding energy) and has dominantly Pb-*s* character, while the antibonding levels are close to the Fermi energy with predominantly Br/Cl-*p* character. Various aspects of this covalence will be discussed in details in the following sections.

Table 5.1: Photoionization cross-section

Energy level	20 eV	31 eV	40 eV
Pb 6*s*	0.0238	0.1240	0.1412
Cl 3*p*	19.86	1.2151	0.6325
Br 4*p*	19.85	3.1982	1.046

5.2.3.2.2 Angle-Resolved Photoemission

Figure 5.13 (a) and (b) displays the 1st derivative of ARPES intensity map along $\overline{X}-\overline{\Gamma}-\overline{M}$ symmetry direction for $CH_3NH_3PbCl_3$ and $CH_3NH_3PbBr_3$ respectively showing the experimental band structure. Strongly dispersing downward band around $\overline{X}$ and $\overline{M}$ symmetry points with dispersion reaching minimum at $\overline{\Gamma}$ point is observed. Absence of any spectral density between E_F and above the top of the stated bands, suggests that the maximum of the valence band projected onto the (100) plane, lies at binding energy of 2.4 eV (2.1 eV) at the $\overline{M}$ point while the band peaks at 3.1 eV (2.4 eV) at the $\overline{X}$ point for $CH_3NH_3PbCl_3$ ($CH_3NH_3PbBr_3$). Large weakly dispersing spectral weight is observed around 4.6 eV (4.1 eV) at the zone center ($\overline{\Gamma}$ point) and below 4.2 eV (3.6 eV) at the two zone edges ($\overline{X}$ and $\overline{M}$ point) of $CH_3NH_3PbCl_3$ ($CH_3NH_3PbBr_3$) which is denoted by D-E (D′-E′) in figure 5.13 (a) ((b)). Noticeably, the parallel component of surface momentum ($k_{\|}$): $\overline{X}$ point is at 0.67 Å^{-1} (0.53 Å^{-1}) and $\overline{M}$ point is at 0.83 Å^{-1} (0.75 Å^{-1}) for $CH_3NH_3PbCl_3$ ($CH_3NH_3PbBr_3$). These observed values of $k_{\|}$ are in good agreement with the values calculated from lattice parameters [41, 103, 176]. To gain insight into the orbital characters of the bands DFT calculated band structure for $CH_3NH_3PbCl_3$ and $CH_3NH_3PbBr_3$ were analyzed and are depicted in figure 5.13 (c) and (d) respectively with fat band representation for Pb *s* and halide *p* orbitals. For the highest occupied valence band at $\overline{X}$, $\overline{M}$ and $\overline{\Gamma}$ points, it is observed that the bands at the $\overline{X}$ point have

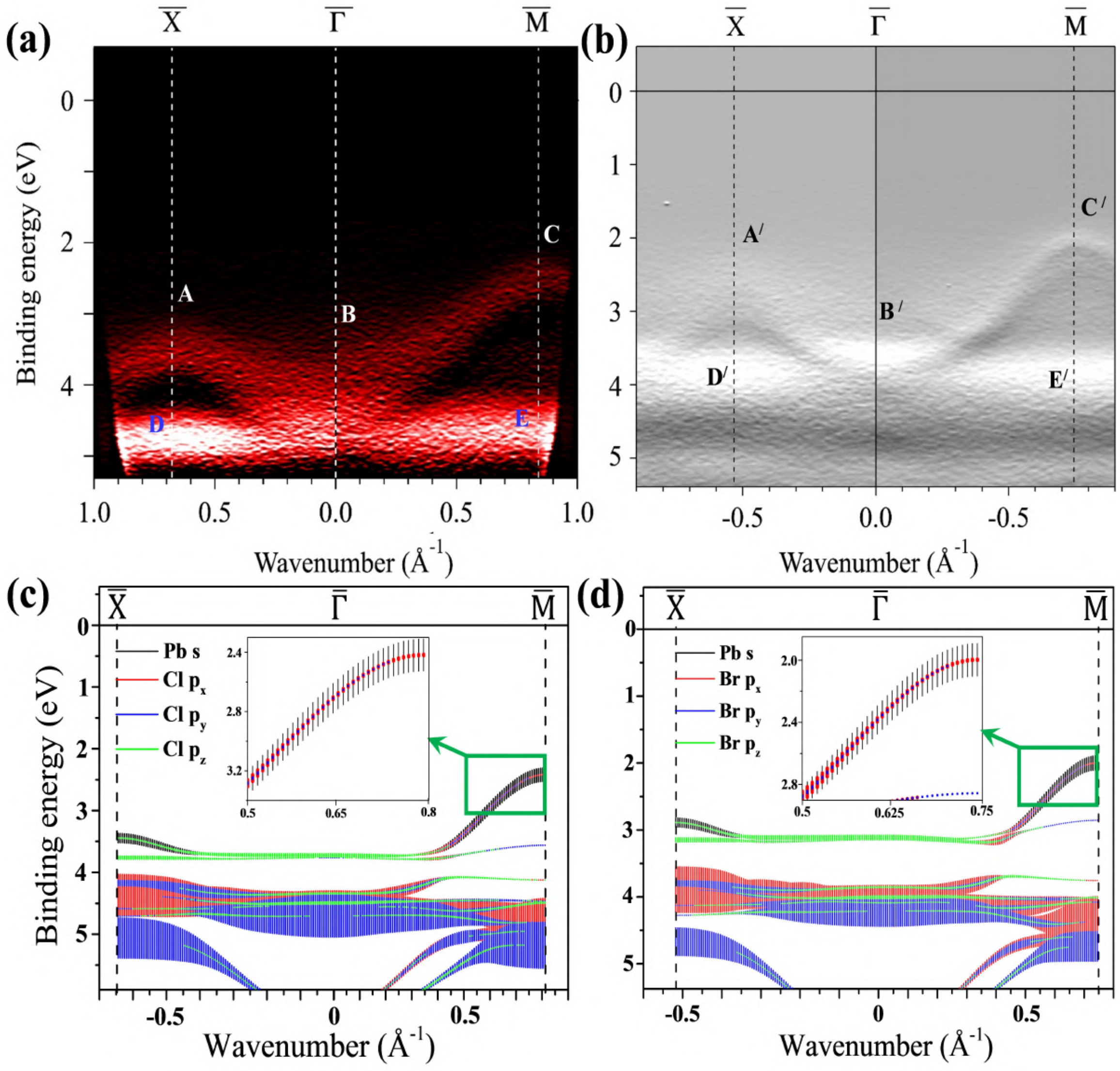

Figure 5.14: Electronic band structure of (a,c) $CH_3NH_3PbCl_3$ and (b,d) $CH_3NH_3PbBr_3$. (a,b) Experimental data obtained from angle-resolved photoemission spectroscopy (ARPES), acquired at a photon energy of 37 eV; (c,d) Calculated band structure data.

contributions from the Pb-s orbital and Cl/Br-p orbitals. The same set of orbitals also contribute to the valence band maximum at $\overline{M}$ point with the difference that at $\overline{X}$ point only the Cl/Br-p_y has substantial contribution while at $\overline{M}$ point both p_y and p_x of Cl/Br atoms orbitals contribute equally to the valence band maximum. However, the highest occupied band at $\overline{\Gamma}$ point entirely has the Cl/Br-p_z character. This analysis also highlights the nature of Pb-Cl/Br covalency, which can be understood by calculating the charge densities at $\overline{X}$, $\overline{\Gamma}$ and $\overline{M}$ points for the highest occupied bands. A plot for the same has been shown in Figure 5.14 for $CH_3NH_3PbCl_3$. In Figure 5.14 (a), the charge density at $\overline{X}$ is plotted for the valence band maximum. It can be observed that at $\overline{X}$ point, the Pb-s and Cl-p_y orbitals are contributing to the valence band maximum while contribution from other Cl-p orbitals are minimal/absent. At $\overline{\Gamma}$ point (Figure 5.14 (b)), only the Cl/Br-p_z orbital is contributing and no $s-p$ (Pb-Cl) hybridization is observed. Further, at $\overline{M}$ point (Figure 5.14 (c)), valence band maximum has contribution from Pb-s as well as Cl-p_x and p_y orbitals at valence band maximum. The same analysis was also done for $CH_3NH_3PbBr_3$ (not shown here) and similar results were observed in that case too. It can hence be concluded from the above analysis that the Pb-Cl/Br covalency is highest at the $\overline{M}$ point and it gradually decreases as $\overline{\Gamma}$ point is approached. At $\overline{\Gamma}$ point covalent character is absent and it again increases when $\overline{X}$ point is approached. A schematic representation of bonding-antibonding hybridization between Pb s and Cl/Br p is shown in figure 5.14 (d), clearly visualizing the orbital contributions to the valence and conduction bands of hybrid perovskites.

From reported literature it is known that CH_3NH_3 orientation has profound effect on the electronic band structure of hybrid perovskite [45]. For configurations where the $CH_3NH_3^+$ cations are oriented parallel to each (polar or ferroelectric ordering), the [100] orientation is favored [186, 187]. In this structure the internal field generated by the CH_3NH_3 cations lowers the cubic symmetry and gives rise to partial removal of the nine

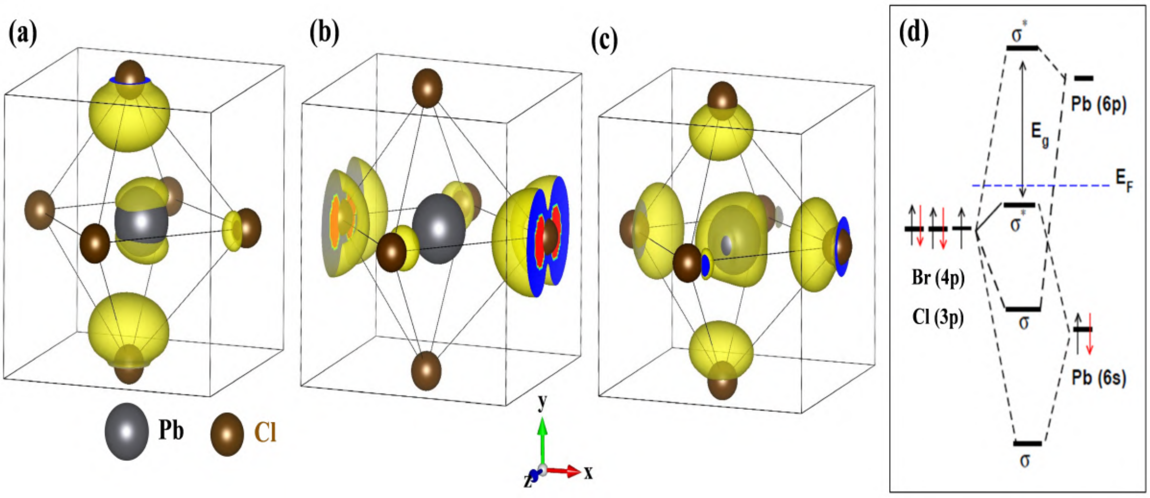

Figure 5.15: The charge density plot of $CH_3NH_3PbCl_3$ at (a) $\overline{X}$ point, (b) $\overline{\Gamma}$ point and (c) $\overline{M}$ point. (d) Schematic representation of $s-p$-hybridization in hybrid perovskites.

fold degeneracy of Cl p-Pb s band, even in the absence of spin-orbit coupling. (Figure 5.15 (a)). Although the picture extracted from our calculations reveals a ferroelectric-like arrangement of the CH_3NH_3 cations as the most stable configuration it also suggests a potentially disordered arrangement of both the orientation of MA^+ cation and of the $PbBr_6$ octahedra, which may dynamically interconvert at room temperature. Notably, rotating the MA molecule along (110) direction (60^0) with respect to (100) direction results in a decrease of bandgap by an amount of 40 meV, which clearly indicates that the orientation of MA^+ ion plays an important role in the electronic band structure. It is widely believed that in the cubic phase CH_3NH_3 cations are dynamically disordered and move in a nearly isotropic potential at a rate approaching that of the freely rotating CH_3NH_3 cation [285]. However, ab-initio electronic structure calculations for such a hindered rotating system is not possible at the present time. One possible way out is direct configuration averaging, where multiple calculations could be performed by considering different orientation of CH_3NH_3 molecule and averaging out the results. Knowing how many possible orientations and finding their statistical weightage for averaging is a challenging task. Else code involving the coherent-potential approximation in DFT to average over the ensemble of various molecular orientations can be used. In absence of such code (with us), we replaced orientationally disordered CH_3NH_3 molecule by spherically symmetric Cs ion and the electronic band structure of $CsPbCl_3$ is presented in Figure 5.15 (b). Interestingly it is observed that 9 fold degeneracy of $CH_3NH_3PbCl_3$ at $\overline{\Gamma}$ point (Figure 5.15 (b)) has reduced to conventional 3 fold degeneracy of Cl p bands for $CsPbCl_3$ which is close to the experimental observation of degenerate bands near the $\overline{\Gamma}$ point with in the experimental resolution, suggesting disordered nature of the CH_3NH_3 ions.

A more detailed look at the calculations of the two systems (i) $CH_3NH_3PbCl_3$, which represents an oriented CH_3NH_3 bond and (ii) $CsPbCl_3$ which suggests an isotropic potential created by disordered CH_3NH_3 orientation, for the top few bands in the valence band, for two cases i.e. with and without SOC is presented in figure 5.16. Rashba type spin-orbit split bands are observed at the $\overline{\Gamma}$ point for the oriented CH_3NH_3 structure when SOC is considered (Figure 5.16 (c)) while no such effect is observed (Figure 5.16 (d)) when disordered nature of CH_3NH_3 molecule is considered in the form of spherical potential (by replacing CH_3NH_3 by CS). More importantly, bands continue to remain doubly degener-

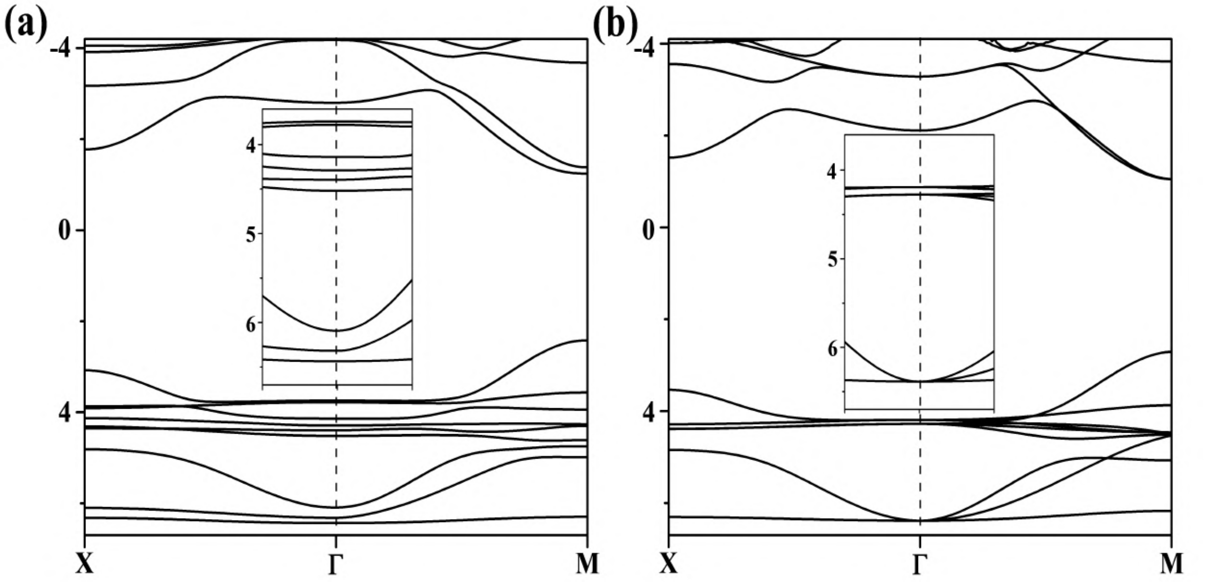

Figure 5.16: Calculated band structure of (a) $CsPbCl_3$ and (b) $CH_3NH_3PbCl_3$; Inset shows the zoomed view near to Γ point.

ate at the $\overline{M}$ and $\overline{X}$ symmetry point at all cases. These results are in direct disagreement with experimentally claimed giant Rashba splitting observed in $CH_3NH_3PbBr_3$ by Niesner *et al.* [103] by angle- resolved photoemission spectroscopy (ARPES) where authors have interpreted ring shaped band contours observed at valence band maxima (i.e. at $\overline{M}$ point) and have associated the same with the splitting of a doubly spin degenerate bands into two bands shifted with respect to each other in k space. Theirs is an isolated result wherein Rashba splitting (if any) is claimed at the $\overline{M}$ point. Che et. al. also investigated the possibility of Rashba effect for 2 × 2 surface reconstructions of $CH_3NH_3PbBr_3$ using first-principles calculations and suggested occurrence of surface-induced Rashba effect but (i) at the $\overline{\Gamma}$ point and (ii) with much smaller amplitude for specific orientation of CH_3NH_3 molecule in line with our results [278]. Frohna *et al.* [286] also predicted that Rashba effect in hybrid perovskite arises due to the net electric field from many randomly oriented polar CH_3NH_3-ions, which was also supported by McKechnie *et al.* [287] These results clearly indicate that the valence band splitting arises due to relativistic spin-orbit coupling in the presence of local asymmetry and "A"-site cation plays a steric role here.

5.2.3.2.3 Constant Energy Contour Mapping

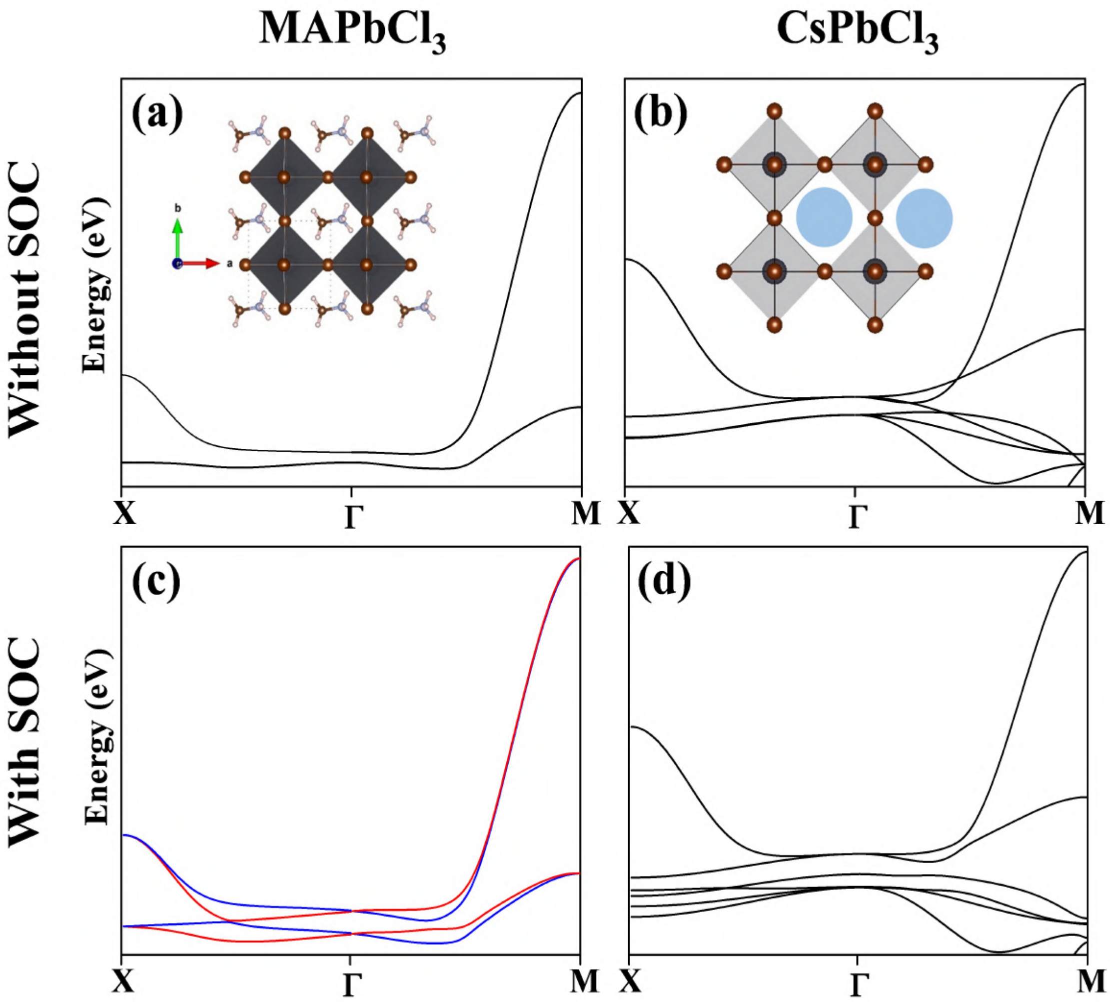

Figure 5.17: Calculated band structure of (a), (b) $CH_3NH_3PbCl_3$ (without and with spin-orbit coupling (SOC)) and (c), (d) $CsPbCl_3$ (without and with SOC).

As ARPES derived intensity maps or constant energy contours provides a direct picture of the electronic bands and is an excellent probes to check the theoretical calculations. We present constant energy plots (iso-energy cuts) derived from 3D band mapping of $CH_3NH_3PbCl_3$ at some selective binding energies in Figure 5.17 (a-h). At 2.35 eV below the Fermi edge (Figure 5.17 (a)), appearance of spectral density in the form of single dot at $\overline{M}$ symmetry point suggests mapping of the top of the valence band. With increasing binding energy dot evolves into a closed band contour. Shape of the band contour is decided by the extend of $s-p$ hybridization of the Pb 6s and Cl 3p orbitals [284]. At

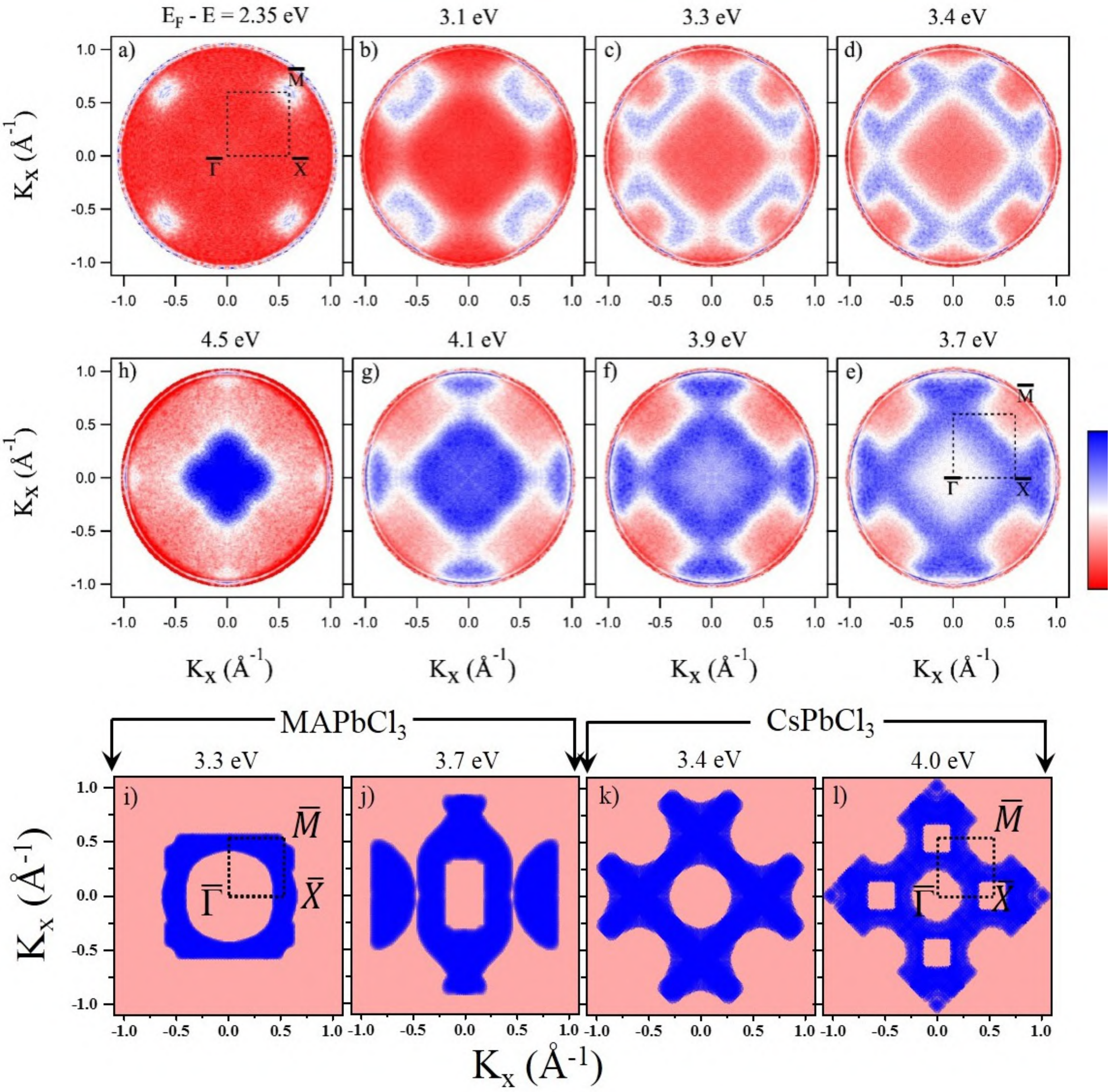

Figure 5.18: (a-h) Constant energy contour of the electronic structure in the plane at different binding energies marked in the figure. Corresponding energy cut from theoretical spectra of (i-j) $CH_3NH_3PbCl_3$ and (k-l) $CsPbCl_3$ are shown below.

around 3.7 eV binding energy, top of the valence band at $\overline{X}$ point appears in the iso-energy cut. Further increase of binding energy, resulted into a cubical band contour around the $\overline{\Gamma}$ point (3.7 – 3.9 eV) with maximum intensity observed at $\overline{\Gamma}$ at $\sim$ 4.5 eV arising from Cl-p_z. orbital. Niesner *et al.* [103] in their ARPES constant maps for $CH_3NH_3PbBr_3$, taken at the top of the valence band maximum, ie, at $\overline{M}$ point for the cubic phase observed a ring shaped contour, with a minimum spectral intensity at the center. This feature around $\overline{M}$

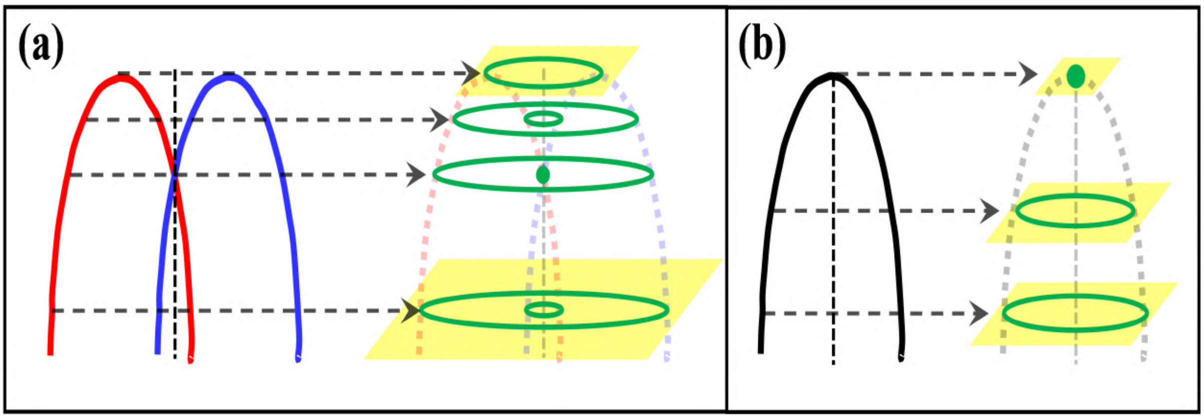

Figure 5.19: Effect of SOC and the resulting Rashba effect on constant energy contour curves (Schematic). (a) In the presence of SOC, valence band (VB) splits into two spin-split bands and corresponding contours at different energies. (b) Without SOC, a doubly spin-degenerate band with a single maximum is expected.

point with a dip at the center was interpreted (as shown in the schematics Figure 5.18 (a)) as arising due to two spin-split bands shifted with respect to each other in k space due to Rashba splitting. However, with in our experimental resolution (for $CH_3NH_3PbCl_3$) we did not observe any drop in the spectral intensity at the top of the valence band maxima (ie. at $\overline{M}$ point) and observed a single ring shaped band contour (Figure 5.15 (b-d)) around $\overline{M}$ symmetry point corresponds to a single downward dispersing band (as suggested in schematic Figure 5.18 (b)) which does not support the idea of Rashba spin-split bands for which concentric bands were expected with increasing energy (figure 5.18 (b)) [288]. Inclusion of spin-orbit coupling in the theoretical calculations though suggests spin-split bands at $\overline{\Gamma}$ point but in most of these calculations disordered nature of CH_3NH_3 molecule is not accounted and calculations are performed with a specific configuration / orientation of CH_3NH_3 molecule also these calculations predicts much smaller band gap than the experimental one [273, 277]. Our results hence gain significance as they suggests that spin-orbit splitting is not a dominating effect, at least in cubic phase. While comparing the experimental constant energy contour with the theoretical one (for $CH_3NH_3PbCl_3$, Figure (5.17 (i-j)), we observe a continuous symmetry breaking in the system. Calculated constant energy contour at 3.3 eV and 3.7 eV are (i) not symmetric about the $\overline{M}$ point and (ii) bands about $\overline{X}$ point are different in the same iso-energy contour. In searching the probable reason behind this anisotropic behavior, we suggest that ferroelectric-like arrangement of $CH_3NH_3^+$ ion in electronic band structure calculation is predominantly responsible for this mismatch as discussed earlier. To counter the directional dependence of $CH_3NH_3^+$ ion as $CH_3NH_3^+$ ion is believed to be disordered, we compare our experimental constant energy contour with $CsPbCl_3$ where Cs ion is symmetric (Figure 5.17 (k-l)). Results of our constant energy contour at 3.4 eV and 4.0 eV matches relatively better with the experimental energy contours of $CH_3NH_3PbCl_3$ at 3.3 eV and 3.9 eV. Thus, the comparative of valence band dispersion between ferroelectric-like (100) direction oriented $CH_3NH_3PbCl_3$ and spherically symmetric ordered $CsPbCl_3$ reveal the real physics of electronic band structure in cubic phase is somewhere between the two; which can be understood by performing coherent-potential approximation in DFT to average over the ensemble of various atomic configurations and provide an average band structure.

5.2.3.2.4 Effective Mass and Mobility of Hybrid Perovskites

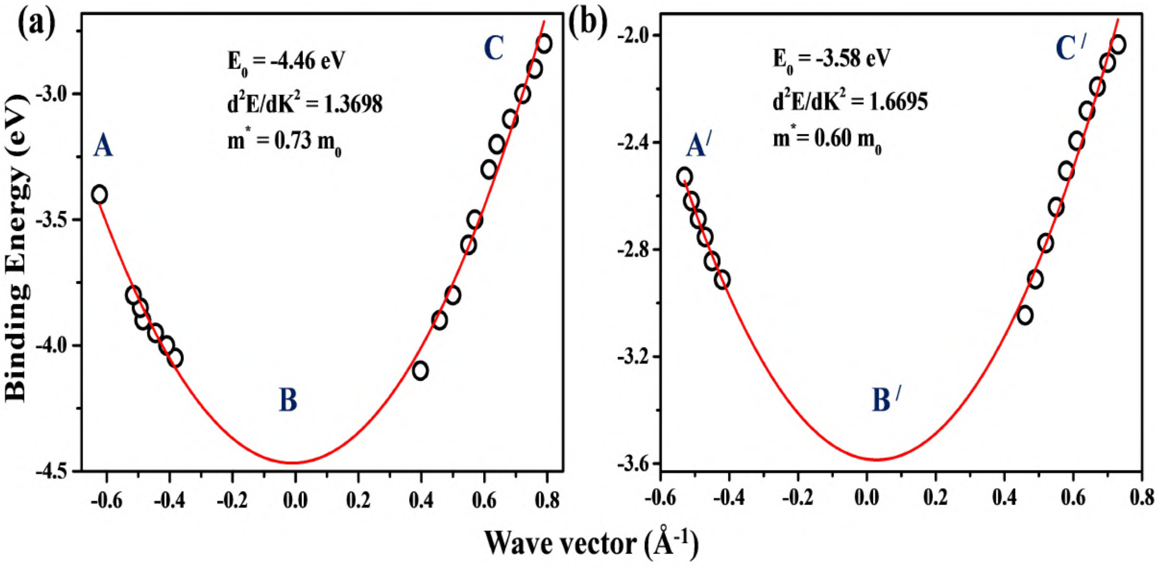

Figure 5.20: Dispersion of ABC band of (a) $CH_3NH_3PbCl_3$ and (A′B′C′) of (b) $CH_3NH_3PbBr_3$ single crystal. The red line denote parabolic fit of these bands.

In addition, effective mass and carrier mobility, two important parameters for the evolution of hybrid perovskite materials as a channel material in high-speed field effect transistor and other optoelectronic applications can also be derived from band dispersions

[289–291]. From the valence band dispersion of first band we have extracted binding energy of the band center and effective mass along $\overline{X}-\overline{\Gamma}-\overline{M}$ direction for $CH_3NH_3PbCl_3$ and $CH_3NH_3PbBr_3$ as shown in figure 5.19 (a) and (b), respectively. Parabolic fitting yields effective mass for $CH_3NH_3PbCl_3$ and $CH_3NH_3PbBr_3$ is 0.73 m_0 and 0.60 m_0 (m_0 is the free electron mass) along $\overline{X}-\overline{\Gamma}-\overline{M}$ direction, whereas theoretical estimated values are 0.51 m_0 and 0.44 m_0 respectively. Further, using one-dimensional tight-binding approximation, effective mass and carrier mobility along $\overline{\Gamma}-\overline{X}$ and $\overline{\Gamma}-\overline{M}$ can also be extracted from figure 5.19 (a) and (b) as follows:

$$E_B = E_0 - 2tcos\big(ak_\parallel\big) \tag{5.6}$$

where 'E_0' is the band center binding energy, 't' is the transfer integral and 'a' is the lattice spacing. Using this formula, t is estimated as 0.533 eV (0.527 eV) along $\overline{\Gamma}-\overline{X}$ and 0.833 eV (0.774 eV) along $\overline{\Gamma}-\overline{M}$ direction for $CH_3NH_3PbCl_3$ ($CH_3NH_3PbBr_3$). Further, the effective hole mass can be extracted by the formula:

$$m_h^* = \frac{\hbar^2}{2ta^2} \tag{5.7}$$

Here m_h^* is the effective hole mass, 't' and 'a' are the transfer integral and lattice spacing, respectively. Extracted value of effective hole mass is found to be 0.87 m_0 (0.81 m_0) (m_0 is the free electron mass) along $\overline{\Gamma}-\overline{X}$ and 0.57 m_0 (0.53 m_0) along $\overline{\Gamma}-\overline{M}$ for $CH_3NH_3PbCl_3$ ($CH_3NH_3PbBr_3$). As the band width of both the samples are larger than k_BT (26 meV), the lower limit of hole mobility along above two directions are estimated using the formula:

$$\mu_h > 20\left(\frac{m_0}{m_h^*}\right)\left(\frac{300}{T}\right) \tag{5.8}$$

Here μ_h, m_0, m_h^* and T are hole mobility, free electron mass, effective hole mass and temperature, respectively. The extracted value of hole mobility is found to be 22.98 $cm^2V^{-1}s^{-1}$ (35.09 $cm^2V^{-1}s^{-1}$) along $\overline{\Gamma}-\overline{X}$ and 24.87 $cm^2V^{-1}s^{-1}$ (37.45 $cm^2V^{-1}s^{-1}$) $\overline{\Gamma}-\overline{M}$ for $CH_3NH_3PbCl_3$ ($CH_3NH_3PbBr_3$), respectively. These extracted values of hole mobilities are comparable with the previous reports, where they were extracted the hole mobility of hybrid perovskites from photoluminescence (19.4 to 56.1 $cm^2V^{-1}s^{-1}$) [292], dark current-voltage measurements (24 to 42 $cm^2V^{-1}s^{-1}$) [99, 100], hall effect measurements (20 to 60 $cm^2V^{-1}s^{-1}$) [102] and time of flight measurements (115 $cm^2V^{-1}s^{-1}$) [45, 102]. We believe that extracted charge carrier mobilities from valence band dispersion of perovskite single crystals will help to understand intrinsic and extrinsic limit of charge carrier mobilities.

5.2.4 Conclusion

Electronic structures of $CH_3NH_3PbX_3$ (X = I, Br and Cl) are addressed using photoelectron spectroscopy. We assert that DFT-based medeling and the computation of DOS spectra led us to rationalize the correct trends in corresponding valence band spectra successfully. We also speculate that the core level shift of Pb 4f and Pb 5d levels is the nature of the halide ions rather than the geometrical configuration of the perovskites. Further, we have presented a comparative study of valence band dispersion between $CH_3NH_3PbCl_3$ ($CH_3NH_3PbBr_3$) using photoemission (both angle-integrated and angle-resolved) and DFT based computational study. Excellent agreement between theory and experimental results help us to present a clear picture about the spectral contributions at the top of the valence band. These results suggest strong band dispersion at the valence band arise due to hybridization between halide (Cl/Br)-p and Pb s antibonding orbitals. The charge density and constant energy contour mapping of hybrid perovskites allow us to visualize the valence band maxima in reciprocal space in an instructive way, thus demonstrating the orbital contributions at $\overline{\Gamma}$ (only halide-p_z), $\overline{M}$ (Pb-s as well as halide-p_x and p_y) and $\overline{X}$ (hybridization between Pb-s and halide-p_y) points. The measured band dispersion also help us to extract effective hole mass and lower limit of hole mobility using one-dimensional tight binding model for both the compounds. We believe that our findings will help in fine-tuning the energy-matching at several interfaces, and in turn the performance of the solar cell and optoelectronic devices.

Chapter 6

Temperature Dependent Photo induced Phase Separation in Mixed Halide Perovskite

---

Even though tandem solar cells comprised of mixed-halide perovskites $CH_3NH_3Pb(I_{1-x}Br_x)_3$ *were expected to have much higher efficiency, the observation that they undergo photoinduced phase separation/demixing put forth a limitation to their possible utility. In this chapter of thesis, we show that the stated photoinduced phase separation occurs only in a narrow temperature range and above a particular bromine concentration using temperature dependent photoluminescence studies. Our observation of the disappearance of phase separation at elevated temperatures suggests the possibility that these tandem solar cells may indeed work better at elevated temperatures. Further, we provide the first experimental proof for the demixing transition temperature as predicted by Bischak et al. and also observe that demixing and remixing temperatures are pinned to crystallographic phase transition temperatures. Longer carrier lifetime of iodide-rich clusters is observed confirming the strong electron-phonon interaction (polaronic effect) which is absent in the initial mixed states.*

6.1 Introduction

In recent years, $CH_3NH_3Pb(I_{1-x}Br_x)_3$; organic-inorganic mixed lead halide perovskite polycrystalline thin films have generated a surge of excitement for device applications owing to their large absorption coefficients [11], long carrier lifetimes and diffusion lengths [21,22,75,76], and an insensitivity to structural defects [94,95]. Easy solution processability [90] and completely tunable optical bandgap from blue to red regions of wavelength just by changing the halide ion concentration [20], makes the family of mixed halides pervoskites, $CH_3NH_3Pb(I_{1-x}Br_x)_3$, $(0 \leqslant x \leqslant 1)$ potential candidates for applications in multijunction/tandem solar cells [185,293–298] and tunable LEDs [11,20]. It was prediced that coupling of perovskite material with commercially available Si [185, 293–296], Germanium [297] and Copper indium gallium selenide (CIGS) cells [298] could increase the cell efficiency compared to the respective single junction cells. However, when mixed-halides perovskite was employed as solar cell absorber layers by replacing some I with Br, the increase in bandgap (of the perovskite material) did not yield a corresponding increase in open circuit voltage. Subsequently, Hoke et *al.* reported that mixed I/Br perovskites underperform as illumination induces a strong and reversible band gap feature (at lower band gap) which disappeared after several minutes in dark (referred as Hoke effect) [299]. Such insatiability arises due to light induced halide phase separation that leads to the formation of smaller-bandgap “trap” states [54, 73, 299–309]. However, the mechanism driving phase separation and remixing were not well understood by the Hoke effect [73, 303, 304]. D. W. de Quilettes *et al.* also observed a strong correlation between redistribution of iodine away from illuminated region and an increase of photoluminescence (PL) emission peak intensity with illumination time for $CH_3NH_3PbI_3$ films which produced a strong visual demonstration of light induced halide migration [304].

Recently, by combining cathodoluminescence (CL) with scanning electron microscope (SEM) studies Bischak *et al.* showed that small clusters enriched with one halide species get localized near the grain boundaries after prolonged illumination and ascribed this to photogenerated charge carriers and their accompanying lattice distortion, polarons [73]. They argued that photoinduced nanoscale phase separation was mediated through the strain generated by the polaron and provided a rather convincing support for this picture by carring out Molecular Dynamics (MD) simulations both in the absence and in the presence of hole polarons. In addition, they also corroborated this using a Landau theory of atomic phase separation (Br-rich and I-rich) in the presence of excited charge carriers. It was predicted that after continuous illumination, the halide ions get excited and come closer to Pb atoms and a demixed trap state was formed only after applying certain thermal energy. Their MD simulations also suggested that when photoinduced charged excitations generate sufficient local strain, the solid solution phase gets destabilized and a demixed phase appears containing nanodomains, rich in one of the halide ions. The trapped electronic states associated with these nanodomains (due to the dependence of bandgaps on the alloy concentration) play an important role in stabilizing this phase separation. It must here be noted that an actual experimental verification of the critical temperature at which demixing and mixing occurs is due. Since the lifetime of the trapped carriers are strongly temperature dependent, we believe that a temperature dependent study of light induced phase separation in mixed halide perovskite is essential for future advances to mitigate photoinduced effects in these devices. In addition, such a study can provide new opportunities for expanding the functional applications like, sensing, switching and optical memory.

In the present work, we have focussed on understanding the temperature dependence of photoinduced phase separation of $\mathrm{CH_3NH_3Pb(I_{1-x}Br_x)_3}$ (for x = 0.15, 0.24 and 0.27) by employing steady state photoluminescence. We find that the phase separation scenario is valid only in a narrow temperature window and above a certain concentration of Br. Further, by optimizing the film preparation we could enhance the phase separation time, suggesting that larger grains and lower vacancy concentrations may improve phase stability and effectively eliminate phase segregation.

6.2 Experimental Details

6.2.1 Materials

Hydroiodic acid (HI) (57 wt.% in water), hydrobromic acid (HBr) (48 wt.% in water), methylamine (CH_3NH_2) (40 wt.% in water), $PbBr_2$ (99.99%), PbI_2 (99.99%), gamma-

Butyrolactone (GBL, 99.9%) were purchased from Sigma-Aldrich and used as received without further purification.

6.2.2 Synthesis of $CH_3NH_3Pb(I_{1-x}Br_x)_3$ Crystals/thin films

Single crystals of CH_3NH_3Br (CH_3NH_3I) was synthesized by reacting CH_3NH_2 and HBr (HI) in a molar ratio of 1.2:1. HBr (HI) was then added dropwise into the CH_3NH_2 in a flask under nitrogen atmosphere in an ice bath for 3 hours; the resulting solution was evaporated at 60degC in a rotary evaporator to remove the unreacted solvent and white crystals of CH_3NH_3X (X= Br, I) were obtained. To grow single crystals of $CH_3NH_3Pb(I_{1-x}Br_x)_3$, precursor solution with 1 M PbI_2, (1-x) M CH_3NH_3I and x M CH_3NH_3Br was prepared in 1 M GBL. The temperature of $CH_3NH_3Pb(I_{1-x}Br_x)_3$ solution was increased to 95degC and maintained at the temperature until desired $CH_3NH_3Pb(I_{1-x}Br_x)_3$ single crystals formed. Thin films were fabricated on Cleaned FTO glass substrate from single crystals by dissolving them in GBL (40% wt.) and by spin-coating at 2000 rpm for 60 seconds.

6.2.3 Single crystal/powder XRD and SEM

Crystals were mounted on a Hampton cryoloop for single crystal XRD measurements on an Oxford Xcalibur (Mova) diffractometer equipped with an EOS CCD detector using Mo K_α radiation (λ= 0.71073). Data collection, data reduction and numerical absorption corrections were performed using the programs present in the CrysAlisPro software suite [111]. Crystal structures were refined by using SHELXL-97 [112] program present in WinGX suit [113]. Powder X-ray diffraction of bulk and thin film samples were performed in Bruker D8 Advance X-ray diffractometer using CuK_α radiation (λ= 1.5406) equipped with Phenix Oxford closed cycle helium cryostat for temperature dependent studies. The grain sizes of the thin film prepared from single crystal dissolved solution and MAI+MABr+PbI_2 precursor solution were investigated using a field-emission scanning electron microscope (FESEM; Neon 40 cross-beam system, MS Carl Zeiss GmbH).

6.2.4 Temperature Dependent Photoluminescence

Steady state photoluminescence spectra were acquired using an Edinburgh FLS920 spectrometer, using an excitation energy of 325 nm from Xenon lamp with light intensity 1.5 mW/cm^2, while the sample was mounted on Oxford Instruments OptistatDN cryostat (vacuum $\sim$ 4.3 X 10^{-3} mbar) for temperature dependent studies. Further, excitation wavelength and light intensity dependent PL measurements were performed using Xenon lamp with different wavelengths and light intensity using neutral density filter. Time resolved PL experiment was performed on the same FL 920 spectrometer by means of time correlated single photon counting (TCSPC) method using a pulsed diode laser of wavelength 375 nm.

6.3 Results and Discussion

6.3.1 Structural Studies

Conventional method to prepare $CH_3NH_3Pb(I_{1-x}Br_x)_3$ thin films is by dissolving constituent elements (PbI_2, MAI, MABr and $PbBr_2$) in appropriate ratio in either Dimethylformamide (DMF) or gamma-Butyrolactone (GBL). However, maintaining homogeneity and precise stoichiometry of films prepared by this method is tricky as the solubility of PbI_2+MAI is greater in GBL and the solubility of $PbBr_2$+MABr is more in DMF than in other solvents, which may affect the final outcome. Alternatively, to fabricate high quality large-grained perovskite thin films with an improved phase purity and better reproducibility, single-crystals of $CH_3NH_3Pb(I_{1-x}Br_x)_3$ were dissolved in GBL and were used as a precursors [310–313]. The stoichiometric ratios of halides in single crystals and thin films were confirmed by single crystal and powder XRD using different electron cloud density of I and Br as indicated in Table 4.1. Besides this, careful temperature dependent powder X-ray diffraction measurements and Rietveld refinements were performed to understand the crystal structure and crystallographic phase transition temperatures.

Figure 6.1 (a) shows the room temperature (300 K) powder X-ray diffraction patterns of single crystal sample (crushed in powder form before measurements) for three different

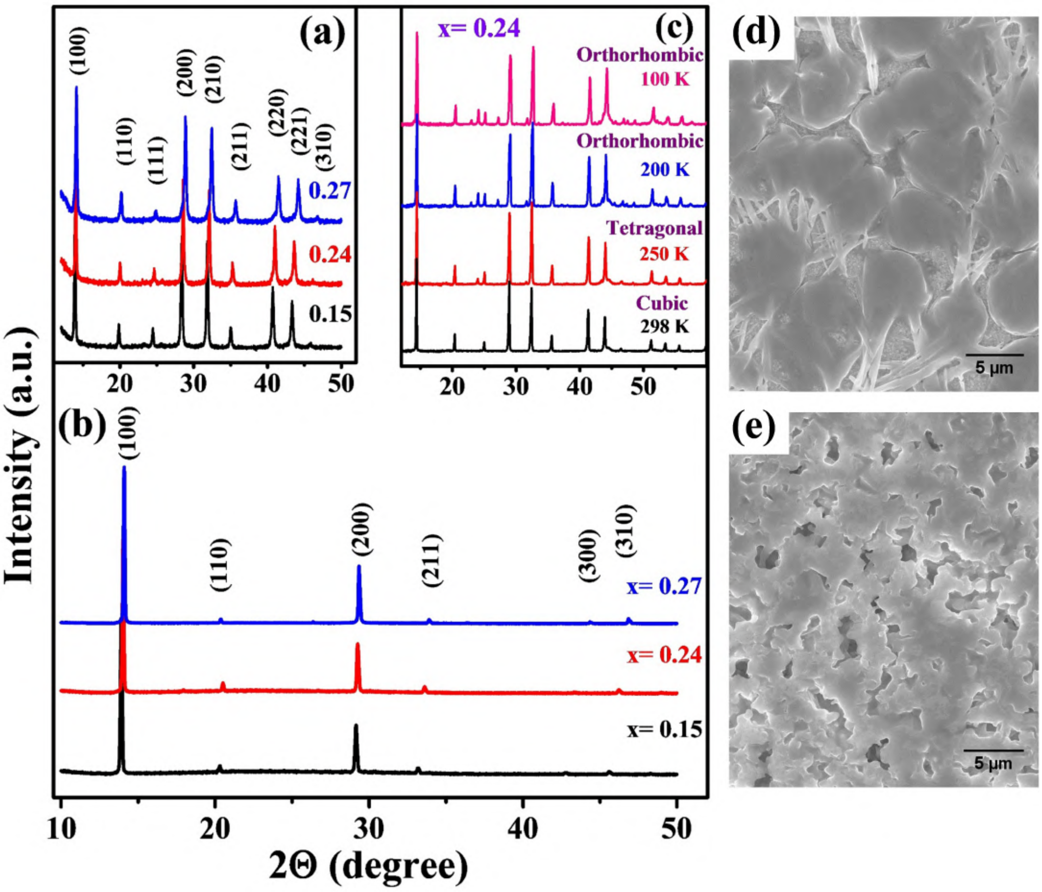

Figure 6.1: X-ray diffraction (XRD) patterns of $CH_3NH_3Pb(I_{1-x}Br_x)_3$ (x=0.15, 0.24, 0.27) powders (a) and thin films (b) collected at room temperature (300 K). Temperature dependent XRD patterns of x = 0.24 shown for some selective temperatures: 100, 200, 250 and 300 K across the crystallographic phase transition (c). SEM images of the perovskite films on FTO glass prepared by the solution prepared from single crystals of $MAPb(I_{0.76}Br_{0.24})_3$ (d) and $MAI+MABr+PbI_2$ (e).

compositions of $CH_3NH_3Pb(I_{1-x}Br_x)_3$ for x = 0.15, 0.24 and 0.27, while Figure 6.1 (b) shows the XRD patterns of the thin films made from these crystals. Observation of sharp well-defined peaks indicate that the samples are highly crystalline in nature [314]. As expected for other members of the organic-inorganic hybrid perovskite family, mixed halides also undergo crystallographic phase transitions from cubic to tetragonal to orthorhombic phase with the decrease of temperature due to the reduction of CH_3NH_3 orientation inside the PbX_6 octahedra [27, 29]. Literature suggests that $CH_3NH_3PbI_3$ and $CH_3NH_3PbBr_3$ transform from cubic to tetragonal phase at 330.8 K and 237.1 K and tetragonal to orthorhombic phase at 161.8 K and 149.4 K, respectively [162]. Temperature dependent

Table 6.1: Crystallographic parameters of $MAPb(I_{1-x}Br_x)_3$ (MA = CH_3NH_3; x = 0.15, 0.24, 0.27) samples obtained from single crystal XRD refinement.

Formula	$MAPbI_{2.55}Br_{0.45}$	$MAPbI_{2.27}Br_{0.73}$	$MAPbI_{2.20}Br_{0.80}$
Formula weight	595.75	585.6	582.31
Color	Black	Black	Black
Crystal form	Cuboid	Cuboid	Cuboid
Crystal size (mm)	0.15 × 0.1 × 0.05	0.12 × 0.1 × 0.07	0.11 × 0.09 × 0.05
Temperature (K)	295	295	295
Radiation	MoK_α	MoK_α	MoK_α
Wavelength (Å)	0.7107	0.7107	0.7107
Crystal system	Cubic	Cubic	Cubic
Space group	$Pm\bar{3}m$	$Pm\bar{3}m$	$Pm\bar{3}m$
a (Å)	6.2238(1)	6.1940(1)	6.1730(1)
Volume (Å^3)	241.083(7)	237.637(7)	235.228(7)
Z	1	1	1
θ range (^{0})	3.27, 30.07	3.29, 30.23	3.30, 30.56
Measured Reflns.	2017	1974	2073
Unique Reflns.	101	102	104
No. of parameters	7	7	7
$R[F^2 > 2\sigma^2(F^2)]$, $wR_2(F^2)$	0.0273, 0.0830	0.0347, 0.0922	0.0344, 0.0819
$\triangle\rho_{min}$, $\triangle\rho_{max}$ (eÅ^{-3})	-0.563, 0.879	-0.960, 1.370	-0.575, 1.139
GooF (S)	1.232	1.199	1.166

X-ray diffraction measurements were performed on the mixed hallide samples, and the results of the same are presented in Figure 6.1 (c) (some representative XRD patterns), where for x=0.24 sample, transition temperatures from cubic to tertagonal and tertagonal to orthorombic phase were found to be around 280 K and 200 K, respectively. We also report scanning electron microscopy (SEM) image of the perovskite films prepared from two different methods: (i) by a dissolving $CH_3NH_3Pb(I_{0.76}Br_{0.24})_3$ single crystals and (ii) by conventional one step deposition route (MAI+ MABr+ PbI_2) as shown in Figure 6.1 (d) and 6.1 (e), respectively. SEM images clearly show large and improved grain size for the thin films synthesized in the first case as compared to the one derived from MAI+ MABr+ PbI_2 precursor solution [310–313]. Hence, crystal dissolved thin films were selected for further experiments.

6.3.2 Optical Studies

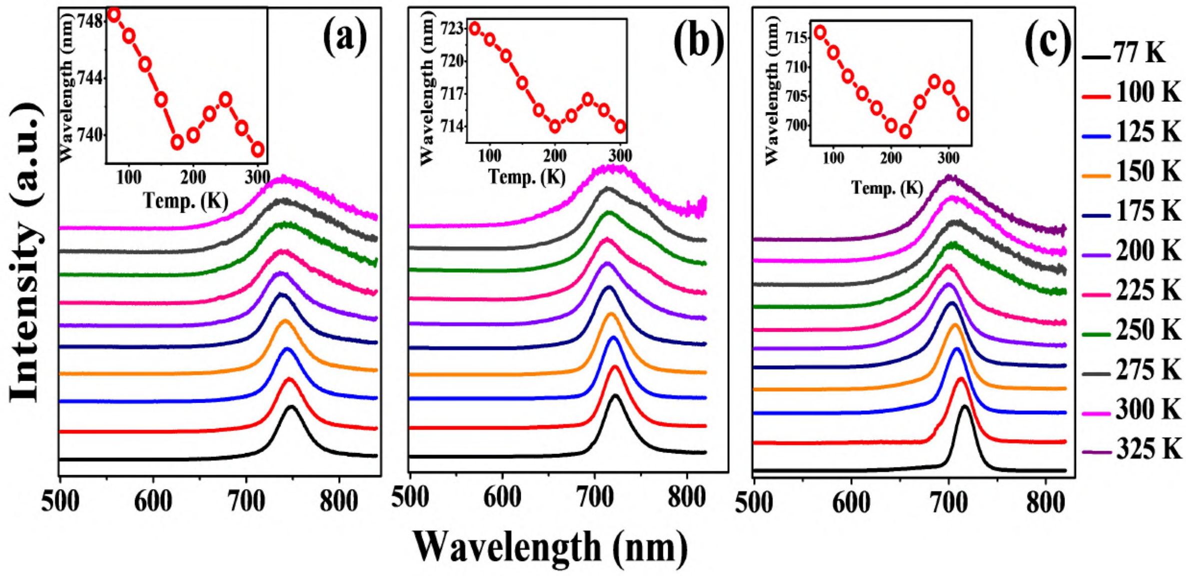

Figure 6.2: Temperature dependent photoluminescence (PL) spectra of $CH_3NH_3Pb(I_{1-x}Br_x)_3$ thin films for a) x = 0.15, b) x = 0.24, and c) x = 0.27; Spectra are shifted vertically and are normalized for help in viewing. Inset shows the temperature dependence of emission peak positions.

Exploring the photoluminescence (PL) of hybrid organic-inorganic perovskites over a wide range of temperature is not only of fundamental interest but also aims to identify the practical applications of the devices based on these perovskites. Figure 6.2 shows the normalized temperature dependent PL spectra of $CH_3NH_3Pb(I_{1-x}Br_x)_3$ (x = 0.15, x = 0.24, x = 0.27) thin films. The temperature dependent PL spectra shows two main characteristics- i) when the temperature is increased from 77 K to room temperature the emission peak wavelength is first blue shifted, then red shifted and again blue shifted, meanwhile the photoluminescence intensity decreases continuously. ii) The PL emission band begins to present asymmetric structure and evolves into two PL bands for x = 0.24 and 0.27 samples in the temperature range 200 K to 275 K. For x=0.15 sample, the emission peak wavelength continuously blue shifted from 748.5 nm to 739.5 nm in the temperature range 77 K to 175 K, then red shifted upto 742.5 nm till 250 K and again blue shifted to 739 nm at 300 K as shown in inset of Figure 6.2(a). Furthermore, while raising the temperature from 77 to 300 K, the linewidth or full width at half maximum (FWHM) of the emission peak increases from 35 nm to 69 nm. Similarly, Figure 6.2(b) shows that emission peak wavelength of $CH_3NH_3PbI_{2.27}Br_{0.73}$ sample has also three regions; first, peak is blue shifted from 723 nm to 714 nm between 77 K and 200 K, then red shifted to 716.5 nm till 250 K and finally blue shifted to 714 nm at 300 K. Irrespective of this, we observe signature of another peak at 746 nm in the temperature range between 200 K and 275 K and the origin of this peak will discuss in next section. Further, FWHM continuously increases from 21 nm to 62 nm. For $x = 0.27$ sample, PL emission peak wavelength decreases from 716 nm to 699 nm between 77 K and 225 K, then increases to 707.4 nm till 275 K and finally decreases to 702 nm at 325 K as shown in Figure 6.2 (c). Similar to $x = 0.24$ sample, we have observed existence of a new peak at 750 nm in between 200 K and 300 K which will discussed later. Our estimated bandgap of $CH_3NH_3Pb(I_{1-x}Br_x)_3$ from photoluminescence at room temperature (E_g at x=0.15 is 1.67 eV; E_g at x=0.24 is 1.74 eV and E_g at x=0.27 is 1.77 eV) is consistent with the literature reports [315, 316]. Thus, above result demonstrated that substitution of Br for I in $CH_3NH_3PbI_3$ lattice increases it's bandgap monotonically. However, this increase of bandgap didn't exhibit the expected higher open-circuit voltage when they incorporated into solar cells. J. H. Noh *et al.* have shown that open-circuit voltage of mixed halide perovskites of the type $CH_3NH_3Pb(I_{1-x}Br_x)_3$ decreases when $x > 0.2$ [316]. Then measuring initial and time evolved photoluminescence and absorption of $CH_3NH_3Pb(I_{1-x}Br_x)_3$ Hoke *et al.* have claimed that incorporation of Br ($x > 0.2$) introduces an inherent instability in this material [299]. They have demonstrated that initial photoluminescence intensity slowly decreased while a new, higher intensity and lower energy peak evolved with the increase of exposure time. Then they hypothesized that iodine and bromine ions segregated into higher bandgap Br rich and lower bandgap I rich grains upon illumination. Further, Bischak *et al.* theoretically hypothesized that after continuous illumination, the halide ions get excited and come closer to Pb atoms and a demixed trap state was formed only after applying certain thermal energy [73]. But there was no experimental evidence behind this hypothesis. Thus we come forward and decided to perform this experiment. To analyze photo-induced phase separation, temperature dependent PL measurements were carried out after different light soaking times ranging from 0 s to 4 hours as depicted in Figures 6.3 and 6.5. Substitution of Br for I in $CH_3NH_3PbI_3$ lattice results in a gradual increase in the band gap. However, Hoke *et al.* found that for Br content x > 0.2, there is an inherent instability in the presence of light with the disappearance of the initial PL peak intensity and corresponding rise of a low-energy peak with exposure time. They argued that iodine and bromine ions were segregated into higher bandgap Br rich and lower bandgap I rich domains upon illumination [299]. Using density functional theory (DFT) a miscible gap of Helmholtz free energy as a function of halide composition at room temperature was observed by Brivio *et al.*, which suggests that illumination supplies the required energy to overcome the kinetic barrier to enter into the metastable state and cause phase segregation [317]. However, this theory fails to explain the reversible behavior upon the removal of illumination. As pointed out earlier in this work, both molecular dynamics (MD) simulation and Landau theory studies by Bischak *et al.* show that due to the interplay between electronic and elastic properties, photoexcited state phase structure of mixed halide perovskite is different from that in the absence of photoexcitation, because of the polaronic strain associated with the excited charge carriers [73]. They show that in the absence of photoexcited carriers, mixed I/Br perovskites exhibited demixing transitions as a function of temperature with a critical temperature of 190 K. In the presence of photoexcited charge carriers which behave like polarons, the demixing to mixing transition temperature increases and the mixing critical temperature is 343 K. Experimentally a careful temperature dependent study of the demixing transition both in the absence and presence of photoexcitation is not yet available. To fulfill this gap and to clarify the nature of phase separation and redistribution of halide ions in the case of $CH_3NH_3Pb(I_{1-x}Br_x)_3$ alloys, we have carried careful temperature dependent PL studies on three samples with varying x (x= 0.15, 0.24 and 0.27). In addition, to understand the underlying dynamics, we have also carried out time resolved measurements of the initial and photoexcited emission states.

Figure 6.3 (a) shows schematics of the experiment protocol. Sample was first cooled

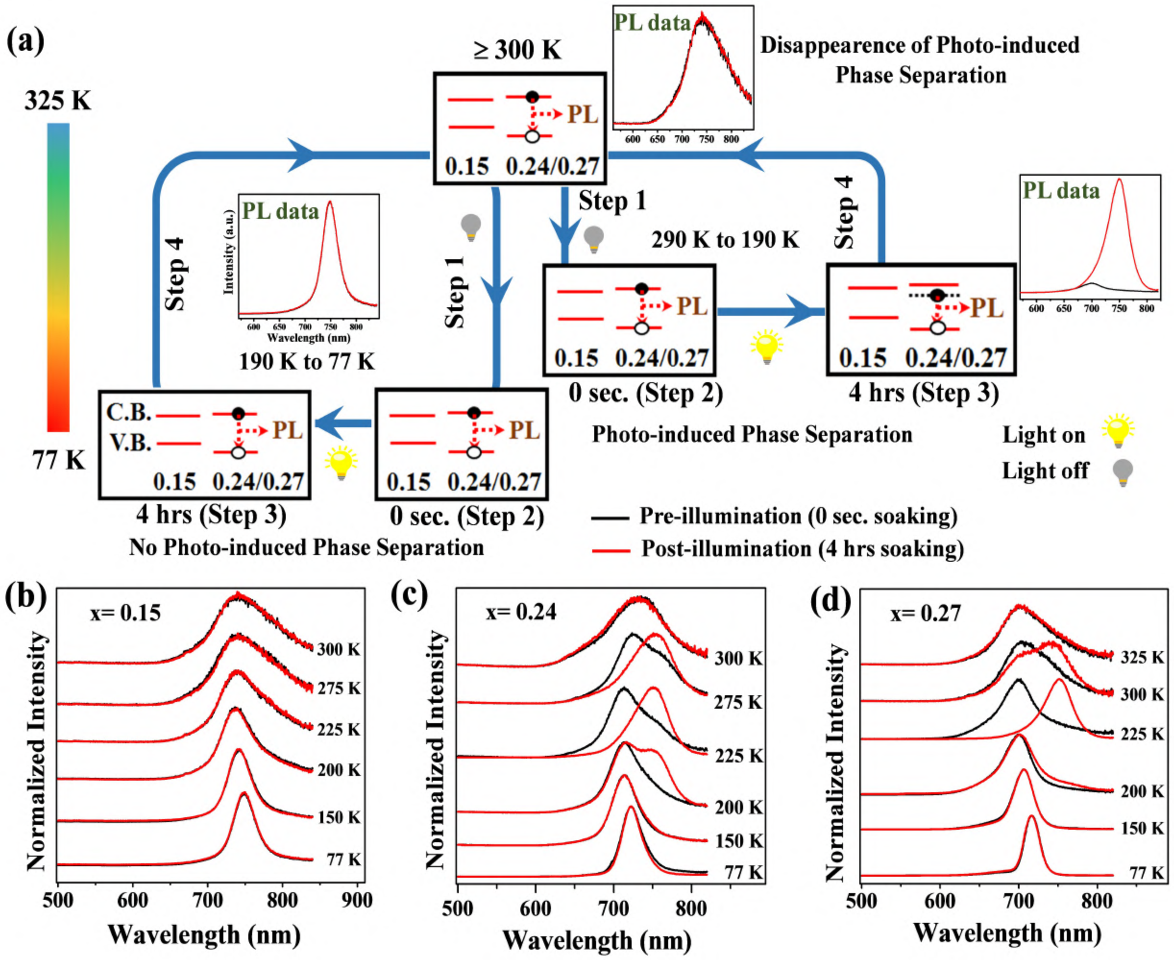

Figure 6.3: (a) Schematics of the experiment protocol for studying temperature dependence of photo-induced phase separation (PS). Temperature dependent PL spectra of (b) x= 0.15; (c) x= 0.24; and (d) x= 0.27 thin films collected after 0 s and 4 hrs of light soaking time, represented by black and red sold lines. Here the spectra taken at different temperatures are shifted vertically and are normalized for help in viewing.

from 300 K to a specified temperature in the absence of light (step 1), and PL spectrum corresponding to 0 second soaking time was recorded (step 2) as represented by solid black line (in Figures 6.3 (b), 6.3 (c) and 6.3 (d)). Thereafter, sample was subjected to prolonged illumination and PL spectra was collected at intermediate stages (Figure 6.5), PL data corresponding to 4 hour soaking time (step 3) is represented by solid red line (in Figures 6.3 (b), 6.3 (c) and 6.3 (d)). Finally, sample was heated back to 300 K (step 4), for x = 0.15 and 0.24 samples; it did not matter if step 4 was carried out in the presence or absence of light. Steps 1-4 were repeated for multiple temperatures.

Results of temperature dependent PL experiments after normalization (for clarity) are summarized in Figures 6.3 (b), 6.3 (c) and 6.3 (d) which correspond to composition x = 0.15, 0.24 and 0.27, respectively. For the x=0.15 sample, the peak position and the full width half maximum (FWHM) of 0 sec. and 4 hrs soaking time emission spectra remained same throughout the temperature regions between 77 K and 300 K as shown in Figure 6.3 (b) indicating that no phase separation occurs for x = 0.15 (low Br concentration) sample under illumination, even at low temperatures. This result is consistent with the room temperature reports where it was claimed that photo-induced phase separation was observed only when Br concentration is greater than 0.2 [299, 300]. Sample with Br concentration x = 0.15 is hence below the percolation threshold (x = 0.2) [299], where in the sea of I rich domains, Br rich domains are randomly distributed and do not form long range connectivity even in the presence of light to give rise to phase separation.

Figure 6.3 (c) shows results from x = 0.24 thin film; it exhibits similar PL spectra for pre- (0 sec. soaking time) and post-illumination (4 hrs soaking time, result is same even for 10 hrs soaking time) between 77 K and 175 K. However, at 200 K, in addition to the initial emission peak at 716 nm, a new emission peak appears at 746 nm, intensity of which gradually increases with time and saturates after continuous illumination. It is interesting to note that at 200 K the intensities of both 716 nm and 746 nm peaks are nearly same, which suggests that, at the stated temperature, charge excitations generate sufficient lattice strain to destabilize I/Br solid solution to initiate photo-induced phase separation. Further, in the temperature range of 225 K to 275 K, the intensity of peak corresponding to 746 nm increases rapidly with time (Figure 6.5 (a)) and overshadows the 716 nm peak after 4 hours of continuous illumination. More strikingly, it is observed that, at 300 K and above, complete annihilation of the secondary peak corresponding to 746 nm occurs, as pre- and post-illumination emission spectra look the same suggesting no phase separation due to illumination.

Our temperature dependent PL studies suggest that demixing of halide ions due to polaronic strain is initiated at around 200 K, is consistent with the mean field theory temperature-composition phase diagram in the photoexcited state by Bischak *et al.* [73].

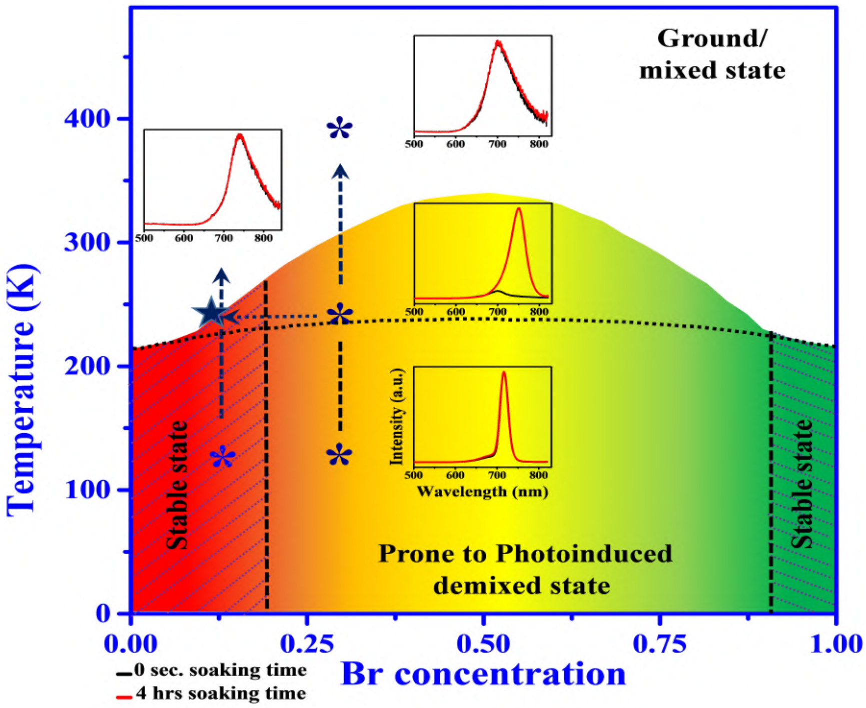

Figure 6.4: Schematic temperature−Br concentration phase diagram indicating ground/ mixed state, stable state and photoinduced demixed states.

Their simulation suggests that mixed I/Br perovskite undergoes demixing transition with a critical temperature of 190 K and we provide a direct experimental proof of temperature induced demixing, validating their theoretical claims (Figure 6.4). Further, disappearance of the photo-induced phase separation (or remixing) is observed at an elevated temperature (300 K and above), which can be explained from the dynamic behavior of electron-phonon interactions. At higher temperatures electron phonon interaction results in decreased electron hole mobility, thereby hindering ion migration and formation of phase separated domains. Also, theoretical calculations revealed that above a critical temperature (343 K) solid solutions of hybrid perovskites are stable for any composition, which supports our observation of an upper limit of the critical temperature for I/Br solid solutions [317]. Surprisingly, the crystallographic phase transition temperatures of x = 0.24 composition *i.e.*, 200 K and 280 K (from orthorhombic to tetragonal and from tetragonal to cubic phase), are in close proximity to the formation and annihilation of photo-induced phase separation temperatures. Similar behavior was also observed for the x = 0.27 composition, which is depicted in Figure 6.3 (d). Here the only difference is that the demixing and remixing (of halide ions) transition temperatures are slightly offset as evident from the emergence and disappearance of the light induced secondary peak in the PL spectra owing to different crystallographic phase transition temperatures. As a result, light induced phase separation still persists at room temperature and it disappears at an elevated temperature around $\sim$ 325 K. A more detailed and careful study (which is beyond the scope of the present work) is required to pin down the origin of correlation between crystallographic phase transition and photo-induced phase separation, if any. It may be noted that most of the mixed halide samples studied in the literature are with composition $x \geqslant 0.3$ for which photo-induced phase separation is observed at room temperature and remixing temperature is expected at much higher temperature ($\geqslant$ 325K) [299–309]. Through our careful experiments and judicious choice of composition we are able to catch the demixing and remixing transition as a function of temperatures for these mixed halide systems. Based on the above observations, we propose that tandem solar cells using mixed halides may work more efficiently at elevated temperatures where there is no photo-induced phase separation.

To gain further insight about the dynamic behavior of carrier-strain interaction, *i.e.*, formation and break down of iodide rich clusters, the time evolution of the PL spectra both in the presence and absence of light at 225 K are presented in Figure 6.5. In this figure we see that for 0 sec soaking time only one emission peak (peak 1) is seen, 716 nm for x = 0.24 and 699 nm for x = 0.27. It was found that this original peak disappears and a new emission peak associated with the iodide-rich region gradually appears at 746 nm (peak 2), as a function of time. Growth of integrated intensity of peak-2 continues with time and saturates around 4 hours after which no further iodide-rich cluster formation takes place, as shown in the inset of Figures 6.5 (a) and (c). We further investigated the sample by turning off the continuous illumination (after 5 hours of soaking time) and recording the PL spectra at regular intervals (Figures 6.5 (b) and (c)). Photo induced peak (peak-2) intensity does not fall to zero as soon as the light is turned off; it decreases gradually and the spectra corresponding to 0 sec soaking time is recovered after 6-10 hours, confirming the reversibility of photo-induced phase separation. Further, to understand the dependence of photo-induced phase separation on the wavelength and intensity of the incident

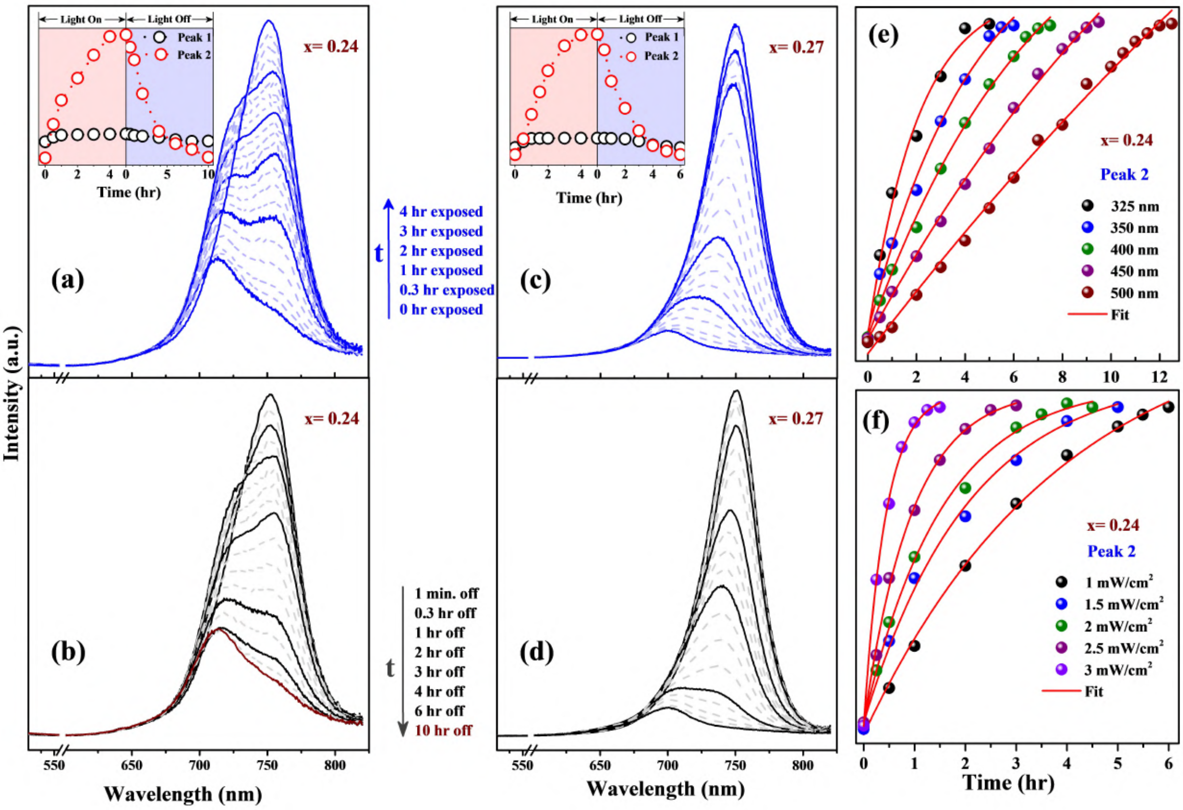

Figure 6.5: Evolution of PL spectra at 225 K in the presence (a, c) and absence (b, d) of light for the compositions as marked in the figure. Inset shows integrated intensity of peak 1 and peak 2 as a function of time. Evolution of PL peak intensity at 225 K by varying the (e) excitation light wavelength and (f) light intensity/power (λ = 325 nm).

light, PL experiments were performed with five different wavelengths (325 nm, 350 nm, 400 nm, 450 nm and 500 nm) with $\sim$ 1.5 mW/cm^2 power on the sample, and with five different light intensities (1 mW/cm^2, 1.5 mW/cm^2, 2 mW/cm^2, 2.5 mW/cm^2, 3 mW/cm^2) at 325 nm at three different temperatures *i.e.*, 77 K, 225 K and 300 K for x = 0.24 sample. No significant photo-induced phase-separation (*i.e.*, evolution of PL intensity with illumination time) was observed by changing either excitation intensity or wavelength of the excited light at 77 K and 300 K. However, there was a systematic evolution of 746 nm peak intensity with time was observed in PL spectra at 225 K, which is depicted in Figure 6.5 (e) and 6.5 (f) and is fitted by mono-exponential time constant [318]. Fitting yielded a time constant of 2.07 hrs, 3.58 hrs, 5.01 hrs, 7.32 hrs and 10.58 hrs under 325 nm, 350 nm, 400 nm, 450 nm and 500 nm illumination. Gradual increase of time constant or slowing down of photo induced phase separation with increased wavelength may be due to the dependence of absorption coefficient on wavelength [318]. Additionally, evolution of PL peak with time by changing the intensity/power of the excitation light (325 nm) is depicted in Figure 6.5 (f), and the extracted time constants by fitting mono-exponential behavior are 4.2 hrs, 2.07 hrs, 1.54 hrs, 0.95 hrs and 0.43 hrs for 1 mW/cm^2, 1.5 mW/cm^2, 2 mW/cm^2, 2.5 mW/cm^2 and 3 mW/cm^2 illumination, respectively; as expected, a higher power of incident light resulted in faster phase separation [303]. Literature suggests that the formation of demixed state takes fraction of minutes for thin films [73] and hours for bulk samples/crystals under illumination while the remixing time after the illumination is turned off, which is also the annihilation time of the iodide-rich clusters, is in hours [319]. Our results are consistent with the literature reports with the only exception being that it takes a much longer time for our thin film samples to phase separate indicating better quality of the samples, with lesser defects [320] and large crystal domains [321] (with lesser grain boundaries) which kinetically limit the “Hoke effect” and effectively reduce the phase segregation [322]. This observation supports the idea that continuous illumination generates a finite steady state concentration of charged carriers near the grain boundaries which by coupling to the local strain are responsible for polaronic cluster formation and phase separation [73, 323]. Hence the grain size of mixed halide perovskites play a crucial role in forming the light induced phase separation or formation of metastable states.

6.3.3 Carrier Lifetime Measurements

To know more about the real-time dynamics of the photo-excited charge carriers, life time measurements of pre-illuminated (black dots) and photo-excited demixed states (blue dots) for x = 0.24 composition were performed at 225 K. The results, presented in Figure 6.6, are quite striking. The lifetime of pre-illuminated peak shows a single decay with carrier lifetime of 0.46 ns, whereas the lifetimes of carriers associated with photo-excited demixed state (after 5 hours of continuous illumination) shows two characteristic decay times, namely, one 0.43 ns with 44.8% weight and a second, 11.79 ns with 55.2% weight [319, 324]. In the mixed or pre-illuminated case where the system is homogeneous, light absorption creates an electron–hole pair which quickly recombine to produce single

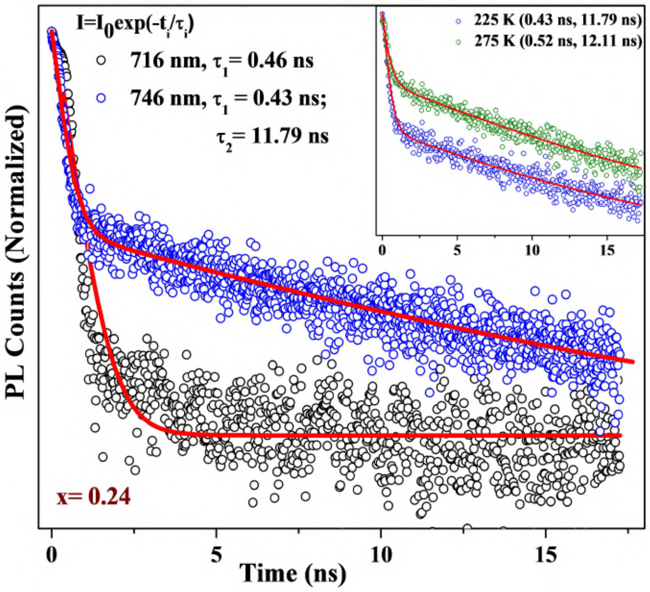

Figure 6.6: Lifetime measurement of peak 1 corresponding to 716 nm (black dots) and photo-excited peak 2 (746 nm) (blue dots) with corresponding exponential fit (red solid line) for x = 0.24 sample. Inset shows comparison of life time measurements spectra of peak 2 at 225 K and 275 K with corresponding fit.

native emission (corresponding to life time of 0.46 ns). Weakly bound electron-hole can also rapidly dissociate, travel long distances, deforming the surrounding lattice through electron-phonon coupling, and induce halide anion rearrangement. Upon prolonged illumination, generated polarons funnel into the reduced bandgap I-rich domains driving the perovskite to form microscopic phase segregation into iodide- and bromide-rich domains, as shown in Figure 6.7. In tandem, electron-hole pairs can also recombine, reversing the phase separation process. Observation of two types of carrier decay times in phase separated samples can be interpreted as one arising from quick recombination of electron–hole pair as soon as they are formed (0.43 ns, like in mixed state) reversing the effect of phase separation and the other from the iodide-rich domains (11.79 ns). The reason the latter has a longer life time ($\sim$ 25 times larger) can be ascribed to the strong polaronic effect. This is also referred to as emission from the “trap” state confined to the iodide-rich clusters. To identify the carrier lifetime of photogenerated charge carriers at an elevated temperature, lifetime measurement of peak 2 was also performed at 275 K and a comparative study between 225 K and 275 K is shown in inset of Figure 6.6. Enhanced lifetime at higher temperature is consistent with the longer life time of polarons under photoirradiation [325]. It is believed that halide migration in perovskites occurs through halogen vacancies [314], and ion mobility in these materials are more facile at grain boundaries compared to the bulk material [29]. Therefore, reducing defect density and the number of grain boundaries should decrease the rate at which phase segregation occurs. Through our carefully controlled sample preparation process we ensured higher-quality films with larger grain size and lower defect densities (Figure 6.1 (d)) resulting in longer time for phase separation to occur (4-5 hours) compared to the conventionally grown films (grown by one step process) which has smaller grain sizes (figure 6.1 (e)) and photo induced phase separates occur much faster ($\sim$ 2.5 hours).

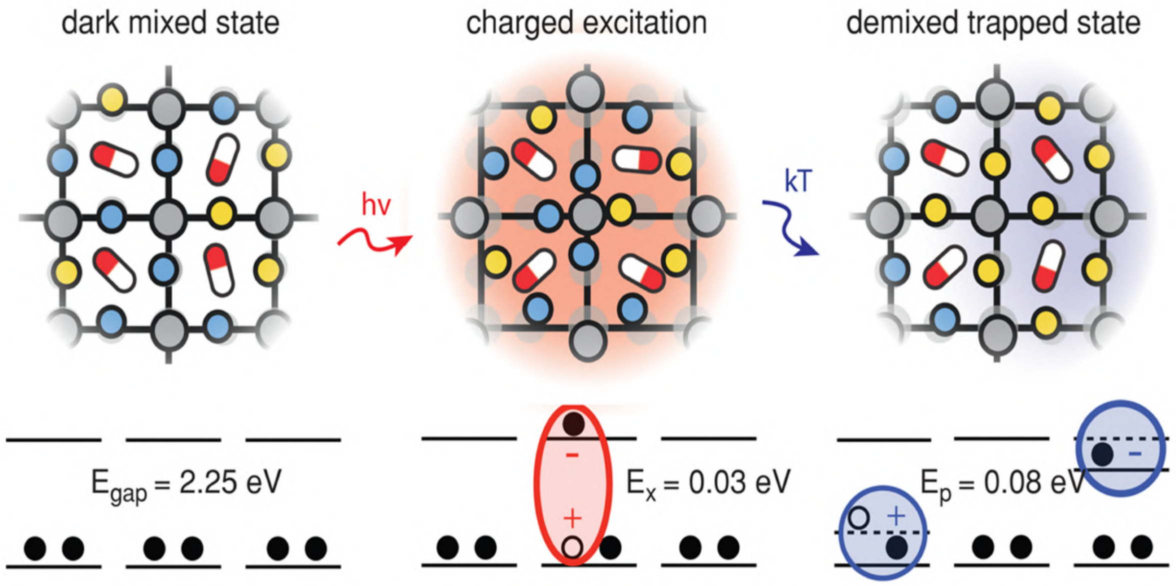

Figure 6.7: Photoinduced polaron trapping and corresponding energy scales associated with phase separation. Here yellow and blue spheres represent I and Br, respectively, the red and white pill shapes represent CH_3NH_3 and lead atoms are represented by gray circles.

(Taken from : Nano Lett., 2017, 17, 1028–1033)

6.4 Conclusion

In conclusion, we have successfully demonstrated the temperature dependent nature of photo-induced phase separation in the mixed halide perovskites in this chapter. PL studies revealed that demixing of halide ions into iodine-rich and bromine-rich domains occurred above a critical temperature and concentration of Br, in a narrow temperature window. Above this temperature window, *i.e.*, at elevated temperature, the electron-phonon interaction results in a decreased electron hole mobility and they recombine to form mixed state. Our findings may hence pave a relook at further optimization of tandem solar cell comprising of mixed halides for higher temperature applications, where there is no photo-induced phase separation, than at room temperature. Our observation also suggests that demixing and remixing temperatures are pinned to crystallographic phase transition temperatures, hence providing an ample playground for fundamental research as well. Further, appearance of longer lifetime of carriers in the phase separated state confirms the presence of strong electron-phonon interaction while longer saturation time of the cluster formation confirms that grain boundary/sample quality plays a crucial role in phase separation.

Chapter 7

Solar Cell Device

In this chapter, we use antisolvent vapor assisted crystallization technique for the controlled nucleation and crystallization of methylammonium lead iodide film for fabricating mesoporous perovskite solar cells. Solar cells based on hybrid perovskite $CH_3NH_3PbI_3$ *as an absorber were deposited on top of mesoporous* TiO_2 *using spin-coating technique. Further, high (DCM) and low (EA) boiling point antisolvents were treated to the* $CH_3NH_3PbI_3$ *films and a new morphology (microrods) were evolved for the case of EA treated films. Hole transport material (HTM) and Au were deposited on top of it using spin-coating and thermal vapor deposition, respectively, to make a prototype solar cell device. The mesoporous solar cell prepared from EA treated absorber material exhibits a power conversion efficiency of 7.7%, which is 32% higher than that of DCM treated (5.8%) and without antisolvent diffused films (5.6%).*

7.1 Introduction

Perovskite solar cells based on different hybrid organic-inorganic perovskite materials, such as $MAPbX_3$ (MA= CH_3NH_3), $FAPbX_3$ (FA= $HC(NH_2)_2$) and mixed (MA,FA,Cs) PbX_3 (X=I, Br, Cl) have sprung to prominence in recent years, due to their remarkable improvements of photovoltaic power conversion efficiencies (PCEs) over the last few years [10, 51, 326–328]. The best photovoltaic devices have already exceeded 22% PCE at the laboratory scale and 15% at the large scale (>1 cm^2) [10, 51, 327]. Easy and cost effective fabrication [92], strong absorption coefficients [11], long carrier diffusion length [21, 32, 75, 76], high charge-carrier mobilities [22, 48] and apparent defect tolerance [94, 95] make these devices suitable alternatives to the crystalline silicon and thin-film solar cells [7, 8, 185]. However, abnormal hysteresis [329], poor long-term stability [54, 330], high lead toxicity [331], and surface/interface issues prevent their entry into the photovoltaic device market [210].

The first record of perovskite-based solar cell efficiency was reported by Kojima *et al.* in 2009 [19], and achieved an power conversion efficiency (PCE) of 3.8% based on a DSSC structure. The stability of this solar cell device was very weak due to the use of liquid electrolyte (0.15 M LiI and 0.075 M I_2 dissolved in methoxyacetonitrile) as a hole-transport material (HTM). Similar composition was used by Im *et al.* in 2011 with the increased efficiency of 6.5% [332], but stability was still the main problem because of the instability of HTM layer due to the liquid medium.

The application of solid-state HTM (2,2 ,7,7 -tetrakis(N,N-di-pmethoxyphenylamine)-9,9 -spirobifluorene, i.e., Spiro-OMeTAD), instead of liquid HTM, onto the highly-crystallized perovskite layer triggered the PCE to 9.7% [84]. At the same time, Lee *et al.* reported a breakthrough device efficiency of 10.9% with the open-circuit voltage higher than 1.1 V [86]. Further, Wang *et al.* introduced graphene into perovskite solar cell and acquired an efficiency of 15.6% [333] and the application of another perovskite material, formamidinium iodide ($HC(NH_2)_2PbI_3$) together with poly-triarylamine (PTAA) as a new HTM brought a remarkable 20.1% efficiency in 2015 [334]. The current record efficiency of PSCs is 22.1%, created in 2017 by Seong Sik Shin *et al.* [10]. In the course of its development, various oxide electron transport materials (ETM), HTM and vacuum/non-vacuum fabrication methods have been developed as shown in figure 7.1 [335]. At present, long-term efficiency measurements (> 1000 h) is still not adequate for the commercialization of hybrid perovskite solar cells. Thus, we believe that it is very important to understand the degradation mechanism of both perovskite materials and other device components such as hole transport medium (HTM) and electron transport medium (ETM).

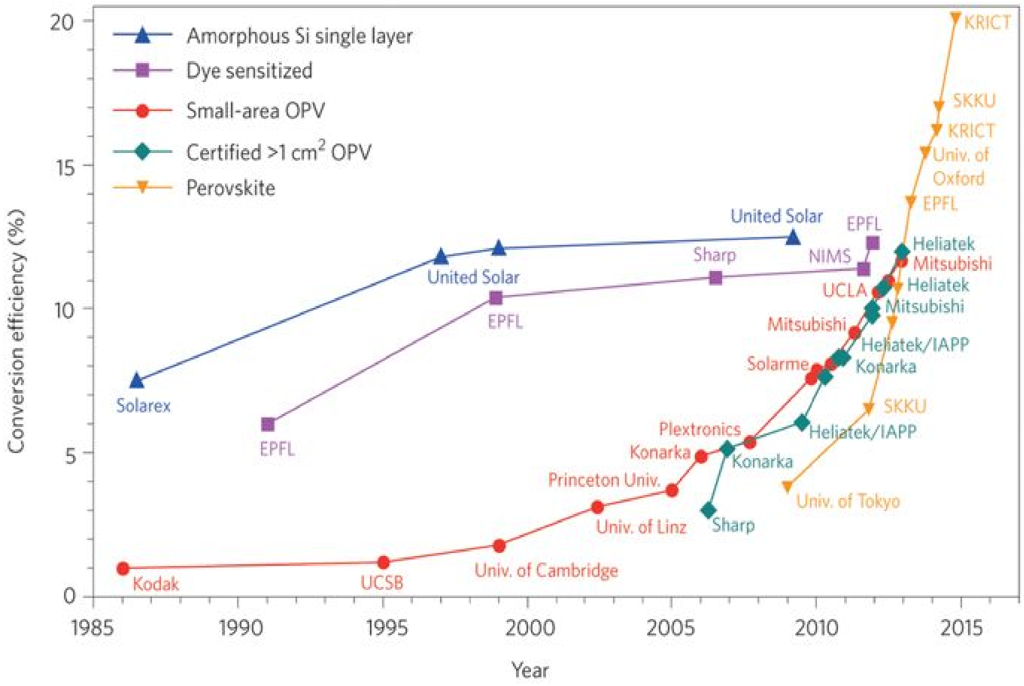

Figure 7.1: A comparison of perovskite efficiency progress with other kinds of photovoltaic (PV) devices. Abbreviation used in the figure are: OPV, organic photovoltaic; EPFL, École polytechnique fédérale de Lausanne; IAPP, Institut für Angewandte Photophysik; KRICT, Korean Research Institute of Chemical Technology; NIMS, National Institute for Materials Science; SKKU, Sungkyunkwan University; UCLA, University of California, Los Angeles; UCSB, University of California, Santa Barbara.
(Taken from: Nature Nanotechnology, 2015, 10, 574–575)

To date, several techniques have been employed to resolve the above issues and aid the commercialization of perovskite solar cells. Recently, it was observed that antisolvent engineering was an effective approach to improve the PCE of perovskite solar cells [88,90,155,210,211,336–338]. We know that perovskite precursor (PbI_2 and CH_3NH_3I) are miscible with Dimethylformamide (DMF) and immiscible with the non-polar antisolvent, which can remove the residual solvents of DMF and boost nucleation and crystallization of the perovskite film. Till date, diethyl ether [336], chlorobenzene [210], chloroform [337], toluene [211], isopropanol [338], and dichloromethane (DCM) [337] have been used as an anti-solvent in the literature. As an example Jeon *et al.* [211] and Ahn *et al.* [336] have improved crystallization of perovskite films by drip-casting toluene and diethyl ether during the spin-coating process, respectively. However, this technique is not suitable to obtain uniform morphology for large scale devices because the anti-solvent drip at the center of the film during spin-coating results radial gradient morphology of perovskite films [90]. Later, Zhou *et al.* [155] have immediately immersed the large area (1.2 cm^2) spin-coated film in diethyl ether and a uniform morphology was obtained. Irrespective of improvement of morphology , these devices could achieve a PCE as high as 15.3% in the case of films with an area of 1.2 cm^2. However, dipping of perovskite films in anti-solvent might create non-stoichiometry in the sample.

Herein, we develop an antisolvent vapor assisted crystallization (AVC) method for the controlled nucleation and crystallization of hybrid organic-inorganic hybrid perovskite thin-films. The key steps of this process are: (a) spin-coated films were kept in an anti-solvent environment; but not immersed in anti-solvents and (b) use of low (DCM) and high (EA) boiling point anti-solvents. In this study, we show that choice of antisolvent (depending on their boiling point) plays a significant role in controlling the morphology of perovskite films. Microrods of diameter 1μm were formed when spin-coated films were kept in EA environment (Figure 1); while no microrod formation was observed when DCM was used. X-ray diffraction and energy dispersive x-ray spectrometry (EDS) measurements confirmed phase purity of the sample; while UV-visible absorption studies, photoluminescence and x-ray photoelectron spectroscopy helped to draw the schematic energy level diagram of this perovskite. Further, as deposited, DCM treated and EA treated films were used as an absorber material in mesoscopic metal oxide heterojunction solar cell devices. 1.45 times PCE enhancement was observed for the case of EA treated films (7.7%) than that of as deposited (5.3%) and DCM treated films (5.4%) under atmospheric conditions with > 85% humidity. 16.5% PCE was observed when the films were grown (including EA diffusion) inside the glove-box.

7.2 Experimental details

7.2.1 CH_3NH_3I Preparation

The methylammonium halide precursor (CH_3NH_3I) was synthesized according to the previous report with some modifications [54,90]. In brief, 14 mL methylammonium (CH_3NH_2, 40wt% in methanol) was reacted with 15 mL of hydroiodic acid (HI, 57wt% in water) and the mixture was stirred for two hours under nitrogen atmosphere in an ice bath. The resulting solution was evaporated using a rotary evaporator until white microcrystals were found. These microcrystals of CH_3NH_3I were washed three times in ethyl acetate and dried at 60^0C in a vacuum oven overnight and kept in vacuum for further use.

7.2.2 Perovskite Film Preparation

Fluorine-doped tin oxide (FTO) transparent conducting substrates (7 Ω/cm^2) were cut into 1.5 × 1.5 cm^2 pieces. They (FTO) were then cleaned by sequential sonication in soap solution, Millipore water, isopropanol, followed by drying in Ar flow and plasma treatment for 30 minutes. A $CH_3NH_3PbI_3$ precursor solution was prepared by dissolving 691.5 mg PbI_2 (99.9% Sigma Aldrich) and 238.6 mg as prepared CH_3NH_3I in 1.5 mL Dimethylformamide (DMF). The solution was then filtered through 0.2μm PTFE syringe filter before use. Aforementioned solution was then spin-coated on FTO glass at 2500 rpm for 40 seconds. Upon completion, solvent engineering was performed by transferring the films to EA and DCM environment immediately (except as deposited film) and kept for 15 minutes (Figure 7.2 (e)). Thereafter, films were dried by heating it at 80^0C for 5 minutes.

7.2.3 Solar Cell Device Fabrication

Prior to device fabrication, fluorine-doped tin oxide (FTO) transparent conducting substrates (7 Ω/cm^2) were cut into 1.5 × 1.5 cm^2 pieces and cleaned by sequential sonication in soap solution, millipore water, isopropanol, followed by drying in Ar flow and plasma treatment for 30 minutes. First, a compact hole-blocking layer (HBL) of TiO_2 was applied to the clean substrate by the spin-coating (5000 rpm for 50 second) in air followed by annealing at 500^0C for half an hour. Solution required for forming HBL was prepared by mixing Titanium (IV) isopropoxide ($Ti[OCH(CH_3)_2]_4$, 2 mL) with 2-methoxyethanol ($C_3H_8O_2$, 10 mL) and ethanolamine ($NH_2C_2H_4OH$, 1mL) and heated to 80^0C for 2 hours under continuous stirring [339]. On top of HBL, a mesoporous layer of TiO_2 was deposited by spin-coating at 5000 rpm for 30 second using commercially obtained TiO_2 paste diluted in ethanol (2:7 weight ratio) and annealed at 500^0C for half an hour [90, 339, 340]. After cooling to room temperature, perovskite film was deposited on top of mesoporous TiO_2 as discussed in last section. Further, 100 μL solution of hole transport material (HTM) (84 mg 2,2 ,7,7 -tetrakis(N,N-di-pmethoxyphenylamine)-9,9 -spirobifluorene (Spiro-MeOTAD) in 1mL chlorobenzene, mixed with 15 μL of 170 mg/mL bis (trifluoromethane) sulfonamide lithium salt dissolved in acetonitrile and 7 μL of tert-butylpyridine) was applied by spin-coating at 2000 rpm for 30 seconds [86,340]. To complete device fabrication, 100 nm gold contacts were deposited (at a rate of 2 Å/sec) on the top of hole transport layer by thermal evaporation using a shadow make inside a vacuum chamber with pressure 10^{-6} mbar.

7.2.4 Characterization

The morphology of as prepared and antisolvent treated perovskite films were studied by field emission scanning electron microscope (FESEM; Carl Zeiss, Germany), while crystallographic properties of perovskite film on FTO substrate was characterized by X-ray diffraction (XRD) (Bruker, D8-advance) using Cu-K_α radiation (λ = 1.5418 Å) under the Bragg-Brentano geometry. The optical absorption spectra was measured using an ultraviolet-visible-near-infrared (UV-Vis-NIR) spectrophotometer (Shimadzu, 3101PC) in the wavelength range of 400-800 nm and photoluminescence emission spectra (PL) were acquired using FL920 spectrometer from Edinburg instruments with the excitation energy of 325 nm. I-V measurements of the device were performed using a Newport solar simulator connected to the Keithley 2420 I—V measurement system.

7.3 Results and Discussion

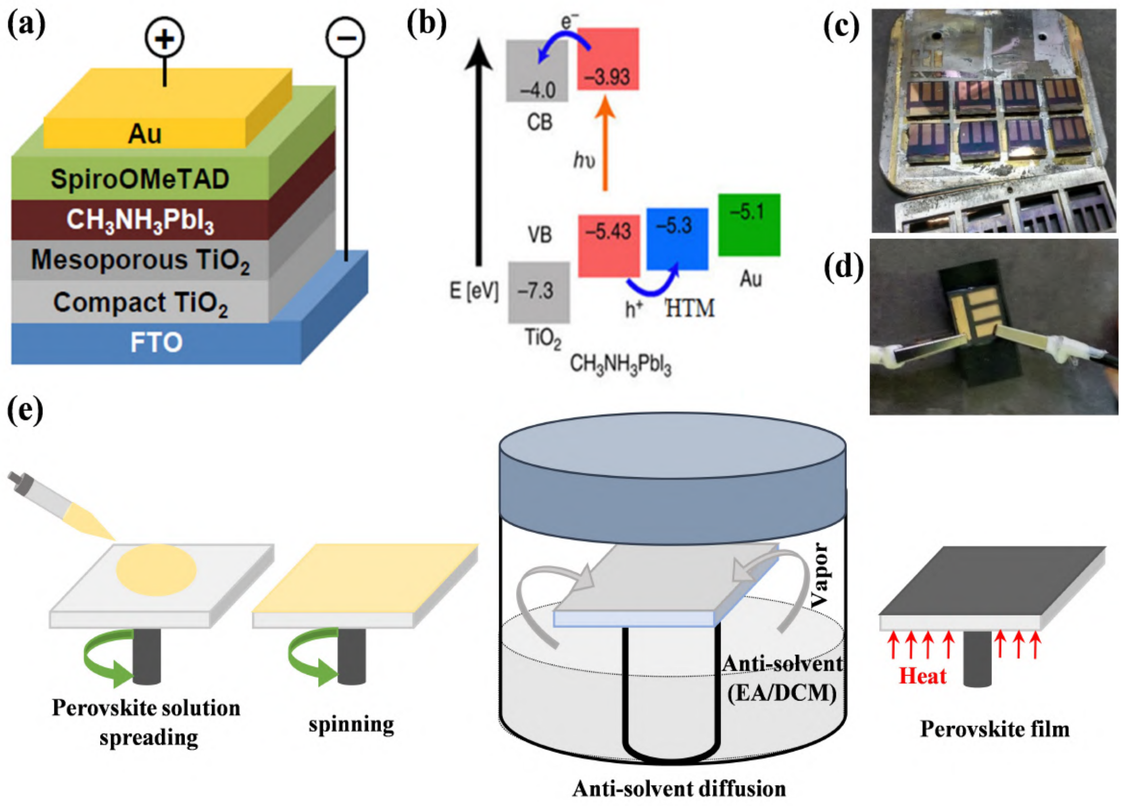

Figure 7.2: Schematic diagram of the (a) cell architecture and (b) energy levels of different layers. (c-d) Representative figure of solar cell made by us. (e) Schematic diagram of the perovskite absorber deposition process using antisolvent vapor diffusion technique.

7.3.1 Structural Studies

Figure 7.2 presents a schematic diagram of the cell architecture and deposition of hybrid perovskite by anti-solvent vapor assisted crystallization technology by means of spin-coating, as well as full devices made by us. The cell architecture (fig. 7.2 (a)) reveals mesoporous hybrid perovskite solar cells are composed of FTO/compact TiO_2 (HBL)/ Mesoporous TiO_2/ $CH_3NH_3PbI_3$/ Spiro-OMeTAD/ Au and the generated electrons and holes in $CH_3NH_3PbI_3$ layer are transported through the TiO_2 electron conductor and the Spiro-OMeTAD hole conductor, respectively [340]. Upon illumination, the charge carriers generated in $CH_3NH_3PbI_3$ are transported through TiO_2 as the separation between

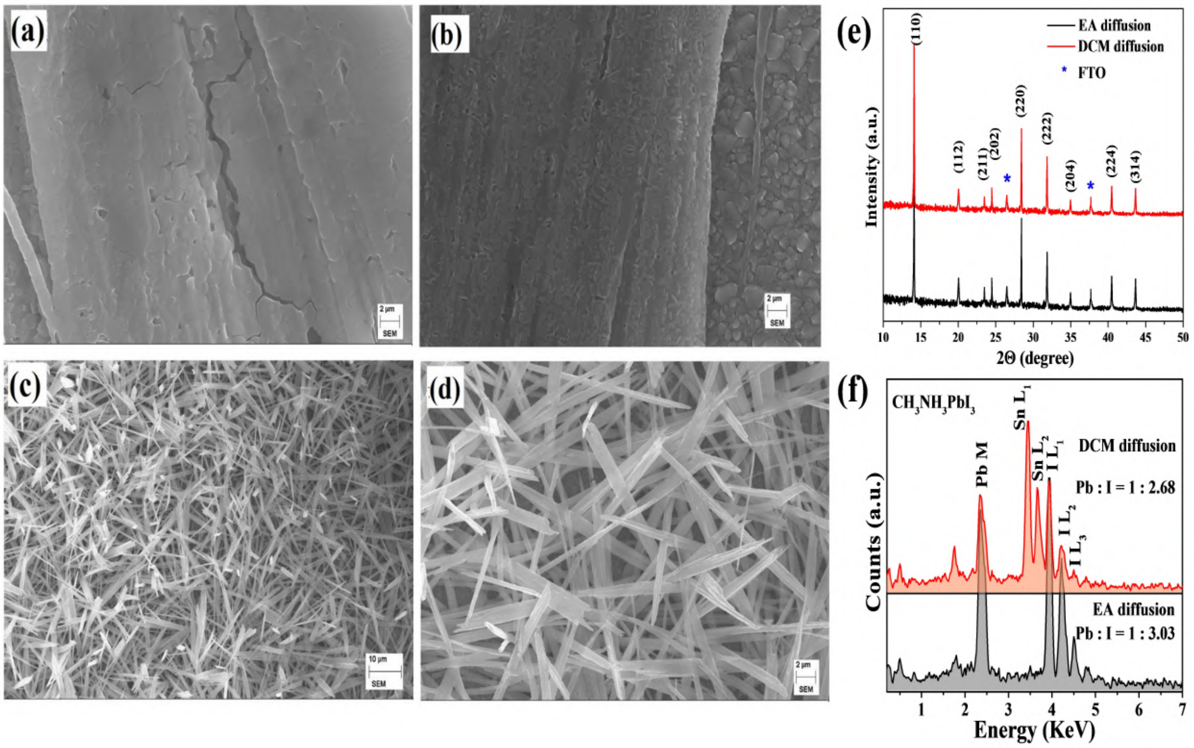

Figure 7.3: SEM images of the perovskite films (a) as-deposited, (b) DCM-diffused, (c-d) EA diffused. (e) XRD patterns and (f) EDS of the perovskite films diffused by EA and DCM antisolvents.

bottom of conduction band is small; on the other way, holes are transported to the Au electrode through Spiro-OMeTAD as top of the valence band of each layer matches well, which is depicted in figure 7.2 (b). As the transportation rate of electrons and holes of organic-inorganic hybrid perovskite are same, solar cell current was detected under reverse bias condition. Solar cell devices made by us are presented in figure 7.2 (c) and (d). In order to obtained these architecture, formation of porous absorber layer is extremely important, and we develop our solvent engineering technology as an effective tool to grow the $CH_3NH_3PbI_3$ layer. This process involved four stages, as depicted in figure 7.2 (e): First, the precursor solution is spread over the FTO substrate; second, spin-coater is accelerated to the desired rotational speed to spread the solution; third, spin-coated film is kept in anti-solvent (EA/DCM) environment (not immersed); finally, the perovskite film is annealed to 80^0C for 5 minute (see previous section for details). It is apparent from figure 7.3 (a-d), the morphology of thin-film layer of $CH_3NH_3PbI_3$ is markedly changed by this solvent engineering process. Figure 7.3 (a) shows the top view of field-emission scanning electron microscopy (FESEM) images of the as deposited $CH_3NH_3PbI_3$ thin film on FTO glass. Notably, diffusion of DCM anti-solvent had very less effect on the film morphology and structure (Figure 7.3 (b)). In contrast, the difference between as deposited/DCM diffused film and EA diffused film is evident. The conventional one step solution deposition without any antisolvent or with low boiling point antisolvent (DCM; 37^0C) treatment induces typical branchlike crystals, and the FTO surface is not fully covered as confirmed by Energy-Dispersive X-ray spectroscopy (EDS) spectrum (Figure 7.3 (f)). Whereas, microrods of diameter 1μm were formed when spin-coated films were kept in EA environment (Figure 7.3 (c and d)), having more coverage than other two. This improved morphology of mesoporous film by the high boiling point antisolvent (EA; 77^0C) is ascribed due to the non-covalent weak interaction between the precursor solvent and antisolvent. During the process of nucleation and crystallization, DCM evaporates quickly as soon as it interacts with the film (as boiling point is low) and have no profound effect on it's morphology; whereas EA can assist crystallization by exploiting non-covalent weak interaction (due to high boiling point) and in the process microstructures are formed. In order to study the local chemical composition and to accesses the relative differences in the elemental compositions in DCM and EA diffused films, EDS analysis were performed and resulted data is depicted in figure 7.3 (f). EDS elemental mapping of figure 7.3 (b) and 7.3 (d) are presented in figure 7.3 (f) and the result confirmed that EA diffused film has more coverage than that of DCM diffused film. In the EA treated film the ratio Pb:I is close to the actual composition (1:3.03), whereas in the DCM treated film the ratio is 1:2.68. Incomplete conversion of the precursor in the synthesis process for the case of DCM diffused film might be responsible for this iodine deficiency. In order to identify the phase purity of both the samples (DCM and EA treated films) and get more information about the structure, X-ray diffraction (XRD) was performed and presented in figure 7.3 (e). The crystalline nature of the perovskite material is confirmed in both the samples, being identified as the tetragonal phase (I4/*mcm*), based on the literature reports [27,90]. Diffraction peaks appearing at 26.49^0 and 37.67^0 and marked by asterisks in figure 7.3 (e) arise from the underlying FTO substrate and peaks at 14.11^0 and 28.44^0 correspond to the (110) and (220) crystal planes within the perovskite film and serve as a metric for the material's crystallinity.

7.3.2 Optical Studies

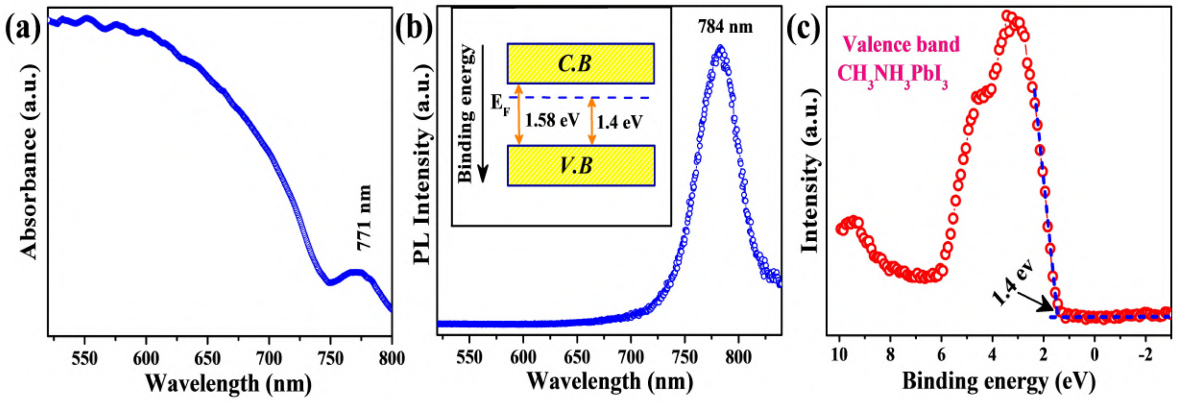

Figure 7.4: (a) UV-visible absorption spectra, (b) Photoluminescence (PL) spectra and (c) Valence band XPS spectra of EA diffused $\mathrm{CH_3NH_3PbI_3}$ thin film. Energy level diagram of EA diffused $CH_3NH_3PbI_3$ film is shown in inset of (b).

Further, optical studies (UV-Visible absorption and photoluminescence) of micro-structured thin film (EA treated $\mathrm{CH_3NH_3PbI_3}$) was performed to find its potential as an absorber material in solar cell. In order to draw the energy level diagram of absorber material (EA treated $\mathrm{CH_3NH_3PbI_3}$) and choose appropriate electron and hole transport materials, optical studies (UV-Vis absorption and photoluminescence) of this micro-structured film were performed. The UV-Visible absorption spectrum of EA treated $\mathrm{CH_3NH_3PbI_3}$ reveals strong absorption in the visible region with absorption edge at 771 nm (figure 7.4 (a)), which is in agreement with the literature [90]. High intensity of the absorption peak in the visible region make it suitable for solar cell absorber material. Further, PL emission of microstructured film was observed at 783 nm (1.58 eV), which can be attributed to band-to-band direct transition and is consistent with the literature reports [341]. In order to identify fermi energy level, valence band (VB) spectrum acquired from this sample is depicted in figure 7.4 (c), where the main feature (2-6 eV) arises due to nonbonding Cl 3*p* orbitals, along with dominant contribution from antibonding Pb 6*s*, as observed from band structure calculations [35]. Schematic energy level diagram (Inset of figure 7.4 (b)) of Fermi energy (E_F), bottom of conduction band (CB) and top of valence band (VB) was constructed using room temperature PL studies (band gap of 1.58 eV) and linear interpolation of VB spectra (1.4 eV) as shown in Figure 7.4 (c). Proper understanding of this energy level diagram is essential to identify the appropriate electron and hole transport materials for the efficient fabrication of solar cell device [90, 176].

7.3.3 Power Conversion Efficiency (PCE) Measurement

Perovskite solar cells with a structure of FTO/compact TiO_2 (HBL)/Mesoporous TiO_2 (ETL)/$CH_3NH_3PbI_3$/Spiro-OMeTAD (HTL)/Au are fabricated, and the photovoltaic performance measured under AM1.5 simulated solar illumination (100mW/cm^2) [340]. It is found that perovskite solar cell prepared by high boiling point antisolvent diffusion exhibits the highest power conversion efficiency (PCE) with negliable hysteris, which is consistent with the SEM and XRD that it maintains better morphology than the other two. The PCE is 7.7% in the forward bias scan and 7.6% in the reverse bias scan. A comparative study on current density *vs.* voltage plots of all three samples are depicted in figure 7.5 (a) and the summary of device performance is presented in Table-7.1.

Table 7.1: Summary of Solar Cell Device Performance (in ambient conditions)

Sample synthesis	Current density (mA cm^{-2})	Open-circuit voltage (Volt)	Fill factor (%)	PCE (%)
As deposited Film (without anti-solvent)	15.15	0.72	51.44	5.6
DCM diffusion	15.43	0.73	51.80	5.8
EA diffusion (Forward Bias)	15.53	0.74	66.13	7.7
EA diffusion (Reverse Bias)	15.52	0.73	67.33	7.6

Table-7.1 clearly demonstrates that the devices made of without antisolvent or low boiling point (DCM) antisolvent diffused perovskite active layer results poor device performance than high boiling point (EA) antisolvent diffused active layer. As seen from table-7.1, devices made by above three methods yielded almost same J_{sc} and V_{oc}, how-

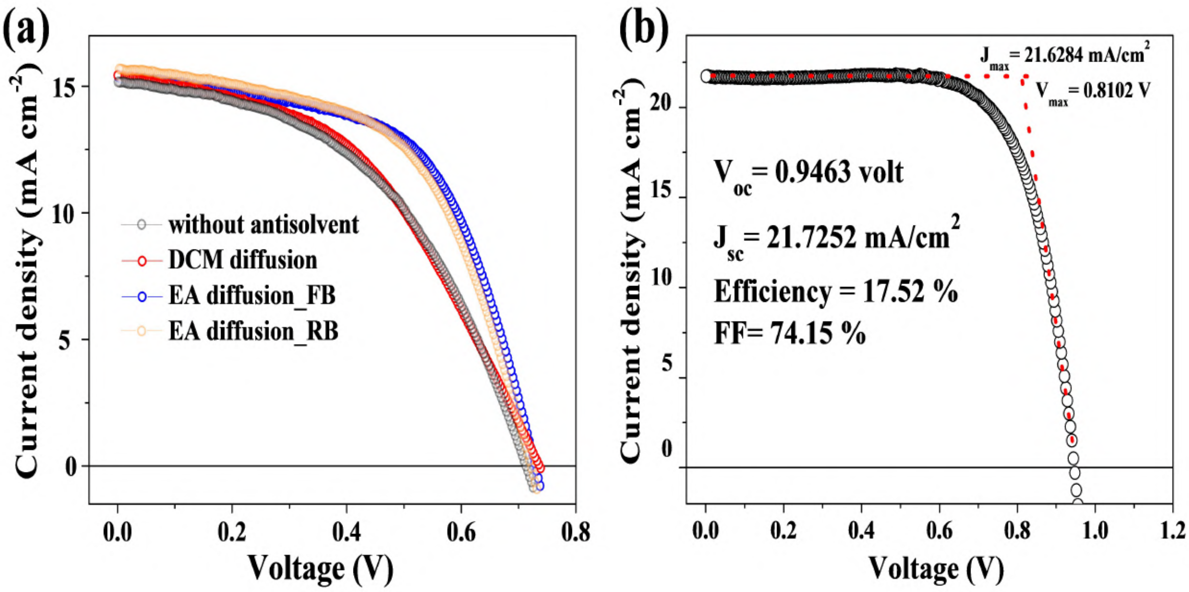

Figure 7.5: (a) Effects of different antisolvents (DCM and EA) on the photovoltaic device performance in ambient atmosphere. (b) Device performance of EA diffused perovskite film prepared inside the glove box.

ever, due to enhancement of fill-factor(FF) for EA diffused film, efficiency enhanced. As seen from SEM images in figure 7.3, formation of perovskite microrods enhances the sample coverage in the film and prevent electric shunting between the electrodes, and markedly enhanced the FF of the device. Thus, high device performance is attribute to the formation of microrods due to weak interaction between hybrid perovskite and the high boiling point antisolvent. In order to achieve better device performance which can be comparable with the previous reports [10, 333], we have synthesized the EA diffused perovskite film inside the glove box. As plotted in figure 7.5 (b), the hybrid cell made of a EA diffused $CH_3NH_3PbI_3$ active layer reported in this work exhibits a V$_{oc}$ of 0.94 V, a J$_{sc}$ of 21.72 mA cm^{-2}, and a FF of 0.74, corresponding to a PCE of 17.52%. These photovoltaic performances are comparable to those of a hybrid cell with a $CH_3NH_3PbI_3$ active layer prepared by different methods [211, 333, 336–338].

7.4 Conclusions

In conclusion, we successfully demonstrated an antisolvent vapor diffusion technique to form microstructured perovskite film for the first time. Our observation also suggested that due to non-covalent weak interaction between the perovskite absorber and the high boiling point antisolvent (EA), microrods were grown. Further, we also observed that due to better morphology for the mesoporous films, EA diffused film exhibits better fill factor and as a result of it there is an 32% power conversion efficiency enhancement than the DCM diffused and as deposited films. Devices made from EA diffused films synthesized inside the glove box resulted power conversion efficiency of 17.52%, which is comparable with the devices using this material. Thus, we believe that high boiling point antisolvent vapor diffusion technique is a potential method to achieve better device performance.

Chapter 8

Summary and Future plans

Final outcome and important findings of this thesis work is summarized in this chapter. We believe that this thesis will offer a valuable perception to the perovskite solar cell community and will encourage further research and applications in solar cell and optoelectronic devices. Future scopes of this thesis work is also presented in this chapter.

8.1 Summary

In this thesis we present detailed structural and spectroscopic investigations of organic-inorganic hybrid perovskites, a light absorbing material, which has shown considerable potential to be used as a solar cell and optoelectronic material. An effective approach to synthesize high-quality defect free single crystals of organic-inorganic hybrid perovskites ($CH_3NH_3PbX_3$; X=Br, Cl) to achieve better device performance is presented in chapter 3. Crystal structures and structural phase transitions of hybrid perovskites using XRD and EXAFS measurements are discussed in chapter 4. Studies on optical and electronic evolutions of hybrid perovskite are presented in chapter 5. Temperature dependence of reversible photo-induced phase separation of mixed halide perovskite are discussed in chapter 6 and fabrication of mesoporous 'methylammonium lead iodide' solar cells and the effect of antisolvent in morphology and power conversion efficiency (PCEs) are presented in chapter 7; while in the following sections we summarize our findings and present future scope of the work as shown in Figure 8.1.

8.1.1 Structural Investigations

As a starting point, we have synthesized single crystals of organic-inorganic hybrid perovskites *via* Inverse Temperature Crystallization (ITC), Solution Temperature Lowering (STL), Anti-solvent Vapor Assisted Crystallization (AVC) and Solvent Evaporation at room temperature (SERT) methods and identified that high boiling point (Ethyl acetate) diffused AVC method produce high quality and well shaped defect free single crystals. We have used these crystals for detailed structural and spectroscopic characterization. Further, crystal structure and crystallographic phase transition of this system is discussed using synchrotron X-ray diffraction and heat capacity measurements. Variation of lattice parameters, tetragonal distortion and linear expansion coefficients clearly indicate that it is a first order phase transition and rule out the possibility of phase coexistence in this system. Detailed EXAFS and XRD studies corroborate the distortion in the structure is associated with the Halide displacement due to CH_3NH_3 orientation inside the PbX_6, which is absent for the case of symmetric $CsPbBr_3$ system.

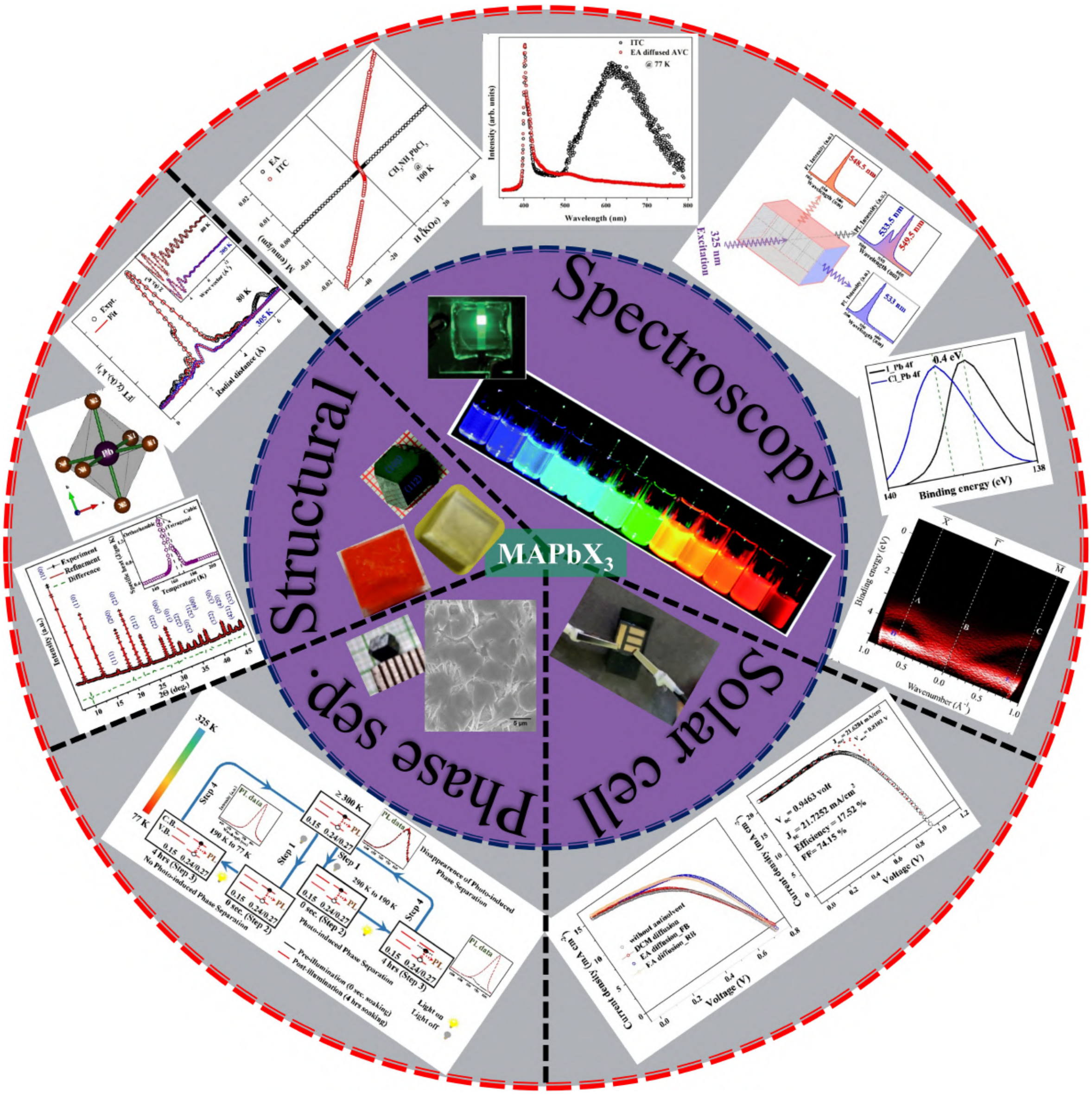

Figure 8.1: Schematic diagram of the important findings of the present work.

8.1.2 Spectroscopic Investigations

Optical spectroscopic measurement (UV-visible absorbance and photoluminescence) of hybrid perovskite revels that the bandgap of this system can be tuned from blue to red region of visible spectra by changing the halide composition from Cl to Br to I and the corresponding bandgap (room temperature) are 405 nm, 532 nm and 785 nm. The observed bandgap changes upon halide substitution are influenced by the electronic states of the anion. Exciton binding energy, exciton-phonon interaction and electron-phonon coupling constant of hybrid perovskites are extracted from temperature dependent PL and ambient temperature Raman measurements. UV-Visible absorption spectra showed the existence of two electronic states in either valence or conduction bands of $CH_3NH_3PbX_3$ (X= I, Br, Cl), which was further confirmed by temperature-dependent PL measurements. However, single peak is observed for the case of $CsPbBr_3$, which implies that the origin of the dual emission is associated with the nature of the organic cation. With the first-principle DFT calculations and MD simulations, we determined the experimentally observed energy difference of dual PL emission peaks is caused most likely by the octahedral distortion which arises due to molecular orientation of CH_3NH_3. Allowing the C-N bonds to rotate in the ac plane about the b-axis, two closely spaced minima were observed and the electronic structure calculations result in two closely spaced valence band at Γ point with a separation of 13.7 meV which matches closely with the experimentally observed energy difference between the two peaks in orthorhombic phase. Further, observation of anisotropic crystal face dependent PL spectra of $CH_3NH_3PbBr_3$ sample strengthen our explanation regarding this issue.

Detailed results of the electronic structure from single crystal samples of $CH_3NH_3PbX_3$ (X= I, Br, Cl) using photoelectron spectroscopy (X-ray photoelectron spectroscopy (XPS), angle-integrated and angle-resolved ultra-violet photoelectron spectroscopy (UPS)) along with the first-principles band structure calculations based on density functional theory are presented in this thesis. The orbital contributions of elements in the valence band spectra were identified as hybridized Pb-s and Cl/Br-p bands by comparing photoionization cross section and projected density of states (PDOS) for each of these elements. Further, analyzing ARPES intensity map along $\overline{X}-\overline{\Gamma}-\overline{M}$ direction reveals downward dispersing bands with maxima occurring at $\overline{M}$ symmetry point and minima at the $\overline{\Gamma}$ point, which is consistent with the calculated band structure for a cubic phase. However, experimental observation of degenerate bands at $\overline{\Gamma}$ point, contrary to the theoretical results, where 9 fold degeneracy was lifted, in a periodic calculation with a specific configuration (specific orientation of CH_3NH_3 molecule) of the disordered system (cubic system) points out the theoretical limitations in understanding electronic structure of hybrid perovskites in cubic phase. We calculated band structure of $CsPbCl_3$ wherein symmetric potential exist at the center of the inorganic cage, due to the presence of Cs atom and were able to reproduce the experimental ARPES intensity map to a large extend, but some discrepancies in reproducing experimental constant energy counters still persists. What is needed is a comprehensive calculations using coherent potential approximation in DFT which is beyond the scope of this thesis. The measured band dispersion also help us to extract effective hole mass and lower limit of hole mobility using one-dimensional tight binding model. We believe that our findings will help in fine-tuning the energy-matching at several interfaces, and in turn the performance of the solar cell and optoelectronic devices.

8.1.3 Photo-induced Phase Separation of Mixed Halide Perovskites

Photoluminescence (PL) studies of mixed halide perovskites revealed that demixing of halide ions into iodine-rich and bromine-rich domains occurred above a critical temperature and concentration of Br, in a narrow temperature window (We provide the first experimental proof for the same). Above this temperature window, *i.e.*, at elevated temperature, the electron-phonon interaction results in a decreased electron hole mobility and they recombine to form mixed state. Our findings may hence pave a relook at further optimization of tandem solar cell comprising of mixed halides for higher temperature applications, where there is no photo-induced phase separation, than at room temperature. Our observation also suggests that demixing and remixing temperatures are pinned to crystallographic phase transition temperatures, hence providing an ample playground for fundamental research as well. Further, appearance of longer lifetime of carriers in the phase separated state confirms the presence of strong electron-phonon interaction while longer saturation time of the cluster formation confirms that grain boundary/sample quality plays a crucial role in phase separation.

8.1.4 Solar cell Device

We have also successfully demonstrated an antisolvent vapor diffusion technique to form microstructured perovskite film for the first time in this thesis. Our observation suggested that due to non-covalent weak interaction between the perovskite absorber and the high boiling point antisolvent (Ethyl acetate; EA), microrods were grown. Further, we also observed that due to better morphology for the mesoporous films, EA diffused film exhibits better fill factor and as a result of it there is an 32% power conversion efficiency (PCE) enhancement than the DCM diffused (PCE = 5.8%) and as deposited films (PCE = 5.6%). Devices made from EA diffused films synthesized inside the glove box resulted power conversion efficiency of 17.52%, which is comparable with the devices using this material. Thus, we believe that high boiling point antisolvent vapor diffusion technique is a potential method to achieve better device performance.

8.2 Future Plans

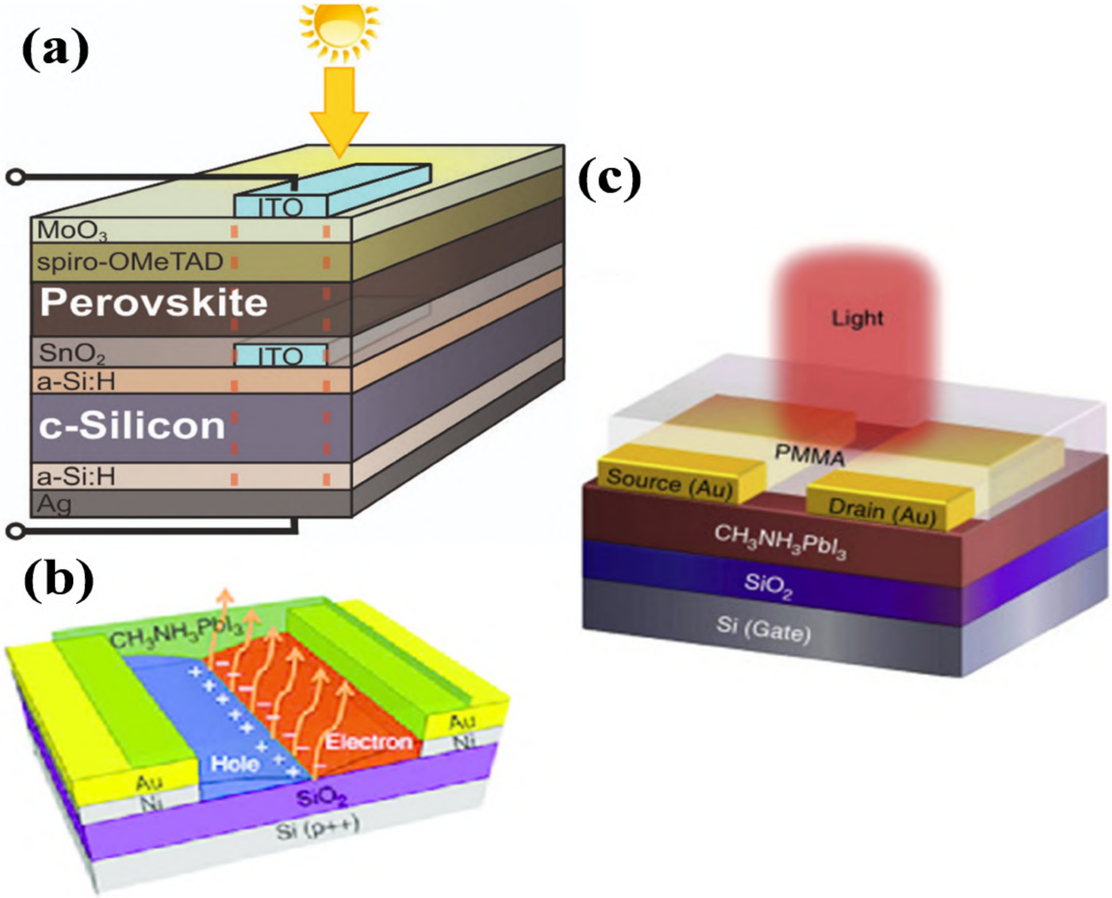

Figure 8.2: Schematic diagram of (a) Tandem solar cell, (b) Field Effect Transistor (FET) and (c) Phototransistor
[Taken from (a) Energy Environ. Sci., 2016, 9, 81-88, (b) J. Mater. Chem. C, 2016, 4, 11-27, (c) Nat. Commun., 2015, 6, 8238.]

8.2.1 Tandem Solar cell

Efficiency of single junction perovskite solar cell is presently $\sim$ 22% while efficiency of a single-junction silicon solar cell $\sim$ 26%, moreover, both these solar cells absorb different parts of solar spectrum, which lead the researchers to work on multijunction solar cells [342]. $CH_3NH_3Pb(I_{1-x}Br_x)_3$, ($0 \leqslant x \leqslant 1$) are potential candidates for applications in multijunction/tandem solar cells and it is prediced that coupling of perovskite material with commercially available Si [185, 293–296], Germanium [297] and Copper indium gallium selenide (CIGS) cells [298] could increase the cell efficiency compared to the respective single junction cells, but at present the light absorber material phase-separates in presence of light. Research is required to curtail this phase separation and look for suitable alternatives.

8.2.2 Field Effect Transistor

For field effect transistor (FET) fast and unimpeded lateral charge transport should occur through the confines of the semiconductor-dielectric interface over much longer distances [23, 343]. As single crystals of hybrid perovskites are less defective and have higher carrier mobility, longer carrier diffusion length and lower trap density than that of polycrystalline thin films, field effect transistor from single crystalline sample will show better device performance than thin-film counterpart.

8.2.3 Photodetector

Photodetectors are used in wide range of applications, spanning from medicine to consumer electronics, optical communication, research and defence. Low defect concentration and longer diffusion length of hybrid perovskite single crystals indicate they are promising candidates to work as an active component in fast photodetector [11, 20, 290, 291, 344].

8.2.4 Solar heat harvesting

The overall power conversion efficiency (PCE) of a solar cell could be improved if heat generated by sun-light can be captured in a single module. This can be achieved by

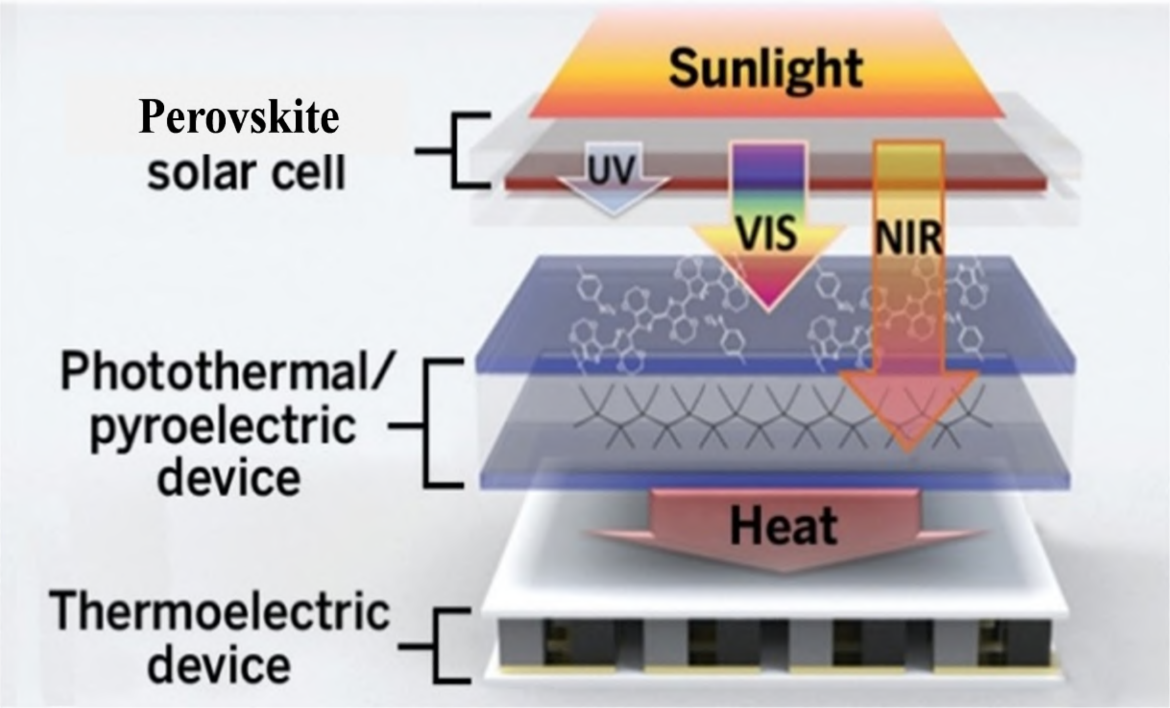

Figure 8.3: Illustration of photovoltaic and photothermal pyro-thermoelectric device [Taken from ACS Nano, 2015, 9, 11830-11839]

coupling a pyroelectric (PE) and thermoelectric (TE) device on the bottom of a perovskite solar cell as shown in Figure 8.3. Perovskite solar cell absorb UV-Visible region of solar spectrum and achieved maximum 22% PCE and near infrared region become transmitted and wasted, which can be reused for PE harvesting, and eventually, for TE conversion. Brief mechanism of this device: under sunlight irradiation, the perovskite solar cell harvest energy through the photovoltaic effect, while heat is generated by the photothermal effect of the PE film from the transmitted light, mainly near IR region, through the perovskite solar cell, to increase the temperature of the PE device and to generate electricity through PE conversion. The unused heat is then transferred to the TE device to generate a temperature gradient and harvest additional energy [345].

References

[1] T. B. Johansson, H. Kelly, A. K. N. Reddy and R. H. Williams, “*Renewable energy: Sources for fuels and electricity*”, 1993.

[2] T. Jackson, “*Renewable energy sources*”, 1998.

[3] britannica.com, “*https://www.britannica.com/technology/solar cell*”, 1999.

[4] B. R. Singh and O. Singh, “*Future scope of solar energy in india*”, Samriddhi **8** (2016) 20–25.

[5] wikipedia.org, “*https://en.wikipedia.org/wiki/solar cell*”, 2019.

[6] P. Würfel and U. Würfel, “*Physics of solar cells: From basic principles to advanced concepts*”, 2016.

[7] L. M. Fraas and L. D. Partain, “*Solar cells and their applications*”, 2010.

[8] J. Poortmans and V. Arkhipov, “*Thin film solar cells: Fabrication, characterization and applications*”, 2006.

[9] B. O’regan and M. Gratzel, “*A low cost, high efficiency solar cell based on dye-sensitized*”, Nature **353** (1991) 24.

[10] W. S. Yang, B.-W. Park, E. H. Jung, N. J. Jeon, Y. C. Kim, D. U. Lee, S. S. Shin, J. Seo, E. K. Kim, J. H. Noh and S. I. Seok, “*Iodide management in formamidinium-lead-halide-based perovskite layers for efficient solar cells*”, Science **356** (2017) 1376–1379.

[11] R. Babu, L. Giribabu and S. P. Singh, “*Recent advances in halide-based perovskite crystals and their optoelectronic applications*”, Cryst. Growth Des. **18** (2018) 2645—2664.

[12] Q. Zhang, R. Su, W. Du, X. Liu, L. Zhao, S. T. Ha and Q. Xiong, “*Advances in small perovskite-based lasers*”, Small Methods **1** (2017) 1700163.

[13] H.-R. Wenk and A. Bulakh, “*Minerals: Their constitution and origin*”, 2004.

[14] M. A. Peña and J. L. Fierro, “*Chemical structures and performance of perovskite oxides*”, Chemical Reviews **101** (2001) 1981–2017.

[15] J. Luxová, P. Šulcová and M. Trojan, “*Study of perovskite compounds*”, Journal of Thermal Analysis and Calorimetry **93** (2008) 823–827.

[16] C. K. MØLLER, “*Crystal structure and photoconductivity of caesium plumbohalides*”, Nature **182** (1958) 1436.

[17] D. Weber, "*$Ch_3nh_3pbx_3$, ein pb(ii)-system mit kubischer perowskitstruktur/$ch_3nh_3pbx_3$, a pb(ii)-system with cubic perovskite structure*", Journal of Natural Sciences B **33** (1978) 1443–1445.

[18] H. Arend, W. Huber, F. H. Mischgofsky and G. K. Richter-Van Leeuwen, "*Layer perovskites of the $(c_nh_{2n+1}nh_3)_2mx_4$ and $nh_3(ch_2)_mnh_3mx_4$ families with m = cd, cu, fe, mn or pd and x = cl or br: Importance, solubilities and simple growth techniques*", J. Cryst. Growth **43** (1978) 213–223.

[19] A. Kojima, K. Teshima, Y. Shirai and T. Miyasaka, "*Organometal halide perovskites as visible-light sensitizers for photovoltaic cells*", J. Am. Chem. Soc. **131** (2009) 6050–6051.

[20] N. K. Kumawat, A. Dey, A. Kumar, S. P. Gopinathan, K. L. Narasimhan and D. Kabra, "*Band gap tuning of $ch_3nh_3pb(br_{1-x}cl_x)_3$ hybrid perovskite for blue electroluminescence*", ACS Appl. Mater. Interfaces **7** (2015) 13119–13124.

[21] S. D. Stranks, G. E. Eperon, G. Grancini, C. Menelaou, M. J. P. Alcocer, T. Leijtens, L. M. Herz, A. Petrozza and H. J. Snaith, "*Electron-hole diffusion lengths exceeding 1 micrometer in an organometal trihalide perovskite absorber*", Science **342** (2013) 341–344.

[22] L. M. Herz, "*Charge-carrier mobilities in metal halide perovskites: Fundamental mechanisms and limits*", ACS Energy Lett. **2** (2017) 1539–1548.

[23] X. Y. Chin, D. Cortecchia, J. Yin, A. Bruno and C. Soci, "*Lead iodide perovskite light-emitting field-effect transistor*", Nat. Commun. **6** (2015) 7383.

[24] T. Miyasaka, "*Perovskite photovoltaics: Rare functions of organo lead halide in solar cells and optoelectronic devices*", Chem. Lett. **44** (2015) 720–729.

[25] G. Kieslich, S. Sun and A. K. Cheetham, "*Solid-state principles applied to organic-inorganic perovskites: New tricks for an old dog*", Chem. Sci. **5** (2014) 4712–4715.

[26] Z. Li, M. Yang, J.-S. Park, S.-H. Wei, J. J. Berry and K. Zhu, "*Stabilizing perovskite structures by tuning tolerance factor: Formation of formamidinium and cesium lead iodide solid-state alloys*", Chem. Mater. **28** (2016) 284–292.

[27] P. Nandi, C. Giri, B. Joseph, S. Rath, U. Manju and D. Topwal, "*$Ch_3nh_3pbi_3$, a potential solar cell candidate: Structural and spectroscopic investigations*", J. Phys. Chem. A **120** (2016) 9732–9739.

[28] T. Baikie, Y. Fang, J. M. Kadro, M. Schreyer, F. Wei, S. G. Mhaisalkar, M. Graetzel and T. J. White, "*Synthesis and crystal chemistry of the hybrid perovskite $ch_3nh_3pbi_3$ for solid-state sensitised solar cell applications*", J. Mater. Chem. A **1** (2013) 5628–5641.

[29] A. Poglitsch and D. Weber, "*Dynamic disorder in methylammoniumtrihalogenoplumbates (ii) observed by millimeter-wave spectroscopy*", J. Chem. Phys. **87** (1987) 6373–6378.

[30] R. E. Wasylishen, O. Knop and J. B. Macdonald, "*Cation rotation in methylammonium lead halides*", Solid State Commun. **56** (1985) 581–582.

[31] N. Onoda-Yamamuro, T. Matsuo and H. Suga, "*Calorimetric and ir spectroscopic studies of phase transitions in methylammoniumtrihalogenoplumbates (ii)*", J. Phys. Chem. Solids **51** (1990) 1383–1395.

[32] A. A. Zhumekenov, M. I. Saidaminov, M. A. Haque, E. Alarousu, S. P. Sarmah, B. Murali, I. Dursun, X.-H. Miao, A. L. Abdelhady, T. Wu, O. F. Mohammed and O. M. Bakr, “*Formamidinium lead halide perovskite crystals with unprecedented long carrier dynamics and diffusion length*”, ACS Energy Lett. **1** (2016) 32—37.

[33] C. C. Stoumpos, C. D. Malliakas, J. A. Peters, Z. Liu, M. Sebastian, J. Im, T. C. Chasapis, A. C. Wibowo, D. Y. Chung, A. J. Freeman, B. W. Wessels and M. G. Kanatzidis, “*Crystal growth of the perovskite semiconductor cspbbr3: A new material for high-energy radiation detection*”, Cryst. Growth Des. **13** (2013) 2722—2727.

[34] P. Postorino and L. Malavasi, “*Pressure-induced effects in organic–inorganic hybrid perovskites*”, J. Phys. Chem. Lett. **8** (2017) 2613–2622.

[35] R. Lindblad, N. R. Jena, B. Philippe, J. Oscarsson, D. Bi, A. Lindblad, S. Mandal, B. Pal, D. D. Sarma, O. Karis, H. Siegbahn, E. M. J. Johansson, M. Odelius and H. Rensmo, “*Electronic structure of* $ch_3nh_3pbx_3$ *perovskites: Dependence on the halide moiety*”, J. Phys. Chem. C **119** (2015) 1818–1825.

[36] Y. Yan, W.-J. Yin, T. Shi, W. Meng and C. Feng, “*Defect physics of* $ch_3nh_3pbx_3$ $(x = i, br, cl)$ *perovskites*”, 2016.

[37] W.-J. Yin, T. Shi and Y. Yan, “*Unique properties of halide perovskites as possible origins of the superior solar cell performance*”, Adv. Mater. **26** (2014) 4653–4658.

[38] T. Shi, W.-J. Yin, F. Hong, K. Zhu and Y. Yan, “*Unipolar self-doping behavior in perovskite* $ch_3nh_3pbbr_3$”, Appl. Phys. Lett. **106** (2015) 103902.

[39] T. Umebayashi, K. Asai, T. Kondo and A. Nakao, “*Electronic structures of lead iodide based low-dimensional crystals*”, Phys. Rev. B **67** (2003) 155405.

[40] C. Li, J. Wei, M. Sato, H. Koike, Z.-Z. Xie, Y.-Q. Li, K. Kanai, S. Kera, N. Ueno and J.-X. Tang, “*Halide-substituted electronic properties of organometal halide perovskite films: Direct and inverse photoemission studies*”, ACS Appl. Mater. Interfaces **8** (2016) 11526–11531.

[41] T. Komesu, X. Huang, T. R. Paudel, Y. B. Losovyj, X. Zhang, E. F. Schwier, Y. Kojima, M. Zheng, H. Iwasawa, K. Shimada, M. I. Saidaminov, D. Shi, A. L. Abdelhady, O. M. Bakr, S. Dong, E. Y. Tsymbal and P. A. Dowben, “*Surface electronic structure of hybrid organo lead bromide perovskite single crystals*”, J. Phys. Chem. C **120** (2016) 21710–21715.

[42] Z. Xiao and Y. Yan, “*Progress in theoretical study of metal halide perovskite solar cell materials*”, Adv. Energy Mater. **7** (2017) 1701136.

[43] E. M. Proupin, P. Palacios, P. Wahnón and J. C. Conesa, “*Self-consistent relativistic band structure of the ch3nh3pbi3 perovskite*”, Phys. Rev. B **90** (2014) 045207.

[44] J.-P. Yang, M. Meissner, T. Yamaguchi, X.-Y. Zhang, T. Ueba, L.-W. Cheng, S. Ideta, K. Tanaka, X.-H. Zeng, N. Ueno and S. Kera, “*Band dispersion and hole effective mass of methylammonium lead iodide perovskite*”, Solar RRL **2** (2018) 1800132.

[45] C. Quarti, E. Mosconi and F. De Angelis, “*Interplay of orientational order and electronic structure in methylammonium lead iodide: Implications for solar cell operation*”, Chem. Mater. **26** (2014) 6557—6569.

[46] C. Motta, F. El-Mellouhi, S. Kais, N. Tabet, F. Alharbi and S. Sanvito, “*Revealing the role of organic cations in hybrid halide perovskite ch3nh3pbi3*”, Nat. Commun. **6** (2015) 7026.

[47] S. Sarkar and P. Mahadevan, “*Role of the a-site cation in determining the properties of the hybrid perovskitech3nh3pbbr3*”, Phys. Rev. B **95** (2017) 214118.

[48] L. D. Whalley, J. M. Frost, Y.-K. Jung and A. Walsh, “*Perspective: Theory and simulation of hybrid halide perovskites*”, J. Chem. Phys. **146** (2017) 220901.

[49] D. L. Wood and J. Tauc, “*Weak absorption tails in amorphous semiconductors*”, Phys. Rev. B **5** (1972) 3144.

[50] C. Delerue, G. Allan, C. Reynaud, O. Guillois, G. Ledoux and F. Huisken, “*Multiexponential photoluminescence decay in indirect-gap semiconductor nanocrystals*”, Phys. Rev. B **73** (2006) 235318.

[51] Y. Li, L. Ji, R. Liu, C. Zhang, C. H. Mak, X. Zou, H.-H. Shen, S.-Y. Leuf and H.-Y. Hsu, “*A review on morphology engineering for highly efficient and stable hybrid perovskite solar cells*”, J. Mater. Chem. A **6** (2018) 12842–12875.

[52] R. Sheng, A. Ho-Baillie, S. Huang, S. Chen, X. Wen, X. Hao and M. A. Green, “*Methylammonium lead bromide perovskite-based solar cells by vapor-assisted deposition*”, J. Phys. Chem. C **119** (2015) 3545–3549.

[53] R. Comin, G. Walters, E. S. Thibau, O. Voznyy, Z.-H. Lu and E. H. Sargent, “*Structural, optical, and electronic studies of wide-bandgap lead halide perovskites*”, J. Mater. Chem. C **3** (2015) 8839–8843.

[54] P. Nandi, C. Giri, D. Swain, U. Manju, S. D. Mahanti and D. Topwal, “*Temperature dependent photo-induced reversible phase separation in mixed halide perovskite*”, ACS Appl. Energy Mater. **1** (2018) 3807–3814.

[55] Y. Ogomi, A. Morita, S. Tsukamoto, T. Saitho, S. Q. Fujikawa, N., T. Toyoda, K. Yoshino, S. S. Pandey, T. Ma and S. Hayase, “*Ch3nh3snxpb(1–x)i3 perovskite solar cells covering up to 1060 nm*”, J. Phys. Chem. Lett. **5** (2014) 1004–1011.

[56] G. Xing, N. Mathews, S. S. Lim, N. Yantara, X. Liu, D. Sabba, M. Grtzel, S. Mhaisalkar and T. C. Sum, “*Low-temperature solution-processed wavelength-tunable perovskites for lasing*”, Nat. mater. **13** (2014) 476–480.

[57] C. Wehrenfennig, M. Liu, H. J. Snaith, M. B. Johnston and L. M. Herz, “*Charge carrier recombination channels in the low temperature phase of organic-inorganic lead halide perovskite thin films*”, APL Mater. **2** (2014) 081513.

[58] D. Niesner, O. Schuster, M. Wilhelm, I. Levchuk, A. Osvet, S. Shrestha, M. Batentschuk, C. Brabec and T. Fauster, “*Temperature-dependent optical spectra of single-crystal (ch3nh3)pbbr3 cleaved in ultrahigh vacuum*”, Phys. Rev. B **95** (2017) 075207.

[59] B. Murali, E. Yengel, C. Yang, W. Peng, E. Alarousu, O. M. Bakr and O. F. Mohammed, “*The surface of hybrid perovskite crystals: A boon or bane*”, ACS Energy Lett. **2** (2017) 846–856.

[60] wikipedia.org, “*https://en.wikipedia.org/wiki/exciton*”, 2014.

[61] W. Y. Liang, "*Excitons*", Phys. Educ. **5** (1970) 226–228.

[62] J. Frenkel, "*On the transformation of light into heat in solids. i*", Physical Review **37** (1931) 17.

[63] J. D. wright, "*Molecular crystals (2nd ed.)*", 1987.

[64] G. Wannier, "*The structure of electronic excitation levels in insulating crystals*", Physical Review **52** (1937) 191.

[65] M. E. Ziffer, J. C. Mohammed and D. S. Ginger, "*Electroabsorption spectroscopy measurements of the exciton binding energy, electron–hole reduced effective mass, and band gap in the perovskite ch3nh3pbi3*", ACS Photonics **3** (2016) 1060–1068.

[66] G. Grancini, A. R. Srimath Kandada, J. M. Frost, A. J. Barker, M. De Bastiani, M. Gandini, L. G. W. A. Marras, S. and A. Petrozza, "*Role of microstructure in the electron–hole interaction of hybrid lead halide perovskites*", Nat. Photonics **9** (2015) 695–701.

[67] V. D. Innocenzo, G. Grancini and S. D. S. M. M. L. G. L. H. J. S. A. P. Alcocer, A. R. S. Kandada, "*Excitons versus free charges in organo-lead tri-halide perovskites*", Nat. Commun. **5** (2014) 3586.

[68] K. Wu, A. Bera, C. Ma, Y. Du, Y. Yang, L. Li and T. Wu, "*Temperature-dependent excitonic photoluminescence of hybrid organometal halide perovskite films*", Phys. Chem. Chem. Phys. **16** (2014) 22476–22481.

[69] J. A. Sichert, Y. Tong, N. Mutz, M. Vollmer, S. Fischer, K. Z. Milowska, R. García Cortadella, B. Nickel, C. Cardenas-Daw, J. K. Stolarczyk, A. S. Urban and J. Feldmann, "*Quantum size effect in organometal halide perovskite nanoplatelets*", Nano Lett. **15** (2015) 6521–6527.

[70] M. Bokdam, T. Sander, A. Stroppa, S. Picozzi, D. D. Sarma, C. Franchini and G. Kresse, "*Role of polar phonons in the photo excited state of metal halide perovskites*", Sci. Rep. **6** (2016) 28618–28625.

[71] wikipedia.org, "*https://en.wikipedia.org/wiki/polaron*", 2004.

[72] N. Lu, L. Li, D. Geng and M. Liu, "*A review for polaron dependent charge transport in organic semiconductor*", Organic Electronics **61** (2018) 223–234.

[73] C. G. Bischak, C. L. Hetherington, H. Wu, S. Aloni, D. F. Ogletree, D. T. Limmer and N. S. Ginsberg, "*Origin of reversible photoinduced phase separation in hybrid perovskites*", Nano Lett. **17** (2017) 1028–1033.

[74] M. Arif, M. Yun, S. Gangopadhyay, K. Ghosh, L. Fadiga, F. Galbrecht, U. Scherf and S. Guha, "*Polyfluorene as a model system for space-charge-limited conduction*", Phys. Rev. B **75** (2007) 195202.

[75] C. Wehrenfennig, M. Liu, H. J. Snaith, M. B. Johnston and L. M. Herz, "*Charge-carrier dynamics in vapour-deposited films of the organolead halide perovskite ch3nh3pbi3−xclx*", Energy Environ. Sci. **7** (2014) 2269–2275.

[76] G. Xing, N. Mathews, S. Sun, S. S. Lim, Y. M. Lam, M. Grätzel, S. Mhaisalkar and T. C. Sum, “*Long-range balanced electron and hole-transport lengths in organic-inorganic ch3nh3pbi3.*”, Science **342** (2013) 344.

[77] M. Hirasawa, T. Ishihara, T. Goto, K. Uchida and N. Miura, “*Magnetoabsorption of the lowest exciton in perovskite-type compound (ch3nh3)pbi3*”, Physica B: Physics of Condensed Matter **201** (1994) 427–430.

[78] F. Brivio, A. B. Walker and A. Walsh, “*Structural and electronic properties of hybrid perovskites for high-efficiency thin-film photovoltaics from first-principles*”, APL Materials **1** (2013) 042111.

[79] E. J. Juarez-Perez, R. S. Sanchez, L. Badia, G. Garcia-Belmonte, Y. S. Kang and B. J. Mora-sero, I., “*Photoinduced giant dielectric constant in lead halide perovskite solar cells*”, J. Phys. Chem. Lett. **5** (2014) 2390–2394.

[80] C. C. Stoumpos, C. D. Malliakas and M. G. Kanatzidis, “*Semiconducting tin and lead iodide perovskites with organic cations: phase transitions, high mobilities, and near-infrared photoluminescent properties*”, Inorg. Chem. **52** (2013) 9019–9038.

[81] E. L. Unger, E. T. Hoke, C. D. Bailie, W. H. Nguyen, H. T. Bowring, A. R., M. G. Christoforod and M. D. McGehee, “*Hysteresis and transient behavior in current–voltage measurements of hybrid-perovskite absorber solar cells*”, Energy Environ. Sci. **7** (2014) 3690–3698.

[82] J. Beilsten-Edmands, G. E. Eperon, R. D. Johnson, H. J. Snaith and P. G. Radaelli, “*Non-ferroelectric nature of the conductance hysteresis in ch3nh3pbi3 perovskite-based photovoltaic devices*”, Appl. Phys. Lett. **106** (2015) 173502.

[83] G. Sharada, P. Mahale, B. P. Kore, S. Mukherjee, M. S. Pavan, C. De, S. Ghara, A. Sundaresan, A. Pandey, T. N. Guru Row and D. D. Sarma, “*Is ch3nh3pbi3 polar?*”, J. Phys. Chem. Lett. **7** (2016) 2412–2419.

[84] H.-S. Kim, C.-R. Lee, J.-H. Im, K.-B. Lee, T. Moehl, A. Marchioro, S.-J. Moon, R. Humphry-Baker, M. J. E. Yum, J.-H., M. Grätzel and N. G. Park, “*Lead iodide perovskite sensitized all-solid-state submicron thin film mesoscopic solar cell with efficiency exceeding 9%*”, Sci. Rep. **2** (2012) 591.

[85] A. Mei, X. Li, L. Liu, Z. Ku, T. Liu, Y. Rong, M. Xu, M. Hu, J. Chen, Y. Yang, M. Grätzel and H. Han, “*A hole-conductor-free, fully printable mesoscopic perovskite solar cell with high stability*”, Science **345** (2014) 295–298.

[86] M. M. Lee, J. Teuscher, T. Miyasaka, T. N. Murakami and H. J. Snaith, “*Efficient hybrid solar cells based on meso-superstructured organometal halide perovskites*”, Science **338** (2012) 643–647.

[87] M. Liu, M. B. Johnston and H. J. Snaith, “*Efficient planar heterojunction perovskite solar cells by vapour deposition*”, Nature **501** (2013) 395–398.

[88] H. Zhou, Q. Chen, G. Li, S. Luo, T.-b. Song, H.-S. Duan, Z. Hong, J. You, Y. Liu and Y. Yang, “*Interface engineering of highly efficient perovskite solar cells*”, Science **345** (2014) 542–546.

[89] G. Yang, H. Tao, P. Qin, W. Ke and G. Fang, "*Recent progress in electron transport layers for efficient perovskite solar cells*", J. Mater. Chem. A **4** (2016) 3970–3990.

[90] P. Nandi, C. Giri, U. Bansode and D. Topwal, "*Ch3nh3pbi3 based solar cell: Modified by antisolvent treatment*", AIP Con. Proce. **1832** (2017) 080065.

[91] D. Gui, L. Ji, A. Muhammad, W. Li, W. Cai, Y. Li, X. Li, X. Wu and P. Lu, "*Jahn-teller effect on framework flexibility of hybrid organic-inorganic perovskites*", J. Phys. Chem. Lett. **9** (2018) 751–755.

[92] G. E. Eperon, V. M. Burlakov, A. Goriely and H. J. Snaith, "*Neutral color semitransparent microstructured perovskite solar cells*", ACS Nano **8** (2014) 591–598.

[93] I. L. Braly, D. W. deQuilettes, L. M. Pazos-Outón, S. Burke, M. E. Ziffer, D. S. Ginger and H. W. Hillhouse, "*Hybrid perovskite films approaching the radiative limit with over 90% photoluminescence quantum efficiency*", Nat. Photon. **12** (2018) 355–361.

[94] K. X. Steirer, P. Schulz, G. Teeter, V. Stevanovic, M. Yang, K. Zhu and J. J. Berry, "*Defect tolerance in methylammonium lead triiodide perovskite*", ACS Energy Lett. **1** (2016) 360–366.

[95] Y. Yang, Y. Yan, M. Yang, S. Choi, K. Zhu, J. M. Luther and M. C. Beard, "*Low surface recombination velocity in solution-grown ch3nh3pbbr3 perovskite single crystal*", Nat. Commun. **6** (2015) 7961.

[96] S. T. Williams, A. Rajagopal, C.-C. Chueh and A. K.-Y. Jen, "*Current challenges and prospective research for upscaling hybrid perovskite photovoltaics*", J. Phys. Chem. Lett. **7** (2016) 811–819.

[97] A. Krishna, S. Gottis, M. K. Nazeeruddin and F. Sauvage, "*Mixed dimensional 2d/3d hybrid perovskite absorbers: The future of perovskite solar cells?*", Adv. Func. Mater. **29** (2019) 1806482.

[98] M. I. Saidaminov, A. D. Abdelhady, G. Maculan and O. M. Bakr, "*Retrograde solubility of formamidinium and methylammonium lead halide perovskites enabling rapid single crystal growth*", Chem. Commun. **51** (2015) 17658–17661.

[99] M. I. Saidaminov, A. D. Abdelhady, B. Murali, E. Alarousu, V. M. Burlakov, W. Peng, I. Dursun, L. Wang, M.-G. He, Y., A. Goriely, M.-O. F. Wu, T. and O. M. Bakr, "*High-quality bulk hybrid perovskite single crystals within minutes by inverse temperature crystallization*", Nat. Commun. **6** (2015) 7586.

[100] G. Maculan, A. D. Seikh, A. D. Abdelhady, M. I. Saidaminov, M. A. Haque, B. Murali, E. Alarousu, O. F. Mohammed, T. Wu and O. M. Bakr, "*Ch3nh3pbcl3 single crystals: Inverse temperature crystallization and visible blind uv-photodetector*", J. Phys. Chem. Lett. **6** (2015) 3781–3786.

[101] Y. Liu, Z. Yang, D. Cui, X. Ren, J. Sun, X. Liu, J. Zhang, Q. Wei, H. Fan, F. Yu, X. Zhang, C. Zhao and S. F. Liu, "*Two-inch-sized perovskite ch3nh3pbx3 (x = cl, br, i) crystals: Growth and characterization*", Adv. Mater. **27** (2015) 5176–5183.

[102] D. Shi, V. Adinolfi, R. Comin, M. Yuan, E. Alarousu, A. Buin, Y. Chen, S. Hoogland, A. Rothenberger, K. Katsiev, Y. Losovyj, X. Zhang, P. A. Dowben, O. F. Mohammed, E. H. Sargent and O. M. Bakr, "*Low trap state density and long carrier diffusion in organolead trihalide perovskite single crystals*", Science **347** (2015) 519–522.

[103] D. Niesner, M. Wilhelm, I. Levchuk, A. Osvet, S. Shrestha, M. Batentschuk, C. Brabec and T. Fauster, "*Giant rashba splitting in ch3nh3pbbr3 organic-inorganic perovskite*", Phys. Rev. Lett. **117** (2016) 126401.

[104] C. Wang, B. R. Ecker, H. Wei, J. Huang, J.-Q. Meng and Y. Gao, "*Valence band dispersion measurements of perovskite single crystal with angle-resolved photoemission spectroscopy*", Phys. Chem. Chem. Phys. **19** (2017) 5361–5365.

[105] W.-Q. Liao, Y. Zhang, C.-L. Hu, J.-G. Mao, H.-Y. Ye, P.-F. Li, S. D. Huang and R.-G. Xiong, "*A lead-halide perovskite molecular ferroelectric semiconductor*", Nat. Commun. **6** (2015) 7338.

[106] H. Daub, M.; Hillebrecht, "*Synthesis, single-crystal structure and characterization of (ch3nh3)2pb(scn)2i2*", Angew.Chem. Int. Ed. **54** (2015) 11016–11017.

[107] wikipedia.org, "*https://en.wikipedia.org/wiki/x-ray-crystallography*", 2005.

[108] M. Eckert, "*Max von laue and the discovery of x-ray diffraction in 1912*", Annalen der Physik **524** (2012) A83–A85.

[109] W. L. Bragg, "*The diffraction of short electromagnetic waves by a crystal*", Scientia **23** (1929) 153.

[110] N. J. C. Ingle, "*In situ characterization of thin film growth*", 2011.

[111] version 1.171.36.32, "*Crysalispro*", 2011.

[112] G. M. Sheldrick, "*Shelxl97; program for crystal structure refinement*", 1997.

[113] L. J. Farrugia, "*Wingx suite for small-molecule single-crystal crystallography*", J. Appl. Crystallogr. **32** (1999) 837–838.

[114] H. M. Rietveld, "*A profile refinement method for nuclear and magnetic structures*", J. Appl.Cryst. **2** (1969) 65–71.

[115] F. Suite, "*https://www.ill.eu/sites/fullprof/php/tutorials.html*", 2006.

[116] Q. Design, "*https://www.qdusa.com/products/ppms.html*", 1990.

[117] J. C. Lashley, M. F. Hundley, A. Migliori, J. L. Sarrao, P. G. Pagliuso, T. W. Darling, M. Jaime, J. C. Cooley, W. L. Hults, L. Morales, D. J. Thoma, J. L. Smith, J. Boerio-Goates, B. F. Woodfield, G. R. Stewart, R. A. Fisher and N. E. Phillips, "*Critical examination of heat capacity measurements made on a quantum design physical property measurement system*", Cryogenics **43** (2003) 369–378.

[118] M. Klicpera, P. Javorsk´y and M. Diviˇs, "*Magnetization and electrical resistivity measurements on cecual3 single crystal*", Journal of Physics: Conference Series **592** (2015) 012014.

[119] wikipedia.org, "*https://en.wikipedia.org/wiki/scanning-electron-microscope*", 2001.

[120] JEOL, "*Scanning electron microscope a to z: Basic knowledge for using the sem*", 2009.

[121] P. Kubelka and F. Munk, "*A contribution to the optics of paint*", Journal of Technical Physics **12** (1931) 593–601.

[122] S. Attal, R. Thiruvengadathan and O. Regev, "*Determination of the concentration of single-walled carbon nanotubes in aqueous dispersions using uv−visible absorption spectroscopy*", Anal. Chem. **78** (2006) 8098–8104.

[123] C. Ronda, "*Luminescence from theory to applications*", 2008.

[124] M. Fox, "*Optical properties of solids*", 2001.

[125] P. Y. Yu and M. Cardona, "*Fundamentals of semiconductors*", 2010.

[126] wikipedia.org, "*https://en.wikipedia.org/wiki/photoluminescence*", 2002.

[127] M. Wahl, "*Time-correlated single photon counting*", 2014.

[128] P. D. Edinburg Instruments, "*What is tcspc?*", 2013.

[129] C. V. Raman and K. S. Krishnan, "*A new type of secondary radiation*", Nature **121** (1928) 501–502.

[130] C. V. Raman, "*A new radiation*", Current Science **74** (1998) 382–386.

[131] wikipedia.org, "*https://en.wikipedia.org/wiki/photoemission-spectroscopy*", 2004.

[132] F. Reinert and S. Hüfner, "*Photoemission spectroscopy—from early days to recent applications*", New J. Phys. **7** (2005) 97.

[133] wikipedia.org, "*https://en.wikipedia.org/wiki/photoelectric-effect*", 2001.

[134] A. Damascelli, "*Probing the electronic structure of complex systems by arpes*", Physica Scripta **T109** (2004) 61–74.

[135] U. Manju, M. Sreemony and A. K. Chakraborty, "*Multi-technique photoelectron spectrometer for micro-area spectroscopy and imaging*", Curr. Sci. **105** (2013) 1056–1060.

[136] wikipedia.org, "*https://en.wikipedia.org/wiki/angle-resolved-photoemission-spectroscopy*", 2006.

[137] A. Damascelli, Z. Hussain and Z.-X. Shen, "*Angle-resolved photoemission studies of the cuprate superconductors*", Rev. Mod. Phys. **75** (2003) 473.

[138] A. A. Kordyuk, "*Arpes experiment in fermiology of quasi-2d metals (review article)*", Low Temperature Physics **40** (2014) 286.

[139] wikipedia.org, "*https://en.wikipedia.org/wiki/x-ray-absorption-spectroscopy*", 2005.

[140] A. Filipponi, A. Di Cicco and C. R. Natoli, "*X-ray absorption spectroscopy and n-body distribution functions in condensed matter*", Phys. Rev. B **52** (1995) 15122–15148.

[141] J. J. Rehr and R. C. Albers, "*Theoretical approaches to x-ray absorption fine structure*", Reviews of Modern Physics **72** (2000) 621–654.

[142] Demeter, "*https://bruceravel.github.io/demeter/*", 2006.

[143] wikipedia.org, "*https://en.wikipedia.org/wiki/density-functional-theory*", 2003.

[144] P. Hohenberg and W. Kohn, "*Inhomogeneous electron gas*", Physical Review **136** (1964) B864.

[145] W. Kohn and L. J. Sham, "*Self-consistent equations including exchange and correlation effects*", Physical Review **140** (1965) A1133.

[146] D. Vanderbilt, "*Soft self-consistent pseudopotentials in a generalized eigenvalue formalism*", Physical Review B **41** (1990) 7892.

[147] G. Kresse and D. Joubert, "*From ultrasoft pseudopotentials to the projector augmented-wave method*", Physical Review B **59** (1999) 1758.

[148] P. E. Blöchl, "*Projector augmented-wave method*", Phys. Rev. B **50** (1994) 17953.

[149] G. Kresse and J. Furthmuller, "*Efficient iterative schemes for ab initio total-energy calculations using a plane wave basis set*", Physical Review B **54** (1996) 11169.

[150] G. Kresse and J. Hafner, "*Ab initio molecular-dynamics for liquid metals*", Phys. Rev. B **47** (1993) 558.

[151] G. Kresse and J. Hafner, "*Ab initio molecular-dynamics simulation of the liquid-metal-amorphous-semiconductor transition in germanium*", Phys. Rev. B **49** (1994) 14251.

[152] S. Mahajan, "*Defects in semiconductors and their effects on devices*", Acta mater. **48** (2000) 137–149.

[153] S. Mahajan, W. D. Johnston Jr., M. A. Pollack and R. E. Nahory, "*The mechanism of optically induced degradation in inp/in1-xgaxasyp1-y heterostructures*", Appl. Phys. Lett. **34** (1979) 717.

[154] B. V. Dutt, S. Mahajan, R. J. Roedel, G. P. Schwartz, D. C. Miller and L. Derick, "*Stacking faults and substructure in gaas/ (ga, al) as heteroepitaxial layers*", J. electrochem. Soc. **128** (1981) 1573–1578.

[155] Y. Zhou, M. Yang, W. Wu, A. L. Vasiliev, K. Zhu and N. P. Padture, "*Room-temperature crystallization of hybrid-perovskite thin films via solvent-solvent extraction for high-performance solar cells*", J. Mater. Chem. A **3** (2015) 8178—8184.

[156] E. R. Dohner, E. T. Hoke and H. I. Karunadasa, "*Self-assembly of broadband white-light emitters*", J. Am. Chem. Soc. **136** (2014) 1718—1721.

[157] E. R. Dohner, A. Jaffe, L. R. Bradshaw and H. I. Karunadasa, "*Intrinsic white-light emission from layered hybrid perovskites*", J. Am. Chem. Soc. **136** (2014) 13154—13157.

[158] T. Hu, M. D. Smith, E. R. Dohner, M.-J. Sher, X. Wu, M. T. Trinh, A. Fisher, J. Corbett, X.-Y. Zhu, H. I. Karunadasa and A. M. Lindenberg, "*Mechanism for broadband white-light emission from two dimensional (110) hybrid perovskites*", J. Phys. Chem. Lett. **7** (2016) 2258—2263.

[159] K. Song and R. T. Williams, "*Self-trapped excitons, 2nd ed.*", 1996.

[160] M. Luan, J. Song, X. Wei, F. Chen and J. Liu, "*Controllable growth of bulk cubic-phase ch3nh3pbi3 single crystal with exciting room-temperature stability*", CrystEngComm. **18** (2016) 5257–5261.

[161] J. B. Hoffman, A. L. Schleper and P. V. Kamat, "*Transformation of sintered cspbbr3 nanocrystals to cubic cspbi3 and gradient cspbbrxi3–x through halide exchange*", J. Am. Chem. Soc. **138** (2016) 8603–8611.

[162] H. Mashiyama, Y. Kurihara and T. Azetsu, “*Disordered cubic perovskite structure of ch3nh3pbx3 (x=cl, br, i)*”, J. Korean Phys. Soc. **32** (1998) S156–S158.

[163] D. Priante, I. Dursun, M. S. Alias, D. Shi, V. A. Melnikov, T. K. Ng, O. F. Mohammed, O. M. Bakr and B. S. Ooi, “*The recombination mechanisms leading to amplified spontaneous emission at the true-green wavelength in ch3nh3pbbr3 perovskites*”, Appl. Phys. Lett. **106** (2015) 081902.

[164] M. I. Dar, G. Jacopin, S. Meloni, A. Mattoni, N. Arora, A. Boziki, S. M. Zakeeruddin, U. Rothlisberger and M. Grtzel, “*Origin of unusual bandgap shift and dual emission in organic-inorganic lead halide perovskites*”, Sci. Adv. **2** (2016) e1601156.

[165] P. Nandi, C. Giri, S. Sarkar, P. Mahadevan, U. Manju and D. Topwal, “*Origin of dual emission on ch3nh3pbbr3 perovskite single crystals*”, (Unpublished result) .

[166] R. Wang, J. Yang, X. Wu and S. Wang, “*Local charge states in hexagonal boron nitride with stone-wales defects*”, Nanoscale **8** (2016) 8210–8219.

[167] Y. Zhou, J. Chen, O. M. Bakr and H.-T. Sun, “*Metal-doped lead halide perovskites: synthesis, properties, and optoelectronic applications*”, Chem. Mater. **30** (2018) 6589–6613.

[168] S. Zou, Z. Gong, B. Liang, L. Hou, R. Liu, H. Zhong, B. Zou and A. V. Kavokin, “*Formation of mn doped ch3nh3pbbr3 perovskite microrods and their collective emp lasing*”, J. Phys. Commun. **1** (2017) 055018.

[169] X. Zhu, H. Su, R. A. Marcus and M. E. Michel-Beyerle, “*Computed and experimental absorption spectra of the perovskite ch3nh3pbi3*”, J. Phys. Chem. Lett. **5** (2014) 3061–3065.

[170] A. Milev, D. M. A. S. Dissanayake, G. S. K. Kannangaraa and A. R. Kumarasinghe, “*Defect induced electronic states and magnetism in ball-milled graphite*”, Phys. Chem. Chem. Phys. **15** (2013) 16294–16302.

[171] R. R. Nair, M. Sepioni, I.-L. Tsai, O. Lehtinen, J. Keinonen, A. V. Krasheninnikov, T. Thomson, A. K. Geim and I. V. Grigorieva, “*Spin-half paramagnetism in graphene induced by point defects*”, Phys. Chem. Chem. Phys. **8** (2012) 199–202.

[172] G. Z. Xing, Y. H. Lu, Y. F. Tian, J. B. Yi, C. C. Lim, Y. F. Li, G. P. Li, D. D. Wang, B. Yao, J. Ding, Y. P. Feng and T. Wu, “*Defect-induced magnetism in undoped wide band gap oxides: Zinc vacancies in zno as an example*”, AIP Advances **1** (2011) 022152.

[173] S. D. Yoon, Y. Chen, A. Yang, T. L. Goodrich, X. Zuo, D. A. Arena, K. Ziemer, C. Vittoria and V. G. Harris, “*Oxygen-defect-induced magnetism to 880 k in semiconducting anatase tio2− films*”, J. Phys.: Condens. Matter **18** (2006) L355–L361.

[174] M. Maeda, M. Hattori, A. Hotta and I. Suzuki, “*Dielectric studies on ch 3nh 3pbx 3 (x = cl and br) single cystals*”, J. Phys. Soc. Jpn. **66** (1997) 1508–1511.

[175] X. Cheng, L. Jing, Y. Zhao, S. Du, J. Ding and T. Zhou, “*Crystal orientation-dependent optoelectronic properties of mapbcl3 single crystals*”, J. Mater. Chem. C **6** (2018) 1579–1586.

[176] P. Nandi, C. Giri, D. Swain, U. Manju and D. Topwal, "*Room temperature growth of ch3nh3pbcl3 single crystals by solvent evaporation method*", CrystEngComm **21** (2019) 656–661.

[177] F. P. G. de Arquer, A. Armin, P. Meredith and E. H. Sargent, "*Solution-processed semiconductors for next-generation photodetectors*", Nature Reviews Matererials **2** (2017) 16100.

[178] H. Wei, Y. Fang, P. Mulligan, W. Chuirazzi, H.-H. Fang, C. Wang, B. R. Ecker, Y. Gao, M. A. Loi, L. Cao and J. Huang, "*Sensitive x-ray detectors made of methylammonium lead tribromide perovskite single crystals*", Nat. Photon. **10** (2016) 333–339.

[179] X. Wen, L. V. Dao and P. Hannaford, "*Temperature dependence of photoluminescence in silicon quantum dots*", J. Phys. D: Appl. Phys. **40** (2007) 3573–3578.

[180] L. T. Tung, K. L. Lin, E. Y. Chang, W. C. Huang, Y. L. Hsiao and C. H. Chiang, "*Photoluminescence and raman studies of gan films grown by mocvd*", Journal of Physics: Conference Series **187** (2009) 012021.

[181] D. S. Jiang, H. Jung and K. Ploog, "*Temperature dependence of photoluminescence from gaas single and multiple quantum-well heterostructures grown by molecular-beam epitaxy*", Journal of Applied Physics **64** (1988) 1371.

[182] Y. P. Varshni, "*Temperature dependence of the energy gap in semiconductors*", Physica **34** (1967) 149–154.

[183] M. A. Lampert and P. Mark, "*Current injection in solids: The regional approximation method*", Semiconductors and Semimetals **6** (1970) 1–96.

[184] F. X. Xie, H. Su, J. Mao, K. S. Wong and W. C. H. Choy, "*Evolution of diffusion length and trap state induced by chloride in perovskite solar cell*", J. Phys. Chem. C **120** (2016) 21248–21253.

[185] L. M. Pazos-Outón, J. M. Lee, M. H. Futscher, A. Kirch, M. Tabachnyk, R. H. Friend and B. A. Ehrler, "*Silicon–singlet fission tandem solar cell exceeding 100% external quantum efficiency with high spectral stability*", ACS Energy Lett. **2** (2017) 476–480.

[186] I. P. Swainson, R. P. Hammond, C. Soullière, O. Knop and W. Massa, "*Phase transitions in the perovskite methylammonium lead bromide, ch3nd3pbbr3*", J. Solid State Chem. **176** (2003) 97—104.

[187] L. Chi, I. Swainson, L. Cranswick, J.-H. Her, P. Stephens and O. Knop, "*The ordered phase of methylammonium lead chloride ch3nd3pbcl3*", J. Solid State Chem. **178** (2005) 1376–1385.

[188] S. Govinda, B. P. Kore, M. Bokdam, P. Mahale, A. Kumar, S. Pal, B. Bhattacharyya, J. Lahnsteiner, G. Kresse, C. Franchini, A. Pandey and D. D. Sarma, "*Behavior of methylammonium dipoles in mapbx3 (x = br and i)*", J. Phys. Chem. Lett. **8** (2017) 4113–4121.

[189] J. Wei, Y. Zhao, H. Li, G. Li, J. Pan, D. Xu, Q. Zhao and D. Yu, "*Hysteresis analysis based on the ferroelectric effect in hybrid perovskite solar cells*", J. Phys. Chem. Lett. **5** (2014) 3937–3945.

[190] I. Deretzis and A. L. Magna, “*Exploring the orthorhombic-tetragonal phase transition in ch3nh3pbi3: The role of atom kinetics*”, Nanoscale **9** (2017) 5896–5903.

[191] A. Bernasconi and L. Malavasi, “*Direct evidence of permanent octahedra distortion in mapbbr3 hybrid perovskite*”, ACS Energy Lett. **2** (2017) 863–868.

[192] Y. Ren, I. W. H. Oswald, X. Wang, G. T. McCandless and J. Y. Chan, “*Orientation of organic cations in hybrid inorganic−organic perovskite ch3nh3pbi3 from subatomic resolution single crystal neutron diffraction structural studies*”, Cryst. Growth Des. **16** (2016) 2945−2951.

[193] S. Sanchez, U. Steiner and X. Hua, “*Phase evolution during perovskite formation-insight from pair distribution function analysis*”, Chem. Mater. (2019) doi: 10.1021/acs.chemmater.9b00748.

[194] T. A. Tyson, W. Gao, S. Ghosh and Y. Yan, “*Large thermal motion in halide perovskites*”, Sci. Rep. **7** (2017) 9401.

[195] Q. Zhu, K. Zheng, M. Abdellah, A. Generalov, D. Haase, S. Carlson, Y. Niu, J. Heimdal, A. Engdahl, M. E. Messing, T. Pullerits and S. E. Canton, “*Correlating structure and electronic band-edge properties in organolead halide perovskites nanoparticles*”, Phys. Chem. Chem. Phys. **18** (2016) 14933–14940.

[196] C. Vorwerk, C. Hartmann, C. Cocchi, G. Sadoughi, S. N. Habisreutinger, R. Felix, R. G. Wilks, H. J. Snaith, M. Bar and C. Drax, “*Exciton-dominated core-level absorption spectra of hybrid organic-inorganic lead halide perovskites*”, J. Phys. Chem. Lett. **9** (2018) 1852–1858.

[197] Z. J. Yong, S. Q. Guo, J. P. Ma, J. Y. Zhang, Z. H. Li, Y. M. Chen, B. B. Zhang, Y. Zhou, J. Shu, J. L. Gu, L. R. Zheng, O. M. Bakr and H. T. Sun, “*Doping-enhanced short-range order of perovskite nanocrystals for near-unity violet luminescence quantum yield*”, J. Am. Chem. Soc. **140** (2018) 9942–9951.

[198] H. Zhang, X. Liu, J. Dong, H. Yu, C. Zhou, B. Zhang, Y. Xu and W. Jie, “*Centimeter-sized inorganic lead halide perovskite cspbbr3 crystals grown by an improved solution method*”, Cryst. Growth Des. **17** (2017) 6426–6431.

[199] C. J. Bartel, C. Sutton, B. R. Goldsmith, R. Ouyang, C. B. Musgrave, L. M. Ghiringhelli and M. Scheffler, “*New tolerance factor to predict the stability of perovskite oxides and halides*”, Science Advances **5** (2019) eaav0693.

[200] J. Järvi, J. Li and P. Rinke, “*Multi-scale model for the structure of hybrid perovskites: analysis of charge migration in disordered mapbi3 structures*”, New J. Phys. **20** (2018) 103013.

[201] P. S. Whitfield, N. Herron, W. E. Guise, K. Page, Y. Q. Cheng, I. Milas and M. K. Crawford, “*Structures, phase transitions and tricritical behavior of the hybrid perovskite methyl ammonium lead iodide*”, Sci. Rep. **6** (2016) 35685.

[202] B. J. Campbell, H. T. Stokes, D. E. Tanner and D. M. Hatch, “*Isodisplace; an internet tool for exploring structural distortions*”, J. Appl. Cryst. **39** (2006) 607–614.

[203] A. M. Glazer, “*Simple ways of determining perovskite structures*”, Acta Cryst. **A31** (1975) 756–762.

[204] J. Slonczewski and H. Thomas, "*Interaction of elastic strain with the structural transition of strontium titanate*", Phys. Rev. B **1** (1970) 3599–3608.

[205] J. M. de Leon, S. D. Conradson, I. Batistić, A. R. Bishop, I. D. Raistrick, M. C. Aronson and F. H. Garzon, "*Axial oxygen-centered lattice instabilities in yba2cu3o7: An application of the analysis of extended x-ray-absorption fine structure in anharmonic systems*", Phys. Rev. B **45** (1992) 2447–2457.

[206] S. Hirotsu, J. Harada, M. Iizumi and K. Gesi, "*Structural phase transitions in cspbbr3*", J. Phys. Soc. Jpn. **37** (1974) 1393–1398.

[207] J. Xue, D. Yang, B. Cai, X. Xu, J. Wang, H. Ma, X. Yu, G. Yuan, Y. Zou, J. Song and H. Zeng, "*Photon-induced reversible phase transitions in cspbbr3 perovskite*", Adv. Funct. Mater. **29** (2019) 1807922.

[208] M. Yu, S. Yuan, H.-Y. Wang, J.-S. Zhao, Y. Qin, L.-M. Fu, J.-P. Zhang and X.-C. Ai, "*Characterization of the influences of morphology on the intrinsic properties of perovskite films by temperature-dependent and time-resolved spectroscopies*", Phys. Chem. Chem. Phys. **20** (2018) 6575–6581.

[209] J. Min, Z.-G. Zhang, Y. Hou, C. O. R. Quiroz, T. Przybilla, C. Bronnbauer, F. Guo, H. A. K. Forberich, E. S. T. Ameri, Y. Li and C. J. Brabec, "*Interface engineering of perovskite hybrid solar cells with solution-processed perylene–diimide heterojunctions toward high performance*", Chem. Mater. **27** (2015) 227–234.

[210] M. Xiao, F. Huang, W. Huang, Y. Dkhissi, Y. Zhu, J. Etheridge, A. Gray-Weale, U. Bach, Y. B. Cheng and L. Spiccia, "*A fast deposition-crystallization procedure for highly efficient lead iodide perovskite thin-film solar cells*", Angewandte Chemie **126** (2014) 10056–10061.

[211] N. J. Jeon, J. H. Noh, Y. C. Kim, Y. W. S., S. Ryu and S. S. II., "*Solvent engineering for high-performance inorganic-organic hybrid perovskite solar cells*", Nat. Mater. **13** (2014) 897–903.

[212] H. J. Snaith, "*Present status and future prospects of perovskite photovoltaics*", Nat. Mater. **17** (2018) 372–376.

[213] S. D. Stranks and H. J. Snaith, "*Metal-halide perovskites for photovoltaic and light-emitting devices*", Nat. Nanotechnol. **10** (2015) 391–402.

[214] H. Cho, S.-H. Jeong, M.-H. Park, Y.-H. Kim, C. Wolf, C.-L. Lee, J. H. Heo, A. Sadhanala, N. Myoung, S. Yoo, S. H. Im, R. H. Friend and T.-W. Lee, "*Overcoming the electroluminescence efficiency limitations of perovskite light-emitting diodes*", Science **350** (2015) 1222–1225.

[215] W. Kong, Z. Ye, Z. Qi, B. Zhang, M. Wang, A. Rahimi-Iman and H. Wu, "*Characterization of an abnormal photoluminescence behavior upon crystal-phase transition of perovskite ch3nh3pbi3*", Phys. Chem. Chem. Phys. **17** (2015) 16405–16411.

[216] H.-H. Fang, R. Raissa, M. Abdu-Aguye, S. Adjokatse, G. R. Blake, J. Even and M. A. Loi, "*Photophysics of organic inorganic hybrid lead iodide perovskite single crystals*", Adv. Funct. Mater. **25** (2015) 2378–2385.

[217] F. Panzer, S. Baderschneider, T. P. Gujar, T. Unger, S. Bagnich, M. Jakoby, H. Bassler, S. Huttner, J. Kohler, R. Moos, M. Thelakkat, R. Hildner and A. Kohler, "*Reversible laser-induced amplified spontaneous emission from coexisting tetragonal and orthorhombic phases in hybrid lead halide perovskites*", Adv. Optical Mater. **4** (2016) 917–928.

[218] A. Walsh, "*Principles of chemical bonding and band gap engineering in hybrid organic-inorganic halide perovskites*", J. Phys. Chem. C **119** (2015) 5755–5760.

[219] V. D'Innocenzo, M. D. B. A. R. S. Kandada, M. Gandini and A. Petrozza, "*Tuning the light emission properties by band gap engineering in hybrid lead halide perovskite*", J. Am. Chem. Soc. **136** (2014) 17730–17733.

[220] H.-Y. Ye, W.-Q. Liao, Y. Z. C.-L. Hu, Y.-M. You, J.-G. Mao, P.-F. Li and R.-G. Xiong, "*Bandgap engineering of lead-halide perovskite-type ferroelectrics*", Adv. Mater. **28** (2016) 2579–2586.

[221] M. Mittal, A. Jana, S. Sarkar, P. Mahadevan and S. Sapra, "*Size of the organic cation tunes the band gap of colloidal organolead bromide perovskite nanocrystals*", J. Phys. Chem. Lett. **7** (2016) 3270–3277.

[222] J.-H. Lee, N. C. Bristowe, J. H. Lee, S.-H. Lee, P. D. Bristowe, A. K. Cheetham and H. M. Jang, "*Resolving the physical origin of octahedral tilting in halide perovskites*", Chem. Mater. **28** (2016) 4259–4266.

[223] J. P. Perdew, K. Burke and M. Ernzerhof, "*Generalized gradient approximation made simple*", Phys. Rev. Lett. **77** (1996) 3865.

[224] D. A. Egger and L. Kronin, "*Role of dispersive interactions in determining structural properties of organic inorganic halide perovskites: Insights from first principles calculations*", J. Phys. Chem. Lett. **5** (2014) 2728–2733.

[225] Y. Wang, T. Gould, J. F. Dobson, H. M. Zhang, H. G. Yang, X. D. Yao and H. J. Zhao, "*Density functional theory analysis of structural and electronic properties of orthorhombic perovskite ch3nh3pbi3*", Phys. Chem. Chem. Phys. **16** (2014) 1424–1429.

[226] S. Grimme, "*Semiempirical gga-type density functional constructed with a long-range dispersion correction*", J. Comput. Chem. **27** (2006) 1787–1799.

[227] H. Mashiyama, Y. Kawamura and Y. Kubota, "*The anti-polar structure of ch3nh3pbbr3*", J. Korean Phys. Soc. **51** (2007) 850.

[228] Z.-Y. Zhang, H.-Y. Wang, Y.-X. Zhang, Y.-W. Hao, C. Sun, Y. Zhang, B.-R. Gao, Q.-D. Chen and S. H.-B., "*The role of trap-assisted recombination in luminescent properties of organometal halide ch3nh3pbbr3 perovskite films and quantum dots*", Sci. Rep. **6** (2016) 27286.

[229] A. Jana, M. Mittal, A. Singla and S. Sapra, "*Solvent-free, mechanochemical syntheses of bulk trihalide perovskites and their nanoparticles*", Chem. Commun. **53** (2017) 3046–3049.

[230] Y.-H. Cho, G. H. Gainer, A. J. Fischer, J. J. Song, S. Keller, U. K. Mishra and S. P. DenBaars, "*S-shaped temperature dependent emission shift and carrier dynamics in ingan/gan multiple quantum wells*", Appl. Phys. Lett. **73** (1988) 1370.

[231] S. Singh, C. Li, F. Panzer, K. L. Narasimhan, A. Graeser, T. P. Gujar, A. Kohler, M. Thelakkat, S. Huettner and D. Kabra, "*Effect of thermal and structural disorder on the electronic structure of hybrid perovskite semiconductor ch3nh3pbi3*", J. Phys. Chem. Lett. **7** (2016) 3014–3021.

[232] J. M. Frost, K. T. Butler, F. Brivio, C. H. Hendon and M. Van Schilfgaarde, "*Atomistic origin of high performance in hybrid halide perovskite solar cells*", Nano Lett. **14** (2014) 2584–2590.

[233] R. Wang, S. Hu, X. Yang, X. Yan, H. Li and C. X. Sheng, "*Circularly polarized photoluminescence and hanle effect measurements of spin relaxation in organic-inorganic hybrid perovskite films*", J. Mater. Chem. C **6** (2018) 2989–2995.

[234] Y. Fu, H. Zhu, A. W. Schrader, D. Liang, Q. Ding, P. Joshi, L. Hwang, X.-Y. Zhu and S. Jin, "*Nanowire lasers of formamidinium lead halide perovskites and their stabilized alloys with improved stability*", Nano Lett. **16** (2016) 1000–1008.

[235] Z. Gu, K. Wang, W. Sun, J. Li, S. Liu, Q. Song and S. Xiao, "*Two-photon pumped ch3nh3pbbr3 perovskite microwire lasers*", Adv. Optical Mater. **4** (2016) 472–479.

[236] K. Tanaka, T. Takahashi, T. Ban, T. Kondo, K. Uchida and N. Miura, "*Comparative study on the excitons in lead-halide-based perovskite-type crystals* $ch_3nh_3pbbr_3$ $ch_3nh_3pbi_3$", Solid State Commun. **127** (2003) 619–623.

[237] Y. Yang, M. Yang, Z. Li, R. Crisp, K. Zhu and M. C. Beard, "*Comparison of recombination dynamics in ch3nh3pbbr3 and ch3nh3pbi3 perovskite films: Influence of exciton binding energy*", J. Phys. Chem. Lett. **6** (2015) 4688–4692.

[238] Y. Chen, H. Jing, F. Ling, W. Kang, T. Zhou, X. Liu, L. Q. W. Zeng, Y. Zhang, L. Fang and M. Zhou, "*Tuning the electronic structures of all-inorganic lead halide perovskite cspbi3 via heterovalent doping: A first-principles investigation*", Chemical Physics Letters **722** (2019) 90–95.

[239] J. S. Bechtel, R. Seshadri and A. Van der Ven, "*Energy landscape of molecular motion in cubic methylammonium lead iodide from first-principles*", J. Phys. Chem. C **120** (2016) 12403–12410.

[240] T. Wang, B. Daiber, J. M. Frost, S. A. Mann, E. C. Garnett, A. Walsh and B. Ehrler, "*Indirect to direct bandgap transition in methylammonium lead halide perovskite*", Energy Environ. Sci. **10** (2017) 509–515.

[241] Z. Chen, C. Yu, K. Shum, J. J. Wang, W. Pfenninger, N. Vockic, J. Midgley and J. T. Kenney, "*Photoluminescence study of polycrystalline* $cssni_3$ *thin films: Determination of exciton binding energy*", Journal of Luminescence **132** (2012) 345–349.

[242] T. J. Savenije, C. S. Ponseca, L. Kunneman, M. Abdellah, K. Zheng, Y. Tian, Q. Zhu, S. E. Canton, I. G. Scheblykin, T. Pullerits, A. Yartsev and V. Sundstrom, "*Thermally activated exciton dissociation and recombination control the carrier dynamics in organometal halide perovskite*", J. Phys. Chem. Lett. **5** (2014) 2189–2194.

[243] T. Ishihara, "*Optical properties of pbi-based perovskite structures*", Journal of Luminescence **60-61** (1994) 269–274.

[244] K. Tanaka and T. Kondo, "*Bandgap and exciton binding energies in lead-iodide-based natural quantum-well crystals*", Science and Technology of Advanced Materials **4** (2003) 599–604.

[245] S. Rudin, T. L. Reinecke and B. Segall, "*Temperature-dependent exciton linewidths in semiconductors*", Phys. Rev. B: Condens. Mater. Phys. **42** (1990) 11218–11231.

[246] A. Maalej, Y. Abid, A. Kellel, A. Daoud, A. Lautié and F. Romain, "*Phase transitions and crystal dynamics in the cubic perovskite* $ch_3nh_3pbcl_3$", Solid State Commun. **103** (1997) 279–284.

[247] E. G. Maksimov and G. P. Motulevice, "*Determination of the electron-phonon coupling constant from optical measurements*", Soviet Physics-JETP **34** (1972) 219–221.

[248] E. Mosconi, A. Amat, M. K. Nazeeruddin, M. Gratzel and F. D. Angelis, "*First-principles modeling of mixed halide organometal perovskites for photovoltaic applications*", J. Phys. Chem. C **117** (2013) 13902–13913.

[249] C. Quarti, G. Grancini, E. Mosconi, P. Bruno, J. M. Ball, M. M. Lee, H. J. Snaith, A. Petrozza and F. D. Angelis, "*The raman spectrum of the* $ch_3nh_3pbi_3$ *hybrid perovskite: Interplay of theory and experiment*", J. Phys. Chem. Lett. **5** (2014) 279–284.

[250] M. A. Pérez-Osorio, Q. Lin, R. T. Phillips, R. L. Milot, M. B. J. L. M. Herz and F. Giustino, "*Raman spectrum of the organic–inorganic halide perovskite ch3nh3pbi3 from first principles and high-resolution low-temperature raman measurements*", J. Phys. Chem. C **122** (2018) 21703–21717.

[251] E. M. Proupin, C. L. B. Rios and P. Wahnon, "*Nonhydrogenic exciton spectrum in perovskite* $ch_3nh_3pbi_3$", Phys. Status. Solidi RRL **9** (2015) 559–563.

[252] M. Ledinský, P. Löper, B. Niesen, J. Holovský, S.-J. Moon, J.-H. Yum, S. D. Wolf, A. Fejfar and C. Ballif, "*Raman spectroscopy of organic–inorganic halide perovskites*", J. Phys. Chem. Lett. **6** (2015) 401–406.

[253] T. G. M. Hirasawa, T. Ishihara, "*Exciton features in 0-, 2- and 3-dimensional networks of* $[pbi_6]^{4-}$ *octahedra*", J. Phys. Soc. Jpn **63** (1994) 3870–3879.

[254] Z. G. Yu, "*Effective-mass model and magneto-optical properties in hybrid perovskites*", Sci. Rep. **6** (2016) 28576.

[255] J. Xu and D. Xue, "*Five branching growth patterns in the cubic crystal system: A direct observation of cuprous oxide microcrystals*", Acta Materialia **55** (2007) 2397–2406.

[256] P. Yang, K. Y. Li and D. F. Xue, "*Anisotropic hardness estimationsof some inorganic functional materials*", Functional Materials Letters **5** (2012) 1250003.

[257] X. Zhao, C. T. Sun, Y. F. Si, M. N. Liu and D. F. Xue, "*Crystallization behaviors of ferroelectric and piezoelectric materials*", Modern Physics Letters B **23** (2009) 3809–3815.

[258] C. Ran, W. Gao, N. Li, Y. Xia, Q. Li, Z. Wu, H. Zhou, Y. Chen, M. Wang and W. Huang, "*Facet-dependent control of pbi2 colloids for over 20% efficient perovskite solar cells*", ACS Energy Lett. **4** (2019) 358–367.

[259] G. Zheng, C. Zhu, J. Ma, X. Zhang, G. Tang, R. Li, Y. Chen, L. Li, J. Hu, J. Hong, Q. Chen, X. Gao and H. Zhou, "*Manipulation of facet orientation in hybrid perovskite polycrystalline films by cation cascade*", Nat. Commun. **9** (2018) 2793.

[260] S. Y. Leblebici, L. Leppert, Y. Li, S. E. Reyes-Lillo, S. Wickenburg, E. Wong, J. Lee, M. Melli, D. Ziegler, D. K. Angell, D. F. Ogletree, P. D. Ashby, F. M. Toma, J. B. Neaton, I. D. Sharp and A. Weber-Bargioni, "*Facet-dependent photovoltaic efficiency variations in single grains of hybrid halide perovskite*", Nat. Energy **1** (2016) 16093.

[261] N. Cho, F. Li, B. Turedi, L. Sinatra, S. P. Sarmah, M. R. Parida, M. I. Saidaminov, B. Murali, V. M. Burlakov, A. Goriely, O. F. Mohammed, T. Wu and O. M. Bakr, "*Pure crystal orientation and anisotropic charge transport in large-area hybrid perovskite films*", Nat. Commun. **7** (2016) 13407.

[262] J. Ding, S. Du, X. Cheng, L. Jing, Y. Zhao, Z. Zuo, H. Cui and X. Zhan, "*Anisotropic optoelectronic performances on (112) and (100) lattice plane of perovskite mapbi3 single crystal*", Materials Chemistry and Physics **204** (2018) 222–227.

[263] Z. Zuo, J. Ding, Y. Zhao, S. Du, Y. Li, X. Zhan and H. Cui, "*Enhanced optoelectronic performance on the (110) lattice plane of an mapbbr3 single crystal*", J. Phys. Chem. Lett. **8** (2017) 684–689.

[264] M. J. Jurow, T. Lampe, E. Penzo, J. Kang, M. A. Koc, T. Zechel, Z. Nett, M. Brady, L.-W. Wang, A. P. Alivisatos, S. Cabrini, W. Brütting and Y. Liu, "*Tunable anisotropic photon emission from self-organized cspbbr3 perovskite nanocrystals*", Nano Lett. **17** (2017) 4534–4540.

[265] C. Motta, F. El-Mellouhi and S. Sanvito, "*Charge carrier mobility in hybrid halide perovskites*", Sci. Rep. **5** (2015) 12746.

[266] X. Chi, K. Leng, B. Wu, D. Shi, Y. Choy, Z. Chen, Z. Chen, X. Yu, P. Yang, Q.-H. Xu, T. C. Sum, A. Rusydi and K. P. Loh, "*Elucidating surface and bulk emission in 3d hybrid organic–inorganic lead bromide perovskites*", Adv. optical Mater. **6** (2018) 1800470.

[267] B. Wu, H. T. Nguyen, Z. Ku, G. Han, D. Giovanni, N. Mathews, H. J. Fan and T. C. Sum, "*Discerning the surface and bulk recombination kinetics of organic–inorganic halide perovskite single crystals*", Adv. Energy Mater. **6** (2016) 1600551.

[268] R. Lindblad, D. Bi, B. W. Park, J. Oscarsson, M. Gorgoi, H. Siegbahn, M. Odelius, E. M. J. Johansson and H. Rensmo, "*Electronic structure of tio2/ch3nh3pbi3 perovskite solar cell interfaces*", J. Phys. Chem. Lett. **5** (2014) 648–653.

[269] A. R. Kirmani, A. E. Mansour, M. I. Saidaminov, X. Cui, D. Shi, A. Alofi, Y. B. Losovyj, G. Gurung, T. R. Paudel, A. J. Yost, P. A. Dowben, E. Y. Tsymbal, A. Amassian and K. Katsiev, "*Contributions of the lead-bromine weighted bands to the occupied density of states of the hybrid tri-bromide perovskites*", Appl. Phys. Lett. **113** (2018) 022101.

[270] J. Endres, D. A. Egger, M. Kulbak, R. A. Kerner, L. Zhao, S. H. Silver, G. Hodes, B. P. Rand, D. Cahen, L. Kronik and A. Kahn, "*Valence and conduction band densities of states of metal halide perovskites: A combined experimental-theoretical study*", J. Phys. Chem. Lett. **7** (2016) 2722–2729.

[271] C. Wang, X. Liu, C. Wang, Z. Xiao, C. Bi, Y. Shao, J. Huang and Y. Gao, "*Surface analytical investigation on organometal triiodide perovskite*", J. Vac. Sci. Technol. B **33** (2015) 032401.

[272] E. Mosconi, U. P. and F. D. Angelis, "*Electronic and optical properties of mapbx3 perovskites (x = i, br, cl): a unified dft and gw theoretical analysis*", Phys. Chem. Chem. Phys. **18** (2016) 27158–27164.

[273] J. Even, L. Pedesseau, J. M. Jancu and C. Katan, "*Importance of spin-orbit coupling in hybrid organic/inorganic perovskites for photovoltaic applications*", J. Phys. Chem. Lett. **4** (2013) 2999–3005.

[274] C. Bernal and K. Yang, "*First-principles hybrid functional study of the organic-inorganic perovskites ch3nh3snbr3 and ch3nh3sni3*", J. Phys. Chem. C **118** (2014) 24383–24388.

[275] F. Zheng, H. Takenaka, F. Wang, N. Z. Koocher and A. M. Rappe, "*First-principles calculation of bulk photovoltaic effect in ch3nh3pbi3 and ch3nh3pbi3−xclx*", J. Phys. Chem. Lett. **6** (2015) 31–37.

[276] J. Even, L. Pedesseau and C. Katan, "*Theoretical insights into multibandgap hybrid perovskites for photovoltaic applications*", Proc. SPIE **9140** (2014) 91400Y.

[277] M. Kepenekian, R. Robles, C. Katan, D. Sapori, L. Pedesseau and J. Even, "*Rashba and dresselhaus effects in hybrid organic-inorganic perovskites: From basics to devices*", ACS Nano **9** (2015) 11557–11567.

[278] X. Che, B. Traore, C. Katan, M. Kepenekian and J. Even, "*Does the rashba splitting in ch3nh3pbbr3 arise from 2 x 2 surface reconstruction?*", Phys. Chem. Chem. Phys. **20** (2018) 9638–9643.

[279] Z. Deng, F. Wei, S. Sun, G. Kieslich, A. K. Cheetham and P. D. Bristowe, "*Exploring the properties of lead-free hybrid double perovskites using a combined computational-experimental approach*", J. Mater. Chem. A **4** (2016) 12025–12029.

[280] D. H. Fabini, T. Hogan, H. A. Evans, C. C. Stoumpos, M. G. Kanatzidis and R. Seshadri, "*Dielectric and thermodynamic signatures of low-temperature glassy dynamics in the hybrid perovskites ch3nh3pbi3 and hc(nh2)2pbi3*", J. Phys. Chem. Lett. **7** (2016) 376–381.

[281] C. W. Myung, J. Yun, G. Lee and K. S. Kim, "*A new perspective on the role of a-site cations in perovskite solar cells*", Adv. Energy Mater. **8** (2018) 1702898.

[282] H. Cho, J. S. Kim, Y.-H. Kim and T.-W. Lee, "*Influence of a-site cation on the thermal stability of metal halide perovskite polycrystalline films*", J. Inf. Disp. **19** (2018) 53–60.

[283] J. R. O. and O. Gunnarsson, "*The density functional formalism, its applications and prospects*", Rev. Mod. Phys. **61** (1989) 689–746.

[284] L. Kronik and S. Kümmel, "*Gas-phase valence-electron photoemission spectroscopy using density functional theory*", Top. Curr. Chem. **347** (2014) 137–192.

[285] A. Mehdizadeh, S. F. Akhtarianfar and S. Shojaei, "*Role of methylammonium rotation in hybrid halide mapbx3 (x= i, br, and cl) perovskites by a density functional theory approach: optical and electronic properties*", J. Phys. Chem. C **123** (2019) 6725–6734.

[286] K. Frohna, T. Deshpande, J. Harter, W. Peng, B. A. Barker, J. B. Neaton, S. G. Louie, O. M. Bakr, D. Hsieh and M. Bernardi, "*Inversion symmetry and bulk rashba effect in methylammonium lead iodide perovskite single crystals*", Nat. Commun. **9** (2018) 1829.

[287] S. McKechnie, J. M. Frost, D. Pashov, P. Azarhoosh, A. Walsh and M. van Schilfgaarde, "*Dynamic symmetry breaking and spin splitting in metal halide perovskites*", Phys. Rev. B **98** (2018) 085108.

[288] C. R. Ast, J. Henk, A. Ernst, L. Moreschini, M. C. Falub, D. Pacilé, P. Bruno, K. Kern and M. Grioni, "*Giant spin splitting through surface alloying*", Phys. Rev. Lett. **98** (2007) 186807.

[289] Z. Xiao, Y. Yuan, Y. Shao, Q. Wang, Q. Dong, C. Bi, P. Sharma, A. Gruverman and J. Huang, "*Giant switchable photovoltaic effect in organometal trihalide perovskite devices*", Nat. Mater. **14** (2015) 193–198.

[290] X. Wang, M. Li, B. Zhang, H. Wang, Y. Zhao and B. Wang, "*Recent progress in organometal halide perovskite photodetectors*", organic Electronics **52** (2018) 172–183.

[291] C. A. R. Perini, A. J. Barker, M. Sala, A. Petrozza and M. Caironi, "*High speed solution-processed hybrid perovskite photodetectors with low dark current enabled by a low temperature metal oxide interlayer*", Semiconductor science and Technology **33** (2018) 094004.

[292] W. Tian, C. Zhao, J. Leng, R. Cui and S. Jin, "*Visualizing carrier diffusion in individual single-crystal organolead halide perovskite nanowires and nanoplates*", J. Am. Chem. Soc. **137** (2015) 12458–12461.

[293] M. T. Hörantner, T. Leijtens, M. E. Ziffer, G. E. Eperon, M. G. Christoforo, M. D. McGehee and H. J. Snaith, "*The potential of multijunction perovskite solar cells*", ACS Energy Lett. **2** (2017) 2506–2513.

[294] M. Filipic, P. Loeper, B. Niesen, S. De Wolf, J. Krc, C. Ballif and M. Topic, "*Ch3nh3pbi3 perovskite/silicon tandem solar cells: Characterization based optical simulations*", Optics Express **23** (2015) A263–A278.

[295] S. Foster and S. John, "*Light-trapping design for thin-film silicon-perovskite tandem solar cells*", J. Appl. Phys **120** (2016) 103103.

[296] K. A. Bush, A. F. Palmstrom, Z. J. Yu, M. Boccard, R. Cheacharoen, J. P. Mailoa, D. P. McMeekin, R. L. Z. Hoye, C. D. Bailie, T. Leijtens, I. M. Peters, M. C. Minichetti, N. Rolston, R. Prasanna, S. Sofia, D. Harwood, W. Ma, F. Moghadam, H. J. Snaith, T. Buonassisi et al., "*23.6%-efficient monolithic perovskite/silicon tandem solar cells with improved stability*", Nat. Energy **2** (2017) 17009.

[297] W. Zia, X. Rena, X. Rena, Q. Weia, F. Gaoa and S. F. Liu, "*Perovskite/germanium tandem: A potential high efficiency thin film solar cell design*", Opt. Commun. **380** (2016) 1–5.

[298] Y. Li, H. Hu, B. Chen, T. Salim, J. Zhang, J. Ding, N. Yuan and Y. M. Lam, "*Reflective perovskite solar cells for efficient tandem applications*", J. Mater. Chem. C **5** (2017) 134–139.

[299] E. T. Hoke, D. J. Slotcavage, E. R. Dohner, A. R. Bowring, H. I. Karunadasa and M. D. McGehee, "*Reversible photo-induced trap formation in mixed halide hybrid perovskites for photovoltaics*", Chem. Sci. **6** (2015) 613–617.

[300] S. J. Yoon, S. Draguta, J. S. Manser, O. Sharia, W. F. Schneider, M. Kuno and P. V. Kamat, "*Tracking iodide and bromide ion segregation in mixed halide lead perovskites during photoirradiation*", ACS Energy Lett. **1** (2016) 290–296.

[301] S. J. Yoon, K. G. Stamplecoskie and P. V. Kamat, "*How lead halide complex chemistry dictates the composition of mixed halide perovskites*", J. Phys. Chem. Lett. **7** (2016) 1368–1373.

[302] G. F. Samu, C. Janaky and P. V. Kamat, "*A victim of halide ion segregation. how light soaking affects solar cell performance of mixed halide lead perovskites*", ACS Energy Lett. **2** (2017) 1860–1861.

[303] S. Draguta, O. Sharia, S. J. Yoon, M. C. Brennan, Y. V. Morozov, J. S. Manser, P. V. Kamat, W. F. Schneider and M. Kuno, "*Rationalizing the light-induced phase separation of mixed halide organic–inorganic perovskites*", Nat. Commun. **8** (2017) 200.

[304] D. W. deQuilettes, W. Zhang, V. M. Burlakov, D. J. Graham, T. Leijtens, A. Osherov, V. Bulovic, H. J. Snaith, D. S. Ginger and S. D. Stranks, "*Photo-induced halide redistribution in organic-inorganic perovskite films*", Nat. Commun. **7** (2016) 11683.

[305] D. J. Slotcavage, H. I. Karunadasa and M. D. McGehee, "*Light-induced phase segregation in halide-perovskite absorbers*", ACS Energy Lett. **1** (2016) 1199–1205.

[306] M. C. Brennan, S. Draguta, P. V. Kamat and M. Kuno, "*Light-induced anion phase segregation in mixed halide perovskites*", ACS Energy Lett. **3** (2018) 204–213.

[307] W. Huang, S. J. Yoon and P. Sapkota, "*Effect of light illumination on mixed halide lead perovskites: Reversible or irreversible transformation*", ACS Appl. Energy Mater. **1** (2018) 2859–2865.

[308] H. Zhang, X. Fu, Y. Tang, H. Wang, C. Zhang, W. W. Yu, X. Wang, Y. Zhang and M. Xiao, "*Phase segregation due to ion migration in all-inorganic mixed-halide perovskite nanocrystals*", Nat. Commun. **10** (2019) 1088.

[309] W. Mao, C. R. Hall, A. S. R. Chesman, C. Forsyth, Y.-B. Cheng, N. W. Duffy, T. A. Smith and U. Bach, "*Visualizing phase segregation in mixed-halide perovskite single crystals*", Angew. Chem. **58** (2019) 2893–2898.

[310] H. Y. Yen, P. W. Liang, C. C. Chueh, Z. B. Yang, A. K. Y. Jen and H. L. Wang, "*Large grained perovskite solar cells derived from single-crystal perovskite powders with enhanced ambient stability*", ACS Appl. Mater. Interfaces **8** (2016) 14513–14520.

[311] B. X. Chen, W. G. Li, H. S. Rao, Y. F. Xu, D. B. Kuang and C. Y. Su, "*Large-grained perovskite films via faxma1− xpb(ixbr1− x)3 single crystal precursor for efficient solar cells*", Nano Energy **34** (2017) 264–270.

[312] D. Prochowicz, P. Yadav, M. Saliba, M. Saski, S. M. Zakeeruddin, J. Lewinski and M. Gratzel, "*Reduction in the interfacial trap density of mechanochemically synthesized mapbi3*", ACS Appl. Mater. Interfaces **9** (2017) 28418–28425.

[313] Y. C. Choi, S. W. Lee, H. J. Jo, D.-H. Kim and S.-J. Sung, “*Controlled growth of organic-inorganic hybrid ch3nh3pbi3 perovskite thin films from phase-controlled crystalline powders*”, RSC Adv. **6** (2016) 104359–104365.

[314] W. Zhu, C. Bao, F. Li, T. Yu, H. Gao, Y. Yi, J. Yang, G. Fu, X. Zhou and Z. Zou, “*A halide exchange engineering for ch3nh3pbi3-xbrx perovskite solar cells with high performance and stability*”, Nano Energy **19** (2016) 17–26.

[315] J. He and T. Chen, “*Additive regulated crystallization and film formation of ch3nh3pbi3-xbrx for highly efficient planar-heterojunction solar cells*”, J. Mater. Chem. A **3** (2015) 18514–18520.

[316] J. H. Noh, S. H. Im, J. H. Heo, T. N. Mandal and S. I. Seok, “*Chemical management for colorful, efficient, and stable inorganic—organic hybrid nanostructured solar cells*”, ACS Appl. Mater. Interfaces **13** (2013) 1764—1769.

[317] F. Brivio, C. Caetano and A. Walsh, “*Thermodynamic origin of photoinstability in the ch3nh3pb(i1-xbrx)3 hybrid halide perovskite alloy*”, J. Phys. Chem. Lett. **7** (2016) 1083–1087.

[318] A. J. Barker, A. Sadhanala, F. Deschler, M. Gandini, S. P. Senanayak, P. M. Pearce, E. Mosconi, A. J. Pearson, Y. Wu, A. R. S. Kandada, T. Leijtens, F. D. De Angelis, S. E. Dutton, A. Petrozza and R. Friend, “*Defect-assisted photoinduced halide segregation in mixed-halide perovskite thin films*”, ACS Energy Lett. **2** (2017) 1416–1424.

[319] B. Zhang, F. Guo, J. Xue, L. Yang, Y. Zhao, M. Ge, Q. Cai, B. Liu, Z. Xie, D. Chen, H. Lu, R. Zhang and Y. Zheng, “*Photoluminescence study of the photoinduced phase separation in mixed-halide hybrid perovskite ch3nh3pb(brxi1-x)3 crystals synthesized via a solvothermal method*”, Sci. Rep. **7** (2017) 17695.

[320] C. Eames, J. M. Frost, P. R. F. Barnes, B. C. O’Regan, A. Walsh and M. S. Islam, “*Ionic transport in hybrid lead iodide perovskite solar cells*”, Nat. Commun. **6** (2015) 7497.

[321] J. S. Yun, J. Seidel, J. Kim, A. M. Soufiani, S. Huang, J. Lau, N. J. Jeon, S. I. Seok, M. A. Green and A. Ho-Baillie, “*Critical role of grain boundaries for ion migration in formamidinium and methylammonium lead halide perovskite solar cells*”, Adv. Energy Mater. **6** (2016) 1600330.

[322] H. Yuan, E. Debroye, K. Janssen, H. Naiki, C. Steuwe, G. Lu, M. Moris, E. Orgiu, H. Uji-i, F. D. Schryver, P. Samori, J. Hofkens and M. Roeffaers, “*Degradation of methylammonium lead iodide perovskite structures through light and electron beam driven ion migration*”, J. Phys. Chem. Lett. **7** (2016) 561–566.

[323] X. Tang, M. v. d. Berg, E. Gu, A. Horneber, G. J. Matt, A. Osvet, A. J. Meixner, D. Zhang and C. J. Brabec, “*Local observation of phase segregation in mixed-halide perovskite*”, Nano Lett. **18** (2018) 2172–2178.

[324] E. Mosconi, D. Meggiolaro, H. J. Snaith, S. D. Stranks and F. De Angelis, “*Light-induced annihilation of frenkel defects in organo-lead halide perovskites*”, Energy Environ. Sci. **9** (2016) 3180–3187.

[325] T. Ivanovska, C. Dionigi, E. Mosconi, F. De Angelis, F. Liscio, V. Morandi and G. Ruani, “*Long-lived photoinduced polarons in organohalide perovskites*”, J. Phys. Chem. Lett. **8** (2017) 3081–3086.

[326] G. E. Eperon, M. T. Horantner and H. J. Snaith, "*Metal halide perovskite tandem and multiple-junction photovoltaics*", Nature Reviews Chemistry **1** (2017) 0095.

[327] J. H. Heo, D. S. Lee, D. H. Shin and S. H. Im, "*Recent advancements in and perspectives on flexible hybrid perovskite solar cells*", J. Mater. Chem. A **7** (2019) 888–900.

[328] J. Huang, Y. Yuan, Y. Shao and Y. Yan, "*Understanding the physical properties of hybrid perovskites for photovoltaic applications*", Nature Reviews Materials **2** (2017) 17042.

[329] A. Rajagopal, S. T. Williams, C.-C. Chueh and A. K.-Y. Jen, "*Abnormal current—voltage hysteresis induced by reverse bias in organic-inorganic hybrid perovskite photovoltaics*", J. Phys. Chem. Lett. **7** (2016) 995—1003.

[330] L. Contreras-Bernal, C. Aranda, M. Valles-Pelarda, T. T. Ngo, S. R. Terrón, J. J. Gallardo, J. Navas, A. Guerrero, I. Mora-Seró, J. Idígoras and J. A. Anta, "*Homeopathic perovskite solar cells: Effect of humidity during fabrication on the performance and stability of the device*", J. Phys. Chem. C **122** (2018) 5341–5348.

[331] Q. Zhang, F. Hao, J. Li, Y. Zhou, Y. Wei and H. Lin, "*Perovskite solar cells: must lead be replaced-and can it be done?*", Science and Technology of Advanced Materials **19** (2018) 425–442.

[332] J. H. Im, C. R. Lee, W. Lee, J., S. W. Park and P. N. G., "*6.5% efficient perovskite quantum-dot-sensitized solar cell*", Nanoscale **3** (2011) 4088–4093.

[333] J. T. W. Wang, J. M. Ball, E. M. Barea, A. Abate, J. A. Alexander-Webber, J. Huang, M. Saliba, I. Mora-Sero, J. Bisquert and S. H. J., "*Low-temperature processed electron collection layers of graphene/tio$_2$ nanocomposites in thin film pscs*", Nano Lett. **14** (2014) 724–730.

[334] W. S. Yang, J. H. Noh, N. J. Jeon, Y. C. Kim, S. Ryu, J. Seo and S. Seok, "*High-performance photovoltaic perovskite layers fabricated through intramolecular exchange*", Science **348** (2015) 1234–1237.

[335] K. Leo, "*Perovskite photovoltaics: signs of stability*", Nat. Nanotechnol. **10** (2015) 574–575.

[336] N. Ahn, D. Y. Son, I. H. Jang, S. M. Kang, M. Choi and N.-G. Park, "*Highly reproducible perovskite solar cells with average efficiency of 18.3% and best efficiency of 19.7% fabricated via lewis base adduct of lead(ii) iodide*", J. Am. Chem. Soc. **137** (2015) 8696–8699.

[337] Y. C. Choi, S. W. Lee and D.-H. Kim, "*Antisolvent-assisted powder engineering for controlled growth of hybrid ch3nh3pbi3 perovskite thin films*", APL Mater. **5** (2017) 026101.

[338] X. Wu, J. Wang and E. K. L. Yeow, "*Ultralong perovskite microrods: One-versus two-step synthesis and enhancement of hole-transfer during light soaking*", J. Phys. Chem. C **120** (2016) 12273–12283.

[339] E. Edri, S. Kirmayer, A. Henning, S. Mukhopadhyay, K. Gartsman, Y. Rosenwaks, G. Hodes and D. Cahen, "*Why lead methylammonium tri-iodide perovskite-based solar cells require a mesoporous electron transporting scaffold (but not necessarily a hole conductor)*", Nano Lett. **14** (2014) 1000–1004.

[340] J. Burschka, N. Pellet, S.-J. Moon, R. H.-Baker, P. Gao, M. K. Nazeeruddin and M. Gratzel, "*Sequential deposition as a route to high-performance perovskite-sensitized solar cells*", Nature **499** (2013) 316–320.

[341] N. Ahn, S. M. Kang, J. W. Lee, M. Choi and N.-G. Park, "*Thermodynamic regulation of ch3nh3pbi3 crystalgrowth and its effect on photovoltaic performance of perovskite solar cells*", J. Mater. Chem. A **3** (2015) 19901–19906.

[342] S. Albrecht, M. Saliba, J. P. C. Baena, F. Lang, L. Kegelmann, M. Mews, L. Steier, A. Abate, J. Rappich, L. Korte, R. Schlatmann, M. K. Nazeeruddin, A. Hegfeldt, M. Gratzel and B. Rech, "*Monolithic perovskite/silicon-heterojunction tandem solar cells processed at low temperature*", Energy Environ. Sci. **9** (2016) 81–88.

[343] J. Chen, S. Zhou, S. Jin, H. Li and T. Zhai, "*Crystal organometal halide perovskites with promising optoelectronic applications*", J. Mater. Chem. C **4** (2016) 11–27.

[344] F. Li, C. Ma, H. Wang, W. Hu, W. Yu, A. D. Sheikh and T. Wu, "*Ambipolar solution-processed hybrid perovskite phototransistors*", Nat. Commun. **6** (2015) 8238.

[345] T. Park, J. Na, B. Kim, Y. Kim, H. Shin and E. Kim, "*Photothermally activated pyroelectric polymer films for harvesting of solar heat with a hybrid energy cell structure*", ACS Nano **9** (2015) 11830–11839.